Accretion Disks and the Formation of Stellar Systems

by

Kaitlin Michelle Kratter

A thesis submitted in conformity with the requirements
for the degree of Doctor of Philosophy
Graduate Department of Astronomy and Astrophysics
University of Toronto

Abstract

Accretion Disks and the Formation of Stellar Systems

Kaitlin Michelle Kratter
Doctor of Philosophy
Graduate Department of Astronomy and Astrophysics
University of Toronto
2010

In this thesis, we examine the role of accretion disks in the formation of stellar systems, focusing on young massive disks which regulate the flow of material from the parent molecular core down to the star. We study the evolution of disks with high infall rates that develop strong gravitational instabilities. We begin in chapter 1 with a review of the observations and theory which underpin models for the earliest phases of star formation and provide a brief review of basic accretion disk physics, and the numerical methods that we employ. In chapter 2 we outline the current models of binary and multiple star formation, and review their successes and shortcomings from a theoretical and observational perspective. In chapter 3 we begin with a relatively simple analytic model for disks around young, high mass stars, showing that instability in these disks may be responsible for the higher multiplicity fraction of massive stars, and perhaps the upper mass to which they grow. We extend these models in chapter 4 to explore the properties of disks and the formation of binary companions across a broad range of stellar masses. In particular, we model the role of global and local mechanisms for angular momentum transport in regulating the relative masses of disks and stars. We follow the evolution of these disks throughout the main accretion phase of the system, and predict the trajectory of disks through parameter space. We follow up on the predictions made in our analytic models with a series of high resolution, global numerical experiments in chapter 5. Here we propose and test a new parameterization for describing rapidly accreting, gravitationally unstable disks. We find that disk properties and system multiplicity can be mapped out

well in this parameter space. Finally, in chapter 6, we address whether our studies of unstable disks are relevant to recently detected massive planets on wide orbits around their central stars.

Dedication

To my mother, for her love, support, and confidence

To my father, who always told me ‘do something interesting, like astrophysics’

To my brother, for setting the bar all along

And to Grandpa Leo, who would have been proudest of all

Acknowledgements

This thesis was funded jointly by the Connaught Doctoral Student Scholarship, the University of Toronto and an Ontario Graduate Scholarship.

First, I would like to thank my thesis advisor, Chris Matzner, for his support, insight, and enthusiasm over the last five years, and for suggesting a first year project that turned out to be far more interesting than either of us imagined.

Secondly, I would like to acknowledge the contributions of my co-authors, without whom I could not have completed these projects. I am grateful to Mark Krumholz for approaching me at a conference when I was just starting out, and for his continued guidance. I would like to thank Ruth Murray-Clay and Andrew Youdin for their important contributions to the final chapter of this thesis. I am also grateful to Richard Klein for his thoughtful comments, and for providing the numerical code used in chapter five.

I would also like to acknowledge the faculty and post docs in the department, CITA, and elsewhere for fruitful discussions, and technical assistance. In particular Jonathan Dursi for lending his extensive computational expertise and crucial moral support. I am also indebted to my first reearch advisor, Charles Liu, for throwing me in to the deep end, in a good way.

Finally, thanks to all the friends who got me here, and kept me going. Especially:

Darren, for the confidence to pursue something hard

Alexis, Andy, Aleks, and KB, for reminding me how to have fun

Bart, Julia, Derek, and Oasis, for their crucial contributions to Chapter 7 of this thesis

Lawrence, for setting all the right examples, and showing inconceivable tolerance to an over-eager first year

Sha-non, Aroy, Nicky, and Pena, for the company, 12th floor pride, and Timmy's

And Andrew, for all the catches, the unfrozen water, the snowy drives, and the warm meals. And most of all, for holding my hand.

Contents

List of Tables

List of Figures

Chapter 1

Introduction

1.1 Motivation

The focus of this thesis is on understanding the role of accretion disks in the earliest phases of star formation, with careful consideration of the differences between single and multiple systems. In particular, we focus on the role of gravitational instabilities in driving accretion and fragmentation in young, massive, protostellar disks.

In order to explore these questions we employ two complimentary techniques. On the one hand, we use simplified semi-analytic models to tease out the important parameters of the problems we explore. These simple models allow us to take into account different physical effects and explore a broad range of parameter space. This technique is key to our ability to make general inferences about the behavior of accretion disks across the entire stellar mass function. Of course this type of analysis is limited because we must use somewhat crude approximations of complex phenomena: for example, we reduce complex non-linear instabilities to a few algebraic definitions. And so to complement these investigations, we also perform high resolution, targeted numerical experiments informed by our simple models. This combined approach has provided insight into angular momentum transport via gravitational instability, and in particular the saturation of the instability in massive disks with ongoing mass accretion.

This work began as an investigation into the role of disks in the formation of massive stars. We first used a quasi-steady state model to delineate the parameters of gravitationally unstable disks around massive stars, showing that fragmentation was likely, and that such disks might have much in common with AGN (chapter 3). Our initial inquiry led to a much broader exploration of the role of massive accretion disks in the formation

of binaries and hierarchical multiples. We produced evolutionary tracks for non-steady state, gravitationally unstable disks around stars across a broad mass range in order to track the state of disks and system multiplicity throughout the embedded phase of star formation (chapter 4). To check our prescription for accretion in self-gravitating disks, we conducted numerical experiments using a new parameterization for rapidly accreting disks, which appear to be common in many astrophysical contexts (chapter 5). Finally, following the discovery of widely orbiting planets around massive stars, we conducted a careful case study of a single system to assess the viability of disk fragmentation for producing massive planets (chapter 6). In future work will we turn our attention toward other astrophysical disk settings which may benefit from the analysis tools developed here: Population III protostellar disks, active galactic nuclei, and black hole-binary systems.

Based on this work, we make three main predictions. First, we predict that the bulk of stars greater than about a solar mass will experience a massive disk phase soon after the formation of the disk. Secondly, we predict that many binary and multiple systems with separations less than a few hundred AU may have a been produced in disks, at least around more massive stars. Finally, we suggest that these two predictions together may help explain two long-standing problems in star formation: the so-called "angular momentum" problem, and the "luminosity problem."

In this introductory chapter, I review our current understanding of the early phases of star formation, along with a summary of observed properties of protostellar and protoplanetary disks. I then discuss standard accretion disk theory, and review possible mechanisms for angular momentum transport in disks. I conclude with a brief discussion of the numerical techniques we have used for the simulations presented in chapter 5. In chapter 2, I review the standard models for binary formation, and some of the successes and shortcomings of these theories.

1.2 Disks and the Earliest Phases of Star Formation

It is difficult to pinpoint the beginning of the star formation process, and researchers in different subfields tend to disagree on the important indicators of the onset of star formation. For example, when viewed from cosmological scales, star formation starts when a Giant Molecular Cloud (GMC) begins to form. Zooming in to the scale of an entire galaxy, star formation begins when the GMC starts to collapse on itself. If only

the GMC, or a subsection of it, is considered, then the onset of star formation becomes even trickier to define. Is it the formation of a marginally bound core that is important? Is it the formation of a central hydrostatic protostar?

These uncertainties arise because we can never see more than a snapshot in one protostar's or cloud's evolution. We cannot see that something we define as a "prestellar core" ever goes on to form a star. As with all astronomical sources, we place different objects into an evolutionary sequence in order to tell the complete story of the star formation process. Observationally, much effort has been put into classifying cold, star-forming clumps of gas by age and evolutionary state based on their infrared spectral slope. Although there are many uncertainties due to source geometry, this method appears to be a reliable predictor of evolutionary state. Protostellar cores are divided into three classes (Adams et al., 1987; Andre et al., 1993; McKee & Ostriker, 2007).

Class 0 sources are the youngest, thought to contain embedded protostars less than 10^5 years old. The dust and gas efficiently obscure the light shortward of about $10\mu m$, and so the sources are bright in the submillimeter. While disks are presumably present at this time, and their contribution is included in many radiative transfer models (Robitaille et al., 2007), they are difficult to detect unambiguously. Significant progress towards understanding disks in the Class 0 phase of low mass star formation has been made recently by combining infrared spectra from IRS with submillimeter data from CARMA (Enoch et al., 2009); however, many modeling uncertainties persist. Investigations are also limited to the nearest objects.

By the time the source reaches the Class I phase, defined by a positive infrared (IR) spectral slope, $b_{IR} = d\ \log\lambda \mathrm{F}_\lambda / \mathrm{d}\ \log\lambda$, both the disk and the envelope contribute to the observed IR luminosity. The optical depth through the envelope is thought to be reduced due to both accretion onto the central object and by protostellar outflows. Systems move into the Class II phase when the bulk of the core mass is in either the disk or the star, with little ongoing infall, as indicated by a negative IR spectral slope ($0 > b_{IR} > -3/2$). Finally Class III systems are classic, low accretion rate T Tauri stars. Such systems have a spectral slope $b_{IR} < -3/2$. While the stars have not yet reached the main-sequence, the core mass has been either accreted or blown out, leaving a revealed, low mass disk in which we presume planet formation begins. Due to the longer duration of this phase, we are able to observe many more systems in the later evolutionary stage. Moreover, because they are unobscured, we can observe these disks at shorter wavelengths, and thus higher resolution.

This thesis focuses on the role that disks play during the Class 0-I phase of star formation. Although this embedded phase is likely the one during which most accretion onto the star occurs, the properties of disks during this period have received relatively little attention. This phase is difficult to model analytically because embedded disks are subject to large, non-linear perturbations due to rapid accretion of mass and angular momentum, making local models and linear stability analyses insufficient.

While our knowledge of the embedded phase of today is limited, it will soon come into sharp focus as new instruments such as the Expanded Very Large Array (EVLA) and Atacama Large Millimeter Array (ALMA) become operational. In this thesis we aim to make predictions for these next generation telescopes.

1.2.1 Observations of Protostellar Disks

Data from optical, infrared, and submillimeter telescopes provide an ever more complete description of revealed protostellar disks at different ages, masses, and size scales. In the optical we typically observe starlight scattered by the upper and lower surfaces of young, irradiated disks (Padgett et al., 1999). Sub-millimeter and millimeter date provide information on large scales ($\sim 1000's$ of AU), and estimates of disk masses and dust properties (e.g Andrews & Williams 2007). Infrared data has helped to constrain disk temperatures, and search for dusty substructures in the inner disk, sometimes providing evidence for inner-disk holes (Calvet et al., 2005). These observations provide end-state boundary conditions for the kinds of models presented here. We can glean several important features from these data sets.

Disk Masses

Disk masses are primarily constrained by measurements of (sub)millimeter fluxes. The most widely used method to deduce disk masses is to observe disks at long wavelengths where they are presumably optically thin, and then use a model for dust opacities to convert fluxes into dust masses. This is converted into a gas mass assuming that the ratio of gas to dust (100 to 1) holds in disks as it does in the ISM (Beckwith et al., 1990; Eisner et al., 2008). Each of these assumptions provides large room for error. First, the assumption that the disks are optically thin at submillimeter wavelengths may be incorrect, and secondly the dust opacity models are quite uncertain due to grain growth from ISM like sub-micron sized grains up to mm-cm sizes or greater. While multi-

wavelength data can be used to better constrain the dust size spectrum, up to an order of magnitude uncertainties in final masses remains (McKee & Ostriker, 2007; Andrews et al., 2009). In particular, information about the presence of much larger bodies that are expected to seed planet formation (100m-100km) remains elusive.

Disregarding the large bodies, observations show that the bulk of $>$ Myr old disks around most solar-type stars are very low in mass, only $10^{-3}M_{\odot}$. More recent work on younger clusters has found disks with inferred masses up to a few tenths of a solar mass (Eisner et al., 2008), but these are relatively rare. Thus many protoplanetary disks have inferred masses lower than the combined planetary mass in comparable exoplanetary systems. This suggests that some larger bodies may already have formed on Myr timescales (Andrews et al., 2009). For modelers of early stage disks, it suggests that whatever transport mechanisms are at work must successfully drain the disk of most material during the embedded phase. Perhaps being embedded, e.g. having periods of high mass infall rates, is the key to driving accretion.

Disk Lifetimes

By looking at the relative fraction of stars with infrared excess in young clusters (Hernández et al., 2007), and by searching for signatures of accretion in stellar spectra (Jayawardhana et al., 2006), we find that typical gas disks around low mass stars live for several to 10 Myr. The constraints on disks around higher mass stars are less clear, but Herbig AeBe disks appear to be shorter lived than their low-mass counterparts. The fraction of 3 Myr old B, A, and F stars with IR excess is an order of magnitude lower than that for stars with $M \leq M_{\odot}$ (Hernández et al., 2005).

These measurements also provide constraints on the formation of gas giant planets, reinforcing the conclusions that planet formation must take place within a few million years (though rocky planets might still form at later times). The accretion rates measured in old T-Tauri disks are quite low compared to those expected during the embedded phase (only a few $10^{-8}M_{\odot}$/Yr). It seems likely that different angular momentum transport mechanisms are at work at different phases of disk evolution. Directly measuring accretion rates in the youngest sources is difficult, but as we discuss in chapter 2, we can infer high accretion rates from the star formation timescale, stellar masses, and late time accretion rates. With these observational results in hand, we now review the physical mechanisms responsible for driving accretion and angular momentum transport.

1.3 Disk Physics: Mechanisms for Angular Momentum Transport

In the past half century, enormous progress has been made towards understanding the physical mechanism which drives inward accretion of material and outward transport of angular momentum. The entire literature of accretion disk physics is too broad to review here, so we focus on mechanisms for angular momentum transport in protostellar disks.

To study the behavior and evolution of accretion disks, it is useful to transform the fluid equations into their vertically integrated forms by making the thin disk approximation: we assume that the vertical length scale, H, is much less than the disk radius, r. In general this also implies that the disk is in hydrostatic equilibrium in the vertical direction, which allows one to define the disk scaleheight, $H = c_s/\Omega$, where c_s is the disk sound speed, and $\Omega = \sqrt{GM_*/r^3}$ is the Keplerian orbital frequency around a star with mass M_*.

Although we shall see through the course of this thesis that protostellar disks are not always in this limit, it makes the problem more tractable. An even greater simplification can be made by assuming that the disk is in steady-state, with a constant accretion rate, $\dot{M}$, throughout, but we follow Papaloizou & Lin (1995) and allow for the addition / subtraction of matter and angular momentum, as we will study disks which are growing and changing in time. In cylindrical coordinates, the continuity equation becomes:

$$\frac{\partial \Sigma}{\partial t} + \frac{1}{r}\frac{\partial}{\partial r}(\Sigma r v_r) = S_\Sigma, \tag{1.1}$$

where $\Sigma = \int \rho dz$ is the disk surface density, v_r is the radial velocity, and S_Σ is a source term to account for accretion onto or out of the disk.

Translating the angular momentum conservation equation into the thin disk limit we have:

$$v_r \frac{d}{dr}(r^2\Omega) = \frac{1}{r\Sigma}\frac{d}{dr}(r^2\langle T_{r\phi}\rangle) + \frac{S_\Sigma j}{\Sigma} + \Lambda \tag{1.2}$$

where j is the specific angular momentum carried in or out with any accreted/expelled material, Λ is the rate of angular momentum injection due to an external torque or perturbation, and $\langle T_{r\phi}\rangle$ is the average of the vertically integrated stress tensor:

$$\langle T_{r\phi}\rangle = \langle \nu \rangle \Sigma r \frac{d\Omega}{dr} \tag{1.3}$$

$$\langle \nu \rangle = \frac{\int_{-\infty}^{\infty} \nu \rho dz}{\int_{-\infty}^{\infty} \rho dz} \tag{1.4}$$

Together, these two equations can be combined to give a single diffusion equation that governs the change in surface density in the disk in response to the various mechanisms for transport. Note that we have left out an energy equation, although vertical integration presumes that the disk is in hydrostatic balance. We return to details of disk thermodynamics in chapters 3 and 4. The combined diffusion equation is:

$$\frac{\partial \Sigma}{\partial t} - \frac{1}{r}\frac{\partial}{\partial r}\left[3r^{1/2}\frac{\partial}{\partial r}(\Sigma\langle\nu\rangle r^{1/2}) - \frac{2S_\Sigma j}{\Omega} - \frac{2\Sigma\Lambda}{\Omega}\right] - S_\Sigma = 0 \tag{1.5}$$

This formulation allows for several different modes of angular momentum transport as indicated by the different source terms in the square brackets. The first term is the familiar viscous transport term, often used in conjunction with a Shakura & Sunyaev (1973) α-viscosity parameterization (see §1.3.1). The second and third terms account for advection and external perturbations, due to, for example, disk winds (Pelletier & Pudritz, 1992) and the gravitational influence of companions (Goldreich & Tremaine, 1979) respectively. This diffusion equation (or its steady-state cousin) is the basis for much of the study of accretion disk behavior. We now proceed to discuss the proposed sources for the different terms in the diffusion equation.

In general, we neglect large scale magnetic fields in this work. As a consequence we do not discuss the role of magnetic braking on large sales, nor the possible role of disk winds. It is possible that magnetic braking plays a significant role in angular momentum transfer within cloud cores; however, numerical simulations in which the field remains well coupled to the fluid at all times often have difficulty producing the flattened disks that we observe (Mellon & Li, 2008). If ambipolar diffusion effectively allows the collapsing gas to decouple from the field, then neglecting magnetic braking in the disk may be a reasonable assumption. Moreover, if disk winds are best described by the so-called X-wind model of (Shu et al., 1994), then they are not likely responsible for removal of angular momentum on larger scales in the disks. Note that X-winds have also been invoked to explain the super heated Calcium Aluminim Inclusions (CAIs) found in meteorites. Protostellar outflows may also remove angular momentum; however, so long as they are launched from the inner disk, there must be a secondary mechanism for removal of angular momentum on large scales. For other mechanisms for global angular momentum transport by magnetic fields see Shu et al. (2007a).

1.3.1 Turbulence and Disk Viscosity

The most prominent mechanisms for angular momentum transport in disks are those which act as a local viscosity. In a differentially rotating flow, viscosity transports momentum orthogonal to the background velocity. We follow Frank et al. (2002), and argue that the exchange of gas parcels across a radius in a Keplerian flow will produce net outward angular momentum transport.

In a plane shearing flow (no gravity), it is straight forward to show that shear viscosity acts to try to smooth out velocity gradients. The exchange of particles (e.g. molecular viscosity) or fluid parcels (e.g. turbulent eddies) along the velocity gradient results in positive correlations between the streamwise and orthogonal velocities. Imagine the shear flow illustrated by Fig. 1.3.1 in which fluid parcels are exchanged across some height z_0 from above and below, conserving their linear momentum in the x direction, and exchanging no net mass. Here d is the characteristic length scale for exchange: in the case of molecular viscosity this would be comparable to the mean free path, and in the case of turbulent viscosity, an eddy scale length. The total upward momentum flux density in this interaction is:

$$\delta l \approx \rho v_z (v_x(z_0 - d/2) - (v_x(z_0 + d/2)). \tag{1.6}$$

Since the second term in brackets is larger, δl is negative, implying that angular momentum flows downward.

Thus shear viscosity will act to smooth out the velocity gradient, extracting linear momentum from the high velocity material. If we simply apply this logic to a Keplerian disk, where velocity increases inwards, we get the desired result: outward transport of angular momentum. Of course in this case viscosity will not actually change the velocity gradient which is set by the central object's potential, instead it causes material to move inwards to balance the outward transport of angular momentum.

However, there is a complication: in the plane shear flow, conserving linear momentum is equivalent to conserving the x-velocity (and angular momentum). In a Keplerian flow we could either imagine that parcels conserve angular momentum as they exchange places across some boundary, or that they retain their azimuthal velocities. Clearly in the former case, angular momentum would be transported *inwards*, and in the latter case outwards, because the velocity and angular momentum gradients in a Keplerian disk have opposite sign.

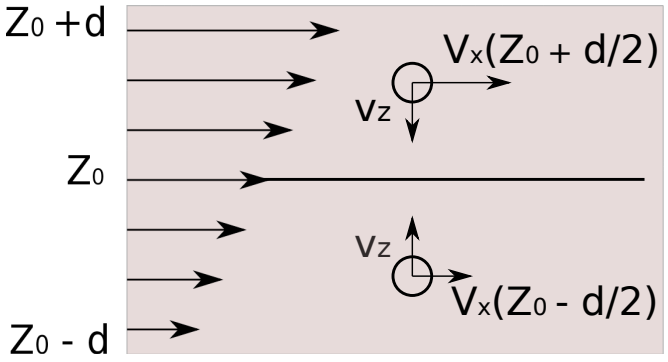

Figure 1.1: Exchange of fluid parcels in a plane shear flow as shown by Frank et al. (2002). v_z represents the average random velocity in the z direction at which particles are exchanged and v_x is the background shear velocity. d is the characteristic lengthscale of the interaction. In this example, shear viscosity tries to smooth out the velocity gradient.

There has been significant debate in the last half century over the direction of transport by turbulence in a disk. As shown by Greenberg (1988), in the case of particle disks like Saturn's rings, angular momentum is transported outwards when particles collide due to the shapes of epicyclic orbits. Unlike particle disks, gas disks feel pressure forces, and so unlike the idealized example above, or particle disks, fluid parcels cannot exchange places without interacting with the background flow. That turbulence generically generates outward transport of angular momentum under these circumstances remains unclear (see for example Lesur & Ogilvie 2010), although in the specific circumstances we discuss below, outward transport is expected.

Note that a range of numerical simulations of turbulence in disks show outward transport of angular momentum as well. However, caution is advised when taking this alone as evidence that the above interpretation is correct: many features of hydrodynamic codes (e.g. numerical viscosity due to the grid, artificial viscosity required to ensure stability) can mimic these effects.

The outward transport of angular momentum is also the energetically favorable direction for transport. Viscosity extracts energy from the differential rotation, and allows

it to dissipate as heat. This is consistent with our picture of an accretion disk in the sense that for matter to be moved towards the central object, it must lose energy from its orbit.

Moving forward with the assumption that shear viscosity does transport angular momentum outwards, what is its cause in observed accretion disks? The most familiar source on Earth, molecular viscosity, can be ruled out due to the high Reynolds numbers in astrophysical disks. The Reynolds number is the ratio of inertial forces to viscous forces in a flow. Assuming that particles move at the sound speed, c_s, and have a mean free path, λ, the effective Reynolds number in a disk is

$$\mathrm{Re} = \frac{r v_{\mathrm{kep}}}{c_s \lambda}. \tag{1.7}$$

The mean free path for molecules in terms of the disk column density is:

$$\lambda_d \approx 1/(N\sigma)\mathrm{cm} = \frac{\mathrm{c_s}\mu}{\Sigma\Omega\sigma}, \tag{1.8}$$

where σ is the molecular cross-section, Σ is the disk column density, N is the particle number density and μ is the mean particle mass. Substituting this in to equation (1.7), and plugging in reasonable values for a protostellar disk gives:

$$\mathrm{Re} \approx 5 \times 10^{14} \left(\frac{M_*}{1M_\odot}\right) \left(\frac{T}{400K}\right)^{-1} \left(\frac{\Sigma}{5 \times 10^3 \mathrm{g\ cm^{-2}}}\right) \left(\frac{r_d}{1\mathrm{AU}}\right) \left(\frac{\sigma}{10^{-15}\mathrm{cm}^2}\right). \tag{1.9}$$

Clearly, molecular viscosity is unimportant in this context. However, the extremely high Reynolds number (inadvertantly) leads us to the more likely candidate for effective disk viscosity: turbulence. As we discuss below, this is inadvertant in the sense that we have no evidence for hydrodynamically driven turbulence. Note that the magnetic Reynolds number (inertial forces compared to magnetic diffusion) in disks may also be large, depending on the local ionization fraction.

Shakura & Sunyaev (1973) made a simple *Ansatz* to parameterize disk viscosity generated by turbulence. In their case they were concerned with turbulence caused by magnetic fields in black hole accretion disks, but the expression can be defined independently. They posited that the effective viscosity should be proportional to pressure. In this case they were concerned with the magnetic pressure, however more generally we write:

$$\nu = \alpha \frac{c_s^2}{\Omega} = \alpha c_s H. \tag{1.10}$$

When we write the (vertically integrated) Reynolds stress tensor using α we see the pressure scaling more explicitly:

$$T_{r\phi} =< \Sigma v_R v_\phi >= \alpha \Sigma c_s^2 \left| \frac{\mathrm{d\ ln\ } \Omega}{\mathrm{d\ ln\ R}} \right|, \tag{1.11}$$

where Σc_s^2 is like a vertically integrated pressure.

The assumption inherent in this parameterization is that α is a numerical factor less than unity. If we envision the turbulent eddies acting as the fluid parcels described above, we expect the eddies to be no larger than the disk scale height (if this were not true, than clearly the scaleheight is being defined incorrectly), and the turbulence to be subsonic (supersonic eddies would quickly shock and heat the disk). Dimensional analysis then requires that $\alpha \lesssim 1$. If we return to our expression for the disk Reynolds number, equation (1.7), and imagine that the viscosity is due to turbulence rather than molecules, we find a Reynolds number of order $\alpha^{-1}(r/H)^2 \approx 10^2 - 10^4$ for H/R and α of $0.01 - 0.1$. Although still potentially a large number, turbulence is clearly more "viscous."

While this parameterization has proved useful in analytic studies of accretion disks – it allows us to place much of our uncertainty about angular momentum transport into a single number – it has perhaps stunted our exploration of true transport phenomena. For example, many subsequent studies of accretion disks have used a temporally and spatially constant value of α, although Shakura & Sunyaev (1973) explicitly warn that there is no reason to expect this. In this vein, in chapter 4 we construct a time variable α model for protostellar disks. Recent work has grown even more sophisticated, and there now exist α models which take into account different transport phenomena at different disk radii in order to model non-steady state disks (Zhu et al., 2008).

Another concern with the use of α-viscosity is the notion of locality. This prescription implies that the effective transport depends on the local pressure only. We shall see that for some physical mechanisms responsible for turbulence (e.g. the magnetorotational instability) this is a reasonable supposition, whereas for other types of transport (e.g. global gravitational instability) this is not the case.

Moreover, it now seems that reliance on the α-model may have led to the misinterpretation of instabilities such as the thermal instability (Lightman & Eardley, 1974) in radiation pressure dominated disks. In hot, radiation pressure dominated disks surrounding black holes, the thermal instability arises in an α model because of a positive feedback loop between heating and cooling. While heating due to dissipation scales as T^8/Σ, cooling due to radiative diffusion sales as T^4/Σ. Thus a positive temperature

perturbation causes a greater increase in heating than cooling, leading to thermal runaway (Hirose et al., 2009). While numerical simulations show that the turbulent stresses are proportional to the total (gas plus radiation) pressure, they do not find thermal instability. Instead they see that the rise in pressure lags behind the rise in stress. The pressure does not set the level at which turbulent stresses saturate; rather, the pressure responds on timescales longer than the thermal time to fluctuations in stresses (Hirose et al., 2009). This delay prevents the positive feedback loop implied by an α model.

Magnetic Fields as a Source of Turbulent Viscosity

The α parameterization originally dealt with magnetically generated stresses, but the dynamo mechanism described by Shakura & Sunyaev is not what we believe to be responsible for accretion disk turbulence. One of the most promising mechanisms for magnetized disk turbulence is the magnetorotational instability, or MRI (Balbus & Hawley 1994, Chandrasekhar 1961). A non-magnetized disk (or more generally, a Couette flow) is stable to axisymmetric perturbations according to the Rayleigh criterion:

$$\frac{d}{dr}|\Omega r^2| > 0, \tag{1.12}$$

which states that the flow is stable so long as angular momentum does not decrease outwards. However the addition of a weak, poloidal, magnetic field modifies this criterion so that is it the angular velocity, not angular momentum, which must not decrease outwards. The weak field acts as a spring that connects a fluid parcel perturbed radially to its original location. Imagine that a fluid parcel is displaced outwards as shown in Fig. 1.3.1. The magnetic tension acts to accelerate the parcel up to the angular velocity at its previous radius, which gives it more angular momentum, causing it to move outwards, which in turn creates greater tension in the field line and more transport. This runaway leads to outward angular momentum transport. Numerous numerical simulations show that this process efficiently generates turbulence under realistic conditions in protostellar disks. Although there were recently concerns about numerical convergence in simulations with no net flux (Fromang et al., 2007) it appears that even in the absence of net flux, vertical stratification allows the MRI to produce sufficient turbulence to be relevant for angular momentum transport in protostellar accretion disks, with effective $\alpha \sim 10^{-2}$ (Davis et al., 2010). This α is sufficiently large to explain the observed accretion in the T Tauri disks described above, however it is unclear that this mechanism provides sufficient transport in young, massive disks.

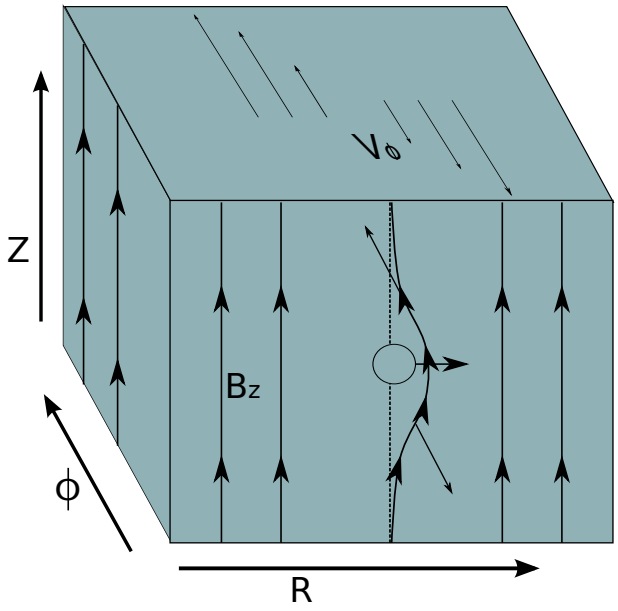

Figure 1.2: Small section of an accretion disk in the shearing box approximation. The disk is threaded by vertical field lines. A fluid parcel perturbed outwards will continue to be moved outwards as tension in the magnetic field line transfers angular momentum to the gas.

The main obstacle for the MRI in this context is that the disk must remain sufficiently ionized for the ideal MHD assumption of flux freezing. If the disk resistivity is too high, so that the field diffuses out of a fluid parcel faster than the MRI growth timescale, the MRI will not operate.

In many astrophysical accretion disks, the ionization fraction of the gas is not a concern. Disks around black holes and cataclysmic variables are likely to be thermally ionized. The inner regions of protostellar disks may be either thermally ionized, or x-ray ionized by the young protostar. However at larger distances from the host star, from a few to 10's of AU, the disk becomes colder and denser while the flux of ionizing photons drops. Because the disk is optically thick to cosmic rays at surface densities of order $100\mathrm{g/cm}^2$, and to ionizing photons at smaller columns, the ionization fraction becomes too small to maintain the MRI. At very large distances the disk can once again become coupled to the magnetic field due to decreasing optical depth (Gammie, 1996). Although the outer layers of the disk can remain ionized at all radii, and well coupled to a magnetic field, the interior becomes a so-called "dead zone" where there is no obvious mechanism for transport (Gammie, 1996). In Class 0-I disks, it seems that the bulk of the disk mass might comprise these dead zones, leading us to consider other mechanisms for angular momentum transport. Note that while dead zones pose a problem for accretion, they may be vital to another important process in protostellar disks: planet formation.

In an unmagnetized disk, there are two other proposed mechanisms for generating angular momentum transport: hydrodynamic instabilities and gravitational instabilities. One proposed hydrodynamic mechanism is a non-linear shear instability (Balbus & Hawley, 2006; Lithwick, 2007). Although unmagnetized Keplerian disks are linearly stable, linearly swinging modes, which have a non-zero radial wavenumber, can be amplified as the relative ratio of their wavenumbers evolves as they "swing" around the disk. If these modes couple together non-linearly they may produce turbulence. Lithwick (2007) has shown that non-linear coupling can occur leading to the generation of large vorticies in two-dimsional flows. Whether or not this can lead to sustained three-dimensional turbulence has yet to be demonstrated. Another model for generating vortices is the subcritical baroclinic instability of Lesur & Papaloizou (2010), which does appear to persist in local, three-dimensional simulations, but only generates relatively weak outward transport. In general, our ability to simulate hydrodynamic turbulence may be limited by the fact that our simulations cannot probe sufficiently high Reynolds number flows. Some have also proposed that convection within the disk could drive transport, but the direction of

transport is unclear (Ryu & Goodman 1992, Lesur & Ogilvie 2010). Since hydrodynamic mechanisms have thus far proved ineffective, we consider the other alternative: transport driven by disk self-gravity.

1.3.2 Transport in Self Gravitating Disks

Spiral Density Wave Theory

Global gravitational instabilities (hereafter GI) and mechanisms for generating spiral structure in disks have a long history in the literature (see for example Toomre 1977, and references therein), with applications to galaxies, and protostars, and pressureless and gaseous fluids. In the context of galaxies, there are two primary theories of spiral structure formation due to the interaction of self-gravity and shear. The first, due to Lin & Shu (1964) suggests that quasi-stationary density waves exist in the disk, causing material to concentrate at certain places in the potential creating the appearance of material spiral arms. These are thought to be long lived because the spiral pattern rotates slowly (and thus does not wind up due to differential rotation), allowing material to flow in and out of the troughs in the potential. Note that this is not an actual instability, as the waves do not grow exponentially, but propagate. The second theory, due to Toomre (1964) and Goldreich & Lynden-Bell (1965) suggests that spiral arms are formed and destroyed by waves growing, reflecting and being sheared out in the disk (Toomre (1981) later identified this as the so-called SWING mechanism). A half century on, the debate between these two theories continues. In the galactic context long-lived spiral structure may also result from interactions with triaxial halos (Dubinski & Chakrabarty, 2009) or interactions between the collisionless stellar and collisional gas components (Sellwood, 2010). In the context of protostellar disks, numerical simulations tend to show the formation of relatively short-lived material spiral arms, but the analysis used to find growing modes is common to all of these mechanisms.

Unstable (growing) modes are found via a WKB analysis of a differentially rotating fluid. The simplest case of an infinite shearing sheet was explored by Toomre (1964), and Safronov (1960). Modifying the analysis to include pressure, Lin & Shu (1964) and Goldreich & Lynden-Bell (1965) showed that waves of the form $e^{ikr+im\phi-i\omega t}$ follow the dispersion relation:

$$(\omega - m\Omega)^2 = k^2 c_s^2 + \kappa^2 - 2\pi G\Sigma|k|, \tag{1.13}$$

where ω is the wave frequency, m is the azimuthal mode number, and k the radial

wavenumber. There exists an exponentially growing $m = 0$ mode when:

$$Q = \frac{c_s \kappa}{\pi G \Sigma} < 1 \tag{1.14}$$

(Toomre, 1964) where the epicyclic frequency $\kappa \rightarrow \Omega$ for a Keplerian disk. This occurs because the region surrounding corotation ($\omega = m\Omega$) where waves are evanescent shrinks as $Q \rightarrow 1$ so that waves can tunnel across into the inner regions of the disk. A more intuitive explanation is that Q measures whether or not self-gravity is powerful enough to overcome pressure support on small scales, and the shear on large scales. The latter interpretation, is essentially the Jeans instability in a shearing sheet. The distinction is that when the Jeans length in the disk, $\lambda_J \approx (c_s^2 \pi/(G\rho))^{1/2}$, is large (e.g. high temperatures or low density), the shear in the disk acts as a stabilizing force and prevents collapse. However when the wavelength is sufficiently small, as in a disk with $Q < 1$, the gas can collapse on scales of the fastest growing mode, $\lambda = 2\pi H$, leading to the formation of bound objects in the disk (Toomre, 1964; Goldreich & Lynden-Bell, 1965)

In addition to $m = 0$ modes, there are also non-axisymmetric growing low m modes that can be excited at the outer Lindblad resonance ($\omega = \Omega + \kappa/m$), or at higher values of Q. Numerical simulations of protostellar disks also show spiral arm formation due to the non-linear interaction of linearly stable modes, and reflection of waves between Lindblad resonances (Laughlin & Bodenheimer, 1994; Laughlin & Rozyczka, 1996; Shu et al., 1990). We discuss these in more detail in chapters 4 and 5.

Transport by Spiral Arms

Independent of the generating mechanism, one can write down an expression for the effective transport by spiral arms. Lynden-Bell & Kalnajs (1972) showed that only trailing spiral arms transport angular momentum outward. The stress tensor due to gravitational torques is:

$$T_{r\phi,G} = \int dz \frac{g_\phi g_r}{4\pi G} \tag{1.15}$$

where, g_r and g_ϕ are the components of the gravitational field. These two terms take the place of velocities in the Reynolds stress tensor. As with Reynolds stresses, positive correlations between g_r and g_ϕ cause outward transport (Lynden-Bell & Kalnajs, 1972). Fig. 1.3 shows how a trailing spiral arm generates positive correlations between the r and ϕ accelerations.

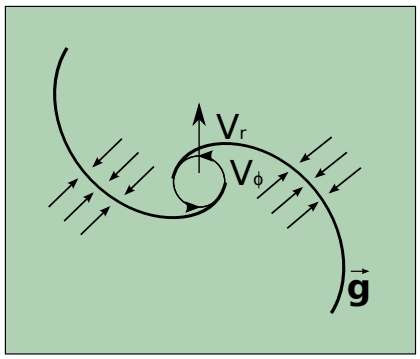

Figure 1.3: Trailing spiral wave induces positive correlations between g_ϕ and g_r following Figure 1 of Lynden-Bell & Kalnajs (1972). For example, the arrows in the lower right quadrant indicate that material inside the arm is accelerated in the positive ϕ and r directions, while material outside of the arm is accelerated in the negative ϕ and r directions.

Although this form of the stress tensor can be translated into an effective α_{GI} by equating equations (1.15) and (1.11), Balbus & Papaloizou (1999) have stressed that in general the energy dissipation by GI is not identical to that in the viscous case. Waves in a self-gravitating disk will not necessarily dissipate locally, and angular momentum can be transported without corresponding local dissipation.

Also, note that equation (1.15) only takes into account the torques directly driven by disk self gravity. Spiral arms can also induce velocity correlations in the fluid directly which show up in the Reynolds stress term $u_r u_\phi$ (see chapter 5).

An alternative expression for the gravitational stress tensor can be derived under the assumption that angular momentum is transported outwards when the density waves cross corotation. Although its applicability for interpreting numerical simulations is somewhat limited, it demonstrates interesting scalings, which give a similar order of magnitude estimate for the strength of transport as local models for GI turbulence.

Following Bertin (1983) and Lodato & Rice (2005), the torque associated with a wave with azimuthal mode, m, radial wavenumber, k and amplitude $\Delta = \delta\Sigma/\Sigma$ can be written as:

$$T_{r\phi} = m\Sigma c_s^2 \left(\frac{1}{Q^2 R k} - \frac{H}{R}\frac{1}{Q} \right) |\Delta|^2 \tag{1.16}$$

This expression is derived from the wave action and group velocity of an individual spiral

density wave. [1]

For comparison with other transport mechanisms, we can again translate the stress tensor into an effective α_{GI}, although doing so is somewhat suspect since we are describing a single, large scale mode. Nevertheless, this gives:

$$\alpha_{GI} = m \left| \frac{\mathrm{d} \ln \Omega}{\mathrm{d} \ln \mathrm{R}} \right|^{-1} \left(\frac{1}{Q^2 R k} - \frac{H}{R} \frac{1}{Q} \right) |\Delta|^2 \tag{1.17}$$

For a tightly wound spiral we expect that $k = 1/(\eta H)$, where η is a small numerical coefficient. In a Keplerian disk, the above equation becomes:

$$\alpha_{GI} \approx \frac{2}{3} m \frac{H}{R} \left(\frac{\eta}{Q^2} - \frac{1}{Q} \right) |\Delta|^2. \tag{1.18}$$

In line with expectations, the angular momentum transport increases with decreasing Q, and increasing mode amplitude (overdensity). The dependence on m is less obvious. Numerical simulations (Laughlin & Korchagin, 1996a) show that low order spiral modes dominate transport, likely due to their higher amplitudes and growth rates at larger Q. At $Q = 1$ and $\eta = 1$ this formalism becomes invalid because the stress tensor changes sign (excursions below unity are valid for smaller Q). In other words, this prescription is only valid for a relatively small range of k values. The WKB analysis implies that $k \gg 1/R$, so that this expression is valid for $1/R \ll k < 1/H$. Only in very thin disks, $H \ll R$, can this inequality be satisfied, when the wavelength can be a few scaleheights, but remain much smaller than the disk radius. It is in this limit where a local, turbulent description of GI may also be valid.

Note that for values of $\eta \gtrsim 1$, and order unity overdensities in marginally thick disks, the effective α can approach 1, $\alpha_{GI} \to 2mH/3R$. We shall see that arguments tied to the dissipation of GI waves or turbulence also lead us to expect an upper limit near unity.

Turbulence driven by GI

There are special cases where self-gravitating disks will act like local α disks. Near corotation, if waves cannot propagate, energy and angular momentum may be deposited locally. Self-gravitating disks whose fastest growing unstable wavelengths are very small

[1] The numerical simulations of Lodato & Rice (2005) calculate an effective $\alpha_{GI} \approx 10^{-2}$ with this formula, consistent with the measured accretion rate. However, application of the above formula directly is complicated by the fact that it is difficult to measure an exact value for k in a full hydrodynamical simulation (see chapter 5).

compared to the radial extent of the disk (large $\eta \equiv 1/(kH)$) are also amenable to a local α treatment.

The importance of the latter case, where gravitational instability successfully generates small scale, α-like turbulence was first demonstrated by the numerical simulations of Gammie (2001), who showed that a gaseous self-gravitating disk could enter into a self-regulated state of turbulence if two conditions were satisfied.

A razor thin, $Q \sim 1$ disk satisfies the large wavenumber (small wavelength) requirement. In order for the disk to enter a self-regulated state of local "gravito-turbulence," local dissipation of the turbulence must be balanced by heating. This second, so-called cooling constraint is:

$$t_{\rm cool} = U \left| \frac{dU}{dt} \right|^{-1} \sim \Omega^{-1} \propto \frac{\Sigma c_s^2}{\sigma T_{\rm eff}^4}. \tag{1.19}$$

where σ is the Stefan-Boltzman constant, and U is the internal energy of the disk. If the heating due to turbulent dissipation is too weak, then the disk collapses on scales comparable to the scaleheight as discussed above. If the heating is so strong that it raises the disk temperature, and thus c_s, the disk will restabilize at a value of $Q > 1$. However, if heating by dissipation just balances cooling, the disk can self-regulate to remain unstable and turbulent, but not fragment into bound objects. In this case, the effective transport due to disk self-gravity can be translated directly into an α as:

$$\alpha = \frac{1}{\gamma(\gamma - 1)} \frac{4}{9\Omega t_{\rm cool}} \tag{1.20}$$

where γ is the adiabatic index of the gas. Note that this prescription allows us to determine a maximum α beyond which fragmentation occurs, although its value may depend on γ and the disks energy source (Rice et al., 2005). For a discussion of maximum accretion rates due to disk self gravity in the AGN context, see Shlosman & Begelman (1987).

In chapters 4 and 6 we discuss this process in more detail, review recent literature in the area, and show how this constraint might be altered in different environments. In particular we shall see that for realistic disk densities, temperatures and opacities, heating by dissipation can not always just balance cooling, implying that not all disk locations can become gravitoturbulent.

1.3.3 Transport by an External Perturber

The foundational work on angular momentum transport by external perturbers was conducted by Goldreich & Tremaine (1979). Waves due to external perturbers are launched at the outer Lindblad resonance. If they remain linear, and propogate inward, then they carry with them angular momentum. As they propagate inward, the ratio of the wave pattern speed to the disk orbital frequency decreases. Once waves cross the corotation radius they are then rotating more slowly than the background disk and hence carry negative angular momentum. If the waves eventually dissipate, giving up angular momentum to the local region, the disk loses angular momentum, and the perturber gains it (Goldreich & Tremaine, 1979). Though it is beyond the scope of this discussion, this theory laid the ground work for the theory of planet migration.

For transport to occur, the waves must propagate as weak shocks so that dissipation occurs gradually, rather than on the lengthscale on which it is launched (Savonije et al., 1994). If one requires that the wave amplitudes are marginally non-linear, the effective α scales inversely with the local Mach number of the Keplerian flow (Papaloizou & Lin, 1995). Thus this dissipation mechanism should be most effective in thick disks, where the flow is least supersonic.

For the remainder of the thesis we will mostly ignore the role of external perturbers because we are primarily concerned with the disk processes that lead to the formation of the companion, rather than the evolution thereafter. While perturbations due to a stellar encounter, for example, can drive accretion, they ultimately stabilize marginally gravitationally unstable disks, rather than drive fragmentation (Forgan & Rice, 2010).

In chapters 5 and 6 we discuss some of the effects of companions on disks. In the former we discuss how these effects may control the final orbital distribution of disk born binaries, and in the latter we examine how interaction between the disk and perturber can control the growth of objects born in disks.

1.4 Numerical Techniques

A significant portion of this thesis is based upon numerical experiments, and so I briefly review the methods employed here, and the advantages of the chosen technique. We use the code ORION to conduct our numerical experiments (Truelove et al., 1998; Klein, 1999; Fisher, 2002). ORION is a parallel, adaptive mesh refinement (AMR), multi-fluid,

radiation-hydrodynamics code incorporating self-gravity and Lagrangian sink particles (Krumholz et al., 2004). Radiation transport and multi-fluids are not used in this study.

1.4.1 Hydrodynamic Solver

The gravito-hydrodynamic equations are solved using a conservative, Godunov scheme, which is second order accurate in both space and time. Godunov schemes solve the Riemann problem to calculate the flux of conserved quantities across grid cells. The Riemann problem is a more general version of the shock-tube problem in which the form of a wave traveling across the boundary can be composed of a right or left moving rarefaction wave or shock, joined by a contact discontinuity. The exact Riemann problem is solved by finding the root of an algebraic pressure equation derived from both the Rankine-Hugoniot jump shock conditions, and standard ideal gas equations. A numerical algorithm must be employed to iteratively find the root. Once the pressure equation is solved, the ideal gas equations can be used to find the remaining primitive variables (ρ, u) and thus the conserved quantities $(\rho, \rho u, E)$.

In practice, solving the exact Riemann problem at every interface at every timestep is extremely time consuming and unnecessary to adequately compute the fluxes. Consequently, ORION uses an approximate solution to the Riemann problem, which provides sufficient accuracy with large improvements in efficiency (Toro, 1997). ORION is operator split, meaning that at each time step, each coordinate direction is solved for cyclically. For a more detailed description of the specific Godunov method used in ORION, including a description of the characteristic tracing technique and use of artificial fluxes, see Truelove et al. (1998).

1.4.2 Adaptive Mesh Refinement

Adaptive Mesh Refinement (AMR) is a technique to dynamically and hierarchically allocate new, higher resolution grids within a simulation in regions that are becoming under resolved as defined by some user criteria. For our study of rapidly accreting disks, AMR allows us to achieve two goals simultaneously. First, we can set up simple initial conditions which place the computational boundary far from the disk by adding computationally inexpensive, coarsely refined zones to the outer regions. Secondly, we can resolve both the background flow and disk simultaneously, and let the disk expand in time as it accretes higher angular momentum material. This means that a given run becomes more

computationally expensive in time. The corollary of course is that the requirements at the beginning of a run are relatively modest when there is little to resolve. In addition to adaptive gridding, ORION also uses adaptive time steps, so that low resolution grids are evolved based on the local courant condition, not on that calculated for the highest level. As a result, following the evolution of gas on large scales at low resolution is very computationally efficient.

1.4.3 Gravity Solver

Because ORION uses AMR, it is efficient to take advantage of the hierarchical domain decomposition done by the hydrodynamic solver and use a multigrid method to solve the Poisson equation for the current density distribution. The multigrid method uses a relaxation technique to solve the system of sparse linear equations that result from discretizing the Poisson equation on each level. The advantage of this technique is that the solutions found on coarse grids can be used to correct for low-frequency errors, while the higher resolution ones extract high-frequency errors. The result is faster convergence, because more iterations are done on coarse rather than fine grids. The gravitational potential is then used as a source term in the gravito-hydrodynamic equations.

1.4.4 Sink Particles

Each year, Moore's Law suggests that we can consider previously intractable computational problems. For example, over the course of this thesis, the local available super computers have increased from hundreds of processors to close to 10,000. Nevertheless the dynamic range we can explore remains limited even in adaptive codes such as ORION.

The most stringent limitation on dynamic range in this case comes not from the grid resolution, but from the time resolution. The hydrodynamic timestep is limited by the Courant condition, which requires that the timestep be smaller than the signal crossing time of a grid cell. As densities increase within a given cell, the signal crossing time decreases, requiring very fine timestepping. In particular, in the case of Keplerian flows studied here, as the physical resolution increases, the distance to the central masses decrease, and so the rotational velocities we must resolve increase. Since, as we discuss in chapter 5, we resolve entire disks at the same resolution, small time steps become extremely prohibitive. Moreover, because processor speeds of individual cores are increasing modestly compared to the number of cores over which a problem can be paral-

lelized, limitations on timesteps are much more prohibitive as they cannot be computed simultaneously.

Although not as severe a limitation computationally, to prevent unphysical fragmentation, the Jeans length, which decreases with increasing density, must be resolved by a sufficient number of grid cells (Truelove et al., 1997). This can also make calculations of a high density central star or fragment in a disk computationally prohibitive.

In order to perform a numerical parameter study at high resolution, to follow many disk orbits, and to complete the computations on a thesis timescale, we have employed sink particles rather than resolve very high density regions. Sink particles form when the gas becomes unresolved based on the Truelove criterion, and then continue to accrete nearby gas, and interact with it and any other sink particles gravitationally. See both chapter 5 and Krumholz et al. (2004) for a detailed description of the sink particle algorithm. Generally, the accretion rate onto the sink uses an approximate Bondi-Hoyle formula, where values for the density and sound speed at infinity are set differently depending on the relative ratio of the grid size to the Bondi radius. There is also an additional check on the angular momentum of nearby gas, so that unbound gas does not accrete.

The use of sink particles means that one loses resolution within the accretion scale of a particle, but it makes it feasible to study fragmentation and binary formation in a full three-dimensional disk calculation. Perhaps one of the most important features of this method for our purposes is the ability to have a moving central stellar potential, rather than one fixed to the grid. As discussed in chapter 5, this allows us to study transport driven by both even and odd m spiral modes which perturb the star from the center of mass when the disk mass becomes large. It also enables us to study the influence of on-going accretion and eccentricity in binary orbits.

1.4.5 Three Dimensional Disks and Cartesian Grids

Keplerian accretion disks are approximately two dimensional structures. For the purposes of computational efficiency, many have chosen to follow the approach laid out in §1.3 of integrating over the vertical direction and simulating the disk in two dimensions. This approach is extremely fruitful for studying many aspects of disk behavior including angular momentum transport by gravitational instability. However, for the specific case which we study here – disks fed at their outer edges – resolving the vertical structure

is more important. Massive disks in this regime are not geometrically thin and develop moderate turbulent motions in the vertical direction. Although not borne out by our studies thus far, we initially hypothesized that this stirring could support disks and provide transport at values significantly exceeding $\alpha \sim 1$. Our fully three dimensional setup also gave us insight into interesting shock structures forming where the inflow impacted outward moving spiral arms. These and other features may be examined further in future work.

Although disk problems are inherently ill-suited to cartesian codes due to numerical diffusion effects, ORION provided the best combination of computational features for our chosen problem. As we describe above, a main requirement for this work was a moving central potential. Due to the singularity at the center of cylindrical domains, implementing a moving potential in that geometry can be challenging. Moreover, due to the extensive use of this code implementation for disk-like problems, the numerical diffusion has been well characterized.

Chapter 2

Observational Connections: Multiplicity and Star Formation

2.1 Introduction

The study of binarity dates back at least 250 years to Mitchell (1767), who pointed out the abundance of double stars. Many tout the 21st century as the era of precision cosmology, but we are also entering the era of precision in more classic "astronomy" – understanding the ordering of the stars. Great technological advances including the use of coronography (Hinkley et al., 2007) and adaptive optics (Lafrenière et al., 2009) have brought stellar companions into better focus. Despite the longevity of these studies, and the recent advances, we still lack a comprehensive model for the formation of binaries and higher order multiples.

Theories of star formation have been influenced by our heliocentric bias. Until recently, our models have reflected that we live next to a relatively low mass star (apparently) without a stellar or substellar companion. The seminal work of Duquennoy & Mayor (1991) on the multiplicity of sun-like stars showed that our sun is somewhat unusual in being alone. Although the statistics are incomplete for stars of other masses, it now also seems clear that there is a strong correlation between stellar mass and multiplicity (Lada, 2006; Mason et al., 2009). The M stars, the most common stars in the galaxy, are usually in single systems. As primary mass increases to just a few solar masses, binaries become ubiquitous, even as the stars themselves become quite rare. The data are consistent with all O and B stars having at least one stellar companion at birth. The statistics on higher order multiplicity are still incomplete. It remains difficult to

detect relatively close, small mass ratio pairs, particularly for massive primaries. Upcoming searches with next generation infrared telescopes such as JWST may improve these statistics.

Armed with this new data, it is time to reconsider our models of single and multiple star formation. To be sure, conclusions drawn from the current data require many caveats. We do not have a complete picture of companions at all separations and mass ratios. Moreover, given the diverse nature of these systems, it is unlikely that one mechanism can explain them all. For example, it seems unlikely that equal mass, massive twins (Krumholz & Thompson, 2007), and brown dwarf binaries separated by thousands of AU (Burgasser et al., 2009) could form by the same mechanism.

2.2 Standard Theories of Binary and Multiple Star Formation

There are several prominent theories of binary and multiple star formation in the literature. They can be divided roughly into three categories based on the timescale at which the binary forms relative to the star formation process. I review theories for binary formation (1) at the onset of star formation, (2) during disk-mediated accretion, and (3) during the early phase of star-cluster evolution. In this review I neglect theories of binary formation that occur after the bulk of the star formation process has occurred. There is strong observational evidence that formation happens at early times as seen through the higher binarity fraction in pre-main sequence stars as compared to main sequence stars (Mathieu, 1994). I begin with a brief description of each theory, and proceed to compare them with the best observational evidence to date.

2.2.1 Core Fragmentation Theories

The most common mechanisms in the literature fall into the first category, and are described alternately as prompt or early fragmentation, or more specifically as core or turbulent fragmentation (Hoyle, 1953; Tsuribe & Inutsuka, 1999a; Boss et al., 2000; Padoan & Nordlund, 2002; Fisher, 2002). The earliest fragmentation scenario is that of Hoyle (1953) who argued for opacity-limited hierarchical fragmentation, whereby an unstable cloud keeps fragmenting at the local Jeans mass, which decreases as the cloud collapses to higher densities, until the smallest fragments become optically thick and

can no longer cool efficiently. There are numerous reasons why this mechanism is both unphysical and inconsistent with the observed stellar mass function (for a thorough review see Fisher 2002). Nevertheless, this mechanism gave birth to more modern theories of core fragmentation.

In the subsequent generation of "core" fragmentation scenarios, a collapsing, bound gas clump was thought to fragment into two or more objects depending on the ratio of thermal to gravitational energy, $\alpha = 5c_s^2 R/GM$, and the ratio of rotational to gravitational energy, $\beta = \Omega^2 R^3/3GM$. Inherent in this parameterization is the assumption that any dynamically important magnetic fields have already diffused out (or can be included simply as an extra effective pressure in the calculation of α). When the product $\alpha\beta < 0.12$, cores were initially thought unstable (Inutsuka & Miyama, 1992), although this model has the somewhat counterintuitive result that slowly rotating (small β) virialized cores remain prone to fragmentation. More recent work has shown this criterion to be incomplete, requiring also that $\alpha \lesssim 0.5$ (Tsuribe & Inutsuka, 1999b). Yet this model neglects many thermal effects as the gas collapses to higher densities, and would seem to over produce short period binaries.

The source of angular momentum setting β in the model above was thought classically to be galactic shear (Bodenheimer, 1995), but more recent investigations show that the ubiquitous turbulence in the interstellar medium could also be responsible for the observed line-width size relations interpreted as evidence of core rotation (Fisher, 2004; Goodman et al., 1993). This has led to yet another class of models, appropriately termed turbulent fragmentation. The former scenario relied on a linear instability, whereas the turbulence scenario suggests that non-linear perturbations expected in a turbulent cloud can cause a sub-region within a core to become overdense and collapse more rapidly than the free-fall timescale of the background core, thereby leading to the production of a secondary clump within the bound core. Alternatively, turbulent motions can lead to the formation of filamentary structures which then fragment into multiple objects. These stars are presumed to accrete from their natal core mostly independently.

Note that there is another class of star formation models dubbed turbulent fragmentation or "gravoturbulent fragmentation" which refers to the fragmentation of a molecular cloud on larger scales into many bound objects which form their own stellar systems (Ballesteros-Paredes et al., 2007). The turbulence sets the mass-scale of the cores, and their turbulent structures, but for the purposes of multiple formation we are concerned with the subsequent fragmentation of the turbulent clump, not the process that generated

it.

2.2.2 Disk Driven Formation

Models for binary and multiple formation at a slightly later evolutionary state involve protostellar disks. The two classic disk-driven models are disk fragmentation (Laughlin & Bodenheimer, 1994; Bonnell & Bate, 1994a; Adams et al., 1989; Artymowicz & Lubow, 1996), and disk capture (Clarke & Pringle, 1991; Moeckel & Bally, 2007). The former, to which much of this thesis is dedicated, suggests that some stars will form sufficiently massive protostellar disks that become susceptible to gravitational instabilities. If disks become sufficiently unstable, and the gas can cool efficiently, the disks can fragment to produce one or more coplanar companions that accrete from the parent disk, and depending on the formation epoch, the primary's natal cloud.

Disk fragmentation has received renewed attention from numericists in recent years. Prior work on this topic has been severely limited by two assumptions. The first is that disks can be modelled in isolation. Disks modelled in the absence of ongoing accretion are much less likely to become unstable. As we show in the course of this thesis, ongoing accretion at the outer edge of the disk is often necessary to drive instability.

The second related assumption was that disks are always low in mass relative to the central star. Certainly observed T-Tauri disks tend to be lower in mass, but as observations improve we are beginning to observe more massive disks at early epochs of formation (Andrews & Williams, 2007). Together these two notions led most previous authors to conclude that disk fragmentation might occur rarely, and could only produce very unequal mass ratio objects, which was inconsistent with binary statistics.

However, if disks are more massive and undergo continued accretion, simulations suggest that fragmentation may be more common, and that secondaries born in the disk can accrete quickly to catch up to the primary in mass (Bonnell & Bate, 1994b; Krumholz et al., 2009; Kratter et al., 2010). Together with observations of more massive disks, this suggests that the disk scenario can in fact produce a wide range of mass ratios, although we find that this mechanism is most likely relevant for systems with primaries more massive than our sun.

Following fragmentation, subsequent interactions between circumstellar and circumbinary disks may further alter their orbits: gravitational torques can expel the circumbinary disk carrying away a large fraction of the orbital angular momentum (Chang et al.,

2009). By contrast, tidal interactions between each of the two circumstellar disks allow for transfer of angular momentum from the disks to the orbit, expanding it as in the case of the Earth-Moon system where the rotation of the disk / Earth is faster than that of the orbit of the binary star / Moon. The latter interaction becomes important only when the protostellar disk fills the effective Roche radius of the star-disk system, and so may not be the dominant driver of orbital evolution.

In the capture scenario, a massive disk increases the gravitational cross-section for capturing a nearby star into a bound orbit. Although initial investigations found this process to be highly inefficient around low mass stars at reasonable stellar densities (Clarke & Pringle, 1991), more recent work suggests that the process might be better suited for massive stars with correspondingly more massive disks (Moeckel & Bally, 2007).

2.2.3 Multiple Formation in a dynamically evolving cluster

A final, more global mechanism for multiple formation is that put forth in a series of papers including Bate (2000), Bate et al. (2003), and Bonnell et al. (2004). These modelers suggest that star clusters form through a dynamic process of competitive accretion. In this scenario, a turbulent molecular cloud forms many roughly Jeans mass clumps that interact with one another and compete for mass from the background cloud. In this environment there are multiple mechanisms for binary formation, including the disk methods mentioned above, as well as dynamical interactions between three or more bodies which can eject a low-mass object and tighten the orbits of the remaining bound pair. In addition, dynamical friction between the protostars and background gas is thought to tighten wider binaries. What distinguishes this scenario from those listed above is that a stellar system does not accrete from a fixed, marginally bound core, but rather migrates around in a cloud collecting previously unbound material.

A related model put forth by Goodwin & Kroupa (2005) relies on a combination of the core fragmentation and dynamical evolution hypothesis to reproduce the high multiplicity fraction of young stars in clusters, compared to their field star counterparts. Although they do not specify the precise mechanism for fragmentation, these authors imagine that most cores either break up into 2 or 3+ individual stars. Through dynamical interaction, the higher order multiples evolve into single star systems, tight binaries, and stable hierarchical systems. They posit that different clusters environments (which have different rates of close stellar encounters) will naturally evolve to show different

multiplicity fractions.

2.3 Observational Tests of Theoretical Models

Advances in numerical techniques mean that each of the processes described above has been simulated at high resolution. Though numerical artifacts remain, many of the mechanisms cannot be ruled out on basic physical grounds. Instead they must be evaluated based on their ability to reproduce the observables of the star formation process. This is difficult to measure precisely, as it would require that we know the conditions in a given cloud and core over its entire formation timescale, which is clearly unobservable. Although much progress has been made characterizing the different phases of core formation as described in chapter 1, one must also compare the predicted properties of the stellar mass distribution in terms of mass ratios, periods, eccentricity, etc. Selection effects and the complexities of the theories make this challenging and uncertain, but it is a goal worth pursuing. We must, however, exercise some caution when assessing theories of binary formation which reproduce observed trends, but fail to address the fundamental physics underlying formation. While the effort to create models which reproduce observations is important, we should not neglect detailed modeling of molecular clouds and prestellar cores from which binaries form.

2.3.1 Empirical Models for Turbulent Fragmentation

Semi-empirical models such as Fisher (2004) have had some degree of success producing observed period and mass ratio distributions of low mass stars from the turbulent fragmentation mechanism. This work assumes that the components of binaries are drawn randomly from the initial mass function (IMF), and that there exists a constant efficiency factor with which mass and angular momentum are transferred from the core to the binary. They also draw eccentricities randomly from a thermal distribution, consistent with observations, in order to specify the orbit for a given binary angular momentum. A major limitation of this work is that the physical process which governs the distribution of mass and angular momentum between binary components is ad hoc, and tuned to reproduce the observations. While numerical work has shown that a multiple system can form out of a turbulent core, it remains to be shown in detail that the efficiency of angular momentum and mass removal scales as this model suggests. Moreover, while the

final distribution of binary systems is consistent with the observation distribution of low mass stars, it is not consistent with the orbital parameters and mass ratios for substellar companions and more massive stars. Recent AO surveys by Metchev & Hillenbrand (2009) show that the distribution of substellar companions to solar-type stars is inconsistent with being randomly drawn from the IMF. There is also a dearth of substellar mass companions at large distances. On the opposite end of the mass spectrum there may also be inconsistencies. First, there is no clear explanation for the increase in binarity with core mass in this model. Secondly, recent numerical work (Krumholz et al., 2007b) has shown that radiation from the first star can suppress turbulent fragmentation in massive cores because more massive protostars are luminous even at early times.

2.3.2 Competitive Accretion and the IMF

Similarly, the competitive accretion picture has had moderate success explaining portions of the observed initial mass function (Moeckel & Bate, 2010) and binary statistics. However, these models tend to overproduce the binaries containing the lowest mass stars and brown dwarfs, and have higher star formation efficiencies than observed (Price & Bate, 2009). Another major criticism is that the relative velocities between accreting cores and background gas are so high that the accretion rate onto the cores should be far too low to produce more massive stars (Krumholz et al., 2006). In addition, the intercore velocities appear to be much higher in the simulations than observed between actual star forming cores, calling into question whether or not there can be significant core-core interaction on the timescale of star formation (Kirk et al., 2009; Evans et al., 2009).

The Goodwin & Kroupa (2005) picture does reproduce the observations for stars $\lesssim 1 M_{\odot}$, but like the model of Fisher (2004) it has been tuned to do so. The mechanism which breaks some cores into two versus three stars, and the division of mass and angular momentum between them is not specified in detail.

The dynamical interactions observed here may be key to forming wide, very low mass binaries. Some have suggested that these few body interactions which occur as the initially bound cluster begins to spread could produce weakly bound brown dwarfs (Kouwenhoven et al., 2010).

2.3.3 Disk fragmentation: a possible solution to the luminosity and angular momentum problems

As we show in chapter 5, the disk scenario can produce a range of stellar separations and mass ratios, depending on primary mass, and the epoch of disk instability. Although no statistical study of this process has been completed, investigations are ongoing (Offner & Kratter, 2010 in prep). Nevertheless, the disk fragmentation scenario may be consistent with two observational puzzles in star formation: the so-called luminosity problem (Kenyon et al., 1990) and the angular momentum problem (see Bodenheimer 1995 and references therein).

The luminosity problem refers to the discrepancy between the observed and predicted bolometric luminosity of young protostars based on their accretion luminosities. Given a star formation timescale and stellar mass, we can predict the time-averaged mass accretion rate, and thus the corresponding luminosity. While uncertainties in the opacities and geometry of high extinction cores can complicate the interpretations, recent data from the Spitzer c2d survey confirms that most young sources are underluminous compared to the expected luminosity from the time-averaged rate (Evans et al., 2009). These authors suggest that variable, high accretion rates, particularly in the Class 0/I phase, are all but required by the data. Because so few cores are observed to have luminosities consistent with the time averaged rate (a few $10^{-6} M_{\odot}$/yr) accretion must occur in short bursts ($\sim 10^4$ years) well above this rate.

For more massive protostars, these high, variable accretion rates at early times are consistent with infall at rates such that $\xi \equiv \dot{M}G/c_s^3 \gg 1$, which we shall show are susceptible to fragmentation. Although we study steady accretion here, highly variable accretion from turbulent cores could further promote fragmentation if the disk is fed asymmetrically, which may also be consistent with observations (see e.g. Tobin et al. 2010).

The angular momentum problem refers to the fact that we do not understand how four orders of magnitude of angular momentum are repartitioned between the largest scales in Giant Molecular Clouds (GMCs), where the specific angular momentum is set by the differential rotation in the galaxy (Bodenheimer, 1995) and the scales of binary orbits. By the time dense cores have formed, line-width size observations reveal that the typical specific angular momentum has dropped by two orders of magnitude (Goodman et al., 1993). When we look at binary stars, whose formation is intimately tied to the

core angular momentum, the average specific angular momentum can drop another two orders of magnitude.

Magnetic fields may play an important role in removing angular momentum on the largest scales (Li et al., 2004), although hydrodynamic turbulence can be significant as well (Jappsen & Klessen, 2004). Disk fragmentation may be important on smaller scales: because disk size is regulated by the gas reservoir's angular momentum, if the disk fragments to form a binary or multiple before all of the infalling gas and angular momentum has accreted onto the star-disk system, binaries can form with less orbital angular momentum than that contained in the core. Subsequent few-body interactions in disk-born higher order multiple can also redistribute angular momentum by expelling the lowest mass companions.

Several other trends seem roughly consistent with the disk scenario. Both disk fragmentation and binary frequency increase with primary mass. At lower masses where disks are stabilized by stellar irradiation (Matzner & Levin, 2005), the turbulent cores out of which they form may be more susceptible to early fragmentation (Offner & Kratter, 2010 in prep).

The trend towards equal mass components at very high masses might be related to the fact that massive disks become unstable early on in their accretion histories (Pinsonneault & Stanek, 2006). There are also hints in the high mass multiplicity statistics that mass ratio scales inversely with separation (Mason et al., 2009). Although migration can alter the orbits, disk fragmentation suggests a possible correlation between secondary mass and separation: fragmentation typically occurs towards the outer edge of the disk which is larger at late times at which point there is also less mass available for the secondary to accrete.

A final piece of evidence favorable for the disk scenario is the observation that binaries separated by less than rougly 40 AU are more likely to have the stellar spins aligned with the binary orbit (Hale, 1994). Although this study does not account for higher order multiples, and has significant uncertainties in the measurements (e.g. sin i), this is suggestive that perhaps some objects were born in disks. Of course objects born from clouds with the same net rotation might also tend to be aligned, although stars born from turbulent cores might sample the turbulent spectrum from different parts of the core with different net angular momentum vectors.

2.4 Conclusions

Despite their ubiquity, we still lack a coherent theory of binary and multiple star formation which can explain the enormous range of observed systems. We have demonstrated that disk fragmentation requires more careful consideration as one of several viable mechanisms, especially for stars more massive than our sun. Several on-going projects attempt to quantify this statement. We must investigate whether or not the fraction of cores that produce sufficiently high disk masses for fragmentation are consistent with binary fractions as a function of primary mass. We must also construct a model for the orbital evolution of binaries formed in disks. Current theories are limited to either extreme mass ratios (e.g. planets), or simplified cases (circular orbits).

Chapter 3

Disks in the Formation of Massive Stars

A version of this chapter has been published in the Monthly Notices of the Royal Astronomical Society as "Fragmentation of massive protostellar discs", Kratter, K. M., and Matzner, C. D., vol. 373, pp1563-1576, 2006. Reproduced by permission of MNRAS.

3.1 Introduction

We begin by examining the role of accretion disks in the formation of massive stars. Advances in submillimeter telescopy have enabled the discovery of flattened structures, in some cases clearly Keplerian disks, surrounding massive ($\gtrsim 10 M_\odot$) protostars (Cesaroni, 2005; Chini et al., 2004; Patel et al., 2005; Beuther et al., 2006). The logical inference – that high mass star formation (HMSF) proceeds through disk accretion – raises a question: can such disks process rapid mass accretion, or do they fragment to produce secondary stars? We seek to answer this question by estimating the criterion for disk fragmentation in the vicinity of a massive star.

If massive-star disks typically do not fragment, then disk accretion poses little barrier to massive star formation. Conversely if disk fragmentation occurs, then accretion onto the central star may be (partially) choked off, as suggested by Tan & Blackman (2005) in the context of low-luminosity active galactic nuclei. Moreover each massive star that forms from a fragmenting disk may be surrounded by smaller stars that began as disk fragments. It is therefore important to evaluate models for HMSF in light of the disk fragmentation criterion.

The current work uses and extends the results of Matzner & Levin (2005, hereafter ML05), who showed that protostellar disks around low mass stars are strongly stabilized against fragmentation by a combination of viscous heating and irradiation by the central protostar. Massive star formation is fundamentally different, however, in three important ways. The rapid rise of luminosity with mass implies that stellar irradiation is far more intense; this tends to stabilize disks against fragmentation. However, massive stars must accrete quickly to form at all (e.g., Wolfire & Cassinelli, 1987), and rapid accretion favors fragmentation. These effects compete to set the critical radius outside of which disks fragment. Whether fragmentation actually occurs depends on the initial disk radius, which itself depends on the physical state of the gas prior to accretion. We discuss disk fragmentation in §3.2, considering the stabilizing effect of viscous heating (§3.2.2) before incorporating irradiation by the central star (§3.2.3). This combination allows us to identify (§3.2.4) the disk radius at which fragmentation sets in. The McKee & Tan (2003) core collapse model is examined in more detail in §3.3: we compute angular momentum scales in §4.3.4 using formulae derived in the Appendix. In §3.4 we calculate expected fragmentation radii for a range of masses in the core collapse model.

Turning to the consequences of fragmentation, we examine in §3.5 the likely properties of stars born within fragments and the possibility that fragmentation limits accretion. In §3.5.2 we compare our results with observed regions of HMSF.

3.2 Disk Fragmentation

3.2.1 Criterion for Fragmentation

We shall concentrate on fragmentation due to local gravitational instabilities, which set in when Toomre's parameter

$$Q = \frac{c_{\rm ad}\Omega}{\pi G\Sigma} \tag{3.1}$$

descends toward unity. Here Σ is the disk's surface density, Ω its orbital frequency, and $c_{\rm ad}$ is its adiabatic sound speed. (We shall frequently refer to the isothermal sound speed $c_s = \gamma^{-1/2} c_{\rm ad}$ where γ is the ratio of specific heats.)

Observational inferences of massive circumstellar tori (Cesaroni, 2005) indicate that they may be subject to *global* instabilities as well. We discuss this possibility briefly in §3.4.4; however the local instabilities tend to occur first, and their relation to fragmentation is better understood.

Several authors have identified the fragmentation boundary in terms of a cooling time. Following Gammie (2001) and ML05, we convert this criterion to a critical mass accretion rate at a given midplane temperature. The cooling time τ_c is the ratio of the internal energy per area, $U = c_{\rm ad}^2\Sigma/[\gamma(\gamma-1)]$, to the dissipation rate per unit area – which, in steady accretion, is

$$2F_v = \frac{3\dot{M}\Omega^2}{4\pi} \tag{3.2}$$

where F_v is the flux through each disk face. Eliminating Σ, the maximum accretion rate is

$$\dot{M}_{\rm max} = \frac{4\gamma^{1/2}}{3(\gamma-1)}\frac{c_s^3}{Q\Omega\tau_c G}. \tag{3.3}$$

For later convenience we write this in terms of the isothermal sound speed $c_s = \gamma^{-1/2}c_{\rm ad}$. Extrapolating from Gammie (2001)'s two-dimensional simulations for a stiff equation of state, ML05 estimate $\dot{M}_{\rm max} = 0.89c_s^3/G$ for the case of a three-dimensional, $\gamma = 5/3$ disk. Using smoothed-particle hydrodynamics, Rice et al. (2005) have simulated just such a disk, finding $\Omega\tau_c$ to lie between 6 and 7 when it fragments. Assuming also $Q = 1$, this implies $\dot{M}_{\rm max} = (0.37 \text{ to } 0.43)c_s^3/G$. For a fixed $\dot{M}$, the critical temperature is then significantly (1.6 times) higher than ML05 estimated.

At face value this weakens the conclusion, reached by ML05, that fragmentation is unattainable in low-mass protostellar disks. However, more recent simulations show that disks remain stable at shorter τ_c depending on how abruptly cooling is implemented (E. Harper-Clark 2006, private communication). Due to uncertainties in the aforementioned cooling factor, and in light of the stringent resolution requirements for collapse outlined by Nelson (2006), we consider the value of $\Omega\tau_c$ obtained by Rice et al. (2005) to be uncertain by up to a factor of two. We shall therefore be conservative, by adopting the stricter ML05 criterion that fragmentation occurs when

$$c_s < c_{s,\rm crit} = 1.04(G\dot{M}_{\star d})^{1/3}. \tag{3.4}$$

Since the mass accretion rate is comparable to $\varepsilon c_{\rm eff}({\rm core})^3/G$ in the core collapse scenario, where $c_{\rm eff}({\rm core})^2$ is the ratio of pressure to density in the core, equation (3.4) implies, qualitatively, that a disk fragments if its sound speeds falls below the effective sound speed of its parent core (see equation [3.23] below). This point was made for thermally supported cores by ML05, and equation (3.4) simply extends the rule to turbulent cores.

Equation (3.4) is conservative in the sense that fragmentation may also occur at somewhat higher values of c_s. It is even more conservative given that γ declines from 5/3

at the higher temperatures relevant to massive star formation. We shall make several other conservative estimates in order to show that disk instability is all but inevitable during massive star formation.

When assessing disk stability in a given scenario, we first calculate the midplane temperature profile $c_s(r)$ of the disk given its central mass $M_\star$, central luminosity $L_\star$, and accretion rate $\dot{M}_{\star d}$. For this we adopt the Shakura & Sunyaev α parametrization of viscosity, in which the steady mass accretion rate is

$$\dot{M}_{\rm visc} = \frac{3\pi\alpha\Sigma c_s^2}{\Omega}. \tag{3.5}$$

For the choice of critical temperature made in equation (3.4) this corresponds to $\alpha = 0.30Q$ at the onset of fragmentation. We keep α fixed at 0.30 throughout our analysis, as this correctly reproduces the fragmentation boundary, although this is an overestimate for stable disks.

Having identified the *fragmentation radius* as the location where the disk sound speed falls to the critical value in equation (3.4), we then compare this to the characteristic disk radius

$$R_d = \frac{j^2}{GM_\star} \tag{3.6}$$

for accreting gas with specific angular momentum j.

We set the viscous accretion rate equal to the accretion rate from the envelope, and let $Q = 1$. We then check whether the disk can remain in this steady state with two models for heat generation. In §3.2.2 we ignore the luminosity from the protostar and find a minimum value for $T_d(r)$ using only the viscous generation of heat. Next, in §3.2.3, we include the flux from the protostar received at the disk surface, and again solve for the midplane temperature as a function of radius.

3.2.2 Viscous Heating

In a thermal steady state, the flux of viscous energy radiated by each face of the disk is given by equation (3.2). All of the disks considered in this chapter are optically thick to their own thermal radiation; therefore, the flux can also be derived from radiation transfer across an optical depth $\kappa\Sigma/2$ from the disk midplane to its surface:

$$F_r = \frac{8}{3\tau_R}\sigma T_d^4, \tag{3.7}$$

Subscript	Meaning
cl	Clump
c.....	Core
$\star$.....	Star
d.....	Disk
$\star d$....	Star-disk system
f....	Final value
crit...	Critical value for fragmentation
irr...	Stellar irradiation
v.....	Viscous flux

Table 3.1: Definitions of subscripts.

where $\tau_R = \kappa_R \Sigma_d / 2$ is the optical depth corresponding to the Rosseland mean opacity $\kappa_R(T_d)$. The factor 8/3 in equation (3.7) is derived by assuming that the dissipation rate per unit mass is a constant (Chick & Cassen, 1997). We obtain temperature dependent opacities from Semenov et al. (2003). These opacities are very insensitive to density; we adopt values for $10^{-12.5}\,\mathrm{g\,cm^{-3}}$, an appropriate value for a disk with $Q = 1$ and a period of a few centuries.

Neglecting irradiation of the disk surface, in a steady state $F_v = F_r$ and $\dot{M}_{\rm visc} = \dot{M}_{\star d}$. We solve for Σ in equation (3.5), and then c_s from equations (3.2) and (3.7) using $\mu c_s^2 = k_B T$ (for molecular weight μ), yielding

$$c_s^{10} = \frac{3 k_B^4 \kappa_R \dot{M}_{\star d}^2 \Omega^3}{128 \pi^2 \sigma \mu^4 \alpha}. \tag{3.8}$$

This is an implicit formula for c_s, as κ_R depends on temperature. Equating c_s to $c_{s,\rm crit}$ (equation 3.4) implies fragmentation when

$$\Omega < 8.54 \left(\frac{\sigma \mu^4 \alpha G^{10/3} \dot{M}_{\star d}^{4/3}}{k_B^4 \kappa_R} \right)^{1/3}. \tag{3.9}$$

In practice we calculate the run of $c_s(r)$ and $\kappa_R(r)$ self-consistently in order to evaluate equation (3.9).

Whereas ML05 found a unique value of $\Omega_{\rm crit}$ for optically thick accretion disks around low-mass protostars, we shall show below that equation (3.9) gives a roughly constant fragmentation radius of about 130 AU. The key difference is the higher accretion rate, which implies much higher critical temperature (hundreds of K) in massive star formation

compared to ~ 16 K for the low mass case. As the opacity law does not obey $\kappa_R(T) \propto T^2$ for these higher temperatures, the ML05 result does not hold for these more massive stars.

3.2.3 Stellar Irradiation

Stars of mass somewhat greater than $10 M_\odot$ undergo Kelvin-Helmholtz contraction rapidly enough to settle onto the hydrogen burning main sequence while still accreting. As the main sequence luminosity increases rapidly with $M_\star$, the consequences of stellar luminosity become acute for massive stars. One such consequence is the heating of the disk midplane due to reprocessed stellar radiation. In principle, this stabilizes disks to longer periods (larger radii) than we found in equation (3.9) by considering only viscous heating. We parametrize irradiation through the reprocessing factor f defined as the ratio between the incident flux $F_{\rm irr}$ normal to the disk surface, and the spherical stellar flux at that radius:

$$F_{\rm irr} = \frac{fL}{4\pi R_d^2}. \tag{3.10}$$

A calculation of f requires a model for the reprocessing of starlight onto the disk.

Infall geometry

ML05 model f in the context of an infall geometry similar to that used by Whitney & Hartmann (1993) and Kenyon et al. (1993) for scattered-light images of protostars. Starlight is absorbed at the inner edge of a rotating infall envelope (Terebey et al., 1984) whose innermost streamlines have been removed by the ram pressure of a magnetically collimated protostellar wind. This removal implies a suppression of the star-disk accretion rate relative to the rate at which mass would otherwise accrete – from the surrounding core, for instance, in a core-accretion model:

$$\dot{M}_{\star d} = \varepsilon \dot{M}_c; \tag{3.11}$$

where $\varepsilon = \cos\theta_0$ if streamlines are removed from all angles within θ_0 of the axis. (We assume the prestellar matter is isotropically distributed before it falls in.)

The balance of forces that determines ε is modeled in detail by Matzner & McKee (2000) for low-mass star formation, and we expect that their analysis holds into the massive star regime. The location of the innermost streamline is a simple function of ε: it strikes the disk at a radius

$$(1-\varepsilon^2) R_d. \tag{3.12}$$

The calculation of f is particularly simple if the dust envelope is (1) optically thick to stellar photons; (2) optically thin to dust thermal radiation; and (3) not hot enough to sublimate. Under these conditions, ML05 find

$$f \simeq 0.1\varepsilon^{-0.35} \tag{3.13}$$

for a reasonable range of ε.

Envelope self-opacity and dust sublimation

It is important to examine the assumptions that led to equation (3.13), especially in the context of very rapid accretion onto very massive stars.

In §4.3.4 we will estimate the typical infall column density $\Sigma_{\mathrm{sph},f}$ in a core collapse scenario, and find it to be a few times lower than the core column Σ_c, i.e., $\Sigma_{\mathrm{sph},f} \simeq 0.3$ g cm^{-2}. Given that the Semenov et al. (2003) Planck opacity peaks between 3 and $16\,\mathrm{cm}^2\,\mathrm{g}^{-1}$ for $45 < T < 930$ K, we expect the disk midplane to be shielded by moderate optical depths ($\sim 1-5$) from the reprocessing surface. A solution to the radiation diffusion problem is beyond the scope of this chapter . Instead we will apply equation (3.13); this is conservative, in the sense that it overestimates the stabilizing effect of irradiation.

A further potential complication arises for especially high accretion rates, those in excess of $1.7 \times 10^{-3} M_\odot\,\mathrm{yr}^{-1}$. The critical temperature of such a disk is quite hot, $T_{\mathrm{crit}} > 1050$ K according to equation (3.4). As we shall see in §3.4, the stabilizing effect of irradiation is accentuated in these disks by a sharp drop in Rosseland opacity. If the disk is to reach 1050 K, however, dust in the nearby infall envelope must approach the silicate sublimation temperature of about 1500 K. This leads to the disappearance of dust within the infall envelope inside a certain *sublimation radius* R_s. Monnier & Millan-Gabet (2002) determine $R_s \simeq 35(L_\star/10^6 L_\odot)^{1/2}$ AU by optical interferometry (and note that this value requires the existence of large silicate grains). We expect that disks with $R_d > R_s$ are relatively unaffected by dust sublimation. We do not attempt to calculate disk irradiation in cases where this is not true.

Incorporation into fragmentation calculation

Solving equation (3.10), we can find the equilibrium temperature of the outer reaches of an optically thick disk for which irradiation dominates over viscous heating. While low-mass protostellar disks can be stabilized in this regime (ML05), massive-star disks are

not. We therefore account self-consistently for $T_d(R_d)$, in two steps. The disk's effective (surface) temperature (T_s, say) is determined by the requirement that it emit the viscous flux in addition to re-emitting the incident flux:

$$\sigma T_s^4 = F_v + F_{\rm irr}. \tag{3.14}$$

The midplane temperature T_d is derived from T_s from radiation diffusion of the viscous flux across optical depth τ_R,

$$\begin{aligned} \sigma T_d(R_d)^4 &= \sigma T_s^4 + \frac{8}{3}\tau_R F_v = \left(\frac{8}{3}\tau_R + 1\right) F_v + F_{\rm irr} \\ &\simeq \frac{8}{3}\tau_R F_v + F_{\rm irr}. \end{aligned} \tag{3.15}$$

We account for the temperature dependence of the opacity when solving this equation numerically.

As before, we identify the critical disk radius $R_{\rm crit}$ at which $T_d(R_d) = T_{\rm crit}$. Fragmentation occurs if the disk extends beyond $R_{\rm crit}$.

Other Considerations

We pause to address two minor concerns:

Shock Heating– Infalling matter is decelerated in an accretion shock upon reaching the disk, and heat radiated by this shock warms the disk surface. However the gravitational potential at R_d is very small compared to that at the stellar surface, as $R_d \gg R_\star$. Moreover, the star's emission is dominated by hydrogen burning rather than accretion, and a fair fraction of the starlight is reradiated onto the disk surface in our model (eq. 3.13). Shock heating is thus wholly negligible (by about four orders of magnitude, for a $30\,M_\odot$ star).

Radiation Pressure– When $Q = 1$ the ratio of gas to radiation pressure at a characteristic fragmentation radius is

$$\frac{P_g}{P_{\rm rad}} = \frac{3k_B\Omega^2}{2\pi G a \mu T_{\rm crit}^3} = 10^{1.8}\frac{30\,M_\odot}{M_\star}\left(\frac{t_{\rm acc}}{10^5\,{\rm yr}}\right)^2\left(\frac{150\,{\rm AU}}{\rm R_d}\right)^3, \tag{3.16}$$

where $t_{\rm acc}$ is the duration of accretion (see §§3.2.4 and 3.3.1). Radiation pressure remains negligible out to periods of 3300 years (scaling as $(M_\star\Sigma)^{-3/4}$ in the core model of §3.3). Moreover the photon diffusion time across the scale height H, $t_{\rm diff} \simeq 3\tau_R H/c$, is a few hundred times shorter than the orbital period. Consequently photon pressure is irrelevant for disk fragmentation during massive star formation.

# in fig. 3.3	$\log_{10} j$ (cm^2 s^{-1})	Reference
1	22.3	Cesaroni et al. (2005)
2	21.4	Patel et al. (2005)
5	22.1	Zhang et al. (2002)
6	22.0	Bernard et al. (1999)
9	21.6	De Buizer & Minier (2005)

Table 3.2: Estimates of angular momentum of observed disks in figure 3.3 and corresponding references. Angular momentum estimates are computed from the observed velocity gradient over the extent of the disk. Estimates are only made for data points that showed a clear velocity gradient associated with a disk or torus.

3.2.4 Typical Parameters for Fragmentation

Before treating the core accretion model in detail in §3.3, we wish to draw a few conclusions that are reasonably independent of a scenario for massive star formation. We adopt in our irradiation model a fiducial efficiency parameter $\varepsilon = 0.5$, but we consider other values in §3.4.2.

We begin by mapping the maximum disk radius and maximum disk angular momentum as functions of the stellar mass $M_\star$ and the accretion time, $t_{\rm acc} = 2M_\star/\dot{M}_{\star d}$. (The factor of two derives from the core accretion scenario of McKee & Tan 2003; accretion time is simply a convenient parametrization for accretion rate.) The results for $R_{\rm crit}$ and $j_{\rm crit}$ are shown as the solid curves in figures 3.1 and 3.2, respectively.

Not all of this parameter space is relevant, however. Observations of protostellar outflows emerging from sites of massive star formation imply dynamical ages of order 10^5 years. On both of these figures, we highlight within the dotted lines a plausible range of $t_{\rm acc}$ as the range of values predicted by McKee & Tan (2003) for core column densities (Σ_c) of 0.3 – 3 g cm^{-2}. One may further restrict one's attention to masses between 10 and 120 $M_\odot$, as more massive stars are not known to exist. From this we infer: *for plausible values of the accretion time scale, massive-star accretion disks fragment for radii above about 100-200 AU, with 150 AU being a typical threshold.*

Table (3.2) lists our estimates for the angular momentum of several observed disks, most of which appear likely to fragment.

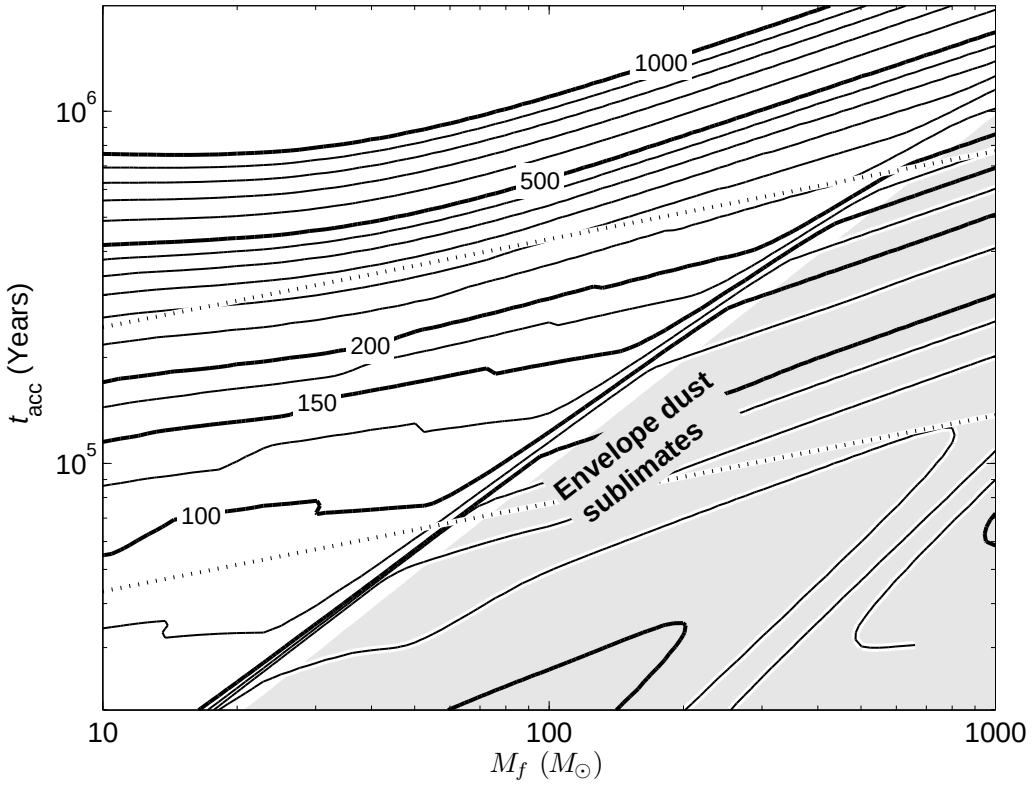

Figure 3.1: The fragmentation radius (in AU) is shown for a range of central star masses and accretion times. Also shown is the star formation time in the core model (*dotted lines*, for $0.3 < \Sigma_{\rm cl} < 3$ g cm^{-2}) and the region affected by dust sublimation in the infall envelope (filled region), where our model does not hold. The sharp kink in the lines of constant radius is due to a drop in opacity for disk temperatures above about 1050K.

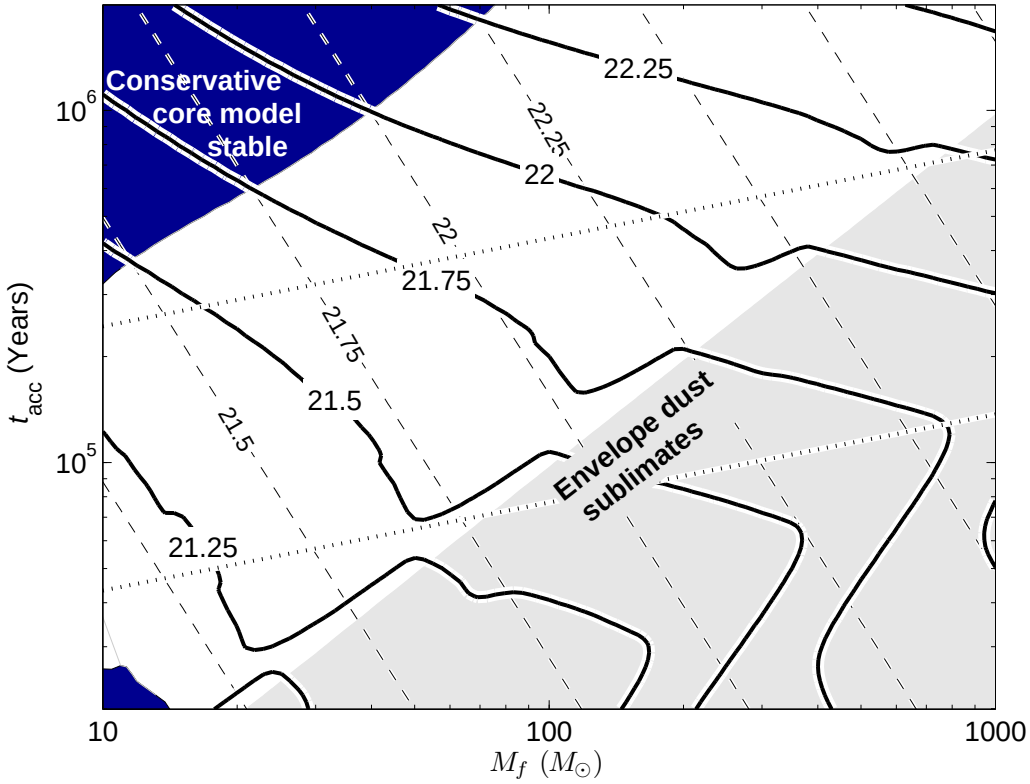

Figure 3.2: Angular momentum and disk fragmentation. The critical value of angular momentum, labeled as $\log_{10}(j_{\rm crit})$, is plotted as *bold curves* for a range of stellar masses and formation times, $t_{\rm acc} = 2M_\star/(\dot{M}_{\star d})$. *Dashed lines* show our predicted angular momentum for the McKee & Tan (2003) core model ($\varepsilon = 0.5, k_\rho = 1.5$). As discussed in §4.3.4, this is also an approximate upper limit to j given $M_\star$ and $t_{\rm acc}$. Disks tend to fragment except in the upper, dark filled region. In the lower, light filled region, envelope dust grains sublimate within R_d; our model is not secure here. *Dotted lines* delimit core model formation times for $0.3 < \Sigma_{\rm cl} < 3$ g cm^{-2}.

3.3 Core Accretion

With these relatively model-independent results in hand, let us evaluate disk fragmentation in the turbulent core model (Myers & Fuller, 1992; McKee & Tan, 2003), which posits that massive stars accrete from hydrostatic structures (cores, subscript "c") that have assembled from an overdense region (clump, subscript "cl") within a larger molecular cloud. This is similar to the standard model of low-mass star formation, except that turbulent motions are subsonic within low-mass cores (e.g., ML05) and supersonic in massive cores.

To calculate core and core collapse properties, we adopt the McKee & Tan (2003) models and fiducial parameters. Turbulent cores are modeled as singular polytropic spheres with density profiles $\rho(r) \propto r^{-k_\rho}$, with $k_\rho \simeq 1.5$. Since they are assumed to be hydrostatic (see also Tan et al., 2006), they must be pressure confined within their parent clumps. McKee & Tan 2003 evaluate the mean hydrostatic pressure within clumps to be

$$\bar{P}_{\rm cl} = 0.88 G \Sigma_{\rm cl}^2 \tag{3.17}$$

Further, they assume that massive cores are segregated to the centers of clumps where the pressure is roughly twice $\bar{P}_{\rm cl}$. Fixing cores' surface pressure to this value implies, for fiducial parameters, that $\Sigma_c = 1.22\Sigma_{\rm cl}$. Observations imply a column density $\Sigma_{\rm cl}$ of around 1 g cm^{-2} for the clumps that host massive star formation (Plume et al., 1997; Hillenbrand & Hartmann, 1998; Figer et al., 1999; Kim et al., 2000; van den Bergh et al., 1991; Gilbert & Graham, 2001; de Marchi et al., 1997; Turner et al., 2000; Faúndez et al., 2004).

As cores are bound and argued not to fragment (Tan et al., 2006), their gas either accretes on the star (a fraction ε) or is blown out by the protostellar wind ($1-\varepsilon$). The final stellar mass is therefore $M_{\star f} = \varepsilon M_c$, with $\varepsilon \simeq 0.5$, and the core radius is

$$R_c = \frac{0.040}{\varepsilon^{1/2}\Sigma_{\rm cl,cgs}^{1/2}} \left(\frac{M_{\star f}}{30 M_\odot}\right)^{1/2} {\rm pc} \tag{3.18}$$

where $\Sigma_{\rm cl,cgs}$ is in g cm^{-2}.

In the following sections we shall refer to $\sigma = \sigma(r)$, the local velocity dispersion of core gas at radius r; in a singular polytropic core,

$$\sigma(r)^2 = \frac{4\pi}{6\phi_B(k_\rho - 1)} \frac{G M_c(r)}{r} \tag{3.19}$$

where $M_c(r)$ is the enclosed mass, and $\phi_B \equiv P/(\rho\sigma^2)$ accounts for magnetic contributions to the total pressure; McKee & Tan (2003) estimate $\phi_B \simeq 2.8$.

We note, in passing, that the fiducial core model implicitly assumes that stellar accretion halts due to a limited mass supply, rather than due to the onset of vigorous stellar feedback, fragmentation of the core or disk, or any other dynamical effect. Alternatively one could either have $\varepsilon = M_{\star f}/M_c \ll 1$, or one could define the core to be the subregion that successfully accretes (for which $\varepsilon \sim 0.5$). In the latter choice, the pressure-equilibrium column, $\sim 1.22\Sigma_{\rm cl}$, would provide only a lower limit to Σ_c. As it is widely held that the upper mass cutoff derives from stellar feedback, we expect columns in excess of this lower limit to prevail for very massive stars. Nevertheless, we evaluate the above equations for $\Sigma_c = 1.22\,{\rm g\,cm^{-2}}$ in the fiducial case.

3.3.1 Collapse

McKee & Tan (2003) show that the accretion time is close to the free-fall time evaluated at the core's surface density. Their equations (3), (4), (5), (35), and (36) specify

$$\dot{M}_{\star d} = \varepsilon\phi_{\rm acc}\frac{\sigma^3}{G} \tag{3.20}$$

where

$$\begin{aligned}\phi_{\rm acc} &= 0.71(3.38-k_\rho)(k_\rho-1)^{3/2}(3-k_\rho)^{1/2} \\ &\quad\times\begin{cases}\frac{\phi_B^{3/2}}{(1+H_0)^{1/2}}, & \text{magnetic}\\ 1, & \text{nonmag.}\end{cases}\\ &\rightarrow 1.9\end{aligned} \tag{3.21}$$

where the magnetic term includes levitation by the static field (the factor $(1+H_0)\simeq 2$) as well as turbulent magnetic pressure (the factor ϕ_B). The second line evaluates the first for a magnetized core with $k_\rho = 1.5$, for which the final accretion time is

$$t_{\rm acc} = 1.3\times 10^5 \Sigma_{\rm cl,cgs}^{-3/4}\left(\frac{0.5}{\varepsilon}\frac{M_{\star f}}{30M_\odot}\right)^{1/4}\ {\rm yr} \tag{3.22}$$

(McKee & Tan, 2003). Equation (3.21) implies fragmentation when

$$c_s < 1.04(\varepsilon\phi_{\rm acc})^{1/3}\sigma, \tag{3.23}$$

i.e., for $c_s < 1.02\sigma$ when $\varepsilon = 0.5$ and $\phi_{\rm acc} = 1.9$.

During collapse, distribution of mass, $M_c(r) \propto r^{3-k_\rho}$, and free-fall time, $t_{\rm ff}(r) \propto \rho(r)^{-1/2}$, imply

$$\begin{aligned} M_\star &= (t/t_{\star f})^{\eta_m} M_{\star f} \quad \text{and} \\ \dot{M}_{\star d} &= \frac{\eta_m M_\star}{t} \propto M_\star^{1-1/\eta_m} \quad \text{where} \\ \eta_m &= \frac{6}{k_\rho} - 2 \quad \to 2. \end{aligned} \tag{3.24}$$

The accretion time is longer than the Kelvin-Helmholtz time for stars $\gtrsim 10 M_\odot$ (Wolfire & Cassinelli, 1987), implying that massive protostars reach the zero age main-sequence (ZAMS) during accretion. When calculating the time evolution of fragmentation in §3.4.3, we employ the McKee & Tan (2003) models for the luminosity of a massive accreting protostar; to calculate irradiation at the end of accretion we also include ZAMS luminosity, using formulae from Tout et al. (1996).

3.3.2 Angular Momentum

To evaluate our fragmentation criterion, we require the angular momentum of material within a collapsing turbulent core. Although this is not included in the McKee & Tan (2003) models, we shall estimate angular momentum within these models by generalizing a calculation by ML05 (itself an analytical version of the Burkert & Bodenheimer 2000 calculation, in the vein of Fleck 1987). This calculation (presented in the Appendix) notes that a core model specifies the turbulent velocity dispersion $\sigma(r)$ as well as the density profile $\rho(r)$. For a special class of velocity fields one can compute the ensemble-averaged specific angular momentum and velocity dispersion. The velocity field must be isotropic; it must have a velocity difference between any two points that scales as $\sigma(|\mathbf{r}_1 - \mathbf{r}_2|) \propto |\mathbf{r}_1 - \mathbf{r}_2|^\beta$ regardless of the underlying density distribution; and its Cartesian components must be uncorrelated (i.e., transport no average shear stress). The ensemble-averaged specific angular momentum and velocity dispersion are calculated in equations (3.44)-(3.47). We define the *spin parameter* θ_j for a turbulent region of size R:

$$\theta_j \equiv \frac{j}{R\sigma(R)} = f_j \frac{\langle j^2 \rangle^{1/2}}{R \langle \sigma(R)^2 \rangle^{1/2}}. \tag{3.25}$$

The rightmost expression involves root-mean-square ensemble averages over the turbulent velocity field, which are calculated in the Appendix. The factor f_j accounts for the difference between the ratio of rms averages and the ratio of amplitudes; since the

amplitudes are random variables, this includes both an overall offset and a disperson. ML05 estimate $\log_{10} f_j = -0.088^{+0.16}_{-0.49}$ on the basis of a Gaussian model for the velocity field.

Our evaluation of the spin parameter is presented in the Appendix and summarized in figure 3.7 and table 3.7. For a turbulence supported region with $\rho \propto r^{-k_\rho}$ one must have $\sigma(r)^2 \propto GM(r)/r \propto r^{2-k_\rho}$, so $\beta = 1 - k_\rho/2 \to 1/4$ (for $k_\rho \to 3/2$). In the McKee & Tan core collapse model, each shell of matter accretes in sequence. For each shell, the spin parameter is

$$\theta_j(\text{shell}) = 0.85\beta^{0.42} f_j \to 0.47 f_j \tag{3.26}$$

(see equation 3.49). However, the last shell to accrete naturally has the highest angular momentum; as the disk accumulates vector angular momentum,3.26 may overestimate the disk radius. Moreover, although collapse is generally super-Alfvénic, magnetic braking may sap j somewhat. A rough lower bound on θ_j is given by the specific angular momentum of the entire core, which corresponds to

$$\theta_j(\text{entire core}) = 0.50\beta^{0.55} f_j \to 0.23 f_j \tag{3.27}$$

(also equation 3.49).

Given upper and lower limits for θ_j, we must decide which value to adopt. The remainder of this chapter is intended to establish that fragmentation is inevitable in the outer reaches of massive-star disks, so we shall adopt the more conservative estimate (eq. 3.27). Please bear in mind that the upper bound to R_d is about four times larger. The protostellar outflow will tend to remove low-j material (see also ML05), but we expect this effect to be rather minor and do not evaluate it.

For convenience we shall define a second rotation-related quantity, ϕ_j, by

$$j = \frac{\phi_j}{\varepsilon} \frac{GM_\star}{\sigma}. \tag{3.28}$$

The factor ϕ_j defined here is related to the spin parameter θ_j by $\phi_j = R\sigma(R)^2\theta_j/[GM(R)]$. Hydrostatic equilibrium requires $R\sigma(R)^2/[GM(R)] = 1/[2(k_\rho - 1)\phi_B]$: therefore

$$\phi_j = \frac{\theta_j}{2(k_\rho - 1)\phi_B} \to 0.36\theta_j \tag{3.29}$$

giving $\phi_j = 0.067$ in the fiducial case.

The disk acquires a final radius which is about 1/40th of the core radius:

$$R_{d,f} \quad = \quad \frac{\theta_j \phi_j}{\varepsilon} R_c$$

$$\rightarrow \quad 300 \left(\frac{0.5}{\varepsilon}\right)^{3/2} \left(\frac{M_{\star f}}{30\,M_\odot}\frac{1}{\Sigma_{\rm cl,cgs}}\right)^{1/2} {\rm AU} \tag{3.30}$$

in the fiducial, conservative case given by equation (3.27). During accretion, the disk radius remains proportional to the current radius of accretion; therefore

$$\frac{R_d}{R_{d,f}} = \left(\frac{M_\star}{M_{\star f}}\right)^{\frac{1}{3-k_\rho}\rightarrow 2/3}, \tag{3.31}$$

at least on average.

It is useful to know the column density scale in the infall for reference in the calculation of disk irradiation. As discussed in ML05, this is characterized by $\Sigma_{\rm sph}(R_d)$: the column outward from R_d in a nonrotating infall of the same accretion rate. We find

$$\begin{aligned} \Sigma_{\rm sph}(R_{d,f}) &= \frac{\epsilon\phi_{\rm acc}}{2^{5/2}(k_\rho-1)\phi_B\theta_j}\Sigma_c \\ &\rightarrow 0.64\Sigma_c \end{aligned} \tag{3.32}$$

i.e., that the final infall column is comparable to the core column (see also ML05). Over the course of accretion,

$$\frac{\Sigma_{\rm sph}(R_d)}{\Sigma_{\rm sph}(R_{d,f})} = \left(\frac{M_\star}{M_{\star f}}\right)^{\frac{1-k_\rho}{3-k_\rho}\rightarrow -1/3}. \tag{3.33}$$

Finally, a note on the relation between a core's density profile and its angular momentum scale. Considering the range of values $1 \le k_\rho \le 2$, the angular momentum of a turbulent sphere decreases sharply toward zero as k_ρ approaches 2 and β approaches zero, as shown in figure 3.7. This trend is easily understood: when $\beta = 0$, the velocity difference between two points is independent of their separation and must therefore be contained in very small-scale motions as in an isothermal gas. Indeed, the three-dimensional power spectrum scales as $k^{-3-2\beta}$ and contains a divergent energy at small scales as $\beta \rightarrow 0$. Angular momentum is dominated by the largest-scale motions that fit within the region of interest, and therefore vanishes if turbulent energy appears only at small scales. However, a core whose hydrostatic support is effectively isothermal ($\beta = 0$) may still contain angular momentum due to *background* turbulence if it is confined in a turbulent region with $\beta > 0$. This situation holds for thermally supported cores within turbulent molecular clouds, and formed the basis for the ML05 estimate of disk radii in low-mass star formation.

Background turbulence may increase j for turbulent cores, as well, if the density profile flattens and the effective value of β increases across the core boundary. Our calculation

in the Appendix assumes that velocity field is described by the same β everywhere, so the corrected value of θ_j should be intermediate between the core's β and that of the parent clump.

3.3.3 Observations of Rotation in HMSF

Goodman et al. (1993) observe velocity gradients of dense cores, including both low and high-mass cores, using $C^{18}O$, NH_3 and CS as tracers. They find that the ratio of rotational to gravitational energy, which we call $\beta_{\rm rot}$ (to avoid confusion with $\sigma \propto r^{\beta}$), takes a rather broad distribution around a typical value of 0.02, i.e., $\log_{10}\beta_{\rm rot} = -1.7$. In our model for rotation within singular polytropic cores,

$$\beta_{\rm rot} = \frac{(5-2k_\rho)^2}{8(3-k_\rho)(k_\rho-1)}\frac{\theta_j^2}{\phi_B}. \tag{3.34}$$

Using $\theta_j = 0.23 f_j$ as we estimated for the entire core (eq. [3.27]) this gives $\log_{10}\beta_{\rm rot} \simeq -2.1 \pm 0.7$, whereas using $\theta_j = 0.47 f_j$ as appropriate to the outer shell (eq. [3.26]), $\log_{10}\beta_{\rm rot} \simeq -1.7 \pm 0.7$. The agreement would thus be good if the Goodman et al. observations traced the outermost core gas, but this seems unlikely. A better explanation is that the observed cores have somewhat flatter density profiles; the discrepancy is removed if $k_\rho = 1.35$ rather than 1.5 (using eqs. [3.42] and [3.49]). As noted above, embedding the core within a clump medium that has a flatter density profile (and higher β) would have the same effect. Protostellar outflows also raise j slightly by removing material on axis. Of course, our model for core angular momentum is based on an idealized turbulent velocity spectrum, and undoubtedly involves some error.

We include observations of disks and toroids in massive star forming regions in figure (3.3) and table 3.3. However it should be noted that such comparisons are limited due to uncertainty in both the values of quoted parameters and in the actual phenomena being observed. Only recently has it been possible to achieve the resolution and sensitivity required to constrain models of massive star formation. Many uncertainties remain when distinguishing between infall, rotation (Keplerian or otherwise), and outflow. Many of the objects show velocity gradients that are consistent with Keplerian rotation, but could also be attributed to another bulk motion, such as infall. Furthermore even when rotation is indeed Keplerian, it is difficult to distinguish the disk edge from its natal core (De Buizer & Minier, 2005; Cesaroni, 2005; De Buizer, 2006). This, and confusion with the outflow (De Buizer, 2006), may cause disk masses and extents to be overestimated. The mass,

luminosity and multiplicity of the central object involve further uncertainties.

We have already noted that the angular momentum seen in observations coincides with our estimated upper bound from the core collapse model. Although we think this agreement is likely to be real, it is also possible that the observed rotation is about a stellar group rather than a single object. This alternative is strengthened by the fact that many rotating envelopes are inferred to be more massive than any single central object, on the basis of the central luminosity. Such overweight disks are subject to strong *global* self-gravitational instabilities quite distinct from the local instability we addressed in §3.2. We refer the reader to Shu et al. (1990) on this point; see also the discussion in §3.4.4 and that given in ML05.

It is notable that the three observations most confidently interpreted as thin massive-star disks (Patel et al., 2005; De Buizer & Minier, 2005; Shepherd et al., 2001) are the best match to our predictions. The other, more extended massive disks or toroids are of uncertain mass and radius and may enclose many stars. As noted by Cesaroni (2005) and Beuther et al. (2006), in these instances we might be seeing proto-cluster, rather than protostellar, disks and toroids.

3.4 Fragmentation of Core-Collapse Disks

A numerical evaluation of fragmentation is presented below in §3.4.1, but first we calculate the scalings that govern these results. Given the fragmentation criterion from §3.2.1 and the fiducial core-collapse model described in §3.3, we can estimate the ratio $T_d/T_{\rm crit}$ by ignoring either irradiation ("active" disks, as in §3.2.2) or viscous heating ("passive" disks, using §3.2.3):

$$\frac{T_d(R_d)}{T_{\rm crit}} = \begin{cases} 0.15 \left(\dfrac{\varepsilon_{0.5}^{7.7} \kappa_{R,\rm cgs}^4 \Sigma_{\rm cgs}^5}{M_{\star f,30}^7} \right)^{1/20}, & \text{(active disk)} \\ 0.35 \left(\dfrac{L_5}{\varepsilon_{0.5}^{1/60} M_{\star f,30}^3 \Sigma_{\rm cgs}^{1/4}} \right)^{1/4}, & \text{(passive disk)} \end{cases} \tag{3.35}$$

where $L_\star = 10^5 L_5 L_\odot$, $\varepsilon = 0.5\varepsilon_{0.5}$, $\kappa_R = \kappa_{\rm R,cgs}\,{\rm cm}^2\,{\rm g}^{-1}$, and $\Sigma = \Sigma_{\rm cgs}\,{\rm g\,cm}^{-2}$.

Note that increasing $M_{\star f}$ destabilizes disks in both regimes. High values of Σ enhance viscous heating relative to irradiation, but neither is sufficient to prevent fragmentation around a 30 $M_\odot$ star when $\Sigma \sim 1\,{\rm g\,cm}^{-2}$. However, if we take $L = 20$ and $\Sigma = 0.034\,{\rm g\,cm}^{-2}$ – values typical of the low-mass star formation studied by ML05 – then $T_d(R_d) > T_{\rm crit}$ for $M > 1.3\,M_\odot$ according to equation (3.35). The evaluation used here

neglects several effects treated in that chapter , such as thermal core support. Nevertheless these scalings explain why disks are intrinsically less stable during massive star formation than in the low-mass case, as seen in detail below.

3.4.1 Results

Fragmentation is expected when $R_{d,f} > R_{d,\mathrm{crit}}$, i.e., when the disk extends past the critical fragmentation radius at some point during formation. Figure 3.3 compares these two radii for a range of stellar masses, using the fiducial, conservative core collapse model ($k_\rho = 3/2$, $\varepsilon = 0.5$, $\Sigma_{\mathrm{cl}} = 1\,\mathrm{g\,cm^{-2}}$, $\theta_j = 0.23 f_j$) to compute R_d.

To address the lowest-mass stars whose disks can fragment, we must account for the thermal component of a core's hydrostatic pressure and for the accretion luminosity, both of which are negligible in very massive stars. We have (1) included a thermal component (at 20 K) in the effective temperature that sets the accretion rate, so that $\dot{M}_{\star d} \geq 10^{-5.3} \varepsilon M_\odot\,\mathrm{yr}^{-1}$ for all masses; (2) added accretion luminosity to the ZAMS luminosity when estimating disk irradiation; and (3) employed the Palla & Stahler (1992) models (for $\dot{M}_{\star d} = 10^{-4} M_\odot$ yr^{-1}, which is appropriate) to estimate the radius of the accreting protostar. Although rather approximate, these amendments are of diminishing importance as $M_{\star f}$ increases beyond $\sim 20 M_\odot$.

Given the expected range of disk radii, all the disks presented in figure 3.3 are candidates for fragmentation. The expected disk radius crosses the fragmentation boundary for $M_{\star f} \simeq 3.5 M_\odot$, and the two remain almost equal until $M_{\star f} \simeq 10 M_\odot$; fragmentation is marginal in this range. Fragmentation becomes increasingly likely as the mass increases, though slowly: R_{crit} is within a factor of 2 of R_d for $M_{\star f} < 23 M_\odot$. For $M_{\star f} > 57 M_\odot$, R_{crit} drops below the range of disk radii implied by the dispersion of f_j given below equation (3.25) – as indicated by the gray region in figure 3.3. The specific masses quoted depend on our model for angular momentum, particularly as the critical radius is relatively constant in the range 100-150 AU.

Recall, however, that the disk angular momentum derives from a turbulent velocity field and is therefore quite stochastic. The spread in j predicted by a Gaussian model for the velocity field allows for the frequent formation of disks twice as large as predicted in equation (3.30). Likewise, much smaller disks (by about a factor of nine) can form equally easily from a chance cancellation within the core velocity field. This dispersion in expected radii is indicated as a shaded band in figure 3.3. Remember also that we adopted

a conservative estimate of the disk angular momentum; otherwise, disk fragmentation would have been even more prevalent. Taking these points into account, we can draw a few conclusions with relative certainty.

1. A *significant portion* of the O star and early B star protostellar disks predicted in the core collapse model are prone to fragmentation, although the exact fraction is sensitive to the (uncertain) angular momentum scale and fragmentation criterion;

2. The tendency of disks to fragment increases with stellar mass ($M_{\star f}$); it decreases with higher column densities ($\Sigma_{\rm cl}$), and with steeper initial density profiles (k_ρ).

3. Disks accreting more rapidly than about $1.7 \times 10^{-3} M_\odot\,{\rm yr}^{-1}$ are destabilized by the sharp drop in dust opacity at ~ 1050 K, according to equation (3.4). In the fiducial core model, this occurs above about 110 $M_\odot$, close to the observed upper limit of stellar masses. More generally, this occurs for $M_{\star f} > 87 (t_{\rm acc}/10^5 {\rm yr}) M_\odot$.

4. At somewhat higher accretion rates, however, dust sublimation invalidates our model for starlight reprocessing in the infall envelope.

5. So long as disks remain optically thick, any effect that decreases the Rosseland opacity is destabilizing. For instance, low-metallicity disks are less stable than those of solar composition. (Primordial disks are however opaque in their inner portions. Tan & McKee, 2004) By adopting the (relatively opaque) Semenov et al. (2003) dust opacities, we have underestimated disk fragmentation.

3.4.2 Effect of Varying Efficiency

Up to this point we have adopted $\varepsilon = 0.5$ as the fiducial accretion efficiency, following McKee & Tan (2003). In the theory of Matzner & McKee (2000), ε is set by the ejection of material by a centrally-collimated protostellar wind. Matzner & McKee show that ε is quite insensitive to the ratio of infall and outflow momentum fluxes. Nevertheless, 0.5 is only an estimate and ε could well vary during accretion. This is especially true if the protostellar wind were ever to truncate accretion, as $\varepsilon(t) \to 0$ when this happens. We briefly consider other values here.

The primary effect of varying ε, while fixing $M_{\star f}$, $\Sigma_{\rm cl}$, and k_ρ, is to change the core mass required to make a star of that mass. Suppose we halve ε, so that M_c must double.

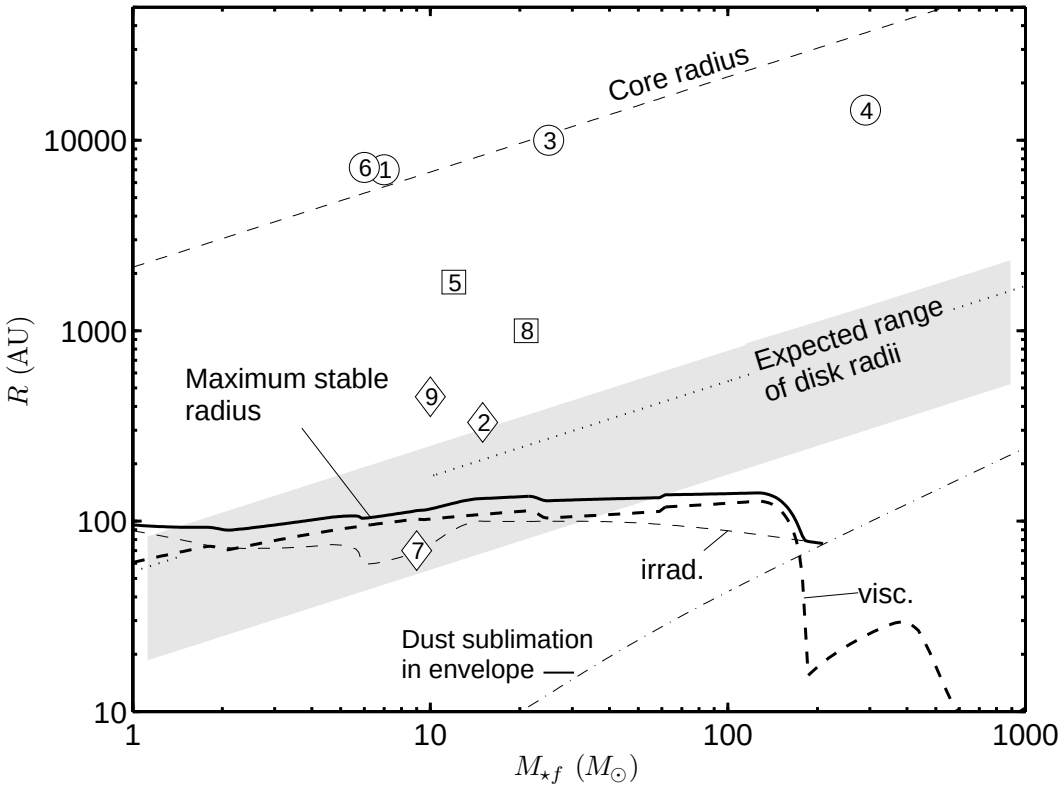

Figure 3.3: Relevant radii. The characteristic disk radius predicted by (fiducial) core accretion is accompanied by a shaded band illustrating our (Maxwellian) model for its dispersion. The largest stable radius is plotted for comparison; this is accompanied by the contributions from pure irradiation (no viscous heat) and pure viscosity (no irradiation). The turnover of $R_{\rm crit}$ above $\sim 20 M_\odot$ is due to the scaling of ZAMS mass and luminosity. The references for the observational points are listed in table (3.3). Circles represent objects that may best be described as cores, whereas diamonds represent those objects whose disks are well resolved. Squares indicate objects for which it is unclear whether they are rotating, infalling, or both; see §3.5.2 for discussion.

Number in figure 3.3	Reference
1	Cesaroni et al. (2005)
2	Patel et al. (2005)
3	Olmi et al. (2003)
4	Olmi et al. (2003)
5	Zhang et al. (2002)
6	Bernard et al. (1999)
7	Shepherd et al. (2001)
8	Shepherd et al. (2001)
9	De Buizer & Minier (2005)

Table 3.3: Observational data points in figure 3.3 and corresponding references.

The accretion time then increases, and $\dot{M}_{\star d}$ decreases, by a factor $2^{1/4}$ (for $k_\rho = 3/2$). This mildly stabilizes the disk. But at the same time, R_c has been increased by $2^{1/2}$, j has gone up by $2^{3/4}$, and $R_{d,f}$ has expanded by $2^{3/2}$. Balancing these contributions, we expect lowering ε to destabilize the disk. This was predicted also in equation (3.35), where lowering ε is seen to decrease stability in an active disk. Passive disks are extremely insensitive to ε.

Figure (3.4) corroborates our expectation by showing that lower values of ε correspond to less stable disks. Indeed, the mass at which fragmentation sets in is sensitive to ε, specifically, $M_{\rm crit} \propto \varepsilon^{2.6}$, while the critical disk radius is relatively constant. Does this mean that a decline in core efficiency over time destabilizes disks? Probably not, since most of the mass will be accreted at an intermediate value of ε (see the discussion below equation 3.18).

3.4.3 Time Evolution of Disk Fragmentation

For those disks that do suffer fragmentation, it is useful to know whether this happens early or late in accretion and how much matter is potentially affected. To address these questions we construct the time history of the accretion rate, stellar mass, and disk radius for a star with $M_{\star f} = 30\,M_\odot$ in the fiducial core collapse model. For this calculation we use the luminosity history of such a star as presented by McKee & Tan (2003). The scalings $R_d(t) \propto M_\star(t)^{1/(3-k_\rho)}$ and $\dot{M}_{\star d}(t) \propto M_\star(t)^{(6-2k_\rho)/(6-3k_\rho)}$ permit us to gauge disk fragmentation through time.

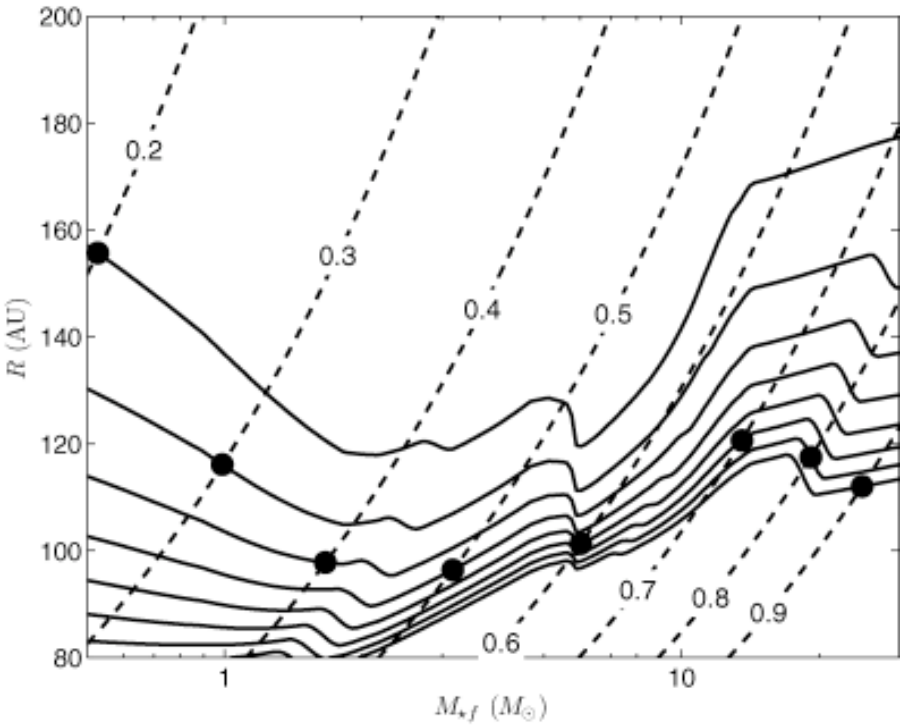

Figure 3.4: Effect of varying the star formation efficiency ε in the fiducial core collapse model. *Dashed lines*: critical disk radius $R_{d,\mathrm{crit}}$ for fragmentation; *solid lines*: expected disk extent R_d. Intersections are as marked.

Figure (3.5) shows the evolution of R_d and $R_{\rm crit}$ during accretion. In this plot, the relative constancy of the fragmentation radius is due to the enhanced effect of irradiation at low masses. We find that a star destined to become $30M_\odot$ (born of a 60 $M_\odot$ core) has a disk that crosses into the regime of fragmentation when the protostar has accreted approximately $5.6M_\odot$. The fact that this is slightly higher than the critical mass identified earlier is to be expected: the inner $5.6M_\odot$ of a larger core is equivalent to a $5.6M_\odot$ core with a slightly higher column density – specifically, $\Sigma_c \propto (M_\star/M_{\star f})^{-1/3}$, for $k_\rho = 3/2$ (cf. equation 3.33). The somewhat higher column density implies a smaller and somewhat stabler disk, leading to a slightly higher mass scale for fragmentation.

We also show on figure (3.5) the radius of the innermost streamline of infalling material from the envelope from Terebey et al. (1984), again assuming an accretion efficiency of 50%. This, along with stochastic variations in disk angular momentum about its typical value, suggest that accretion can coexist with fragmentation so long as the disk is not too far beyond the fragmentation threshold; see §3.5.3 for more discussion.

3.4.4 Disk mass and global instability

At the typical fragmentation radius of $100 - 150$ AU, the mass scale of a disk with $Q = 1$ is

$$\frac{\pi R_d^2 \Sigma_d(R_d)}{M_{\star f}} = 0.10 \varepsilon_{0.5}^{1/12} \left(\frac{R_d}{150\,{\rm AU}} \right)^{1/2} \frac{\Sigma_{\rm cgs}^{1/4}}{M_{\star f,30}^{1/4}}. \tag{3.36}$$

Global instabilities of the disk are triggered by the total disk mass (Adams et al., 1989; Shu et al., 1990), which is larger than $\pi R_d^2 \Sigma_d(R_d)$ by the factor $2/(2 - k_\Sigma)$ if $\Sigma_d \propto r^{-k_\Sigma}$ within R_d. There is therefore the possibility that the fast angular momentum transport by these modes (Laughlin et al., 1998) suppresses local fragmentation, but we consider it unlikely that fragmentation is eliminated by this process.

3.5 Consequences of Instability

3.5.1 Fragment Masses

Once a disk fragments, what objects form? Goodman & Tan (2004) determine the *initial* fragment mass based on the wavenumber of the most unstable mode in the disk. The corresponding wavelength of this axisymmetric mode is:

$$\lambda(r) = 2\pi \frac{c_{\rm ad}^2}{\pi G \Sigma}, \tag{3.37}$$

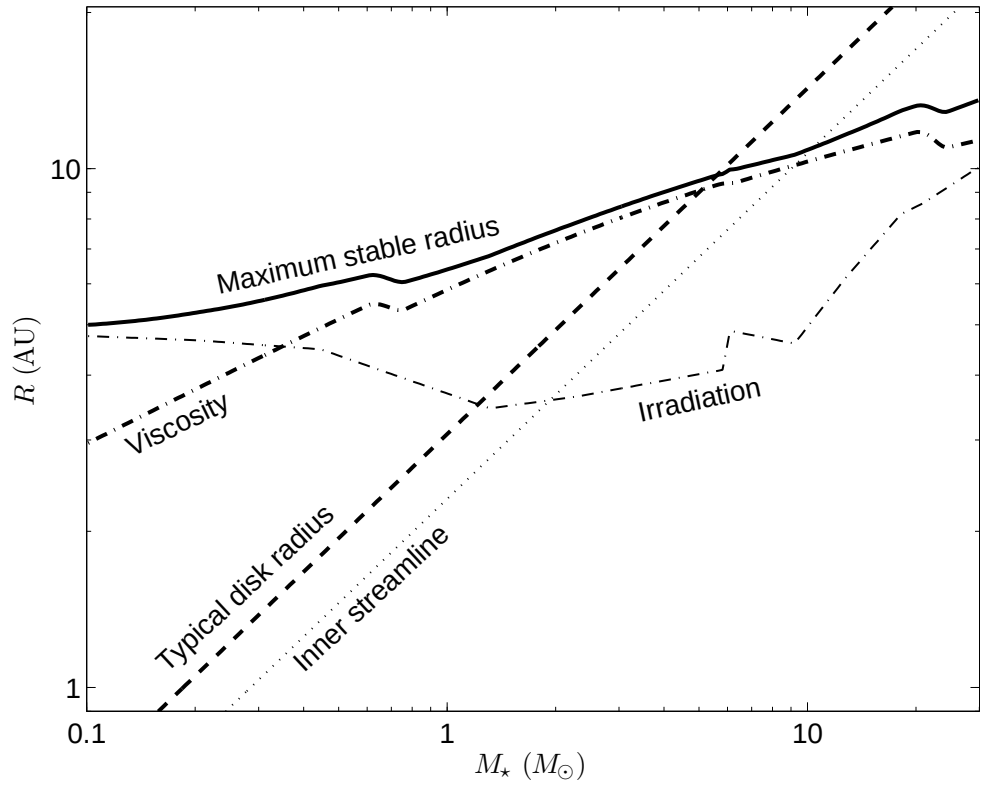

Figure 3.5: Growth of disk and critical radius with the mass of a protostar accreting toward $30M_\odot$ in the fiducial core collapse model. In addition to the expected disk radius, we show the splashdown radius of the inner infall streamline, calculated assuming $\varepsilon = 0.5$.

where Σ and c_s are both functions of radius within the disk. Assuming that the fragment has comparable dimension azimuthally, the corresponding mass scale is (Goodman & Tan, 2004)

$$\begin{aligned} M_{\rm frag} &= \lambda^2 \Sigma \\ &= \frac{4\pi}{\Omega} \frac{c_{\rm ad}^3}{GQ}, \end{aligned} \tag{3.38}$$

i.e., roughly the amount of mass accreted in $2Q$ orbits. We assume fragmentation only occurs when $Q \rightarrow 1$. We consider our rather idealized estimate of $M_{\rm frag}$ uncertain by at least a factor of two. In reality the initial mass is likely a stochastic variable, best determined from numerical simulations (R. Rafikov, private communication).

Once a fragment forms, its growth is controlled by accretion of surrounding gas, migration through the disk, and collisional or gravitational interaction with other fragments. Rather than address these questions in detail, we will draw preliminary conclusions by comparing $M_{\rm frag}$ to two critical scales: the gap opening mass $M_{\rm gap}$ and the isolation mass $M_{\rm iso}$. A fundamental uncertainty is the state of the gas disk: again, we assume $Q = 1$.

When the gravitational torques exerted on the disk by the fragment exceed viscous torques, a gap opens around the fragment. Rafikov (2002) estimates

$$\begin{aligned} M_{\rm gap} &= \frac{2c_{\rm ad}^3}{3\Omega G} \frac{\alpha}{0.043} \\ &= 0.37 \frac{\alpha/0.30}{Q} M_{\rm frag}. \end{aligned} \tag{3.39}$$

Since this is less than $M_{\rm frag}$, and gets even smaller if the disk viscosity goes down and thus cooling time goes up relative to the critical state in the Gammie (2001) simulations, we expect fragments to open gaps immediately.

Gap opening slows but does not necessarily end accretion (Artymowicz & Lubow, 1996). A possible limit to growth is set by the point at which the fragment accretes all the mass within its Hill radius (e.g., Goodman & Tan, 2004, but see Artymowicz & Lubow). This defines the isolation mass

$$M_{\rm iso}(r) \approx \frac{(2\pi f_H r^2 \Sigma)^{3/2}}{9 M_\star^{1/2}} \tag{3.40}$$

where $f_H \simeq 3.5$.

Figure (3.6) compares the initial, gap opening, and isolation masses for a range of $M_{\star f}$, evaluated at $R_{\rm crit}$ near the end of core accretion (in the fiducial core model). Because

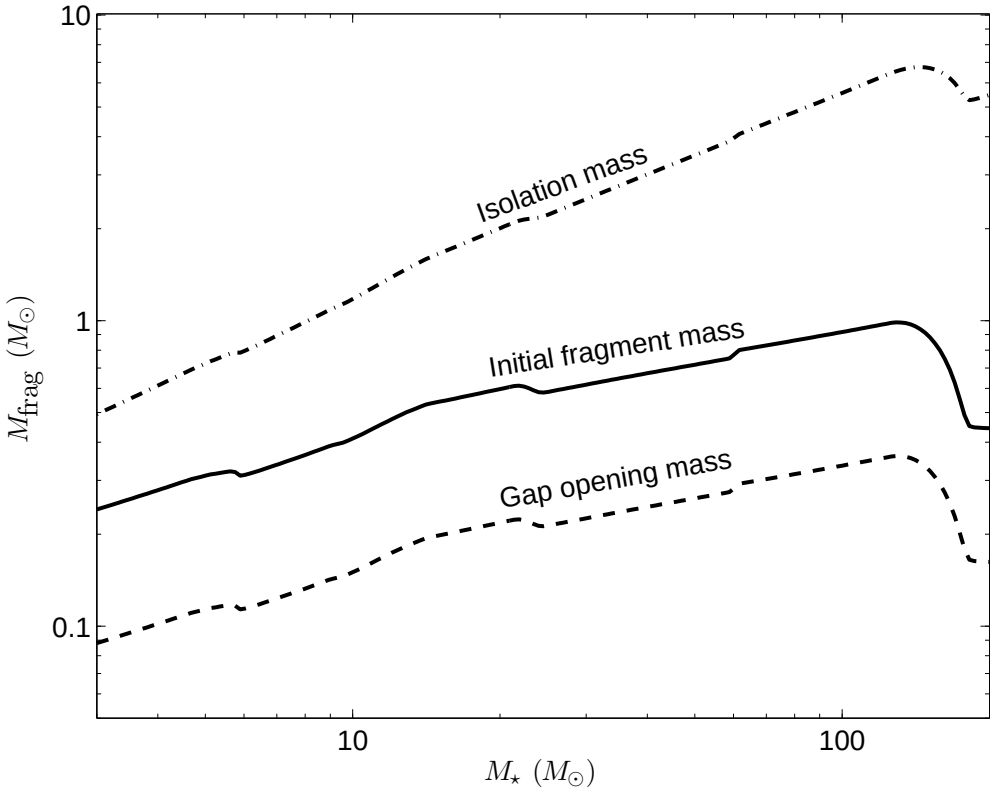

Figure 3.6: Our estimate of the initial fragment mass, compared to the gap opening mass and isolation mass, at the end of accretion in the fiducial core collapse model. We truncate the calculation where dust sublimation in the envelope makes the critical radius determination uncertain.

gap opening slows accretion, we expect the masses of disk-born stars to resemble $M_{\rm frag}$ more than $M_{\rm iso}$. In this case they will be low-mass stars of order 0.2–0.4 $M_\odot$.

Fragmentation tends to set in at $\sim 100 - 200$ AU, as we noted in §3.2.4. However gap-opening fragments should be swept inward if disk accretion continues; only a single disk mass of accretion is required to bring them in to the central object. If they move inward by about a factor of 30, they will be within a few stellar radii at carbon ignition (Webbink, 1985). As candidates for mass transfer and common-envelope evolution, such objects can serve as reservoirs of matter and angular momentum for the relic of the central star's supernova explosion.

3.5.2 Observability of Disk-Born Stars

We have predicted that stars with extended protostellar disks will produce low mass (M5–G5) companions. Thus we would expect many O stars, and perhaps some early B stars, to have multiple coplanar companions at separations of order $\lesssim 100-200$ AU, depending on the amount of migration that occurs following formation. In the closest clusters, for example, Orion, this correspondes to an angular separation of approximately $0.4''$ and an apparent bolometric magnitude difference of, at a minimum, ~ 13 magnitudes. This implies that even in K-band with an AO system such as that of VLT, such objects would be difficult to observe (M. Ahmic, private communication). Similarly, the combination of AO with a coronograph (e.g. the Lyot coronograph on AEOS) can provide a dynamic range of up to up to 8 H-band magnitudes at a few hunderd mas, which is still too small to detect the aforementioned companions (Hinkley et al., 2007). If not detectable during the main sequence life of the primary star, the presence of such companions might be observable via binary interaction once the primary evolves.

3.5.3 Disk Efficiency

If a $30M_\odot$ star will suffer disk fragmentation early in its accretion, as we estimated in §3.4.3 on the basis of the turbulent core model, then we must address how this might impact subsequent accretion. One possibility is that gap-opening fragments will be swept inward to the central star, in which case its final mass will be unaffected. This outcome resembles the scenario outlined by Levin (2003) for gravitationally unstable AGN accretion. Alternatively, Tan & Blackman (2005) suggest low-luminosity AGN may be starved of gas by fragmentation.

In the latter scenario, a strongly unstable disk will have a low *disk efficiency*, $\varepsilon_d \equiv \dot{M}_\star/\dot{M}_{\star d}$. We can estimate ε_d in the limit that none of the gas entering an unstable region of the disk ultimately accretes onto the star. The splashdown radius of the innermost streamline was estimated in expression (3.12). Given that outflow removes matter from the inner streamlines, and that fragmentation removes it from the outer portions of the disk, the fraction of mass that successfully accretes (after striking the disk) is

$$\varepsilon_d = 1 - \varepsilon^{-1}\left[1 - \left(1 - \frac{R_{\rm crit}}{R_d}\right)^{1/2}\right]. \tag{3.41}$$

Of course, this expression is only applicable when it yields $0 \leq \varepsilon_d \leq 1$, i.e., when the disk is partly but not wholly unstable.

Two complications arise when evaluating equation (3.41). First, the critical radius $R_{\rm crit}$ must be calculated using the mass accretion rate outside of itself. Second, recall that the angular momentum of infalling gas derives from its initial turbulent velocity and is likely to vary in direction and magnitude. The fluctuations of j were estimated by the distribution f_j, which appeared in equation (3.25). Accounting for both of these effects, we find that accretion can continue even in an actively unstable disk. For $30 M_\odot$, we find that the infall streamline remains within the stable disk radius through the end of accretion. Even if all the gas entering a fragmenting region is consumed, this need not fully starve the central object. However, the tendency to fragment becomes much stronger for more massive stars. This is especially true for those ($M_{\star f} \sim 110 M_\odot$, from §3.4) that accrete rapidly enough that their disks are destabilized by the drop in dust opacity.

In reality, we expect some gas to accrete through the unstable region. A rough upper limit would be to adopt the accretion rate for a Toomre-critical ($Q = 1$) state, and assume that any surplus is consumed by fragmentation. In this case, the central accretion rate would be limited by the temperature of the coldest region of the disk (according to eq. 3.4). Numerical simulations will ultimately be required to quantify the behaviour of Toomre-unstable disks.

Furthermore, there are numerous feedback mechanisms that have not been addressed. For example, if fragmentation halts accretion, this could change the outflow power, the shape of the outflow and infall cavity and thus the heating of the disk by reprocessed starlight. This interplay will be investigated in future work.

3.6 Discussion

Our primary conclusion (§3.2.4) is that massive-protostar disks that accrete more slowly than $\sim 1.7 \times 10^{-3} M_\odot$ yr^{-1} are subject to fragmentation at disk radii beyond about 150 AU. This critical radius is set primarily by the viscous heating of the disk midplane as it accretes, with reprocessed starlight playing an equal or secondary role for most stellar masses. As all the disks we consider are optically thick, the critical radius depends on the Rosseland opacity law $\kappa_R(T)$ within dusty disk gas.

Comparing to our conservative estimate of the disk radius in the McKee & Tan (2003) model for massive star formation by the collapse of turbulent cores (§3.3), we find that fragmentation is marginal for stars accreting four to 15 solar masses; higher-mass stars are

increasingly afflicted by disk fragmentation. Although the mass at which fragmentation sets in is sensitive to our somewhat uncertain fragmentation criterion (§3.2.1) and angular momentum calculation (§4.3.4 and the Appendix), we have been conservative in five ways: (1) by adopting a fragmentation temperature lower than that implied by the Rice et al. (2005) simulations; (2) by adopting a low estimate of the specific angular momentum that determines the disk radius; (3) by adopting a relatively opaque model for the disk's Rosseland opacity; (4) by ignoring the shielding effect of a moderately opaque infall envelope, and (5) by adopting a low estimate for the cooling time, and a hard equation of state. All of these approximations should, if anything, lead us to underestimate the prevalence of disk fragmentation. Along with the existence of turbulent fluctuations in j (§3.4), these points ensure that *some* massive stars above $\sim 10 M_\odot$ experience disk fragmentation. As noted in §3.4.4, we cannot rule out the possibility that global instabilities flush disk material fast enough to suppress fragmentation, but we consider it unlikely that this prevents *all* fragmentation.

We therefore expect multiple, coplanar, low-mass (M5 to G5, §3.5.1) companions to form around many O (and some B) stars. Given initial separations of order 100-200 AU, their photospheric emission is not observable with present techniques. Disk migration, followed by mass transfer or common-envelope evolution, may however make them evident as the primary evolves (§3.5.2).

Even when disks fragment, we expect some accretion onto the central star – if only because of material that falls within the fragmentation radius (§3.5.3). Although we cannot yet quantify the disk efficiency parameter ε_d, we expect it to be significantly less than unity for those early O stars ($M_{\star f} \gtrsim 50 M_\odot$) whose disks are most prone to fragment.

3.6.1 Imprint on the initial mass function

The stabilizing effect of viscous heating is absent in disks that accrete more rapidly than $1.7 \times 10^{-3} M_\odot\,\mathrm{yr}^{-1}$, thanks to a sharp drop in dust opacity at ~ 1050 K (see §3.4). As this affects stars of mass greater than $87(t_{\rm acc}/10^5 \mathrm{yr}) M_\odot$, or about 110 $M_\odot$ in the fiducial core model, it may be related to the cutoff of the initial mass function (IMF) at about 120 $M_\odot$.

Several other explanations for this cutoff have been proposed, all involving the increasing bolometric luminosity, ionizing luminosity, or outflow force emitted by the central star. Starvation by disk fragmentation has the distinctive feature that it becomes

much more severe at a specific accretion rate. For this reason we expect it to produce a sharper IMF cutoff. (The transition to super-Eddington luminosities could also produce a sharp cutoff, but Krumholz et al. 2005 argue that this can be overcome by asymmetric radiation transfer.)

Note also that disk accretion is *destabilized* by rapid accretion, whereas rapid accretion quenches the effects of direct photon force and of the ionizing radiation (Wolfire & Cassinelli, 1987). Disk fragmentation may close an avenue by which very massive stars would otherwise form.

3.6.2 Proto-binary disks

Pinsonneault & Stanek (2006) state that close massive binaries < 10 year periods) are more likely to have nearly equal masses. More generally, the binarity fraction overall among massive stars is higher than their low mass counterparts (1.5 versus 0.5, Bally et al. (2005)). Due to the high fraction of roughly equal mass binaires, their effect on disk dynamics must be addressed in future work. Moreover, the stellar densities in regions of HMSF are high, suggesting that other cluster stars might be close enough to interfere with disks stretching out to ~ 100 AU (Bate et al., 2003). It is not currently clear whether disk accretion can preferentially grow a low-mass companion until its mass rivals that of the primary star, as Artymowicz & Lubow (1996) suggest. If so, then disk fragmentation may be relevant in the production of equal-mass binaries; if not, they must form by another mechanism. In any case, the multiplicity of the center of gravity should be accounted for in future work. It seems unlikely, though, that a binary with ~ 10 year period will stabilize the fragmenting regions whose periods are $\gtrsim 300$ years.

3.7 Appendix

We present here an estimate of the angular momentum of cores initially supported by turbulent motions, generalizing the results of ML05 to arbitrary line width-size relations. The analytical treatment of this problem rests on several idealizations about turbulent velocities: (1) that they are isotropic and homogeneous; and (2) that the Cartesian velocity components are neither correlated with each other, nor (to any appreciable degree) with density fluctuations. For simplicity we also assume (3) that the core density profile is spherically symmetric and can be captured in a single function $\rho(r)$. When

evaluating our formulae we assume (4) that the velocity difference between two points scales as a power of their separation, and (5), for the purpose of computing fluctuations, that the velocity components are Gaussian random fields.

One might object that condition (1) is inconsistent with the turbulent support of an inhomogeneous density profile. Consider, however, that if the core profile is a power law $\rho(r) \propto r^{-k_\rho}$, then the turbulent line width must scale as $\sigma(r) \propto r^\beta$ where

$$\beta = 1 - k_\rho/2. \tag{3.42}$$

A velocity field with this scaling is consistent with our conditions (1), (2), and (4) if

$$\langle [\mathbf{v}_i(\mathbf{r}_1) - \mathbf{v}_j(\mathbf{r}_2)]^2 \rangle = k|\mathbf{r}_1 - \mathbf{r}_2|^{2\beta}\delta_{ij} \tag{3.43}$$

where angle brackets represent an ensemble average and k is a normalization constant related to the virial parameter α. ML05 considered the case $\beta = 1/2$ appropriate for giant molecular clouds ($k_\rho = 1$); we generalize their formulae to other values of β, including the fiducial value $\beta = 1/4$ corresponding to $k_\rho = 3/2$.

Our goal is to compute the expectation value and dispersion of the core specific angular momentum j, normalized to $R_c\sigma$ where σ is the one-dimensional line width of the core. We find that, under our assumptions,

$$\langle j^2 \rangle = -\int\int \frac{d^3\mathbf{r}_1\rho(r_1)}{M}\frac{d^3\mathbf{r}_2\rho(r_2)}{M}\mathbf{r}_1\cdot\mathbf{r}_2\langle [v_x(\mathbf{r}_1) - v_x(\mathbf{r}_2)]^2\rangle \tag{3.44}$$

and that

$$\langle \sigma^2 \rangle = \frac{1}{2}\int\int \frac{d^3\mathbf{r}_1\rho(r_1)}{M}\frac{d^3\mathbf{r}_2\rho(r_2)}{M}\langle [v_x(\mathbf{r}_1) - v_x(\mathbf{r}_2)]^2\rangle \tag{3.45}$$

where $M = \int \rho d^3\mathbf{r}$ and all integrals are restricted to the region of interest (typically the core interior). These equations, which we will prove below, agree with the formulae in ML05's Appendix but allow $\langle [v_x(\mathbf{r}_1) - v_x(\mathbf{r}_2)]^2\rangle$ to be an arbitrary function of $|\mathbf{r}_1 - \mathbf{r}_2|$. It is important to note that the two formulae are identical up to the factor $-2\mathbf{r}_1\cdot\mathbf{r}_2$ in the integrand. The negative sign in equation (3.44) ensures that $\langle j^2\rangle$ is positive, since $\langle [v_x(\mathbf{r}_1) - v_x(\mathbf{r}_2)]^2\rangle$ takes higher values when $|\mathbf{r}_1 - \mathbf{r}_2|$ is large, hence when $\mathbf{r}_1\cdot\mathbf{r}_2$ is negative.

To evaluate equations (3.44) and (3.45) we make use of spherical symmetry and impose equation (3.43) for the velocity correlations. Defining $\mu = \mathbf{r}_1\cdot\mathbf{r}_2/(r_1r_2)$ as the cosine of the angle between $\mathbf{r}_1$ and $\mathbf{r}_2$,

$$\langle j^2 \rangle = -k\int_0^R dr_1 4\pi r_1^2\frac{\rho(r_1)}{M}\int_0^R dr_2 2\pi r_2^2\frac{\rho(r_2)}{M}r_1r_2\left(r_1^2 + r_2^2\right)^\beta\int_{-1}^1 d\mu\,(1 - q\mu)^\beta\,\mu$$

Profile	$\beta = 1/4$	$\beta = 1/2$
turbulent core	0.2704	0.4206
critical Bonnor-Ebert sphere	0.2730	0.3828
uniform region ($k_\rho = 0$)	0.3430	0.4714
thin shell	0.4714	0.6324

Table 3.4: Values of $\langle j^2\rangle^{1/2}/(R\langle\sigma^2\rangle^{1/2})$ in our model for turbulent angular momentum.

$$= \frac{2\pi^2 k}{M^2}\int_0^R dr_1\int_0^R dr_2\left(r_1^2+r_2^2\right)^{2+\beta} r_1 r_2\rho(r_1)\rho(r_2)\times \left[\frac{(1+q)^{\beta+2}-(1-q)^{\beta+2}}{\beta+2}-\frac{(1+q)^{\beta+1}-(1-q)^{\beta+1}}{\beta+1}\right] \quad (3.46)$$

and

$$\begin{aligned}\langle\sigma^2\rangle &= \frac{1}{2}k\int_0^R dr_1 4\pi r_1^2\frac{\rho(r_1)}{M}\int_0^R dr_2 2\pi r_2^2\frac{\rho(r_2)}{M}\left(r_1^2+r_2^2\right)^{\beta}\int_{-1}^1 d\mu\,(1-q\mu)^{\beta}\\ &= \frac{2\pi^2 k}{M^2}\int_0^R dr_1\int_0^R dr_2\left(r_1^2+r_2^2\right)^{1+\beta} r_1 r_2\rho(r_1)\rho(r_2)\times \left[\frac{(1+q)^{\beta+1}-(1-q)^{\beta+1}}{\beta+1}\right] \quad (3.47)\end{aligned}$$

where $q = 2r_1r_2/(r_1^2+r_2^2)$, as in ML05. Table 3.7 and figure 3.7 provide values of $\langle j^2\rangle^{1/2}/(R\langle\sigma^2\rangle^{1/2})$ for several density profiles, both for the internal spectrum given by equation (3.42), and for $\beta = 1/2$, which may better represent the background spectrum.

Figure 3.7 plots the ratio $\langle j^2\rangle^{1/2}/(R\langle\sigma^2\rangle^{1/2})$ as given by equations (3.46) and (3.47) for a turbulent core profile, a critical Bonnor-Ebert sphere, and a thin shell. The results are very close to power laws in β:

$$\frac{\langle j^2\rangle^{1/2}}{R\langle\sigma^2\rangle^{1/2}} \simeq \begin{cases} 0.655\beta^{0.638} & \text{singular turbulent core}\\ 0.537\beta^{0.488} & \text{critical Bonnor}-\text{Ebert sphere}\\ 0.648\beta^{0.459} & \text{uniform}-\text{density sphere}\\ 0.849\beta^{0.424} & \text{thin shell.}\end{cases} \quad (3.48)$$

The spin parameter θ_j makes reference to the velocity dispersion $\sigma(R)$ at radius R, rather than the mean velocity dispersion $\langle\sigma^2\rangle^{1/2}$ within R. For this we use the scaling $\sigma^2 \propto GM/r \propto M^{2\beta/(3-k_\rho)}$ to derive

$$\frac{\sigma(R)^2}{\langle\sigma^2\rangle} = 1+\frac{2\beta}{3-k_\rho}.$$

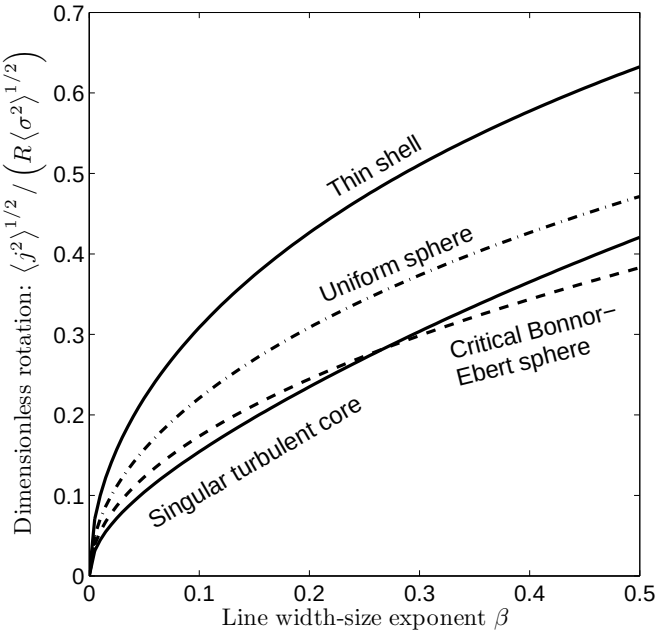

Figure 3.7: Values of $\langle j^2\rangle^{1/2}/(R\langle\sigma^2\rangle^{1/2})$ evaluated for turbulence with line width-size exponent β and three relevant density profiles. For hydrostatic turbulent cores, $\rho \propto r^{-2(1-\beta)}$.

With this correction factor accounted for, θ_j/f_j is still very close to a power law of β:

$$\frac{\theta_j}{f_j} \simeq \begin{cases} 0.504\beta^{0.552} & \text{singular turbulent core} \\ 0.987\beta^{0.651} & \text{uniform} - \text{density region} \\ 0.849\beta^{0.424} & \text{thin shell.} \end{cases} \tag{3.49}$$

(The last line is unchanged, as there is no correction for a thin shell.) These formulae were quoted in §4.3.4.

We now return to the derivation of equation (3.44); equation (3.45) is treated below. The z component of the specific angular momentum of the core is

$$\begin{aligned} j_z^2 &= \int d^3\mathbf{r}_1 \int d^3\mathbf{r}_2 \frac{\rho_1}{M}(x_1 v_{y1} - y_1 v_{x1}) \frac{\rho_2}{M}(x_2 v_{y2} - y_2 v_{x2}) \\ &= \frac{1}{M^2} \int d^3\mathbf{r}_1 \int d^3\mathbf{r}_2 \rho_1 \rho_2 (x_1 x_2 v_{y1} v_{y2} + y_1 y_2 v_{x1} v_{x2} - x_1 y_2 v_{y1} v_{x2} - y_1 x_2 v_{x1} v_{y2}), \end{aligned} \tag{3.50}$$

here, as below, we use subscripts 1 and 2 to indicate functions of $\mathbf{r}_1$ and $\mathbf{r}_2$, i.e., $\rho_1 = \rho(\mathbf{r}_1)$. On ensemble averaging of the second line, the last two terms in equation (3.50) become zero thanks to the δ_{ij} in equation (3.43). The first two terms are equal, thanks to spherical symmetry; thus

$$\langle j_z^2 \rangle = \frac{2}{M^2} \int d^3\mathbf{r}_1 \int d^3\mathbf{r}_2 \rho_1 \rho_2 x_1 x_2 \langle v_{y1} v_{y2} \rangle. \tag{3.51}$$

Spherical symmetry allows us to replace $x_1 x_2$ with $\mathbf{r}_1 \cdot \mathbf{r}_2/3$ and j_z^2 with $j^2/3$, so

$$\begin{aligned} \langle j^2 \rangle &= \frac{2}{M^2} \int d^3\mathbf{r}_1 \int d^3\mathbf{r}_2 \rho_1 \rho_2 \mathbf{r}_1 \cdot \mathbf{r}_2 \langle v_{y1} v_{y2} \rangle \\ &= \frac{1}{M^2} \int d^3\mathbf{r}_1 \int d^3\mathbf{r}_2 \rho_1 \rho_2 \mathbf{r}_1 \cdot \mathbf{r}_2 \left(\langle v_{y1}^2 \rangle + \langle v_{y2}^2 \rangle - \langle (v_{y1} - v_{y2})^2 \rangle \right). \end{aligned} \tag{3.52}$$

The first two terms within the brackets are zero, as spherical symmetry requires them to be even in the space coordinates while $\mathbf{r}_1 \cdot \mathbf{r}_2$ is odd; the surviving term yields equation (3.44).

To prove equation (3.45) we write

$$M\sigma^2 = \int d^3\mathbf{r} \rho(\mathbf{r}) (v_x - \bar{v}_x)^2 = \int d^3\mathbf{r} \rho(\mathbf{r}) (v_x^2 - \bar{v}_x^2) \tag{3.53}$$

where $\bar{\mathbf{v}} = \int \mathbf{v} \rho(\mathbf{r}) / M d^3\mathbf{r}$ is the center of mass velocity. In equation (3.50) we replace $\bar{v}_x^2$ with $\int \int \mathbf{v}_1 \cdot \mathbf{v}_2 (\rho_1/M)(\rho_2/M) d^3\mathbf{r}_1 d^3\mathbf{r}_2$, and we bring the first term into similar form by multiplying it by $\int (\rho_2/M) d^3\mathbf{r}_2 = 1$:

$$\begin{aligned} M\sigma^2 &= \int d^3\mathbf{r}_1 \int d^3\mathbf{r}_2 \rho_1 \rho_2 v_{x1} (v_{x1} - v_{x2}) \\ &= \frac{1}{2} \int d^3\mathbf{r}_1 \int d^3\mathbf{r}_2 \rho_1 \rho_2 (v_{x1} - v_{x2})^2. \end{aligned} \tag{3.54}$$

The second line follows from the first by noting that the integral is antisymmetric under interchange of $\mathbf{r}_1$ and $\mathbf{r}_2$. When averaged, it yields equation (3.45).

Chapter 4

Global Models of Young, Massive Protostellar Disks

A version of this chapter has been published in The Astrophysical Journal as "Global Models for the Evolution of Embedded, Accreting Protostellar Disks", Kratter, K. M., Matzner, C. D., and Krumholz, M. R., vol. 681, pp375-390, 2008. Reproduced by permission of the AAS.

4.1 Introduction

Having determined that disks around massive are susceptible to fragmentation, we now explore the propensity of disks to fragment across a broader mass range. Moreover, we now employ a more sophisticated model for accretion driven by gravitational instability and the magnetorotational instability in order to survey the conditions in protostellar disks as a function of mass and time.

A young star system's visible T Tauri or Herbig stage is preceded by a deeply enshrouded phase of rapid accretion in which its character – multiplicity, disk properties, and tendency to form planets – is first forged. Due to the high obscuration characteristic of this phase, disks are accessible primarily via radio and submillimeter observations, and such techniques provide limited sensitivity and angular resolution compared to what can be achieved for T Tauri and Herbig AE star disks using shorter wavelengths. Our knowledge of massive protostellar disks is particularly limited by this problem, since they do not have a significant unobscured phase, probably due to the destructive effects of ionizing radiation. These difficulties are compounded by the fact that massive stars form

more rarely, and therefore tend to lie farther away. Detections of rotation and infall in a few systems hint at the presence of disks during the embedded phase, but are only preliminary (see recent reviews by Cesaroni et al. 2006, 2007, Beuther 2006, and Beuther et al. 2007).

While our knowledge of the embedded phase today is limited, it will soon come into sharp focus as new instruments such as the Expanded Very Large Array (EVLA) and Atacama Large Millimeter Array (ALMA) become operational. In order to predict what these telescopes will discover about the formation of stars across a very broad mass range, $\sim 1 - 120 M_{\odot}$, we present evolutionary models of star-disk systems reacting to infall at very high rates. We concentrate our efforts on the physical processes that control disk evolution, such as the torque from a turbulent infall, the reprocessing of starlight by the infall envelope, and the character of the self-gravitational instabilities. The disk itself we model with a highly simplified, single-zone treatment. Although multidimensional simulations provide a much more detailed view of disk formation and evolution during the embedded phase (e.g. Goodwin et al., 2004; Krumholz et al., 2007b), their high computational cost and the limited range of physical processes they include mean that these simulations can explore only small regions of parameter space. They cannot easily make predictions across a broad range of stellar mass scales and evolutionary times. In contrast, our semi-analytic approach permits us to incorporate more physical effects and explore the consequences of environmental parameters more rapidly, and in a more systematic way. This serves two complementary ends: the theoretical goal of understanding angular momentum transport and fragmentation in the embedded phase, and the observational goal of making concrete predictions about the properties of young, massive disks.

Although we include a range of physical processes in our models; the most important in driving the evolution of embedded disks in our calculations is self-gravity. Self-gravity plays a central role in mediating angular momentum transport and triggering fragmentation into a binary or multiple system. Its importance in star formation has long been recognized (Larson, 1984), and our study is preceded by evolutionary calculations which incorporate accretion and self-gravity into one-dimensional (Lin & Pringle, 1987, 1990; Nakamoto & Nakagawa, 1994, 1995; Hueso & Guillot, 2005) and two-dimensional (Vorobyov & Basu, 2005, 2006) simulations. Although lower in resolution, our approach is distinguished from these works in several ways:

i. In contrast to all one-dimensional calculations to date, we account for the de-

pendence of gravitational torques on the disk-to-total mass ratio in addition to Toomre's instability parameter.

ii. We consider the possibility that disks will fragment if they become sufficiently unstable.

iii. We consider fluctuations of the vector angular momentum in the infall due to realistic turbulence in the collapsing cloud core.

iv. We employ a realistic model for the irradiation of the disk midplane, in which starlight is reprocessed at the inner wall of an outflow cavity while inflow is occurring.

v. We survey the conditions of intermediate-mass and massive star formation, rather than focusing exclusively on conditions in nearby low-mass star forming regions such as Taurus.

The first of these is important for all protostellar disks, since the disk mass is never negligible when the Toomre parameter is small. Features (*ii*) and (*iii*) are of primary importance in the formation of massive stars, which accrete from strongly turbulent regions (Myers & Fuller, 1992; McLaughlin & Pudritz, 1997) and which are likely to undergo disk fragmentation (Kratter & Matzner 2006, hereafter KM06). Irradiation is most important for low-mass stars, whose disks it strongly stabilizes (Matzner & Levin, 2005), but it remains significant in massive star formation as well.

In §4.2 we outline our model for the infall rate of matter and angular momentum. We develop a model for disk accretion and fragmentation in §4.3. In §4.4 we define the key environmental variables that control protostellar disk evolution and sketch a qualitative evolutionary sequence based on their fiducial values. In §4.5 we present the results for our fiducial case, and explore the effect of varying our parameters. In §4.6 we discuss the observable predictions that our model makes, and finally in § 4.7 we summarize our main results.

4.2 Infall onto Disks

Since we are interested in the behavior of a disk that is subject to strong perturbations from its environment, we begin building our model by constructing a prescription for

the infall of matter and angular momentum onto a disk. This accretion comes from a background "core" (Shu, 1977a; McLaughlin & Pudritz, 1997; McKee & Tan, 2003), whose properties and interaction with a disk we discuss in this section.

4.2.1 Star Formation By Core Collapse

We model the accretion of mass and angular momentum using the two-component core model of McKee & Tan (2003), which is a generalization of the TNT (thermal plus non-thermal) model of Myers & Fuller (1992). In this model, which we summarize here for convenience, the density distribution within a core follows a two-component power law distribution

$$\rho = \rho_s \left(\frac{R_{\rm c}}{r}\right)^{-k_\rho} + \frac{c_{\rm s,c}^2}{2\pi G r^2}, \tag{4.1}$$

where $R_{\rm c}$ is the outer radius of the core, $c_{\rm s,c}$ is the thermal sound speed within it (assumed to be constant), and ρ_s is the density at the core's surface. We follow McKee & Tan (2003) in adopting $k_\rho = 1.5$ as the fiducial value of the turbulence-supported density index. Physically, the first term describes an envelope supported primarily by turbulent motions, while the second describes a thermally-supported region at its center. A model of this sort is fully specified in terms of the three parameters: the core mass

$$M_{\rm c} = \frac{4\pi}{3-k_\rho}\rho_s R_{\rm c}^3 + 2\frac{c_{s,c}^2 R_{\rm c}}{G}, \tag{4.2}$$

surface density

$$\Sigma_{\rm c} = \frac{M_{\rm c}}{\pi R_{\rm c}^2}, \tag{4.3}$$

and temperature

$$T_{\rm c} = \frac{m}{k_B} c_{s,c}^2, \tag{4.4}$$

where $m = 3.9 \times 10^{-24}\,{\rm g}$ is the mean particle mass in a gas of molecular hydrogen and helium mixed in the standard cosmic abundance. Observed regions of star formation contain cores with masses $\sim 1 - 100\ M_\odot$, surface densities $\Sigma_{\rm c} \approx 0.03 - 1$ g cm^{-2}, and temperatures of 10 to 50 K (Johnstone et al., 2001; Plume et al., 1997).

The core is taken to be in approximate hydrostatic balance initially, and this condition specifies the required level of turbulent support. The non-thermal velocity dispersion in the shell at radius r is

$$\sigma(r)^2 = \frac{2\pi}{3\phi_B(k_\rho - 1)}\frac{GM(r)}{r} - c_{\rm s,c}^2 \tag{4.5}$$

where $M(r)$ is the mass at radii of r or less and $\phi_B \simeq 2.8$ approximately accounts for the magnetic contribution to the total pressure. Except when $M(r) \ll 1\ M_\odot$ or $\Sigma_c < 0.1$ g cm^{-2}, the first term is much larger than the second, so that the velocity dispersion is primarily non-thermal.

Core collapse commences at time zero, and a mass shell initially at radius r falls onto the disk in a time comparable to the free fall time evaluated at its initial density, $t_{\rm ff}(r) = [3\pi/32G\rho(r)]^{1/2}$. In practice, we use the McKee & Tan (2003) accretion rate approximation to determine $\dot{M}$ on to the star-disk system as a function of the total core mass and the current amount of mass that has accreted:

$$\dot{M}_{\rm in} \approx \left(\frac{\phi_* M_{*f}}{t_{\rm ff,s}}\right)\left[\left(\frac{M_{*d}}{M_{*f}}\right)^{2q} + \left(\frac{\phi_{*\rm th}}{\phi_{*\rm nth}}\right)^2\left(\frac{\varepsilon M_{\rm th}}{M_{*f}}\right)^{2q}\right]^{1/2}, \tag{4.6}$$

where M_{*f} is the final disk plus stellar mass, M_{*d} is the current disk plus stellar mass, $t_{\rm ff,s}$ is the free-fall time evaluated at the core surface (i.e. at $\rho = \rho(R_c)$),

$$q = \frac{3(2-k_\rho)}{2(3-k_\rho)}, \tag{4.7}$$

$$M_{\rm th} = 10^{-3.1}\left(\frac{T}{20\,{\rm K}}\right)^3\left(\frac{30\varepsilon M_\odot}{M_{*f}}\right)^{1/2}\Sigma_{c,0}^{-3/2} M_\odot, \tag{4.8}$$

$\Sigma_{\rm c,0} = \Sigma_{\rm c}/({\rm g\ cm^{-2}})$, and ϕ_*, $\phi_{*\rm nth}$, and $\phi_{*\rm th}$ are constants of order unity that depend on the polytropic index and magnetic field strength. The efficiency factor

$$\varepsilon = \frac{M_{*f}}{M_c} \tag{4.9}$$

represents the fraction of the core mass that lands on the star-disk system rather than being blown out by protostellar outflows. We again follow McKee & Tan (2003) in adopting $\varepsilon = 0.5$, a value typical of low-mass star formation (Matzner & McKee, 2000).

4.2.2 Angular Momentum of the Infalling Material

Equation (4.6) gives the mass infall rate $\dot{M}_{\rm in}(t)$ from the core as a function of time. The second component of our core model is to specify the corresponding rate of angular momentum infall $\dot{\mathbf{J}}_{\rm in}(t)$. We compute this in several steps. First, we approximate the vector specific angular momentum $\mathbf{j}(r)$ averaged over a shell of material at radius r as described below. Then we compute $M(t) \equiv \int_0^t \dot{M}_{\rm in}(t')/\epsilon\, dt'$, the total mass from the core that has either fallen onto the star-disk system or been ejected at time t. From the

core density profile (equation 4.1) we also compute $M(r) \equiv \int_0^r 4\pi r'^2 \rho(r')\, dr'$, the mass of the initial core enclosed within radius r. Assuming the core accretes inside-out, we set $M(r) = M(t)$ and solve for $r(t)$, which gives the initial radius r of the shell of mass that arrives at the star-disk system at time t. Assuming that the specific angular momentum of the gas does not change before it reaches the disk, the angular momentum accretion rate is then simply given by $\dot{\mathbf{J}}_{\rm in}(t) = \dot{M}_{\rm in}(t)\mathbf{j}(r(t))$.

The remaining step is to specify how we estimate $\mathbf{j}(r)$. Star forming cores are often modeled as solid body rotators characterized by the ratio β of rotational to gravitational energy, but we adopt a more realistic model in which turbulent fluctuations affect the infalling gas. Following Burkert & Bodenheimer (2000), Fisher (2004), Matzner & Levin (2005) and KM06, we assume that the observed angular momenta of cores (Goodman et al., 1993) can be modeled using an idealized turbulent velocity field. Using the method of Dubinski et al. (1995), we generate a numerical realization of an isotropic, homogeneous, Gaussian random velocity field $\mathbf{v}(\mathbf{r})$. We require that the power spectrum $P(k)$ of this turbulent field reproduce the scalings required by turbulent support against gravity: $\sigma(r)^2 \propto GM(r)/r \propto r^{2-k_\rho}$ at large radii, so that $\sigma(r) \propto r^{1/4}$ for $k_\rho = 3/2$. Parseval's theorem or dimensional analysis then require $P(k) \propto k^{-3/2}$.

We note that numerical simulations of supersonic turbulence consistently show the steeper spectral index -2 (Porter et al., 1992) which is understood as the spectrum of an individual shock and as the exact limit of Burgers turbulence. Matzner (2007) and Nakamura & Li (2007) have shown that a shallower index is expected when turbulence is driven by protostellar outflows, however, and our chosen power spectrum is consistent with the line width-size relation for massive cores (e.g., Caselli & Myers, 1995; Plume et al., 1997). Our homogeneous velocity field is surely an idealization, but not a grave one.

After scaling our numerical domain to match the core radius R_c, we normalize $\mathbf{v}$ such that the one-dimensional velocity dispersion of a spherical shell with this radius equals $\sigma(r)$ defined in equation (4.5). In practice we fit R_c within a 256^3 section of a 1024^3 grid of velocities, because periodicity causes artifacts on scales larger than about 1/4 of the box size. From this field we calculate the specific angular momentum $\mathbf{j} = \mathbf{r} \times \mathbf{v}$ at every point and the mean specific angular momentum $\mathbf{j}(r)$ in a shell at radius r. Note that KM06 calculate the expected magnitude and dispersion of $\mathbf{j}(r)$ for velocity fields of precisely this type; our results agree with their predictions to about 50%, which is within the scatter they predict.

4.3 Dynamics of the disk

4.3.1 Approach to disk evolution

Given the rate at which mass and angular momentum accrete, we must calculate the reaction of the disk. At any given time, our star-plus-disk system is characterized by the disk mass M_d, the central star mass M_*, and the total angular momentum content of the disk $\mathbf{J}_d$. Given these quantities, and the rates of mass and angular momentum infall $\dot{M}_{\rm in}$ and $\dot{\mathbf{J}}_{\rm in}$, we wish to compute the time rate of changes $\dot{M}_d$, $\dot{M}_*$, and $\dot{\mathbf{J}}_d$.

Using the separation between the thermal, orbital, and accretion timescales, we assume our disks are in a thermal steady state and draining at a rate determined by their current global parameters. We shall later refer to this as the assumption of thermal and mechanical equilibrium.

In § 4.3.2, we estimate the disk accretion rate onto the central star due to various angular momentum transport mechanisms. In § 4.3.3 we discuss thermal equilibrium in the disk, which together with the aforementioned condition of mechanical equilibrium allows us to self-consistently compute the accretion rate from the disk to the star $\dot{M}_*$. In § 4.3.4 we describe the corresponding angular momentum evolution $\dot{\mathbf{J}}_d$. Finally, in § 4.3.5 and § 4.3.6, we discuss our prescriptions for disk fragmentation and binary formation.

It is helpful before proceeding to define two dimensionless parameters that characterize the strength of the disk's self-gravity. These are the disk-to-total mass ratio

$$\mu = \frac{M_d}{M_d + M_*} \tag{4.10}$$

and Toomre's (1964) instability parameter

$$Q = \frac{c_s \kappa}{\pi G \Sigma_d}, \tag{4.11}$$

where κ is the radial epicyclic frequency, c_s speed of density waves, and Σ_d is the disk's mass surface density. In practice we evaluate Q using $\kappa \to \Omega = (GM_{\rm tot}/R_d^3)^{1/2}$, the total orbital frequency, since the difference between them is only marginally significant even when the disk mass is quite large. Here $R_d = j_d^2/GM_{\rm tot}$. We also approximate c_s using the isothermal sound speed. To characterize gravitational instability, we use the *minimum* value of Q – the value at R_d, the outer boundary of our active disk. In this evaluation we assume a profile $\Sigma_d \propto r^{-1}$ (a choice we justify in § 4.3.4) so that $\Sigma_d(R_d) = M_d/(2\pi R_d^2)$, and we evaluate c_s and Ω at the edge of the disk.

We base our models on the fundamental assumption that the self-gravitational behavior of an accretion disk depends primarily on the structural parameters μ and Q – so that its evolution is controlled by heating and cooling (§ 4.3.3), which alter Q, and accretion onto and through the disk, which alters μ. This approach permits us to treat the disk's mechanical and thermal properties separately, before combining them into a model for its evolution. This division also guides our use of published work, since it implies that simulations with adiabatic equations of state and those with an imposed cooling rate may be combined into a mechanical model for disk evolution, which we may then use to model irradiated protostellar disks. Finally, it prompts us to treat the onset of disk fragmentation and disk fission as boundaries in the space of μ and Q, rather than in terms of a critical cooling rate (which is the natural and conventional description for simulations that include cooling but not irradiation). In § 4.3.5 we argue that these descriptions are effectively equivalent.

Models based on this assumption are guaranteed to be somewhat approximate, because a disk's mechanical evolution must, at some level, reflect additional parameters: its geometry, its equation of state, the specifics of its heating and cooling processes, and the magnitude of external perturbations (like tides), to name a few. However we expect our results to be valid, both because we believe that μ and Q are indeed the most significant parameters for gravitational instability, and because our model is calibrated to realistic numerical models. Additional simulations will be required to test this approach.

4.3.2 Angular Momentum Transport and Disk Accretion

A key element of our model is a prescription for angular momentum transport and the rate $\dot{M}_*$ at which matter accretes onto the central star – or more specifically, the dimensionless rate $\dot{M}_*/(M_d\Omega)$. In practice we first construct a model for an effective Shakura & Sunyaev α parameter, which we define through the steady-state relation

$$\dot{M}_* = \frac{3\alpha c_s^3}{GQ} \tag{4.12}$$

so that

$$\frac{\dot{M}_*}{M_d\Omega} = \frac{3\alpha Q^2}{8}\mu^2, \tag{4.13}$$

where the factor of of 3/8 comes from the assumption that the disk surface density falls as r^{-1}. We do not mean to imply by this that transport induced by gravitational instability

is purely local (Balbus & Papaloizou, 1999), although this does appear to be the case for sufficiently thin and light disks (Gammie, 2001; Lodato & Rice, 2005).

We divide α into two contributions: $\alpha_{\rm MRI}$, due to the magnetorotational instability (MRI), and $\alpha_{\rm GI}$, due to gravitational instability. In keeping with the strategy described in § 4.3.1, we consider $\alpha_{\rm GI}$ to be a pure function of μ and Q. We combine it and the MRI contribution linearly:

$$\alpha = \alpha_{\rm GI} + \alpha_{MRI}. \tag{4.14}$$

We create our model for $\alpha_{GI}(Q, \mu)$ using results from the simulations of Laughlin & Rozyczka (1996), Rice et al. (2003), Lodato & Rice (2004), Lodato & Rice (2005) and Gammie (2001). We adopt a constant value for α_{MRI}, as discussed below.

Overview of Simulations

The three sets of simulations span a large fraction of our parameter space in Q and μ. The global disk simulations of Laughlin & Rozyczka (1996) explore $Q > 1$ and non-negligible values of μ using a two-dimensional hydrodynamic, self-gravity code; they supress local fragmentation by imposing an adiabatic equation of state. The simulations of Gammie (2001) represent the limit $\mu \to 0$, for values of Q which approach unity from above, and are most directly applicable to quasar disks.

Gammie imposes cooling with a fixed cooling time, τ_c, which is proportional to the orbital time. He finds a regime of steady gravity-induced turbulence, for disks that cool over many orbits. If τ_c is too short ($< 3\Omega^{-1}$), however, the disk fragments as Q drops below unity. The disk viscosity is highest at the boundary of fragmentation. Angular momentum transport in this regime is quite local, with an effective value of α that is inversely proportional to the cooling rate. Our third source is the global SPH simulations of Rice et al. (2003), Lodato & Rice (2004), and Lodato & Rice (2005), in which a cooling time $\propto \Omega^{-1}$ is imposed locally; these cover the entire parameter space in μ. In these simulations Q is initially 2, but it descends towards unity. Here again, the disk fragments if $\Omega\tau_c$ is too small, although the critical value of this parameter is different than Gammie found.

Accretion Model

To derive a relatively simple analytic fit to the simulation data, we must extract a characteristic $\alpha_{\rm GI}, Q$, and μ from the simulations listed above. Because the numerical ap-

proaches are varied, we are unable to use the same method for each. The values are derived as follows for each type of simulation:

1. We estimate $\alpha_{\rm GI}$ from Laughlin & Rozyczka (1996) using their equations 24-26; Q and μ are given.

2. Values of α from Rice et al. (2003), Lodato & Rice (2004), Lodato & Rice (2005) are taken directly from plots, when available. Because α varies with radius, we take an approximate value from the outer region of their disk before the density begins to fall off steeply. When plots are not available, we use the critical value of τ_c to calculate $\alpha_{\rm GI}$ at the fragmentation boundary, which we take to be $Q = 1$ (see § 4.3.5). Again, μ is given.

3. Gammie (2001) provides one value of $\alpha_{\rm GI}$ at $Q = 1$ for a disk with $\mu \to 0$, which we adopt.

These values of $\alpha_{\rm GI}$ are shown in Figure 4.1 according to the estimated values of μ and Q that accompany each of them. We treat them as a data set to be fit within our analytical model for $\alpha_{\rm GI}$, which is displayed in the underlying contours in that figure. Imposing the realistic condition that $\alpha_{\rm GI}$ is continuous and equals zero for $Q > 2$ (when the gravitational instability should shut off as suggested by Griv (2006)), we find that two components are required:

$$\alpha_{GI} = \left(\alpha_{\rm short}^2 + \alpha_{\rm long}^2\right)^{1/2} \tag{4.15}$$

where

$$\alpha_{\rm short} = \max\left[0.14\left(\frac{1.3^2}{Q^2} - 1\right)(1-\mu)^{1.15}, 0\right] \tag{4.16}$$

and

$$\alpha_{\rm long} = \max\left[\frac{1.4\times10^{-3}(2-Q)}{\mu^{5/4}Q^{1/2}}, 0\right]. \tag{4.17}$$

In fact we apply equation (4.15) only to the region $Q > 1$. Because we expect the gravitational torque to saturate when fragmentation occurs, we hold α constant, for a given μ, when $Q < 1$; this amounts to replacing $Q \to \max(Q, 1)$ in the above equations. This has no practical consequences for our calculations, however, since our treatment of fragmentation (§ 4.3.5) prevents our disks from sampling values of Q much below unity.

Our nomenclature in equation (4.15) reflects our interpretation. The "short" component $\alpha_{\rm short}$ dominates for $Q \lesssim 1.3$, hence for relatively thin disks. We think of it as arising

from modes with relatively high spatial wavenumbers and short wavelengths (Lodato & Rice, 2004, 2005). Note that its functional form resembles the model of Lin & Pringle (1990) (their eq. 16) modified by a mild μ dependence, which is comparable to the scale height dependence derived in equation (2.5) of Lin & Pringle (1987).

The "long" component $\alpha_{\rm long}$ is important in thicker disks whose instabilities are likely to be dominated by loosely wound, $m = 2$ spiral patterns. We require it because we include the adiabatic simulations of Laughlin & Rozyczka (1996), which sample higher values of Q because they cannot cool. (Indeed, Q rises during these simulations.) Our fundamental assumption (§ 4.3.1) leads us to incorporate these results into a single model for $\alpha(\mu, Q)$, despite the difference in thermal physics. Future simulations can test this assumption by imposing heating (via irradiation, say) as well as cooling: our model implies that the derived $\alpha_{\rm GI}$ will be comparable to Laughlin & Rozyczka's, when Q and μ take similar values. While simulations such as Boley et al. (2006) and Cai et al. (2008) are making dramatic process towards accurately modelling heating, cooling, and irradiation, a wider parameter space is necessary for comparison. We note that Sellwood & Carlberg (1984) and Griv (2006) also find non-axisymmetric instabilities for massive disks with Q in the range $1.3 - 2$.

As shown in Figure 4.1 our model for $\alpha_{\rm GI}$ agrees reasonably well with data from the simulations, though we fail to fit a couple points at very high μ and low Q. Note that $\alpha_{\rm GI}$ for these points from Laughlin & Rozyczka (1996) are uncertain themselves.

It is important to bear in mind that our accretion model is only a rough representation of the numerical results on which it is based, and that it can be improved as more simulations become available. For instance, we place no stock in the weak divergence of $\alpha_{\rm long}$ as $\mu \to 0$: this feature is a product of our fit to numerical results at larger μ, and it would be an unwise extrapolation to use our model for disks with very low μ and moderate Q. It does not affect our results, as our disks do not sample this regime.

Finally, we assume the disk is sufficiently ionized to support magnetic turbulence, and we represent the MRI with the constant value $\alpha_{\rm MRI} = 10^{-2}$. The typical value of $\alpha_{\rm MRI}$ is rather uncertain; see Pessah et al. (2007) for a synthesis of recent work, and Hueso & Guillot (2005) for a recent consideration of observational constraints in low-mass protostellar disks. Gravitational torques exceed those from the MRI for much of the accretion phase. We discuss the influence of $\alpha_{\rm MRI}$ on our results in § 4.5.5

Figure 4.2 illustrates our model for the dimensionless accretion rate $\dot{M}_*/(M_d\Omega)$ as a function of Q and μ. We draw attention to several key features of the plot. First, note

that at low Q there is a tongue-like feature that increases in intensity with increasing disk mass. This is due to the strong dependence of $\alpha_{\rm short}$ on both Q and μ At higher values of Q and lower values of μ the contours steepen due to the weak divergence of $\alpha_{\rm long}$ as $\mu \to 0$, which is probably not physical. The curvature towards higher Q and μ shows the dominance of the MRI for $Q > 2$. The fact that the dimensionless accretion rate takes numerical values up to $10^{-2.4}$, with a typical values $\sim 10^{-3.5}$, implies that massive disks drain on timescales ranging from ~ 40 to a few thousand orbits, with five hundred orbits being typical.

4.3.3 Disk Thermal Equilibrium

We have now specified the rate at which the disk accretes onto a central star as a function of Q and μ. However, this does not fully specify the accretion rate, because while μ may be directly computed from our "primitive" variables M_d, M_*, and $\mathbf{J}_d$, the Toomre stability parameter Q cannot be, because it depends on the sound speed c_s and thus the temperature within the disk. We can determine this by requiring that the disk be in thermal equilibrium.

To compute the disk's thermal state, we follow the approach of KM06, in which disks are heated by a combination of stellar irradiation and viscous dissipation due to accretion. In equilibrium, the disk midplane temperature satisfies the approximate relation

$$\sigma T^4 = \left(\frac{8}{3}\tau_R + \frac{1}{4\tau_P}\right) F_v + F_{\rm irr}, \tag{4.18}$$

where F_v is the rate of viscious dissipation per unit area in the disk, $F_{\rm irr}$ is the flux of starlight (whether direct or reprocessed) onto the disk surface, and $\tau_{R,P} = \kappa_{R,P}\Sigma/2$ are the Rosseland and Planck optical depths to the midplane. The viscous dissipation per unit area is

$$F_v = \frac{3\dot{M}\Omega}{8\pi}, \tag{4.19}$$

and we compute the opacities using the Semenov et al. (2003) model for $\kappa_{R,P}(T)$: in particular, we use their homogeneous-aggregate dust model with normal silicates, calculated at the appropriate density.

Low-mass stars' luminosities are accretion-dominated in the main accretion phase, but those above about 15 $M_\odot$ reach the zero-age main sequence (ZAMS) while still accreting. To include both accretion luminosity and other sources in our calculation of $F_{\rm irr}$, we use the protostellar evolution code of Krumholz & Thompson (2007), based on the McKee &

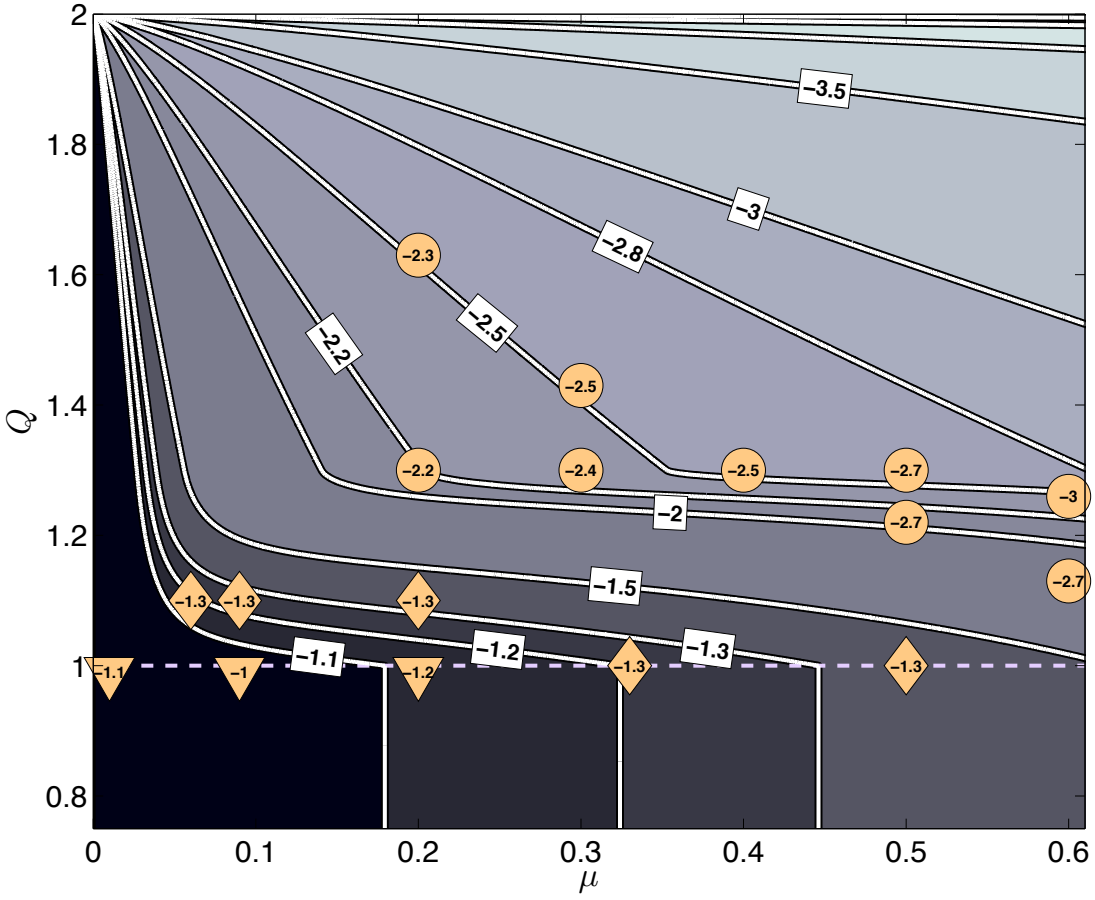

Figure 4.1: Contours of the viscosity parameter $\log(\alpha_{\rm GI})$ due to gravitational instabilities (eq. 4.15); white squares are contour labels. Results from numerical simulations are marked with circles, diamonds, and triangles. Circles show simulations with adiabatic equations of state (Laughlin & Rozyczka, 1996), diamonds show simulations with an imposed cooling rate that reach steady state (Lodato & Rice, 2004, 2005), and triangles show the maximum $\alpha_{\rm GI}$ achieved in simulations with imposed cooling that probe the fragmentation boundary (Gammie, 2001; Rice et al., 2003; Lodato & Rice, 2004, 2005). Note that the point at $\mu = 0$ corresponds to the purely local simulation of Gammie (2001). The $Q = 1$ boundary is marked with a dashed line.

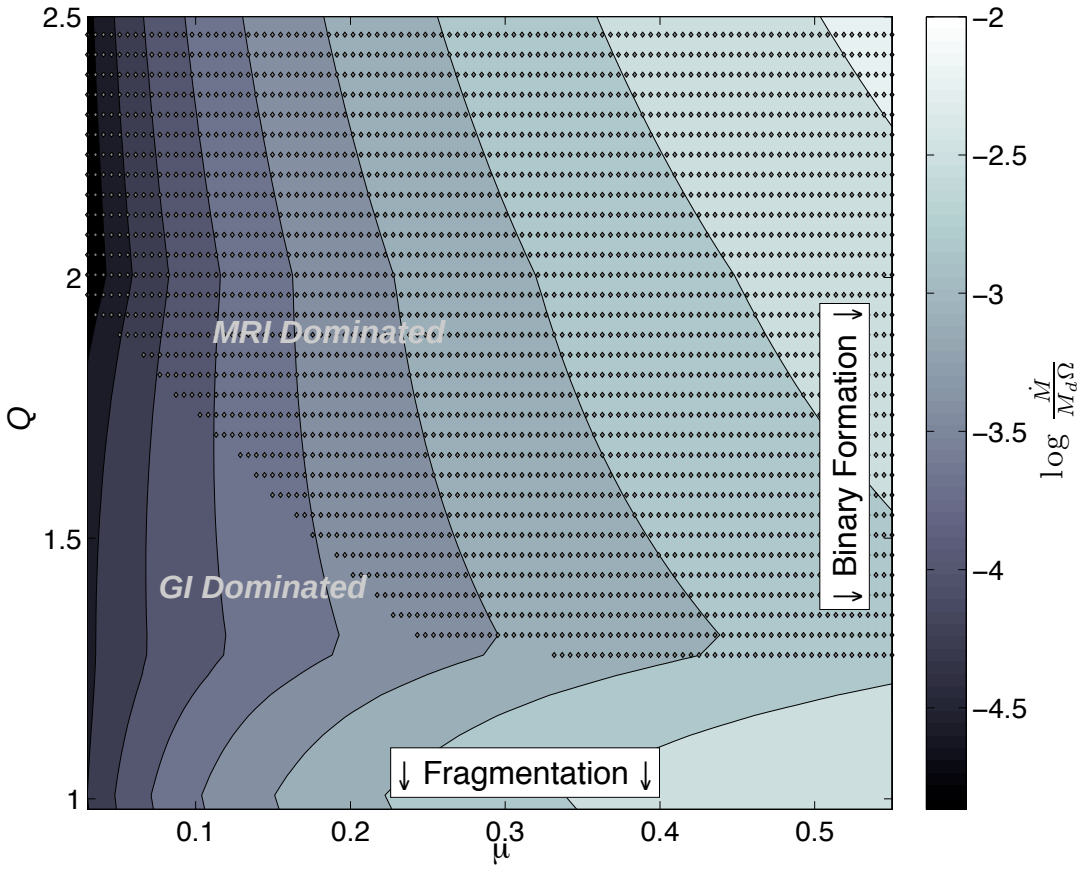

Figure 4.2: Contours of the dimensionless accretion rate from the disk onto the star ($\dot{M}_*/M_d\Omega$) from all transport components of our model. The lowest contour level is $10^{-4.8}$, and subsequent contours increase by 0.3 dex. The effect of each transport mechanism is apparent in the curvature of the contours. At $Q < 1.3$ the horizontal "tongue" outlines the region in which short wavelength instability dominates accretion. The more vertical slope of the contours at lower μ and $Q > 1.3$ shows the dominance of the long wavelength instability. The MRI causes a mild kink in the contours across the $Q = 2$ boundary and is more dominant at higher disk masses due to our assumption of a constant α: equation [4.13] illustrates that a constant α will cause higher accretion rates at higher values of μ.

Tan (2003) protostellar evolution model, to compute the luminosity L_* of the central star as a function of its accretion history. The model includes contributions to the protostellar luminosity from accretion on the stellar surface, Kelvin-Helmholtz contraction, and, once the temperature rises high enough, deuterium and then hydrogen burning.

During the infall, dust within the infall envelope reprocesses starlight and casts it down on the disk. By performing ray tracing within an inflow envelope with a central outflow cavity, Matzner & Levin (2005) determine the fraction of light received by the disk assuming the infall envelope is optically thick to the stellar radiation, and optically thin to its own IR re-radiation: they find

$$F_{\rm irr} = \frac{0.1}{\varepsilon^{0.35}} \frac{L_*}{4\pi R_d^2}. \tag{4.20}$$

The weak dependence on the accretion efficiency ε arises from a picture in which the outflow clears a fraction $1-\varepsilon$ of the core, so that infall streamlines originate from regions separated from the axis by angles θ such that $\cos\theta > \varepsilon$. Recently, Rodríguez et al. (2005) have observed an outflow near an O-type protostar with an opening angle of approximately 25°; this is in reasonable agreement with the model chosen here, since infall occurs at wider angles.

Once the core has accreted entirely and the envelope can no longer re-process starlight, we make an (unrealistically) abrupt switch to a model in which $\dot{M}_{\rm in} = 0$. The star continues to acquire mass from the disk, which represents a non-negligible reservoir. From this point on we calculate $F_{\rm irr}$ in the manner of Chiang & Goldreich (1997). We first identify the fraction of L_* intercepted by the surface which is optically thick to stellar photons, assuming for this purpose that $H \propto R^{9/7}$ and that the dust density is a Gaussian, of scale height H, in the height above the midplane. We also calculate the equilibrium temperature of dust in this reprocessing layer. We then calculate $F_{\rm irr}$ as that fraction of the reprocessed radiation which is reabsorbed by the disk, allowing for the possibility that the disk will be optically thin at the relevant wavelengths. We find the reprocessing height is slightly larger than a scale height ($1.5\,H$ being typical); higher values are typical of more massive disks, which are more opaque.

Though negligible during the accretion phase, we also include a background radiation field due to the cloud (modeled as an optically thin dust layer) and the cosmic microwave background. This prevents disks from becoming unrealistically cold at large radii and late times. Our cloud irradiation serves as a stand-in for one neglected heat source in clusters: irradiation from surrounding stars. This effect is likely important for (a) very

dense regions, and (b) late times when disk radii stretch out to 10^4 AU. Due to the wide variance in the strength of this effect, we do not address heating by neighbors here. There is also minor heating due to the accretion shock that feeds the disk; however, KM06 have argued that this is negligible in general.

While our background heating is only important at late times, we do not report results for $t > 2$ Myr as this may exceed the lifetime of gas disks, even the low-mass ones (Jayawardhana et al., 2006). The uncertainties in our procedure therefore have little effect on the results we obtain.

We have now fully specified the conditions of thermal and mechanical equilibrium for this disk, and we can use them to compute the accretion rate. Equations (4.13) and (4.18) constitute two equations for the unknowns Q and $\dot{M}_*$. For any given M_d, M_*, and $\mathbf{J_d}$, we may solve them to determine $\dot{M}_*$. This in turn also specifies the rate of change of the disk mass

$$\dot{M}_d = \dot{M}_{\rm in} - \dot{M}_*. \tag{4.21}$$

Note that M_d can also be modified by disk fragmentation and binary formation, as described in § 4.3.5 and § 4.3.6.

4.3.4 An Outer Disk and the Braking Torque

When describing standard steady-state disks, one implicitly assumes that when angular momentum is transported radially, it travels out to large radii in an insignificant amount of mass. In our current model, we effectively keep track of an "inner" disk: the portion containing the majority of the mass. This justifies our choice of surface density profile $\Sigma \propto r^{-1}$, since the radius at which this power-law slope is achieved is also the radius that encloses most of the mass. We allow for a small amount (2%) of material raining in from the core to be carried out with the angular momentum.

The disk's angular momentum is then equal to that of the infalling material, in addition to the amount already in the disk, minus some portion which has been transferred to this outer disk. The disk loses a fraction b_j of its angular momentum and a small amount of mass on the viscous timescale $\tau_v = M_d/\dot{M}_*$, *so long as matter is still accreting from the core*:

$$\dot{\mathbf{J}}_d = \mathbf{j}_{\rm in}\dot{M}_{\rm in} - b_j \left(\frac{\dot{M}_{\rm in}}{\dot{M}_*}\right) \frac{\dot{M}_{\rm in}}{M_d}\mathbf{J}_d. \tag{4.22}$$

As above, the subscript "in" denotes newly accreted matter. The factor $(\dot{M}_{\rm in}/\dot{M}_*)$ is

roughly unity in the main accretion phase, but goes to zero when accretion stops. We thus assume the outer disk only applies a torque when it gains matter from the inner disk. Without accretion the outer disk has no effect, and thus after accretion ends, the inner disk is free to expand self-similarly at constant $\mathbf{J}_d$. We consider this a conservative approach, considering that we do not treat effects like photoionization that might remove material from the inner and outer disk, especially in massive stellar clusters.

We consider $b_j = 0.5$ to be typical; in this case an accreting disk loses about half its angular momentum each viscous time. Since the disk sheds mass at the same rate, this allows its radius to remain comparable to the circularization radius of the infalling material. Although our choice of b_j is somewhat arbitrary we demonstrate that our parametrization makes the disk evolution somewhat independent of this value. See §4.5.6 for discussion.

4.3.5 Disk Fragmentation

Since we have now computed $\dot{M}_d$, $\dot{M}_*$, and $\dot{\mathbf{J}}_d$, our model is almost complete. However, as demonstrated by both previous analytic work (KM06) and numerical simulations (Krumholz et al., 2007b; Vorobyov & Basu, 2006; Lodato & Rice, 2005), our parameter space extends deeply into the regime where disk fragmentation is expected. We must account for this to model disk evolution. It is not our intent to follow the detailed evolution of the fragments formed, nor their mass spectrum; we are interested primarily in how they help the disk regulate Q.

In keeping with the approach outlined in § 4.3.1, we make the important assumption that the disk fragments into small objects when Q drops below a critical value, $Q_{\rm crit}$, which we take to be unity. Other authors (Gammie, 2001; Rice et al., 2003) have pointed out the importance of a disk's thermal physics in setting the fragmentation boundary. In particular they find, in simulations with imposed cooling, a critical value of $\tau_c\Omega$ above which disks do not fragment, and below which they do.

Our fragmentation model reproduces these results (indeed, it is calibrated to the same simulations) and we believe that the two views are in fact equivalent. Within our model, a disk whose Q is close to unity will be heated by accretion at a rate close to the critical cooling rate found in these simulations. In the absence of any additional heating, the cooling rate must exceed the critical value in order for Q to fall below unity, so that fragmentation can commence. In other words, since in our model Q is calculated

based on the competition between cooling and the combination of viscous dissipation and irradiation, if Q falls below unity then it is necessarily the case that the cooling rate is sufficient to overwhelm viscous heating, and therefore to satisfy a cooling condition similar to those identified by Gammie (2001) and Rice et al. (2003).

The benefit of our fragmentation model is that it can be easily extended into the realistic regime of irradiated disks, whereas a model that refers solely to the cooling time cannot.

We note, in support of our model, that we know no examples of disks for which $Q < 1$ that do not fragment, nor those with $Q > 1$ that do. Moreover, Rice et al. (2003) note that a sufficiently slowly cooling disk reaches an equilibrium at a Q value *higher* than unity; this is consistent with a heating rate that drops sharply as Q increases, as our accretion model would predict.

To implement fragmentation within our numerical models, we must specify how much mass goes into fragments each time step when $Q < 1$. We first define a critical density, $\Sigma_{d,c}$:

$$\Sigma_{d,c} = \frac{c_s \Omega}{\pi G Q_{\rm crit}}; \tag{4.23}$$

a reduction of surface density from Σ_d to Σ_c would return the disk to stability. Because we expect fragmentation to happen over a dynamical time, we assume that it depletes the disk surface density at the rate:

$$\dot{\Sigma}_{\rm frag} = -(\Sigma_d - \Sigma_{d,c})\Omega, \tag{4.24}$$

This rate is fast enough to ensure that Q never dips appreciably below $Q_{\rm crit}$.

For simplicity, we assume that while fragments contribute to the mass of the disk, they do not enter in Toomre's stability parameter Q except insofar as they contribute to the binding mass. (One could consider a composite Q: Rafikov 2001.) Nor do we follow the migration of fragments in the disk. Instead, we allow them to accrete onto the central star at the rate

$$\dot{M}_{*,\rm frags} = \phi_f M_{\rm frag} \Omega, \tag{4.25}$$

with $\phi_f = 0.05$. The assumption is simply that some fraction of the fragments accrete each orbit. Fragments form preferentially at large distances from the star, and thus only a small amount of the fragment mass will make it into the central star each orbit. Changing this parameter by an order of magnitude only marginally alters the disk evolution.

We also make the important assumption that disks will always fragment to maintain stability, and allow accretion to proceed. While this is likely a good assumption based on

the existence of massive stars that appear to have formed via disk accretion, the persistence of rapid accretion during fragmentation has not been satisfactorily demonstrated in numerical simulations. See §4.7.1.

4.3.6 Binary Formation

A majority of stars, especially massive stars, are found in binary and multiple systems. Though we present a very simplified scenario for star formation, we do account for the possibility that a single secondary star will form if $M_d > M_*$, that is, if the disk grows unphysically large with respect to the central star. (As we discussed in § 4.3.4, this may well be conservative – in the sense that secondaries may form at even lower values of μ, or at earlier times through core fragmentation as described in Bonnell et al. 2004.) When $\mu > 0.5$, we remove the excess mass and store it (and the associated angular momentum) in a binary star. Because this tends to happen before the disks have become very extended, we assume the binary separation will be small; we therefore ignore the binary as a source of angular momentum for the disk. As with fragments, we assume the disk is affected by the secondary star only through the increased binding mass. We make no attempt to account for its contribution to the total luminosity.

4.3.7 Summary of Model

We summarize our model via the flowchart shown in Figure 4.3, which illustrates a simplified version of the code's decision tree. At a given time t we know the current disk and star mass, and the current angular momentum and mass infall rates as prescribed in §4.2.1 and §4.2.2. We can calculate R_d and Σ_d directly, and find the appropriate stellar luminosity based on its evolution, current mass, and accretion rate. Using these variables we self-consistently solve for the appropriate temperature, Q, and disk accretion rate as described in §4.3.3. With this information in hand, we determine whether the disk is stable, locally fragmenting, or forming a binary. If the disk is stable, we proceed to the next iteration. If $Q < 1$, then the disk puts mass into fragments according to equation [4.23]. If $\mu > 0.5$ we consider binary formation to have occurred, and the net angular momentum and disk mass over the critical threshold is placed into a binary (see §4.3.6). We stop simulations after 2 Myr for two reasons: first, the most massive stars in our parameter space are significantly evolved and so our stellar evolution models are no longer sufficient; and second, because many other effects begin to dominate the

disks appearance at late stages due to gas-dust interaction and photo-evaporation (Keto, 2007).

4.4 Expected Trends

Before examining the numerical evolution, it is useful to make a couple analytical predictions for comparison.

First, can we constrain where disks ought to wander in the plane of Q and μ? This turns out to depend critically on the dimensionless system accretion rate

$$\Re_{\rm in} \equiv \frac{\dot{M}_{\rm in}}{M_{*d}\Omega(R_{\rm circ})} = \frac{\dot{M}_{\rm in} j_{\rm in}^3}{G^2 M_{*d}^3} \tag{4.26}$$

which is the ratio of the mass accreted per radian of disk rotation (at the circularization radius $R_{\rm circ}$) to the total system mass $M_{*d} = M_* + M_d$. Since the active inner disk has a radius comparable to $R_{\rm circ}$, this controls how rapidly the disk gains mass via infall.

The importance of $\Re_{\rm in}$ is apparent in the equation governing the evolution of the disk mass ratio μ:

$$\begin{aligned} \frac{\dot{\mu}}{\mu\Omega} &= \frac{\dot{M}_{\rm in}}{M_{*d}\Omega}\left(\frac{1}{\mu} - 1\right) - \frac{\dot{M}_*}{M_d\Omega} \\ &= \frac{\Omega(R_{\rm circ})}{\Omega}\left(\frac{1}{\mu} - 1\right)\Re_{\rm in} - \frac{\dot{M}_*}{M_d\Omega}. \end{aligned} \tag{4.27}$$

Since we consider $\dot{M}_*/(M_d\Omega)$ to be a function of μ and Q, we must know the disk temperature to solve for $\mu(t)$. Regardless, equation (4.27) shows that larger values of $\Re_{\rm in}$ tend to cause the disk mass to increase as a fraction of the total mass. We may therefore view $\Re_{\rm in}$ and Q as the two parameters that define disk evolution – of which $\Re_{\rm in}$ is imposed externally and Q is determined locally.

Moreover, $\Re_{\rm in}$ takes characteristic values in broad classes of accretion flows, such as the turbulent core models we employ. Suppose the rotational speed in the pre-collapse region is a fraction f_K of the Kepler speed, so that $j_{\rm in} = f_K r v_K(r) = f_K[GrM_c(r)]^{1/2}$, and suppose also that the mass accretion rate is a fraction $\varepsilon f_{\rm acc}$ of the characteristic rate $v_K(r)^3/G$. Then,

$$\Re_{\rm in} = \frac{f_K^3 f_{\rm acc}}{\varepsilon^2}. \tag{4.28}$$

(In this expression, negative two powers of ε appear because the binding mass is ε times smaller for the disk than for the core, generating three powers of ε; one of these is compensated by the reduction of the accretion rate by the same factor.)

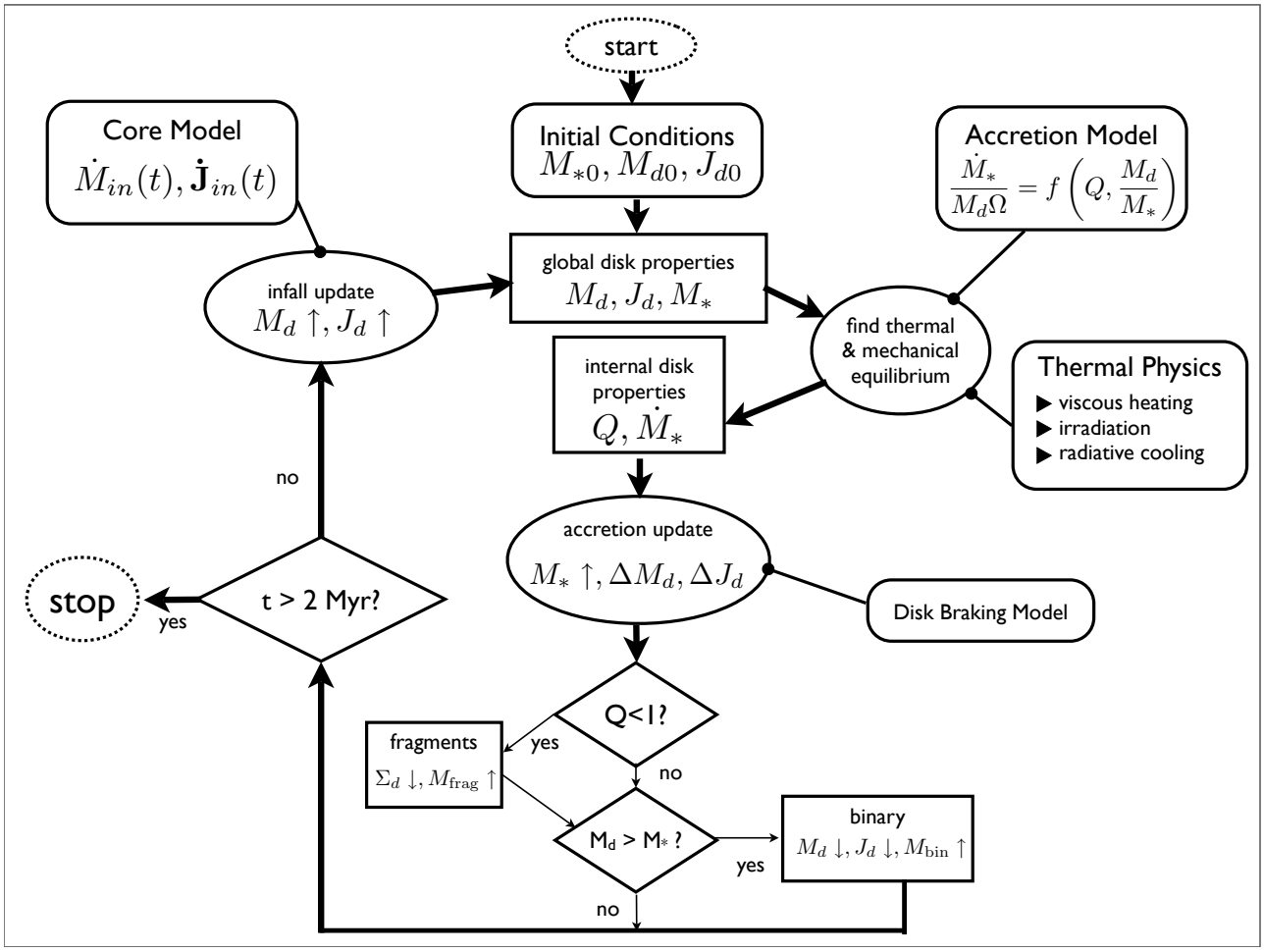

Figure 4.3: A simplified schematic of the decision tree in the code. The primitive variables, M_d, M_*, and $\mathbf{J_d}$, together with the core model, $\dot{M}_{in}(t)$ and $\dot{\mathbf{J}}_{in}(t)$, allow for the determination of all disk parameters at each time step. Note that c_s, Q, and $\dot{M}$ are solved for simultaneously. Once the self-consistent state is found, the values of Q and μ determine whether either the binary or fragmentation regime has been reached. See §4.3.7 for a description of the elements in detail.

In § 4.2.1 we adopted the McKee & Tan (2003) model for massive star formation due to core collapse of a singular, turbulent, polytropic sphere in initial equilibrium. Their equations (28), (35), and (36) imply

$$f_{\rm acc} = 0.84(1 - 0.30k_\rho)\left(\frac{3-k_\rho}{1+H_0}\right)^{1/2} \tag{4.29}$$

within 2%, where $1 + H_0 \simeq 2$ represents the support due to static magnetic fields (Li & Shu, 1996). (Note, their equation [28] is a fit made by McKee & Tan 2002 to the results of McLaughlin & Pudritz 1997.)

KM06 predicted the turbulent angular momentum of these cores; our parameter f_K equals $(\theta_j\phi_j)^{1/2}$ in their paper. Their equations (25), (26), and (29) imply

$$f_K = \frac{0.49}{\phi_B^{1/2}}\frac{(1-k_\rho/2)^{0.42}}{(k_\rho-1)^{1/2}}, \tag{4.30}$$

with excursions upward by about 50% and downward by about a factor of three expected around this value; here $\phi_B \simeq 2.8$ represents the magnetic enhancement of the turbulent pressure. All together, we predict

$$\begin{aligned}\Re_{\rm in} &= \frac{0.10}{\varepsilon^2\phi_B^{3/2}}\left(\frac{3-k_\rho}{1+H_0}\right)^{1/2}\frac{\left(1-\frac{k_\rho}{2}\right)^{1.26}}{(k_\rho-1)^{3/2}}(1-0.30k_\rho) \\ &\rightarrow 0.02\left(\frac{0.5}{\varepsilon}\right)^2 \end{aligned} \tag{4.31}$$

where the evaluation uses $1 + H_0 \rightarrow 2$, $\phi_B \rightarrow 2.8$, and $k_\rho \rightarrow 1.5$.

Importantly, $\Re_{\rm in}$ is a function of $(1 + H_0)$, ϕ_B, ϵ, and k_ρ, but *not* the core mass. We therefore expect similar values of $\Re_{\rm in}$ to describe all of present-day massive star formation, at least insofar as these other parameters take similar values. Suppose, for instance, that the formation of $10M_\odot$ and $100M_\odot$ stars were both described by the same $\Re_{\rm in}$. According to equation (4.27), the difference in μ between these two systems would be controlled entirely by the thermal effects that cause them to take different values of Q.

A few additional expectations regarding Q itself can be gleaned from the analytical work of Matzner & Levin (2005) and KM06:

- The Toomre parameter remains higher than unity for low-mass stars ($\lesssim 1M_\odot$) in low-column cores ($\Sigma_{c,0} \ll 1$), but falls to unity during accretion for massive stars and for low-mass stars in high-column cores;

- A given disk's Q drops during accretion, reaching unity when the disk extends to radii beyond $\sim 150\,\mathrm{AU}$ (in the massive-star case), or to periods larger than $\sim 460\,\mathrm{yr}$ (in the case of an optically thick disk accreting from a low-mass, thermal core).

- At the very high accretion rates characteristic of the formation of very massive stars ($\gtrsim 1.7 \times 10^{-3} M_\odot\,\mathrm{yr}^{-1}$), disk accretion is strongly destabilized by a sharp, temperature-dependent drop in the Rosseland opacity of dust.

(For more detailed conclusions, see the discussion surrounding equation [35] in KM06.) With the help of equation (4.27) we also deduce that more massive stars will have generally higher disk mass fractions, because: (1) they are described (in our model) by the same value of $\Re_{\rm in}$; (2) more massive stars achieve lower values of Q; and (3) in our model, lower Q leads to lower values of $\dot{M}_*/(M_d\Omega)$, so long as $Q > 1.3$. The conclusion that higher-mass stars have relatively more massive disks follows from these three points by virtue of equation [4.27].

More generally, *any* effect which causes $\dot{M}_*/(M_d\Omega)$ to drop (without affecting $\Re_{\rm in}$) will tend to increase μ, and vice versa; this conclusion is not limited to our adopted disk accretion model.

Within our model, $\dot{M}_*/(M_d\Omega)$ increases with Q unless $1 < Q < 1.3$, in which case the dependence is reversed. Disks ought therefore to traverse from high Q and low μ, to low Q and high μ, until $Q = 1.3$; but for $1 < Q < 1.3$, μ and Q should decline together. In physical terms, this reversal represents a flushing of the disk due to the strong angular momentum transport induced by the short wavelength gravitational instability.

We now turn to our suite of numerical models to test these expectations.

4.5 Results

We begin by examining the evolution of disks through their accretion history for a range of stellar masses, determining when and if they are globally or locally unstable, and the dominant mechanism for matter and angular momentum transport through disk lifetimes. Next, we explore how these results are influenced by varying the other main physical parameters: T_c, Σ_c, $\alpha_{\rm MRI}$, and by varying the angular momentum prescription. For this purpose we first define a fiducial sequence of models in § 4.5.1, and then expand our discussion to the wider parameter space encompassed by the aforementioned variables.

Parameter	Fiducial	Range
b_j	0.5	$0 - 1.0$
$\Sigma_{\rm c,low}$	0.03 g cm^{-2}	$0.03 - 1$ g /cm^2
$\Sigma_{\rm c,high}$	0.5 g cm^{-2}	$0.03 - 1$ g /cm^2
T_c	20 K	$10 - 50$K
$\alpha_{\rm MRI}$	0.01	$0.001 - 0.1$
ϕ_f	0.05	$0 - 0.5$
ε	0.5	N/A

Table 4.1: Fiducial parameters for disk models for low and high mass stars, and the accompanying ranges explored.

Figures 4.4 – 4.6 show results from our fiducial model, and Figures 4.8 and 4.9 explore the effects of our environmental variables.

Because our prescription for disk accretion and fragmentation is necessarily approximate, any specific predictions are unlikely to be accurate. We concentrate instead on drawing useful observational predictions from our models' evolutionary trends.

4.5.1 The fiducial model

Our fiducial model explores a range of masses with a standard set of parameters, which we list in Table 4.1. For our exploration of the stellar mass parameter space, we allow Σ_c to vary as $\Sigma_c = 10^{-1.84}(M_c/M_\odot)^{0.75}$ (with an enforced minimum at 0.03 g cm$^-$2 so that Σ_c varies from $0.03 - 1$g cm^{-2} across the mass range $0.5 - 120M_\odot$). This relationship ensures that for our fiducial model, each system is forming at a Σ_c that is characteristic of observed cores. Enforcing this $\Sigma_c - M_c$ correspondence specifies the core radius. We explore the effects of Σ_c independently in §4.5.3. All "low mass" runs that are shown e.g. $1M_\odot$, have $\Sigma_{\rm c,low} = 0.03$ g cm^{-2}, and "high mass", e.g. $15M_\odot$, have $\Sigma_{\rm c,high} = 0.5$ g cm^{-2}. All systems start out with an initial stellar mass of $0.10M_\odot$, disk mass of $0.01M_\odot$ and $j_d = 10^{19}$. Varying these parameters over an order of magnitude effects the initial evolution for a few thousand years, but runs converge quickly. One can find pathological initial conditions, particularly for small mass values. We believe this is due to the lack of sensitivity of a one zone model. The initial disk radius is calculated self-consistently from the amount of mass collapsed into the system at the first time step, the initial J_d is typically smaller by a factor of a few than j_{in}.

As illustrated by the evolutionary tracks of accreting stars in the $Q - \mu$ plane in Figure 4.4, our model agrees with the general trends of previous work and with the expectations described in § 4.4, in that low mass systems are stable and have low values of μ, while more massive systems undergo a period of strong gravitational instability (Krumholz et al. 2007b, KM06). Here we see that as we go to higher stellar masses, disks spend more of their time at high μ and undergoing disk fragmentation. For stars of $\leq 1M_{\odot}$, Q stays above unity, and the disks remain Toomre stable, although still subject to gravitational instability due to their non-negligable disk masses (see Figure 4.6). (Note that due to our abrupt shift in the disk irradiation model, there is a small discontinuity in the temperature calculation at the end of accretion which can cause unphysical fragmentation even at low masses, and a jump in Q at all masses.) The expectation that Q and μ evolve in opposite directions until $Q < 1.3$ is also roughly borne out. However, note that for the $15M_{\odot}$ star-disk system (right plot), the accretion rate is great enough that there is a build up of mass in the disk once Q reaches unity, and the local instability saturates. This saturation leads to binary formation (see §4.5.7).

Figure 4.5 shows the evolution of Q through the accretion history of a range of masses. We see that disks become increasingly susceptible to fragmentation with increasing mass. Disks born from cores that are smaller than about $2M_{\odot}$ remain stable against fragmentation throughout their evolution, although we expect moderate spiral structure (as is seen in the models of Lodato & Rice, 2004). Recall that with $\varepsilon = 0.5$, a $2M_{\odot}$ core makes a $1M_{\odot}$ star-disk system. Figure 4.6 illustrates the corresponding evolution of μ throughout the accretion history for the same set of masses. As described in §4.4 the typical disk mass increases with stellar mass. At high masses, binary formation occurs during the peak of accretion just before 10^5 years, and for stars $\geq 100M_{\odot}$, there is an early epoch of binary formation at roughly 10^4 years.

We also see that for higher mass cores there are three relatively distinct phases through which disks evolve:

- Type I: Young, $< 10^4$ yr systems, whose disks are described by small mass fractions and relatively high Q. These would appear as early Class 0 sources, deeply embedded in their natal clouds.

- Type II: Systems between $10^4 - 10^5$ yrs in age, whose disks are subject to spiral structure, and in high mass systems, fragmentation. Disk mass fractions are $\sim 30\% - 40\%$, substantially higher than in Type I systems. These disks would appear

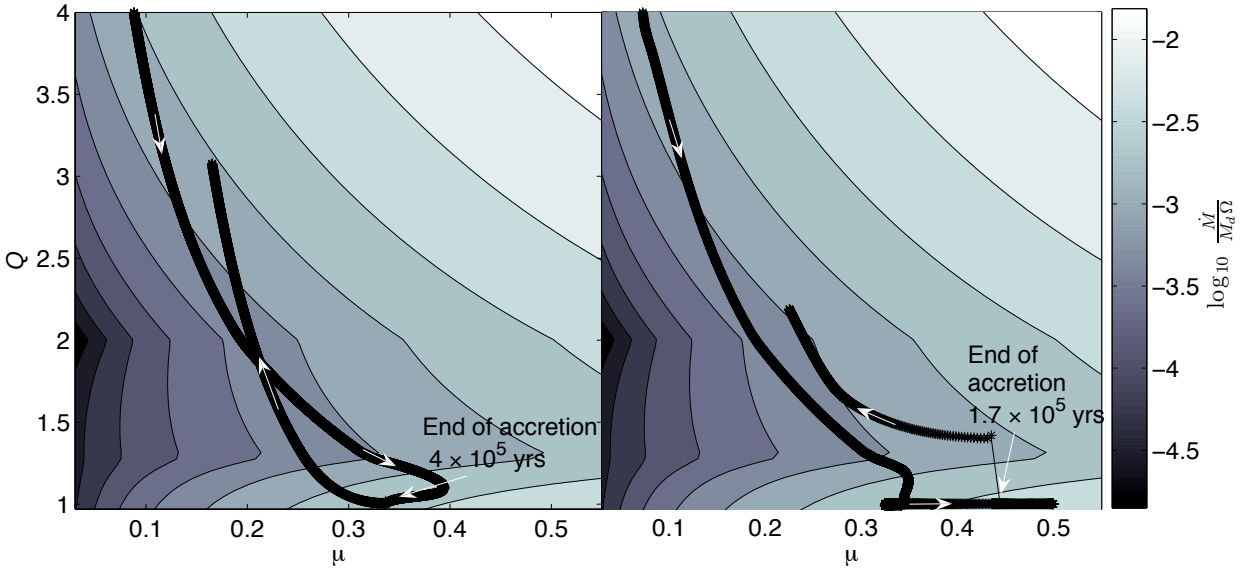

Figure 4.4: Evolutionary tracks in the Q, μ plane of a $1M_{\odot}$(left) and 15 $M_{\odot}$ (right) final star-disk system overlayed on the contours of our accretion model (contour spacing is identical to Figure 4.2). The white arrows superposed on the tracks show the direction of evolution in time. The low mass star remains stable against fragmentation throughout its history, while the more massive star undergoes fragmentation and more violent variation in disk mass. The jump a the end of accretion in the 15 $M_{\odot}$ system is due to the switch in the irradiation calculation.

in Class 0-I sources.

- Type III: Systems older than 10^5 yrs, which have stopped accreting from the core, and consequently acquire low disk mass fractions as the disks drain away. These are the disks that are most like those observed in regions of LMSF as Class I objects.

These three stages serve as a useful prediction for future observations; see §4.6 for more details.

4.5.2 Influence of vector angular momentum

The accretion disk's radius plays a critical role in determining whether or not the disk fragments. Consequently, we expect our results to depend somewhat on effects that change the disk's specific angular momentum. Because we track the vector angular momentum of the inner disk, and because our turbulent velocity field is three dimensional, we account for a possible misalignment between the disk's angular momentum axis, $\hat{\mathbf{J}}$, and that of the infalling angular momentum, $\hat{\mathbf{j}}_{\rm in}$. The wandering and partial cancellation that result provide a more realistic scenario than given by the KM06 analytic approximations, in which vector cancellation is accounted for only in an average sense. In practice, however, the disk and infall remain aligned rather well ($\hat{\mathbf{J}} \cdot \hat{\mathbf{j}}_{\rm in} \sim 0.8$), so misalignment plays only a minor role in limiting the disk size. This is illustrated by Figure 4.7, in which we compare the disk radius in two numerical realizations of the turbulent velocity field, against one in which $j_{\rm in}$ has a fixed direction and obeys the KM06 formulae. We also plot the infall circularization radius $R_{\rm circ}$ (of one numerical realization) for comparison. In general we find that the analytic prescription slightly over-predicts the disk radius at early times; this is partly due to "cosmic" variance in the numerical realization, and partly due to disk-infall misalignment.

4.5.3 Varying Σ_c

We explore the effect of individual parameters by considering one or two systems along our fiducial sequence, and varying parameters one by one relative to their fiducial values. First, we vary Σ_c over 0.03-1 $\mathrm{g\,cm^{-3}}$, spanning the range from isolated to intensely clustered star formation (Plume et al., 1997). Column density affects star formation in two primary ways: it influences the core radius (by determining the confining pressure) and the accretion rate during collapse (again, by setting the outer pressure and thus the

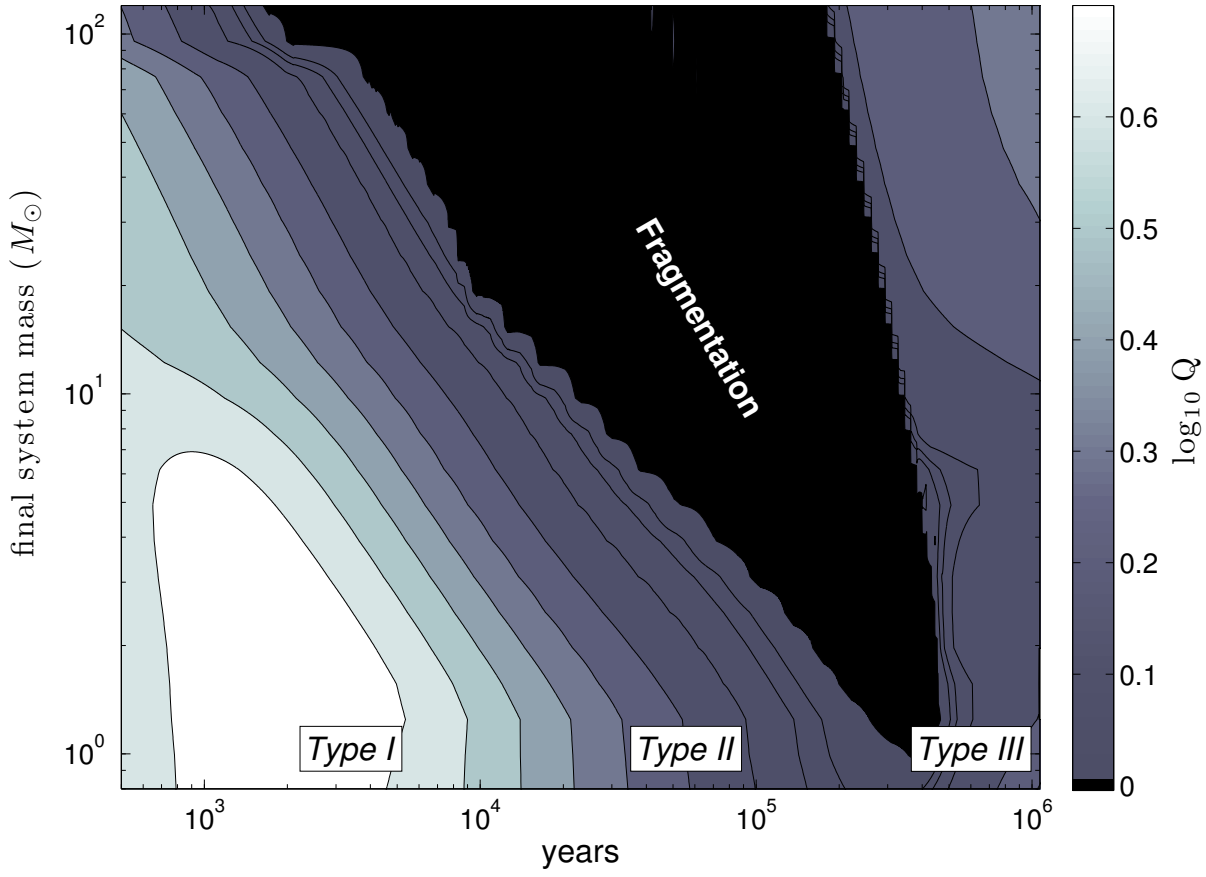

Figure 4.5: Contours of Q over the accretion history of a range of masses for the fiducial sequence. Masses listed on the y-axis are for the total star-plus-disk system final mass – because the models halt at 2 Myr, some mass does remain in the disk. Contours are spaced by 0.3 dex. At low final stellar masses, disks remain stable against the local instability throughout accretion. At higher masses, all undergo a phase of fragmentation. One can see three distinct phases in the evolution as described in §4.5. Disks start out stable, subsequently develop spiral structure as the disk mass grows and become unstable to fragmentation for sufficiently high masses. As accretion from the core halts, they drain onto the star and once again become stable.

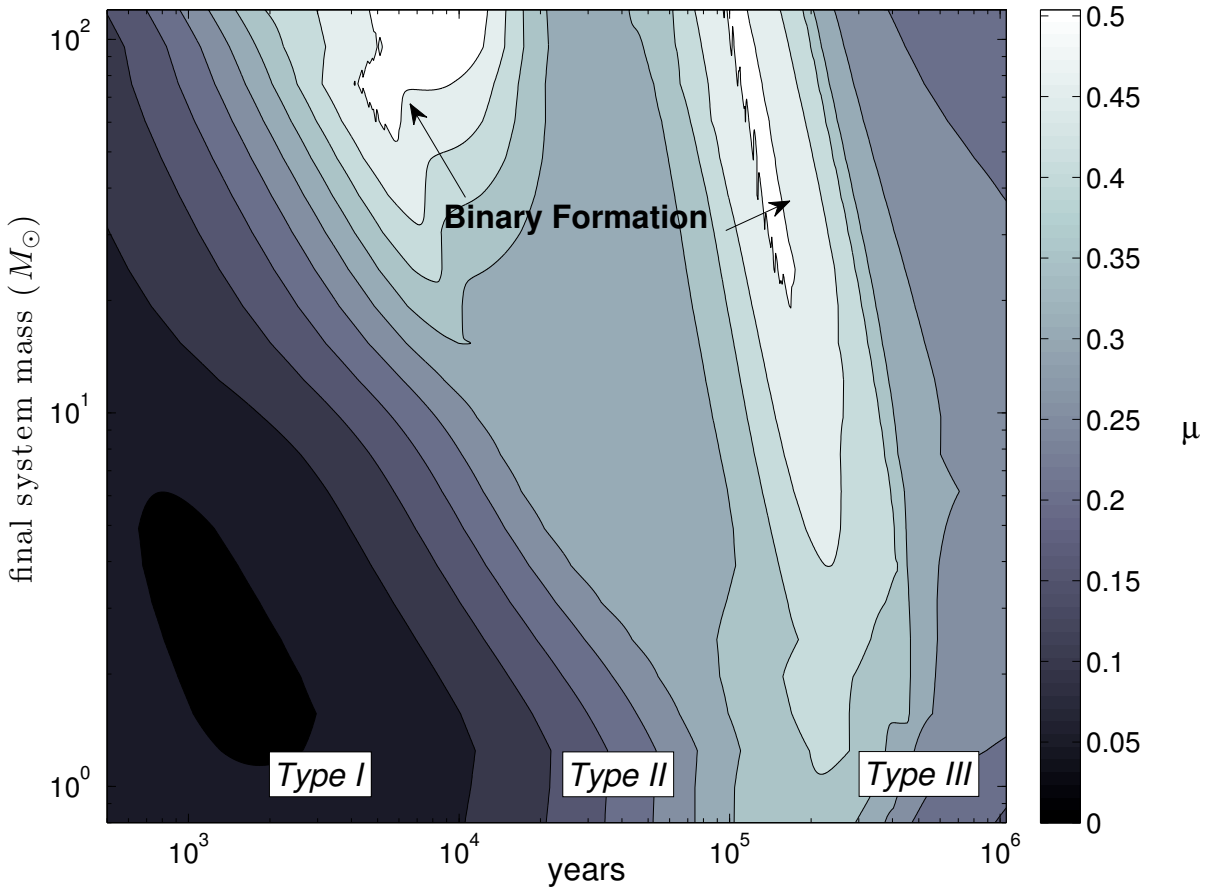

Figure 4.6: Contours showing the evolution of $\mu = \frac{M_d}{M_d+M_*}$ for the fiducial sequence. Each contour shows an increase of 0.05 in μ. Again one can see the division into three regimes: low mass disks at early times, higher mass, unstable disks that may form binaries during peak accretion times, and low mass disks that drain following the cessation of infall. Systems destined to accrete up to $\sim 70 M_\odot$ or more experience two epochs of binary formation in our model. In these systems the accretion from the core exceeds the maximum disk accretion rate very early, causing the disk mass to build up quickly.

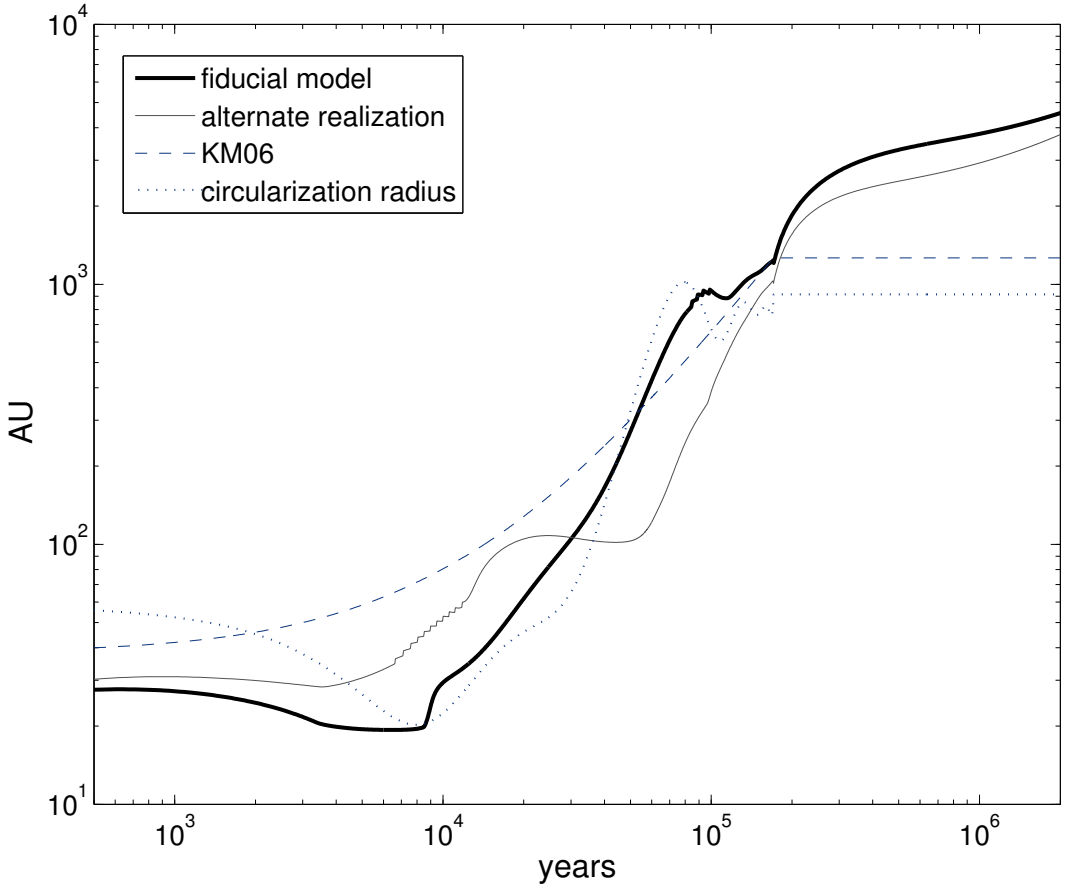

Figure 4.7: Comparison of disk radius over the evolution of a 20 $M_\odot$ star-disk system in four cases: the KM06 analytic calculation, the circularization radius of the currently accreting material, and two realizations of the numerical model. The analytic case overestimates the expected radius at early times because it does not allow for cancellation of vector angular momentum. Similarly the circularization radius is an overestimate because the disk has no "memory" of differently oriented j. At later times, the circularization radius approaches the standard radius calculation for that realization (thick black line) demonstrating the concentration of turbulent power at large scales.

velocity dispersion). However, these two effects counteract one another: smaller values of Σ_c correspond to larger cores and larger, thus more unstable disks ($R_d \propto \Sigma_c^{-1/2}$), but smaller Σ_c also leads to lower accretion rates and thus stabler disks ($\dot{M} \propto \Sigma_c^{3/4}$). The thermal balance of the disk midplane is affected by these trends. An analysis by KM06 (see their equation [35]) shows that higher Σ_c inhibits fragmentation if the disk temperature is dominated by viscous heating (which is proportional to the accretion rate), but enhances fragmentation if irradiation dominates (when the increase in accretion generated heating is insignificant), and that the two effects are comparable along our fiducial model sequence. We therefore expect fragmentation to be quite insensitive to Σ_c, for massive star formation along our fiducial sequence. This is precisely what we find in our models: disks born from lower-Σ_c cores, in lower pressure environments, evolve in essentially the same way, but more slowly.

In contrast, disks around low-mass stars – those with final masses comparable to the thermal Jeans mass – are stable at low Σ_c (as predicted by Matzner & Levin, 2005), and because irradiation dominates at larger radii, higher Σ_c tend to enhance fragmentation there. Figure 4.8 illustrates the evolution of Q for a $1M_\odot$ accreting star for a range of column densities.

4.5.4 Varying T_c

Observations of infrared dark clouds, and sub-mm core detections find typical temperatures from $10 - 50$K (Johnstone et al., 2001). In our models T_c determines the amount of thermal, and therefore turbulent, support: higher temperatures require less turbulent support in the core. Temperature also sets the thermal Jeans mass $M_{\rm th}$ within the McKee & Tan (2003) two component core model. Accretion from this thermal region leads to more stable disks; therefore, higher core temperatures increase the mass of a star which can accrete stably.

Figure 4.8 shows the evolution of Q during the accretion of a system with final mass $1M_\odot$ over a range of temperatures (all other parameters take their fiducial values). The difference in evolution is negligible for high mass stars, as these accrete from supersonic cores.

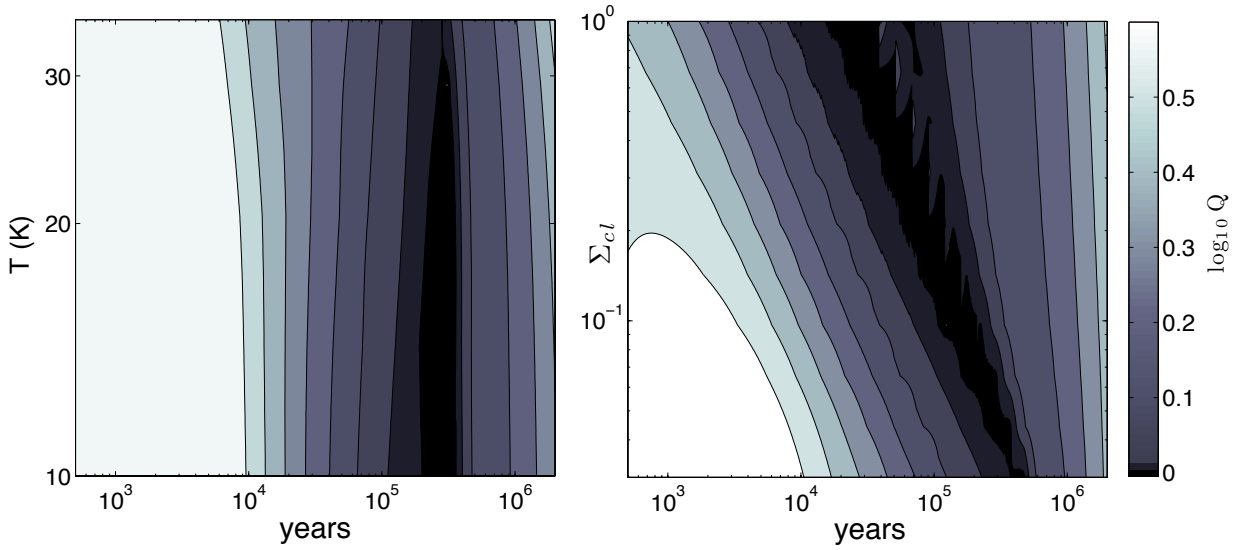

Figure 4.8: Contours of Q showing the effect of initial core temperature T_c (left) and Σ_c (right) on the evolution of a 1 $M_\odot$ final star-disk system. Contour spacing is 0.1 dex (except the lowest two contours which are spaced by .05 dex). Increasing Σ_c tends to marginally destabilize the disk, while higher temperatures stabilize the disk. We exclude temperatures too high for the $2M_\odot$ core to collapse given its initial density, i.e., those above 40 K.

4.5.5 Varying $\alpha_{\rm MRI}$

This work is not an exploration of the detailed behavior of the MRI; we include it as the standard mechanism for accretion in the absence of gravitational instabilities, which in most scenarios (aside perhaps from low mass stars whose disks Shu et al. 2007b have argued may be strongly sub-Keplerian) overpower the MRI. However, the strength of the MRI does influence the transition to gravitationally dominated accretion in the $Q - \mu$ plane as shown in Figure 4.2. The strength of the MRI also influences the maximum disk mass obtained before gravitational instabilities set in: higher values of $\alpha_{\rm MRI}$ reduce the influence of gravitational instabilities by insuring that the disk drains more quickly, whereas lower values expedite the transition to gravitational instability driven accretion. Figure 4.9 shows the influence of $\alpha_{\rm MRI}$ on μ; the influence on Q is less dramatic: the descent of Q towards unity is marginally delayed for the strong MRI case.

4.5.6 Varying b_j

Our most uncertain variable is the braking index b_j, which determines the rate of angular momentum exchange with an outer disk. However, disk evolution turns out to be rather insensitive to this parameter. The primary reason for this is the concentration of power in the turbulent velocity field on the largest scales: $j_{\rm in}$ is always large compared to the disk-average j. This reduces the importance of the loss term in equation (4.22). As a result, although the period in which the disk is fragmenting is reduced in the high b_j case, it is merely postponed by $\sim 10^4$ yrs. The braking index does have moderate influence on the disk mass during the peak of accretion, and thus on the formation of binaries. Figure 4.9 shows the evolution of μ for a system accreting towards $15 M_\odot$ from a $30 M_\odot$ core. Here one can see the influence of b_j on binary formation. Low values of b_j corresponding to higher net angular momentum produce binaries at lower masses by allowing the disk mass to grow larger. Notably, even for the $15 M_\odot$ final mass star shown here, the smallest mass for which binaries form in the fiducial model, the change in disk mass is only $\sim 10\%$.

4.5.7 The formation of binaries

Within the context of our model for disk fission into a binary system, (described in §4.3.6), the formation of a companion is strongly dependent on the infalling angular momentum

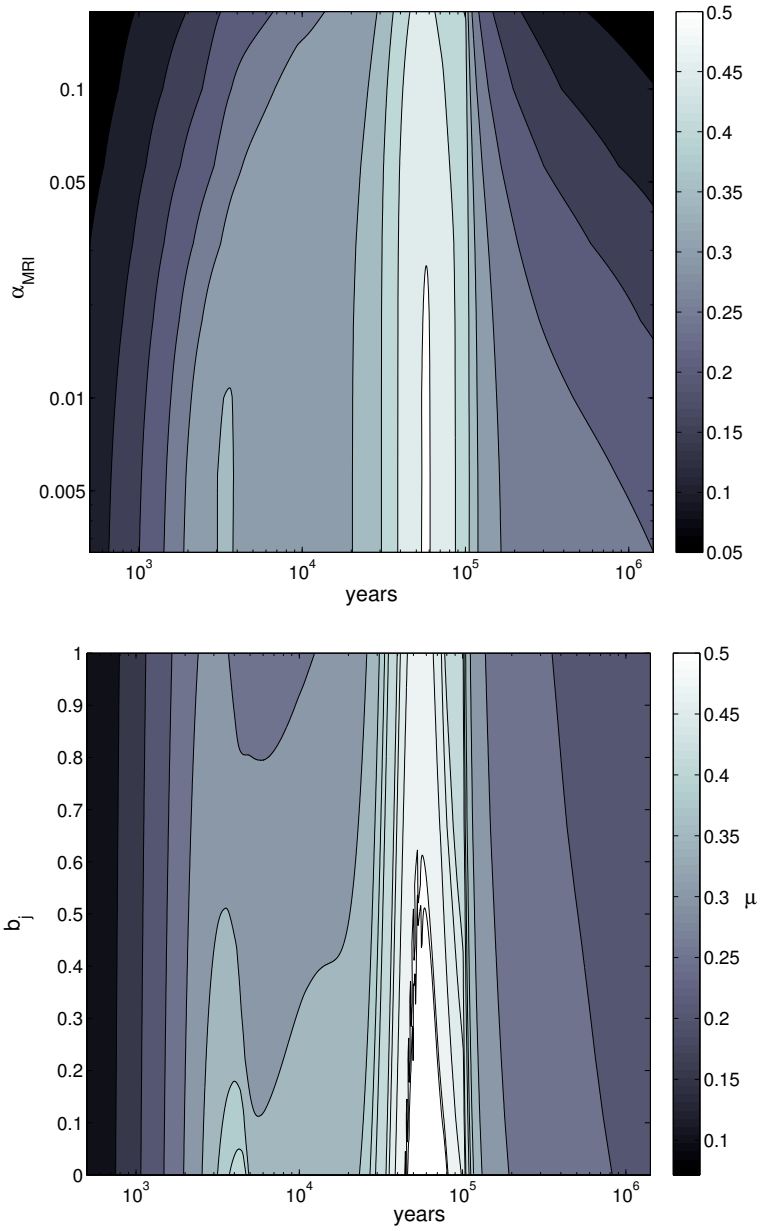

Figure 4.9: Contours in μ illustrating the influence of varying $\alpha_{\rm MRI}$ (top) and the braking index, b_j (bottom) for a star-disk system of final mass $15 M_\odot$, the lowest mass at which a binary forms in our fiducial model. Contours of μ are spaced by 0.05. The upper plot shows the effect of varying $\alpha_{\rm MRI}$ from $10^{-2.5} - 10^{-1.5}$. While the change has little effect on the evolution of Q, the disk fraction μ decreases with increasing $\alpha_{\rm MRI}$. As a result, the mass at which binary formation begins is pushed to higher masses. The lower plot shows the effect of varying the braking index b_j. An increase of b_j lowers the disk angular momentum, reducing the disk mass and inhibiting binary formation. Note that the variation in disk mass is only $\sim 10\%$.

distribution, and on the turbulent velocity profile of the particular core. In our fiducial model, binary formation occurs for cores above $30M_{\odot}$. For cores $\gtrsim 140M_{\odot}$, there are two epochs of binary formation, the first one at roughly 10^4 years. This mass boundary is quite sensitive to our conservative threshold for disk fission, $\mu = 0.5$: binaries may well form at lower values of μ, and thus at lower masses (see Figure 4.6). The mass of the binaries that form increases with initial core mass. This increase simply indicates that the mass ratio exceeds the critical value for more time, as we do not include a mechanism for accretion onto the binary. As such, we do not predict values for the binary mass ratio q, but simply indicate the regimes in which binary formation seems likely. The $30M_{\odot}$ core cut-off is fairly robust to variations in Σ_c, T_c and b_j over the ranges discussed above for our fiducial turbulent field. Cosmic variance in the field from one realization to another has a much larger effect on binary formation than any of our other model parameters (aside from $\mu_{\rm crit}$).

In our fiducial model disk fission only occurs when the gravitational instability has saturated and $Q \sim 1$. This means that the disk is draining at the maximum rate given its mass. If matter is falling in from the core more rapidly than this rate, the disk mass will increase: if the accretion rate from the core exceeds the maximum rate at $Q = 1$ and $\mu = 0.50$, disk fission occurs. In our fiducial model, this corresponds to an accretion rate on to the disk: $\dot{M}_{\rm in}/M_d\Omega = 10^{-2.36}$. The early epoch of binary formation at very high masses is a consequence of this limit: since the accretion rates begin to exceed the critical rate sooner, the disk's mass increases earlier in its evolution. This critical value is in agreement with the prediction of KM06 that disks are sharply destabilized when accreting at rates higher than $1.7 \times 10^{-3} M_{\odot}$ yr^{-1}.

The time at which binaries form is also very dependent on the angular momentum profile. In the fiducial model, the lowest mass binaries form during the peak of accretion, at $\sim 10^5$ years, but as the final system mass increases, binary formation pushes to earlier times $\sim 10^4$ years. In certain runs we find earlier binary formation at smaller masses ($< 10^4$ years) when there is a peak in the infalling angular momentum profile which rapidly sends Q towards unity. The presence of binaries in much of our parameter space illustrates that heavy circumbinary disks may be critical to binary evolution.

Observations suggest that a range of binary systems exist as a result of variations in angular momentum as evidenced by the presence or lack of disks around each component. Submillimeter observations of lower mass objects in Taurus have revealed evidence for a binary with circumstellar and circumbinary disks (Osorio et al., 2003), where the binaries

are close enough to cause disk truncation (~ 45 AU). Anglada et al. (2004) have found another Class 0/I binary system in NGC 1333 in which only the primary has a disk: the diversity of systems is likely due to the variations in angular momentum of the infalling material. As Bate & Bonnell (1997) suggest, binaries forming from low angular momentum material will likely not form their own disks, while those with higher angular momentum may. It seems plausible that the absence or presence of secondary disks is indicative of the formation process of the system.

As illustrated by these observations, the dependence we find on core angular momentum is a sensible outcome: one expects the chance rotation to have a stronger effect on multiplicity than other parameters like temperature and density, which set the minimum fragmentation mass. We emphasize that we are only exploring one possible path for binary formation, and predict that disk fragmentation is an important, if not the dominant mechanism at high masses and column densities. This is especially true since, as argued by Tan et al. (2006), who has shown that for massive stars, once the central core has turned on, the Jeans mass rapidly increases due to the stellar luminosity, significantly reducing the possibility for Jeans-instability induced core fragmentation.

4.6 Observable Predictions

Our models make strong predictions for the masses and morphologies of disks during the embedded, accreting phase, and these will be directly testable with future observations. Detailed calculations based on radiation-hydrodynamic simulations of massive protostellar disks indicate that disks with μ of a few tenths around stars with masses $\gtrsim 8\ M_\odot$, corresponding to embedded sources with bolometric luminosities $\gtrsim 10^4\ L_\odot$, should produce levels of molecular line emission that are detectable and resolvable with ALMA in the sub-millimeter out to distances of a few kpc, and with the EVLA at centimeter wavelengths at distances up to ~ 0.5 kpc (Krumholz et al., 2007a). The ALMA observations will be particularly efficient at observing protostellar disks, since ALMA's large collecting area will enable it to map a massive disk at high resolution in a matter of hours. Dust continuum emission at similar wavelengths should be detectable at considerably larger distances, although the lack of kinematic information associated with such observations makes interpretation more complex. Regardless of whether dust or lines are used, observations using ALMA should be able to observe a sample of hundreds of protostellar disks around embedded, still-accreting sources, with masses up to several tens of $M_\odot$.

The main observational prediction of our model is the existence of type II disks – those with μ of a few tenths or greater and $Q \approx 1$ – and the mass and time-dependence of the type II phase. Examining Figures 4.5 and 4.6, we see that our model predicts that protostellar cores with masses $\lesssim 2\ M_\odot$ should experience only a very short type II disk phase, or none at all. In contrast, cores with larger masses have type II disks for a fraction of their total evolutionary time that gets larger and larger as the core mass rises, reaching the point where type II disks are present during essentially the entire class 0, accreting phase for cores $\gtrsim 100 M_\odot$ in mass.

Type II disks have several distinct features that should allow observations to distinguish them from type I or type III disks, and from older disks like those around T Tauri and Herbig AE stars. First, since type II disks are subject to strong gravitational instability, they should have strong spiral arms, with most of the power in the $m = 1$ or $m = 2$ modes. This is perhaps the easiest feature to pick out in surveys, since it simply requires observing the disk morphology and can therefore be measured using continuum rather than lines.

Second, because their self-gravity is significant, type II disks will deviate from Keplerian rotation due to non-axisymmetric motions, and will also be super-Keplerian in their outer parts compared to their inner ones. The latter effect arises because, when the disk mass is comparable to the stellar mass, the enclosed mass rises as one moves outward in the disk. Recent work by Torrelles et al. (2007) provides a possible example of this phenomenon. The source HW2 in Cepheus A is predicted to have a central mass of order $15 M_\odot$, and a disk radius of 300AU, with a temperature slightly under 200 K (Patel et al., 2005; Torrelles et al., 2007). High resolution VLA observations now show evidence of non-Keplerian rotation (Jiménez-Serra et al., 2007), consistent with our predictions for type II disks.

Third, a type II disk is massive enough for the star-disk system center of mass to be significantly outside of the stellar surface if the disk possesses significant non-axisymmetry. As a result, the star will orbit the center of mass of the system, and this will produce a velocity offset of a few km s^{-1} between the stellar velocity and the zero velocity of the inner, Keplerian parts of the disk (Bertin & Lodato, 1999; Rice et al., 2003; Krumholz et al., 2007a). This should be detectable if the stellar velocity can be measured, which may be possible using Doppler shifts of radio recombination lines for stars producing hypercompact HII regions, or using proper motions for stars with large non-thermal radio emission (Bower et al., 2003). In fact recent work by Torrelles et al.

(2007) has observed said offset. As suggested by Lodato & Bertin (2001, 2003), one could also look for the effect in the unresolved radio emission from FU Orionis objects.

A final point concerns the limited range of the disk-to-system mass ratio in our simulations, with $0.2 < \mu < 0.5$ during most of embedded accretion (our type II disks). The upper envelope of μ depends in part on our binary fragmentation threshold $\mu = 0.5$. However, in the absence of disk fission, disks in our fiducial model never grow larger than $\mu = 0.55$. The fact that most accretion occurs with $\mu \sim 0.3$ provides strong evidence that accretion disks do not become very massive compared to the central point mass (as argued by Adams et al., 1989). Current observations such as those of Cesaroni (2005) describe massive tori with sub-Keplerian rotation and comparable infall and rotation velocities. These structures are distinct from the disks that we model: our finding that disks hover around $\mu = 0.3$ suggests that higher resolution observations may reveal the Keplerian structures within the tori. The underlying physical reason for this is that it is not possible to support a mass comparable to the central star in a rotationally supported disk for long periods of time; gravitational instabilities will destabilize such a disk on orbital timescales, causing it to lose mass either through rapid accretion or fragmentation.

4.7 Conclusions

We have constructed a simple, semi-analytic one-zone model to map out the parameter space of disks in $Q - \mu$ space across a range of stellar masses throughout the Class 0 and Class I stage, pushing into the Class II phase. We include angular momentum transport driven by two different mechanisms: gravitational instability and MRI transport modeled by a constant α. Our model for angular momentum infall is unique in that we keep track of an inner and outer disk, and infall direction so that cancellation may occur as the infall vector rotates. We allow for heating by the central star, viscous dissipation and a background heat bath from the cloud accounting for both the optically thin and optically thick limit within the disk and accreting envelope. By requiring that the disk maintain mechanical and thermal equilibrium, we determine the midplane temperature at each time step, and thus Q in the disk.

4.7.1 Caveats

In interpreting the results of our calculations, it is important to keep several caveats in mind. Our model for fragmentation, though rooted in simulations, includes one important assumption: no matter how violently unstable a disk becomes, it can always fragment, return to a marginally stable state, and continue accreting. While the existence of stars well into the mass regime of fragmentation makes this outcome seem likely, it has yet to be demonstrated in simulations. Equally untested is the hypothesis that when fragmentation is strong enough, i.e., when $\dot{M}_{\rm in} \gg c_s^3/G$ so that $Q \ll 1$ (Gammie, 2001), accretion onto the central star will be choked off. KM06 have argued that accretion is sharply destabilized when its rate exceeds $1.7 \times 10^{-3}\,M_\odot\,{\rm yr}^{-1}$, due to a drop in the Rosseland opacity, and that this may be related to the stellar upper mass limit.

In order to explore a wide parameter space, we do not carry out detailed hydrodynamic calculations to determine the onset of instability, but instead use results from previous simulations, and develop analytic formulae that describe behavior intermediate between the regimes which they explore. Although our approach is very approximate, it can be made increasingly more realistic as additional numerical simulations become available. Due to our one-zone prescription, we cannot resolve spiral structure or measure the degree of non-Keplerian motion. In addition, we do not follow the evolution of fragments, nor their interaction with the disk. Although we allow for the formation of binaries, we do not follow their evolution and accretion, which limits our ability to make predictions about mass ratios and angular momentum transfer between the disk and the companion. Our model for angular momentum infall is responsible for the largest uncertainty in our conclusions because different realizations of the turbulent velocity field can alter the disk size at a given epoch by a factor of a few. Nevertheless, these variations are well within the analytic expectations for range of angular momenta in cores (KM06). Moreover, our approach aims only to predict characteristics of the outer accretion disk, and lacks the resolution to track the radial profiles of the disk's properties.

Lastly, recall that our models rely on the fundamental assumption (§ 4.3.1) that a disk's behavior can be separated into dynamical and thermal properties, and in particular that its dynamics are governed primarily by its mass fraction μ and Toomre parameter Q.

With these caveats in mind, we summarize our results for two different regimes: $< 2M_\odot$ and $> 2M_\odot$.

4.7.2 The Low Mass Regime

Our fiducial models predict that low mass stars will have higher values of μ than typically assumed during early phases of formation. However, they should remain stable against fragmentation throughout their evolution, dominated by MRI, long wavelength gravitational instability, and once again MRI through their evolution through the three types of disks discussed in §4.5. During the main accretion phase, disks will have masses of order 30% of the system mass. Typical outer radii are of order 50 AU, with outer temperatures of 40 K during the main accretion phase, dropping to $\sim$ 10 K at 2 Myr. The surface density is $10 - 20$ g cm^{-2} during the main accretion phase, dropping off rapidly at late times causing the disk to become optically thin to its own radiation. As accretion shuts down, and disks grow due to conservation of angular momentum, two key effects must be considered: truncation and heating by other stars. At distances of 1000 AU, very tenuous disks are prone to truncation by passing stars particularly in denser clusters where average stellar densities are as high as 10^5 stars pc^{-3} (Hillenbrand & Hartmann, 1998). Similarly, as the disk edge extends towards other, potentially more luminous stars, the actual flux received will increase, heating the disk above the $\sim$ 10K temperature that we routinely find (Adams et al., 2006).

For core column densities more typical of high-mass star forming regions, local instabilities do set in, despite the stabilizing influence higher temperatures associated with these regions (neglecting the effects of nearby stars). This implies that environment may be important in understanding disk evolution.

In contrast to our previous work (Kratter & Matzner, 2006; Matzner & Levin, 2005), we find fragmentation at smaller radii. This is primarily due to our modified model for $\alpha_{\rm GI}$, which predicts lower accretion rates and consequently more fragmentation then previously assumed. We note that our results for low-mass systems (final mass $\sim 1 M_\odot$) are rather sensitive to details of the model, such as the value of $\alpha_{\rm MRI}$ and the way it is combined with $\alpha_{\rm GI}$.

4.7.3 The High Mass Regime

For more massive stars, we find high values of $\mu \sim 0.35$ and an extended period of local fragmentation as the accretion rates peak. Temperatures at the disk outer edge at $\sim$ 200 AU approach 100K for systems $> 15 M_\odot$ during accretion. surface densities hover around 50 g cm^{-2} during the main accretion phase, although by 2 Myr, the disks

become optically thin in the FIR, as expected. Binary formation occurs regularly for cores of order $30M_{\odot}$ and higher, though as discussed in §4.3.6 this is strongly dependent on the cosmic variance of the angular momentum: cores as small as $20M_{\odot}$ form binaries in our model when there is excess angular momentum infall. Although fragments accrete with the disk according to equation [4.25], more massive stars maintain a small mass in fragments ($10^{-1} - 10^{-2}M_{\odot}$) in the disk when we end our simulations, suggesting that fragments may persist to form low mass companions, as predicted in KM06 and suggested by the simulations of Krumholz et al. (2007b).

Unlike their low mass counterparts, the conclusions we draw for massive stars are minimally effected by the environmental variables in our model. For the entire range of temperatures, densities, and nearly all angular momentum realizations, the conclusions listed above hold true.

Chapter 5

Numerical Models of Rapidly Accreting Disks

A version of this chapter has been published in The Astrophysical Journal as "On the Role of Disks in the Formation of Stellar Systems: A Numerical Parameter Study", Kratter, K. M., Matzner, C. D., Krumholz, M. R., and Klein, R. I., vol. 708, pp1585-1597, 2010. Reproduced by permission of the AAS.

5.1 Introduction

We have surveyed the role of disks in the formation of stellar systems analytically, but our results are ultimately dependent on our model of gravitational instability driven accretion. Although semi-analytical and low-dimensional studies can illuminate trends and provide useful approximate results, disk fragmentation is inherently a nonlinear and multidimensional process. For this reason we have embarked on a survey of idealized, three-dimensional, numerical experiments to examine the role of GI as the mediator of the accretion rate in self-gravitating disks, and as a mechanism for creating disk-born companions.

We focus on the dynamics of disks around young, rapidly accretings protostars, for which self-gravity is the key ingredient (Lin & Pringle, 1987; Gammie, 2001; Kratter et al., 2008). GI plays a strong role in AGN disks as well, and possibly in other contexts where disks are cold and accretion is fast.

We emphasize that these are numerical experiments, not simulations of star formation. Our goal in conducting experiments is to isolate the important physical process, GI,

which dictates angular momentum transport and fragmentation. To do so, we separate the dynamical problem from the thermal one. We exclude thermal physics from our simulations entirely, while scanning a thermal parameter in our survey.

By this means we reduce the physical problem to two dimensionless parameters: one for the disk's temperature, another for its rotation period – both in units determined by its mass accretion rate. We hold these fixed in each simulation by choosing well-controlled initial conditions corresponding to self-similar core collapse. This parameterization is a central aspect of our work: it forms the basis for our numerical survey; it allows us to treat astrophysically relevant disks, including fragmentation and the formation of binary companions, while also maintaining generality; and it distinguishes our work from previous numerical studies of core collapse, disk formation, GI, and fragmentation. We demonstrate that idealized disks like those presented here can capture many of the important features of simulations with more complicated physics, with significantly lower computational cost.

In this chapter we focus on the broad conclusions we can draw from our parameter space study. We begin here by introducing our dimensionless parameters in §5.2. We describe the initial conditions and the numerical code used in §5.3. In §5.4 we derive analytic predictions for the behavior of disks as a function of our parameters. We describe the main results from our numerical experiments in §5.5, with more detailed analysis in §5.7. We compare them to other numerical and analytic models of star formation in §5.8.

5.2 A New Parameter Space for Studying Accretion

We consider the gravitational collapse of a rotating, quasi-spherical gas core onto a central pointlike object, mediated by a disk. In the idealized picture we will explore in this chapter, the disk and the mass flows into and out of it can be characterized by a few simple parameters. At any given time, the central point mass (or masses, in cases where fragmentation occurs) has mass M_*, the disk has mass M_d, and the combined mass of the two is M_{*d}. The disk is characterized by a constant sound speed $c_{s,d}$. Material from the core falls onto the disk with a mass accretion rate $\dot{M}_{\rm in}$, and this material carries mean specific angular momentum $\langle j \rangle_{\rm in}$, and as a result it circularizes and goes into Keplerian rotation at some radius $R_{k,\rm in}$; the angular velocity of the orbit is $\Omega_{k,\rm in}$.

Note that $\dot{M}_{\rm in}$, $j_{\rm in}$, $R_{\rm k,in}$ and $\Omega_{\rm k,in}$ characterize the material that is just reaching the disk at a given instant, and as a result they can vary with time – indeed, we will set up

our initial conditions to guarantee that they do vary with time in precisely the manner required to ensure that certain dimensionless numbers remain constant as gas accretes. In general in what follows, we refer to quantities associated with the central object with subscript *, quantities associated with the disk with a subscript d, quantities associated with infall with subscript in. Angle brackets indicate mass-weighted averages over the disk (with subscript d) or over infalling mass (with subscript in).

We characterize our numerical experiments using two dimensionless parameters which are well-adapted to systems undergoing rapid accretion. Because the behavior of young protostellar disks will be dominated by infall, modelling their behavior in terms of dimensionless accretion rates is a natural choice.

We encapsulate the complicated physics of heating and cooling through the thermal parameter

$$\xi = \frac{\dot{M}_{\rm in} G}{c_{s,d}^3}, \tag{5.1}$$

which relates the infall mass accretion rate $\dot{M}_{\rm in}$ to the characteristic sound speed $c_{s,d}$ of the disk material. Our parameter ξ is also related to the physics of core collapse leading to star formation. If the initial core is characterized by a signal speed $c_{{\rm eff},c}$ then $\dot{M}_{\rm in} \sim c_{{\rm eff},c}^3/G$, implying $\xi \sim c_{{\rm eff},c}^3/c_{s,d}^3$ – although there can be large variations around this value (Larson, 1972; Foster & Chevalier, 1993). The second, rotational parameter

$$\Gamma = \frac{\dot{M}_{\rm in}}{M_{*d}\Omega_{k,{\rm in}}} = \frac{\dot{M}_{\rm in}\langle j\rangle_{\rm in}^3}{G^2 M_{*d}^3}, \tag{5.2}$$

compares the system's accretion timescale, $M_{*d}/\dot{M}_{\rm in}$ to the orbital timscale of infalling gas. For the initial conditions we use in this work, the quantities $\langle j\rangle_{\rm in}$ and M_{*d} evolve in time while $\dot{M}_{\rm in}$ remains constant. They can be evaluated as functions of time, or the current radius from which material is falling onto the system. To hold Γ fixed, we specify a core rotation profile such that $\langle j\rangle_{\rm in} \propto M_{*d}$. Unlike ξ, Γ is independent of disk heating and cooling, depending only on the core structure and velocity field. In general, Γ compares the relative strength of rotation and gravity in the core. Systems with a large value of Γ (e.g. accretion-induced collapse of a white dwarf) gain a significant amount of mass in each orbit, and tend to be surrounded by thick, massive accretion disks, while those with very low Γ (e.g. AGN) grow over many disk lifetimes, and tend to harbor thin disks with little mass relative to the central object. We consider characteristic values for our parameters in §5.2.1, and their evolution in the isothermal collapse of a rigidly rotating Bonnor-Ebert sphere in §5.8.1.

The parameters ξ and Γ are more flexible than other dimensionless parameters used to characterize collapsing cores like $\alpha_{\rm therm} = E_{\rm therm}/E_{\rm grav}$ and $\beta_{\rm rot} = E_{\rm rot}/E_{\rm grav}$ (Bodenheimer et al., 1980; Miyama et al., 1984). While the latter rely implicitly on a quasi-static core model, ξ and Γ can be evaluated for arbitrary infall models, and therefore for a wider range astrophysical disk scenarios. Whereas $\alpha_{\rm therm}$ and $\beta_{\rm rot}$ are zero dimensional descriptions of the collapse problem, ξ and Γ can be functions of mass and hence describe time (or scale) evolution.

In order to model disk behavior in terms of these two parameters, we hold ξ and Γ fixed for each experiment via the self-similar collapse of a rotating, isothermal sphere (§5.3.2). This strategy allows us to map directly between the input parameters, and relevant properties of the system. Specifically, we expect dimensionless properties like the disk-to-star mass ratio, Toomre parameter, $Q = c_s\Omega/(\pi G\Sigma)$ (Toomre, 1964), stellar multiplicity, etc., to fluctuate around well-defined mean values (see §5.3.4).

We aim to use our parameters ξ and Γ to: (a) explore the parameter space relevant to a range of star formation scenarios; (b) better understand the disk parameters, both locally and globally, which dictate the disk accretion rate and fragmentation properties; (c) make predictions for disk behavior based on larger scale, observable quantities; and (d) allow the results of more complicated and computationally expensive simulations to be extended into other regimes.

5.2.1 Characteristic values of the accretion parameters

We base our estimates of Γ and ξ on observations of core rotation in low-mass and massive star-forming regions (Myers & Fuller, 1992; Goodman et al., 1993; Williams & Myers, 1999), as well as the analytical estimates of core rotation and disk temperature in Matzner & Levin (2005), Krumholz (2006), KM06, and KMK08. Using simple models of core collapse in which angular momentum is conserved in the collapse process and part of the matter is cast away by protostellar outflows (Matzner & McKee, 2000), we find that both ξ and Γ are higher in massive star formation than in low-mass star formation. In our models, the characteristic value of Γ rises from $\sim 0.001 - 0.03$ as one considers increasingly massive cores for which turbulence is a larger fraction of the initial support.

The value of ξ is more complicated, as it reflects the disk's thermal state as well as infalling accretion rate, but the models of KMK08 and Krumholz (2006) indicate that its characteristic value increases from < 1 to ~ 10 as one considers higher and higher mass

cores – although the specific epoch in the core's accretion history is also important. In the case of massive stars, such rapid accretion has been observed as in Beltrán et al. (2006) and Barnes et al. (2008). Numerical simulations also find rapid accretion rates from cores to disks. Simulations such as those of Banerjee & Pudritz (2007) report $\xi \sim 10$ at early times in both magnetized and non-magnetized models. We note that Γ has significant fluctuations from core to core when turbulence is the source of rotation, and both ξ and Γ are affected by variations of the core accretion rate around its characteristic value (Foster & Chevalier, 1993).

A major goal of this work is to probe the evolution of disks with $\xi \geq 1$, as mass accretion at this rate cannot be accommodated by the Shakura & Sunyaev (1973) model with $\alpha < 1$. Values of α exceeding unity imply very strong GI, and possibly fragmentation.

5.3 Numerical Methodology

5.3.1 Numerical Code

We use the code ORION (Truelove et al., 1998; Klein, 1999; Fisher, 2002) to conduct our numerical experiments . ORION is a parallel adaptive mesh refinement (AMR), multi-fluid, radiation-hydrodynamics code with self-gravity and lagrangian sink particles (Krumholz et al. 2004). Radiation transport and multi-fluids are not used in the present study. The gravito-hydrodynamic equations are solved using a conservative, Godunov scheme, which is second order accurate in both space and time. The gravito-hydrodynamic equations are:

$$\frac{\partial}{\partial t}\rho = -\nabla \cdot (\rho \mathbf{v}) - \sum_i \dot{M}_i W(\mathbf{x} - \mathbf{x}_i) \tag{5.3}$$

$$\begin{aligned} \frac{\partial}{\partial t}(\rho \mathbf{v}) &= -\nabla \cdot (\rho \mathbf{v}\mathbf{v}) - \nabla P - \rho \nabla \phi \\ &- \sum_i \dot{\mathbf{p}}_i W(\mathbf{x} - \mathbf{x}_i) \end{aligned} \tag{5.4}$$

$$\begin{aligned} \frac{\partial}{\partial t}(\rho e) &= -\nabla \cdot [(\rho e + P)\mathbf{v}] + \rho \mathbf{v} \cdot \nabla \phi \\ &- \sum_i \dot{\mathcal{E}}_i W(\mathbf{x} - \mathbf{x}_i) \end{aligned} \tag{5.5}$$

Equations (5.3)-(5.6) are the equations of mass, momentum and energy conservation respectively. In the equations above, $\dot{M}_i$, $\dot{\mathbf{p}}_i$, and $\dot{\mathcal{E}}_i$ describe the rate at which mass and

momentum are transfered from the gas onto the ith lagrangian sink particles. Summations in these equations are over all sink particles present in the calculation. $W(\mathbf{x})$ is a weighting function that defines the spatial region over which the particles interact with gas. The corresponding evolution equations for sink particles are

$$\frac{d}{dt}M = \dot{M}_i \tag{5.6}$$

$$\frac{d}{dt}\mathbf{x}_i = \frac{\mathbf{p}_i}{M_i} \tag{5.7}$$

$$\frac{d}{dt}\mathbf{p}_i = -M_i\nabla\phi + \dot{\mathbf{p}}_i. \tag{5.8}$$

These equations describe the motion of the point particles under the influence of gravity while accreting mass and momentum from the surrounding gas.

The Poisson equation is solved by multilevel elliptic solvers via the multigrid method. The potential ϕ is given by the Poisson equation

$$\nabla^2\phi = 4\pi G\left[\rho + \sum_i M_i\delta(\mathbf{x}-\mathbf{x}_i)\right], \tag{5.9}$$

and the gas pressure P is given by

$$P = \frac{\rho k_{\rm B}T_{\rm g}}{\mu_p} = (\gamma-1)\rho\left(e - \frac{1}{2}v^2\right), \tag{5.10}$$

where $T_{\rm g}$ is the gas temperature, μ_p is the mean particle mass, and γ is the ratio of specific heats in the gas. We adopt $\mu_p = 2.33m_{\rm H}$, which is appropriate for standard cosmic abundances of a gas of molecular hydrogen and helium.

We use the sink particle implementation described in Krumholz et al. (2004) to replace cells which become too dense to resolve. Sink particle creation and AMR grid refinement are based on the Truelove criterion (Truelove et al., 1997) which defines the maximum density that can be well resolved in a grid code as:

$$\rho < \rho_j = \frac{N_J^2\pi c_s^2}{G(\Delta x^l)^2}, \tag{5.11}$$

where, N_J is the Jeans number, here set to 0.125 for refinement, and 0.25 for sink creation, and Δx^l is the cell size on level l. When a cell violates the Jeans criterion, the local region is refined to the next highest grid level. If the violation occurs on the maximum level specified in the simulation, a sink particle is formed. Setting N_J to 0.125 is also consistent with the resolution criterion in Nelson (2006). Sink particles within 4 cells

of each other are merged in order to suppress unphysical n-body interactions due to limited resolution. At low resolution, unphysical sink particle formation and merging can cause rapid advection of sink particles inwards onto the central star, generating spurious accretion. Moreover, because an isothermal, rotating gas filament will collapse infinitely to a line (Truelove et al., 1997; Inutsuka & Miyama, 1992), an entire spiral arm can fragment and be merged into a single sink particle. To alleviate this problem, we implement a small barotropic switch in the gas equation of state such that

$$\gamma = 1.0001, \ \rho < \rho_{J^s}/4 \tag{5.12}$$

$$\gamma = 1.28, \ \rho_{J^s}/4 < \rho < \rho_{J^s}, \tag{5.13}$$

where the J^s subscript indicates the Jean's criterion used for sink formation. With this prescription, gas is almost exactly isothermal until fragmentation is imminent, at which point it stiffens somewhat. This modest stiffening helps turn linear filaments into resolved spheres just prior to collapse and provides separation between newborn sink particles. The primary effect of this stiffening is to increase the resolution of the most unstable wavelength in a given simulation, at the expense of some dynamical range. We describe the influence of this stiffening on our results in §5.7.1, where we conduct some experiments in which it is turned off.

As described via equations (5.3)-(5.6), sink particles both accrete from and interact with the gas and each other via gravity. Accretion rates are computed using a modified Bondi-Hoyle formula which prevents gas which is not gravitationally bound to the particles from accreting. See Krumholz et al. (2004) and Offner et al. (2008) for a detailed study of the effects of sink particle parameters. Note that we also use a secondary, spatial criterion for AMR refinement based on an analytic prediction for the disk size as a function of time (see §5.3.3).

5.3.2 Initial conditions

We initialize each run with an isothermal sphere:

$$\rho(r) = \frac{A c_{s,\mathrm{core}}^2}{4\pi G r^2}. \tag{5.14}$$

There is a small amount of rotational motion in our initial conditions, but no radial motion. A core with this profile is out of virial balance when $A > 2$, and accretes at a

rate

$$\dot{M} = \frac{c_{s,\mathrm{core}}^3}{G} \times \begin{cases} 0.975, & (A = 2) \\ (2A)^{3/2}/\pi. & (A \gg 2) \end{cases} \tag{5.15}$$

The value for $A = 2$ represents the Shu (1977b) inside-out collapse solution, whereas the limit $A \gg 2$ is derived assuming pressureless collapse of each mass shell. It is possible to predict $\dot{M}$ analytically (Shu, 1977b), but in practice we initialize our simulations with a range of values $A > 2$ and measure $\dot{M}$ just outside the disk. Because our equation of state is isothermal up to densities well above the typical disk density ($c_{s,d} = c_{s,\mathrm{core}}$), $\dot{M}G/c_{s,\mathrm{core}}^3$ is equivalent to our parameter ξ.

In order to set the value of our rotational parameter Γ and hold it fixed, we initialize our cores with a constant, subsonic rotational velocity:

$$v_{\mathrm{rot}} = \varpi\Omega = 2Ac_s \left(\frac{\Gamma}{\xi}\right)^{1/3}, \tag{5.16}$$

where ϖ is the cylindrical radius. We arbitrarily choose a constant velocity rather than rigid rotation on spheres in order to concentrate accretion near the outer disk radii. Our definition of Γ in terms of the mean value of j_{in} rather than its maximum value is intended to reduce the sensitivity of our results to the choice of rotational profile.

Given these initial conditions, our parameters ξ and Γ remain constant throughout the simulation, while the collapsed mass and disk radius (as determined by the Keplerian circularization radius of the infalling material) increase linearly with time. We define a resolution parameter,

$$\lambda = \frac{R_{\mathrm{k,in}}}{dx_{\mathrm{min}}}, \tag{5.17}$$

to quantify the influence of numerics on our results. Because we hold the minimum grid spacing dx_{min} constant, λ increases $\propto t$ as the simulation progresses.

By artificially controlling the infall parameters of our disks, and then watching them evolve in resolution, we gain insight into the physical behavior of accretion with certain values of ξ and Γ, as captured in a numerical simulation with a given dynamical range (λ). Our initial conditions are necessarily ideal, allowing us to perform controlled experiments. That we use a "core model" at all is purely for numerical convenience. Realistic star-forming cores will undoubtedly look very different with turbulence, and time varying accretion of mass and angular momentum, but before addressing more complicated scenarios we must establish the predictive value of our parameters.

5.3.3 Domain and Resolution

Due to the dimensionless nature of these experiments, we do not use physical units to analyze our runs. The base computational grid is 128^3 cells, and for standard runs we use nine levels of refinement, with a factor of two increase in resolution per level: this gives an effective resolution of $65,536^3$. More relevant to our results, however, is the resolution with which our disks are resolved: $\lambda \lesssim 10^2$. To compare this to relevant scales in star formation, this is equivalent to sub-AU resolution in disks of $\sim 50 - 100$ AU.

The initial core has a diameter equal to one half of the full grid on the base level. The gravity solver obeys periodic boundary conditions on the largest scale; as the disk is 2.5 to 3 orders of magnitude smaller than the grid boundaries, disk dynamics are unaffected by this choice. The initial radius of the current infall is $(\pi\Gamma)^{-2/3} R_{\rm k,in}$ (from equations (5.2), (5.14), and (5.15)); although this is much larger than the disk itself, it is still $\sim 15 - 40$ times smaller than the initial core and $\sim 30 - 80$ times smaller than the base grid. Tidal distortions of the infall are therefore very small, although they may be the dominant seeds for the GI. We return to this issue in §5.7.3, where we compare two runs in which only the tidal effects should be different.

In addition to the density criterion for grid refinement described in §5.3, we also refine spatially to ensure that the entire disk is resolved at the highest grid level. We use ξ and Γ to predict the outer disk radius (see §5.4), and refine to the highest resolution within 1.5 times this radius horizontally, and within 0.4 times this radius vertically. We find that we accurately capture the vertical and radial extent of the disk with this prescription, and the density criterion ensures that any matter at disk-densities extending beyond these radii will automatically be refined.

5.3.4 Dynamical Self-Similarity

Because our goal is to conduct a parameter study isolating the effects of our parameters ξ and Γ, we hold each fixed during a single run. At a given resolution λ, we expect the simulation to produce consistent results regarding the behavior of the accretion disk, the role of GI, and the fragmentation of our idealized disks into binary or multiple stars. Since λ increases linearly in time, each simulation serves as a resolution study in which numerical effects diminish in importance as the run progresses. Because GI is an intrinsically unsteady phenomenon, a disk should fluctuate around its mean values even when all three of Γ, ξ, and λ are fixed. Because of this, and because λ changes over the

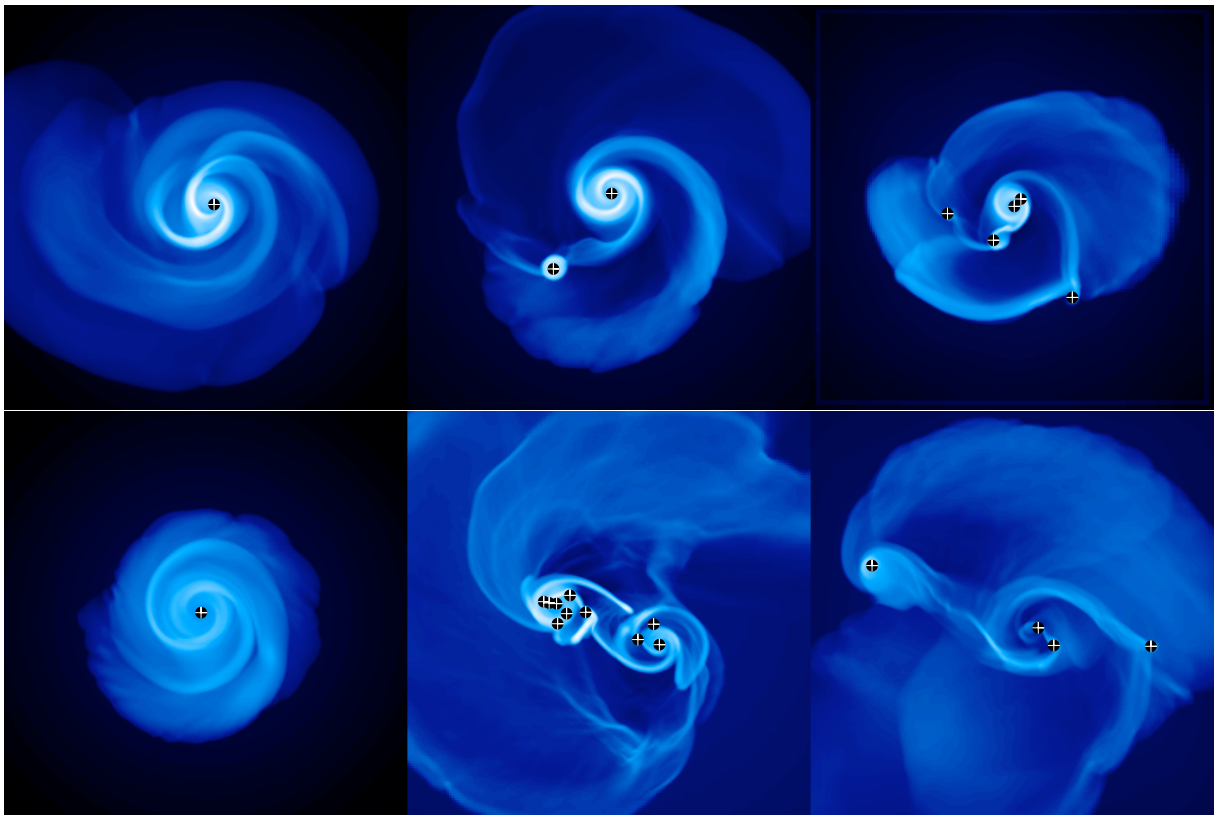

Figure 5.1: Two examples of single, binary, and multiple systems. The resolution across each panel is 328x328 grid cells. The single runs are $\xi = 2.9, \Gamma = 0.018$ (top), $\xi = 1.6, \Gamma = 0.009$ (bottom). The binaries are $\xi = 4.2, \Gamma = 0.014$ (top), $\xi = 23.4, \Gamma = 0.008$, (bottom). The multiples are $\xi = 3.0, \Gamma = 0.016$ (top), $\xi = 2.4, \Gamma = 0.01$ (bottom). Black circles with plus signs indicate the locations of sink particles. These correspond to runs 5, 1, 9, 16, 7, and 4 respectively.

run, we expect our runs to be self-similar, but only in a limited, statistical sense.

Moreover, whereas many physical systems are captured perfectly in the limit of infinite resolution ($\lambda \to \infty$), this is not true of isothermal, gravitational gas dynamics, in which the minimum mass and spacing of fragments both scale as λ^{-1} (Inutsuka & Miyama, 1992). For this reason we quote the resolution λ whenever reporting on the state of the disk-star system.

We note that there exists a minimum scale in real accretion disks as well, namely the opacity-limited minimum fragment mass (Rees, 1976). The finite dynamical range of our numerical simulations is therefore analogous to a phenomenon of Nature, albeit for entirely different reasons.

5.4 Disk properties in terms of the accretion parameters

To assess the physical importance of ξ and Γ, it is useful to consider the case of a single star and its accretion disk. Because many ξ, Γ pairs lead to fragmentation, this assumption is only self-consistent within a subregion of our parameter space; nevertheless it helps to guide our interpretation of the numerical results. In order to associate results from our parameters with those of previous studies, we also derive expressions for disk averaged quantities such as Q and the disk-to-system mass ratio, μ as a function of ξ and Γ.

The combination

$$\left(\frac{\Gamma}{\xi}\right)^{1/3} = \frac{\langle j \rangle_{\rm in} c_{s,d}}{G M_{*d}} = \frac{c_{s,d}}{v_{\rm k,in}} \tag{5.18}$$

is particularly useful, since it provides an estimate for the disk's aspect ratio (the scale height compared to the circularization radius). Being independent of $\dot{M}$, it is more a property of the disk than of the accretion flow.

The other important dimensionless quantity whose mean value depends primarily on ξ and Γ (and slowly on resolution) is the disk-to-system mass ratio

$$\mu = \frac{M_d}{M_{*d}}. \tag{5.19}$$

When the disk is the sole repository of angular momentum, the specific angular momentum stored in the disk is related to the infalling angular momentum via:

$$j_d = \left(\frac{J_{\rm in}}{\langle j \rangle_{\rm in} M_{*d}}\right) \frac{\langle j \rangle_{\rm in}}{\mu} \tag{5.20}$$

where $J_{\rm in}$ is the total angular momentum accreted, so that $J_{\rm in}/(\langle j \rangle_{\rm in} M_{*d}) = 1/(l_j + 1)$ in an accretion scenario where $\langle j \rangle_{\rm in} \propto M_{*d}^{l_j}$. In our simulations $l_j = 1$, so $j_d = \langle j \rangle_{\rm in} /(2\mu)$. Given the relation between j_d and $\langle j \rangle_{\rm in}$, we can define

$$\begin{aligned} R_d &= [(l_j+1)\mu]^{-2} R_{\rm k,in} \\ \Omega_d &= [(l_j+1)\mu]^{3} \Omega_{\rm k,in} \end{aligned} \tag{5.21}$$

which relate the disk's characteristic quantities (*not* the location of its outer edge) to conditions at the current circularization radius $R_{\rm k,in} = \langle j \rangle_{\rm in}^2 /(G M_{*d})$. Such "characteristic" quantities are valuable for describing properties of the disk as a whole, rather than at single location, with an effective mass weighting. If we further suppose that

the disk's column density varies with radius as $\Sigma(r) \propto r^{-k_\Sigma}$ (we expect $k_\Sigma \simeq 3/2$ for a constant Q, isothermal disk), we may define its characteristic column density $\Sigma_d = (1 - k_\Sigma/2)M_d/(\pi R_d^2)$:

$$\Sigma_d \simeq f_\Sigma \frac{G^2 M_{*d}^3}{\langle j \rangle_{\rm in}^4} \mu^5 \tag{5.22}$$

where $f_\Sigma = (1 - k_\Sigma/2)(1 + l_j)^4/\pi$. Using equations (5.18) and (5.21)-(5.22), we can rewrite the Toomre stability parameter Q (ignoring the difference between Ω and the epicyclic frequency,κ, for simplicity):

$$Q = \frac{c_s \kappa}{\pi G \Sigma} \rightarrow \frac{c_s \Omega_d}{\pi G \Sigma_d} \tag{5.23}$$

$$\begin{aligned} Q_d &\simeq \frac{f_Q^{-1}}{\mu^2} \frac{c_{s,d} \langle j \rangle_{\rm in}}{G M_{*d}} \\ &= \left(\frac{\Gamma}{\xi}\right)^{1/3} \frac{f_Q^{-1}}{\mu^2}. \end{aligned} \tag{5.24}$$

where $f_Q = (1 - k_\Sigma/2)(1 + l_j)$. To the extent that we expect $Q_d \sim 1$ in any disk with a strong GI, this suggests $\mu \sim (\Gamma/\xi)^{1/6}(1 - k_\Sigma/2)^{-1/2}(1 + l_j)^{-1/2}$; and because we expect that μ has an upper limit of around 0.5 (see §5.5 and discussion in KMK08 and Shu et al., 1990), we see there is an upper limit to ξ/Γ above which the system is likely to become binary or multiple. This is not surprising, as μ is proportional to scale height when Q is constant; equation (5.24) simply accounts self-consistently for the fact that μ also affects R_d.

To go any further with analytical arguments, we must introduce a Shakura & Sunyaev (1973) α viscosity parameterization, in which steady accretion occurs at a rate

$$\dot{M}_* = \frac{3\alpha}{Q_d} \frac{c_{\rm s,d}^3}{G} \tag{5.25}$$

Using the definition of ξ

$$\xi \simeq \frac{3\alpha}{Q_d} \frac{1}{1 - \mu} \tag{5.26}$$

Insofar as $Q \sim 1$ when the GI is active, the effective value of α induced by a strong GI is directly proportional to ξ. We have made the simplifying assumption that accretion through the disk is roughly constant, although the factor of $(1 - \mu)$ accounts for the difference between the infall rate and the rate at which the disk processes material onto the star.

The magnitude of Γ has important implications for disk evolution. As discussed previously by KMK08, Γ (called $\Re_{\rm in}$ there) affects μ through the relation

$$\begin{aligned}\frac{\dot{\mu}}{\mu\Omega_{\rm k,in}} &= \Gamma\left(\frac{1}{\mu}-1\right)-\frac{\dot{M}_*}{M_d\Omega_{\rm k,in}}. \\ &\simeq \Gamma\left(\frac{1}{\mu}-1\right)-3\left(1-\frac{k_\Sigma}{2}\right)(1+l_j)\alpha\mu\left(\frac{\Gamma}{\xi}\right)^{2/3},\end{aligned} \tag{5.27}$$

where the second line uses disk-averaged quantities to construct a mean accretion rate from equation (5.25). Our runs approach a statistical steady state, $\dot{\mu}\simeq 0$ (although the dimensional quantity M_d continues to increase.) We expect μ to saturate at the value for which the two terms on the right of equation (5.27) are equal,

$$\mu\rightarrow(B^2+2B)^{1/2}-B,\quad\text{where}\quad B=\frac{\Gamma^{1/3}\xi^{2/3}}{3(2-k_\Sigma)(1+l_j)\alpha}. \tag{5.28}$$

Here B is the linear coefficient for the quadratic in equation (5.27). The disk mass fraction μ increases with B, so both Γ and ξ have a positive effect on μ, whereas α tends to suppress the disk mass.

The scaling of disk properties with ξ is in accord with intuitive expectations. An increase in ξ corresponds to an increase in accretion rate at fixed disk sound speed, and as a result the equilibrium disk mass rises. Similarly, an increase in α corresponds to an increase in the rate at which the disk can transport angular momentum and mass at a fixed rate of mass and angular momentum inflow, allowing the disk to drain and reducing its relative mass.

Less intuitive, however, is the fact that equations (5.24) and (5.28) predict that rotation has a *stabilizing* effect on massive disk systems, in the sense that Q_d increases with Γ so long as $\mu>0$. This can be seen by noting that $d\ln\mu/d\ln B=(1-\mu)/(2-\mu)$. Note that, when B is small and $\mu\simeq\sqrt{2B}$, equation (5.23) implies $Q_d\simeq 3\alpha/\xi$ in accordance with equation (5.25). Thus for small values of μ, we recover the dependence of Q solely on ξ, in accord with Gammie (2001). As μ grows and saturates, Γ becomes more important in setting Q. We discuss the stabilizing influence of Γ in §5.5.3.

Because the effective value of α induced by the GI is a function of disk parameters, we cannot say more without invoking a model for $\alpha(\Gamma,\xi)$ or $\alpha(Q,\mu)$ as in KMK08. We use the above relations to guide our interpretation of our simulation results, specifically the dependence of disk parameters like μ, Q_d, α, and the fragmentation boundary, on ξ and Γ.

5.5 Results

Each of our runs produces either a disk surrounding a single star, or binary or multiple star system formed via disk fragmentation; Figure 5.1 depicts examples of each outcome. We use these three possible morphologies to organize our description of the experiments. We explore the properties of each type of disk below as well as examine the conditions at the time of fragmentation.

The division between single and fragmenting disks in ξ and Γ is relatively clear from our results, as shown in Figure 5.2. Several trends are easily identified. First, there is a critical ξ beyond which disks fragment independent of the value of Γ. Below this critical ξ value, there is a weak stabilizing effect of increasing Γ. As ξ increases, disks transition from singles in to multiples, and finally into binaries. We discuss the distinction between binaries and multiples in §5.6. This stabilizing effect of Γ is predicted by equation (5.23), although it is somewhat counter intuitive. We discuss in §5.5.3 that the stabilization is often masked thermal effects in real collapsing systems.

In table 5.1 we list properties of the final state for all of our runs, their final multiplicity (S, B, or M for single, binary, or multiple, respectively), and the disk-to-star(s) mass ratio μ_f measured at the time at which we stop each experiment, as well as the maximum resolution λ_n. Note that the disk extends somewhat beyond $R_{\rm k,in}$: therefore the disk as a whole is somewhat better resolved than the value of λ_n would suggest. For the disks which fragment, we also list the value of μ_f, λ_f and Q just before fragmentation occurs.

In table 5.2 we describe those disks which do not fragment: we list the analytic estimate for the characteristic value Toomre's Q, Q_d, the measured minimum of Q_{2D} (equation 5.29), the radial power law k_Σ which characterizes $\Sigma(r)$ for a range of radii extending from the accretion zone of the inner sink particle to the circularization radius $R_{\rm k,in}$, the final disk resolution, λ_n, and the characteristic disk radius, R_d (equation (5.21).

5.5.1 The Fragmentation Boundary and Q

It is difficult to measure a single value of Q to characterize a disk strongly perturbed by GI, so we consider two estimates: a two dimensional measurement $Q_{\rm 2D}$, and a one-dimensional measure $Q_{\rm av}(r)$ based on azimuthally-averaged quantities.

$$Q_{\rm 2D}(r,\phi) = \frac{c_s \kappa}{\pi G \Sigma}, \tag{5.29}$$

#	ξ	$10^2\Gamma$	N_*	μ_f	λ_f	Q_{2D}	μ	λ_n
1	1.6	0.9	S	...	...	...	0.49	99
2	1.9	0.8	S	...	...	...	0.40	88
3	2.2	2.5	S	...	...	...	0.56	82
4	2.4	1.0	M	0.43	77	0.69	0.16	98
5	2.9	1.8	S	...	...	...	0.53	86
6	2.9	0.8	M	0.40	51	0.72	0.14	78
7	3.0	0.4	M	0.33	50	0.48	0.11	77
8	3.4	0.7	M	0.40	66	0.37	0.16	70
9	4.2	1.4	B	0.51	56	0.19	0.33	72
10	4.6	2.1	M	0.54	71	0.42	0.23	123
11	4.6	0.7	B	0.35	28	0.52	0.12	52
12	4.9	0.9	B	0.37	26	0.74	0.19	59
13	5.4	0.4	B	0.38	38	0.33	0.19	64
14	5.4	0.7	B	0.31	49	0.85	0.21	62
15	5.4	7.5	B	0.72	99	0.20	0.59	129
16*	23.4	0.8	B	0.25	5	0.83	0.10	84
17*	24.9	0.4	B	0.15	3	0.59	0.11	61
18*	41.2	0.8	B	0.13	5	1.33	0.10	58

Table 5.1: Each run is labelled by ξ, Γ, multiplicity outcome, the final value of the disk-to-star(s) mass ratio,μ and the final resolution, λ_n. Values of Γ are quoted in units of 10^{-2}. For fragmenting runs the disk resolution λ_f, Q_{2D} (equation 5.29) and μ_f at the time of fragmentation are listed as well. S runs are single objects with no physical fragmentation. B's are binaries which form two distinct objects each with a disk, and M are those with three or more stars which survive for many orbits. * indicates runs which are not sufficiently well resolved at the time of fragmentation to make meaningful measures of μ_f, and Q.

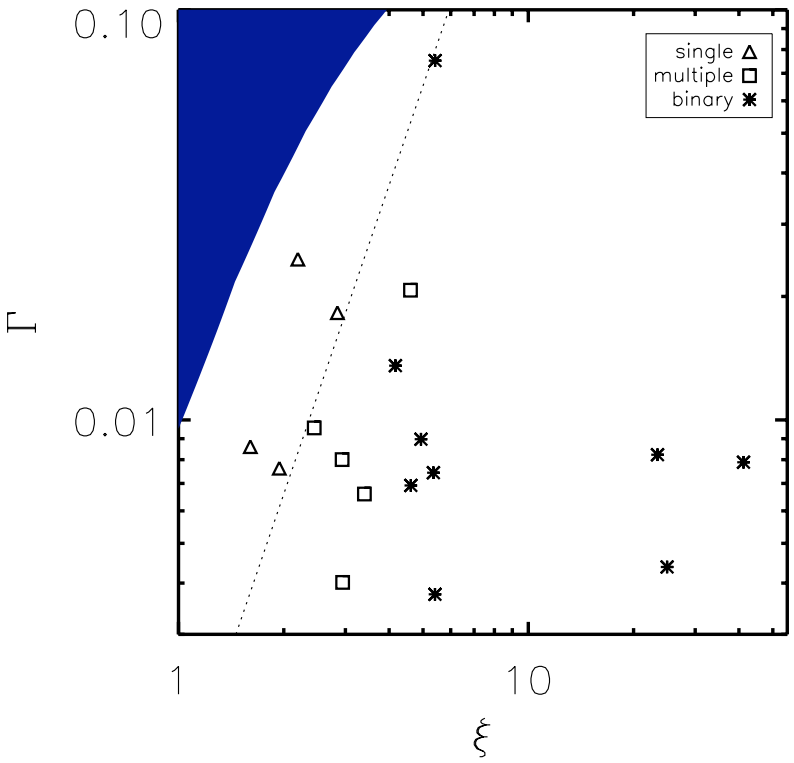

Figure 5.2: Distribution of runs in $\xi - \Gamma$ parameter space. The single stars are confined to the low ξ region of parameters space, although increasing Γ has a small stabilizing effect near the transition around $\xi = 2$ due to the increasing ability of the disk to store mass at higher values of Γ. The dotted line shows the division between single and fragmenting disks: $\Gamma = \xi^{2.5}/850$. As ξ increases disks fragment to form multiple systems. At even higher values of ξ disks fragment to make binaries. We discuss the distinction between different types of multiples in §5.6. The shaded region of parameter space shows where isothermal cores no longer collapse due to the extra support from rotation.

#	ξ	$10^2\Gamma$	μ	Q_d	Q_{2D}	k_Σ	λ_n	R_d
1	1.6	0.9	0.49	1.6	0.96	1.5	99	103
2	1.9	0.8	0.40	1.5	1.10	1.3	88	138
3	2.2	2.5	0.56	3.7	0.83	1.8	82	65
5	2.9	1.8	0.53	2.2	0.56	1.7	86	77

Table 5.2: Non-fragmenting runs (numbers as from table 5.1). We list values for the characteristic predicted value of Toomre's Q, Q_d (equation 5.23), as well as the measured disk minimum, Q_{2D} equation (5.29). We also list the slope of the surface density profile, k_Σ averaged over several disk orbits, the final resolutions, and R_d at the end of the run (equation 5.21)

$$Q_{\rm av}(r) \quad = \quad \frac{\bar{c}_s(r)\bar{\kappa}(r)}{\pi G\bar{\Sigma}(r)} \tag{5.30}$$

where bars represent azimuthal averages, and κ is calculated directly from the gravitational potential of the disk+stars. As Figure 5.3 shows, the two-dimensional estimate shows a great deal of structure which is not captured by the azimuthal average, let alone by Q_d. Moreover, while the minimum of the averaged quantity is close to two, the two dimensional quantity drops to $Q \sim 0.3$. We find that the best predictor of fragmentation is the minimum of a smoothed version of the two-dimensional quantity (smoothed over a local Jeans length to exclude meaningless fluctuations), although Q_d shows a similar trend. We use this smoothed minimum quantity in table 5.1, and compare it to the analytic estimate Q_d in table 5.2 for non-fragmenting disks.

The critical values of Q at which fragmentation sets in depend on the exact method used for calculation (e.g. $Q_{\rm av}$ or Q_{2D}). The canonical $Q = 1$ boundary only indicates the instability of axisymmetric perturbations in razor-thin disks (Toomre, 1964). As discussed by numerous authors, the fragmentation criterion is somewhat different for thick disks (Goldreich & Lynden-Bell, 1965; Laughlin et al., 1997a, 1998), and for the growth of higher order azimuthal modes (Adams et al., 1989; Shu et al., 1990; Laughlin & Korchagin, 1996b).

Because our disks are thick, the fragmentation boundary cannot be drawn in Q-space alone. We use Q_{2D} and μ in Figure 5.4 to demarcate the fragmentation boundary. Labeled curves illustrate that the critical Q for fragmentation depends on the disk scale height (equation 5.18). At a given value of Q, a disk with a larger value of μ will have a larger aspect ratio, and will therefore be more stable. Recall from equation (5.18), that

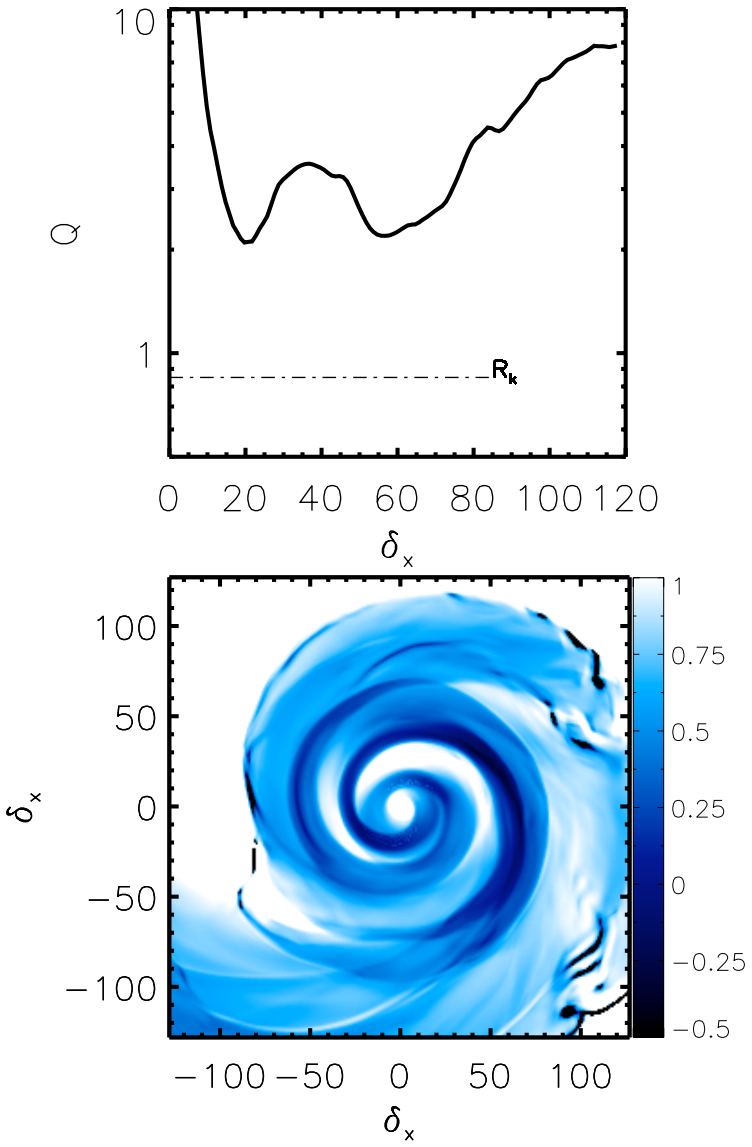

Figure 5.3: Top: $Q_{\rm av}$ in a disk with $\xi = 2.9, \Gamma = 0.018$. The current disk radius, $R_{\rm k,in}$ is shown as well. Bottom: Log(Q_{2D}) (equation 5.29) in the same disk. While the azimuthally averaged quantity changes only moderately over the extent of the disk, the full two-dimensional quantity varies widely at a given radius. Q is calculated using κ derived from the gravitational potential, which generates the artifacts observed at the edges of the disk. Here and in all figures, we use δ_x to signify the resolution.

the disk aspect ratio is proportional to $(\xi/\Gamma)^{1/3}$.

This trend is consistent with the results of Goldreich & Lynden-Bell (1965) for thick disks; because the column of material is spread out over a larger distance, H, its self-gravity is somewhat diluted. The fact that two parameters are necessary to describe fragmentation is also apparent in Figure 5.2, where the boundary between single and multiple systems is a diagonal line through the parameter space.

Although two criteria are necessary to prescribe the fragmentation boundary, we observe a direct correspondence between μ and Γ, and ξ and Toomre's Q. Figure 5.5 shows that $\mu \approx 2\Gamma^{1/3}$ for both single star disks, and just prior to the onset of fragmentation in disks that form binaries and multiples. We find a similar correspondence between ξ and the combination $Q_d\mu$, which is a direct correlation between ξ and Q defined with respect to the disk circularization radius (using R_d in the definition of Q_d brings in an extra factor of μ.)

5.5.2 Properties of non-fragmenting disks

Although we quote a single power law value for the surface density profiles of disks in table 5.2, the surface density structure is somewhat more complex. We find that the disks show some evidence of a broken power law structure: an inner region, characterized by k_Σ, where disk material is being accreted inwards, and an outer region characterized by a steep, variable power law due to the outward spread of low-density, high angular momentum material. We find disks characterized by slopes between $k_\Sigma = 1 - 2$. Clustering around $k_\Sigma = 3/2$ is expected, as this is the steady-state slope for a constant Q, isothermal disk. Our measurements of $Q(r)$ (equation 5.29) show fluctuating, but roughly constant value over the disk radius. Note that the slope of the inner disk region tends to increase with Γ. Figure 5.6 shows normalized radial profiles for the non-fragmenting disks. Profiles are averaged over approximately three disk orbital periods. The flattening at small radii is due to the increasing numerical viscosity in this region (§5.7.3).

We find an upper mass limit of $\mu \sim 0.55$, for single stars, which means that disks do not grow more massive than their central star. A maximum disk mass has been predicted by Shu et al. (1990) as a consequence of the SLING mechanism. Such an upper limit is expected as eccentric gravitational instabilities in massive disks shift the center of mass of the system away from the central object. Indeed, we observe this wobble in binary forming runs. The subsequent orbital motion of the primary object acts as an indirect

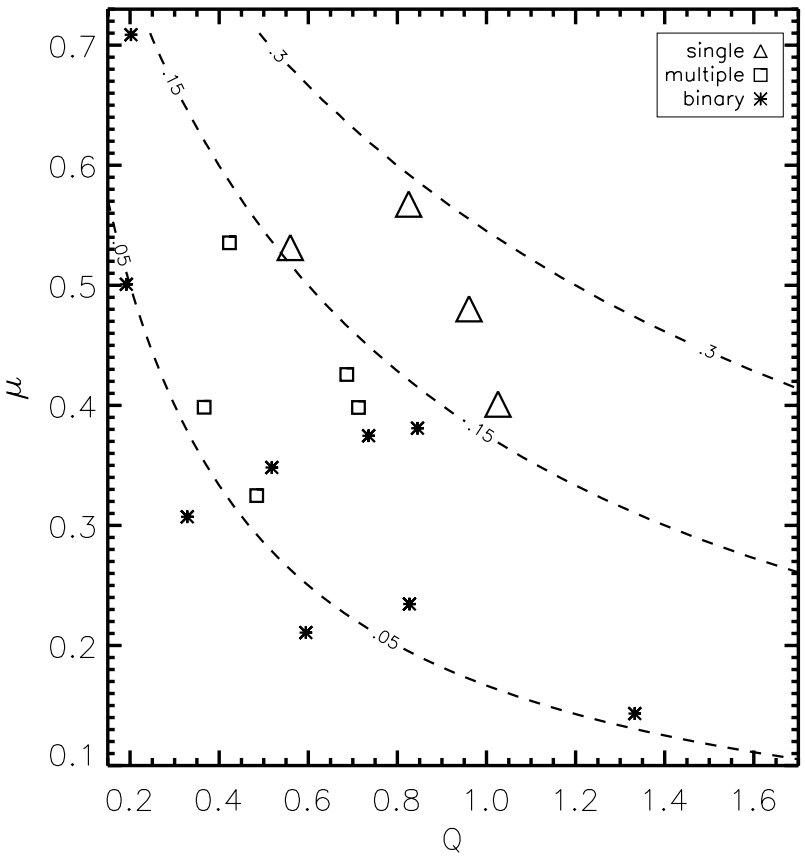

Figure 5.4: Steady-state and pre-fragmentation values of Q and μ for single stars and fragmenting disks respectively. We use the minimum of Q_{2D} as described in §5.5.1. Symbols indicate the morphological outcome. Note that the non-fragmenting disks (large triangles) have the highest value of μ for a given Q. Contours show the predicted scaleheight as a function of Q and μ. It is clear that the single disks lie at systematically higher scale heights. We have assumed $k_\Sigma = 3/2$ in calculating scaleheight contours as a function of Q and μ.

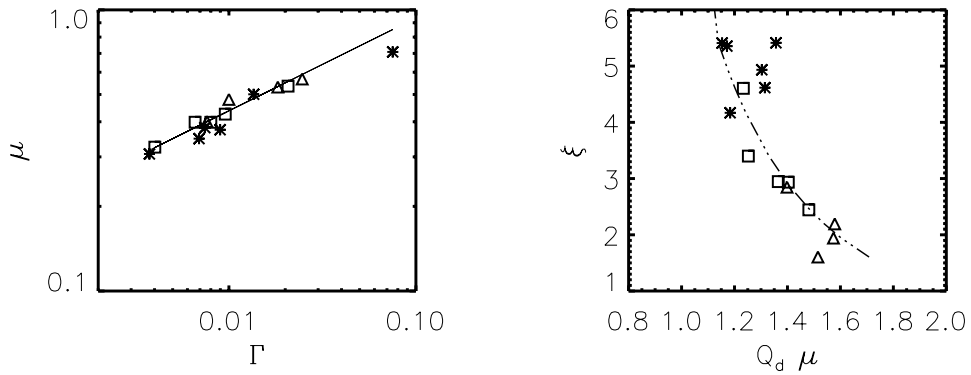

Figure 5.5: At right Γ vs μ with the fit in equation (5.31) overplotted. At left, $Q_d\mu$ vs ξ with the scaling $Q \propto \xi^{-1/3}$ overplotted. Runs, 16, 17, 18 are omitted as the low resolution at the time of fragmentation makes measurements of μ and therefore Q_d unreliable.

potential exciting strong $m = 1$ mode perturbations which can induce binary formation (Shu et al., 1990). We find that this maximum value is consistent with their prediction.

Using the analytic expressions above, we can also derive an expression for an effective Shakura-Sunyaev α. In this regime of parameter space, ξ and Γ are always such that $B \ll 1$ (assuming α does not stray far from unity). We therefore expect that $\mu \propto \Gamma^{1/6}\xi^{1/3}\alpha^{-1/2}$. Using this relation we can find a functional form of $\alpha(\xi, \Gamma)$. Our fit to the data shown in Figure 5.5 implies

$$\mu \approx 2\Gamma^{1/3}, \tag{5.31}$$

with some scatter for both single disks and fragmenting disks just prior to fragmentation. We can use this fit to infer a scaling relation for α using equation (5.28) in the limit $\mu \sim \sqrt{2B}$:

$$\alpha_d \approx \frac{1}{18(2 - k_\Sigma)^2(1 + l_j)^2} \frac{\xi^{2/3}}{\Gamma^{1/3}}. \tag{5.32}$$

The scaling is consistent with our expectation that driving the disk with a higher ξ causes it to process materially more rapidly, while increasing Γ decreases the efficiency with which the disk accretes. Equation (5.32) predicts disk averaged values of α for single star disks between $\sim 0.3 - 0.8$. These values are consistent with the observed accretion rates, and numerically calculated torques (§5.5.4).

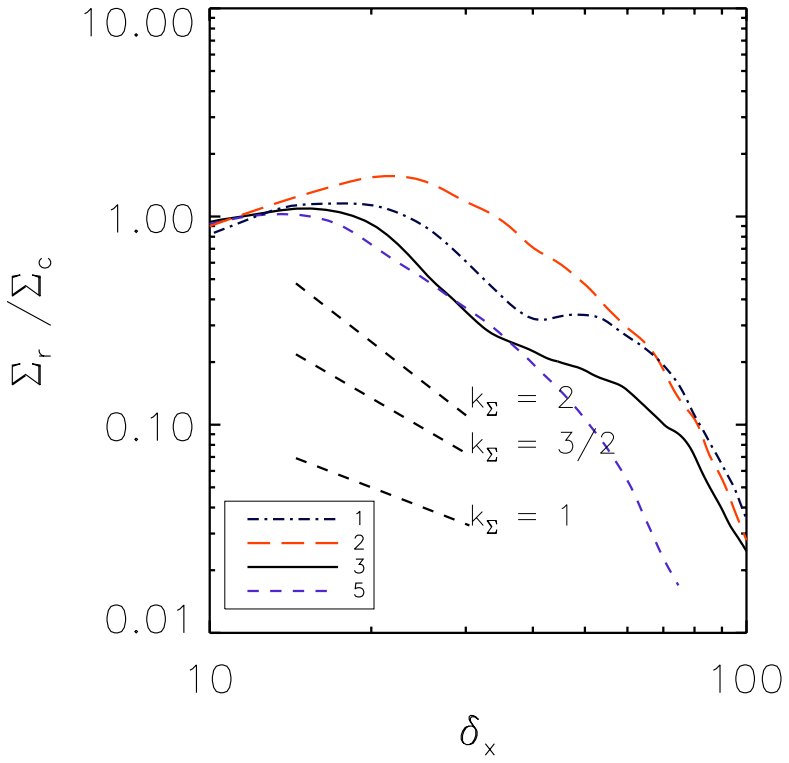

Figure 5.6: Normalized density profiles for the single-star disks. Profiles are azimuthal averages of surface densities over the final ~ 3 disk orbital periods. We find that while the inner regions are reasonably approximated by power law slopes, the slope steepens towards the disk edge. For comparison, slopes of $k_\Sigma = 1, 1.5$, and 2 are plotted as well. Runs are labelled according to their values in table 5.1.

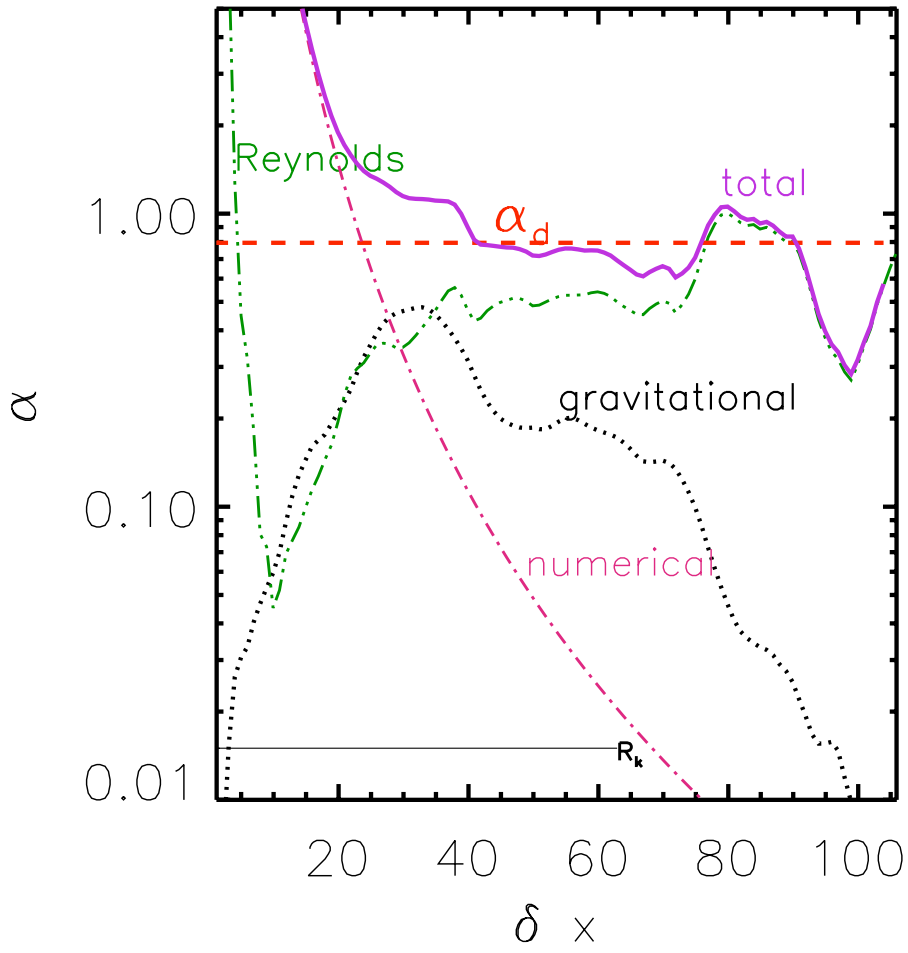

Figure 5.7: Azimuthal averages of different components of torque expressed as an effective α (equation 5.34) for run #8. The straight line, α_d (equation 5.32) is plotted for comparison. The agreement between the analytic value of α_d and the combined contribution from the other components is best near the expected disk radius $R_{\rm k,in}$.

5.5.3 The fragmentation boundary

We find that the division between fragmenting and non-fragmenting disks can be characterized by a minimum value of Γ at which disks of a given ξ are stable. In Figure 5.2 we have plotted this empirically derived boundary as $\Gamma = \xi^{2.5}/850$. Although the fragmentation boundary may be influenced by disk resolution, our analytic predictions suggest that the moderate Γ dependence is physical. This result is consistent with the findings of Tohline (1981) and Tsuribe & Inutsuka (1999a) who find cloud fragmentation below a critical value of $\alpha_{\rm therm}\beta_{\rm rot}$. For the cores which describe our initial conditions, $\alpha_{\rm therm} = 3(\xi\pi)^{-2/3}$, while $\beta_{\rm rot} = (\Gamma\pi)^{2/3}/4$. Although the mechanism for fragmentation is not identical (here fragmentation occurs after the central object has formed, in contrast to Tsuribe & Inutsuka 1999b), the $\alpha_{\rm therm}\beta_{\rm rot}$ criterion is equivalent to a restriction on $(H/R)^2$, which is related to the flatness of the collapsing core.

In disks with realistic temperature gradients, the stabilizing influence of rotation is overwhelmed by the fact that larger disks are typically colder, and have shorter cooling times relative to their orbital period, and therefore are more prone to fragmentation. In this case, more rotation does correspond to more fragmentation, as often observed (Walch et al., 2009a). However, in our models we can distinguish between the effects of temperature and disk size (angular momentum). In the absence of a temperature gradient, a larger disk will be more stable because it can store more mass at lower column densities. In addition, Γ increases the disk aspect ratio, H/R, which also lowers the critical Q threshold for fragmentation.

5.5.4 Gravitational Torques and Effective α

We verify that the accretion observed in our disks is generated by physical torques by computing the net torque in the disk. It is convenient to analyze the torques in terms of the stress tensor, $T_{R\phi}$, which is made up of two components: large scale gravitational torques and Reynolds stresses. Following Lodato & Rice (2005) we define:

$$T_{R\phi} = \int \frac{g_R g_\phi}{4\pi G} dz + \Sigma \delta \mathbf{v}_R \delta \mathbf{v}_\phi, \tag{5.33}$$

where $\delta \mathbf{v} = \mathbf{v} - \bar{v}$. In practice, we set $\delta \mathbf{v}_R = \mathbf{v}_R$, while $\delta \mathbf{v}_\phi$ is calculated with respect to the azimuthal average of the rotational velocity at each radius. In reality there is an extra viscous term attributable to numerical diffusion. We discuss the importance of this term in §5.7.3.

The first term in equation (5.33) represents torques due to large scale density fluctuations in spiral arms, while the second is due to Reynolds stresses from deviations in the velocity field from a Keplerian (or at least radial) velocity profile. To facilitate comparison with analytic models, the torques can be represented as an effective α where:

$$T_{R\phi} = \left|\frac{\mathrm{dln}\Omega}{\mathrm{dln}R}\right| \alpha \Sigma c_s^2 \tag{5.34}$$

We can compare these torques to the characteristic disk α_d in equation (5.32) at a snapshot in time. Figure 5.7 compares α_d to the azimuthal average of the physical torques for one of our runs. We also show the expected contribution from numerical diffusion (see §5.7.3). The accretion expected from these three components is consistent with the time averaged total accretion rate onto the star. Due to the short term variability of the accretion rate, the two do not match up exactly. It is interesting to note the radial dependence of the Reynolds stress term, which in the inner region decays rapidly, before rising again, due to the presence of spiral arms. In both the azimuthal average and the two dimensional distribution we see that at small radii numerical diffusion dominates, whereas at large radii deviations in the azimuthal velocity which generate Reynolds stresses are spatially correlated with the spiral arms.

5.5.5 Vertical Structure

When the disks reach sufficient resolution, we can resolve the vertical motions and structure of the disk. We defer a detailed analysis of the vertical structures to a later paper, but discuss several general trends here. Depending on the run parameters, the disk scale height is ultimately resolved by 10-25 grid cells. We observe only moderate transonic motions in the vertical direction of order $\mathcal{M} \sim 1 - 2$. Figure 5.8 shows two slices of the z-component of the velocity field for a single system, one through the X-Z plane, and the other through the disk midplane. Although there is significant substructure, the motions are mostly transonic.

We also observe a dichotomy in the vertical structure between single and binary disks. Although the values of ξ and Γ should dictate the scaleheight (see equation (5.11)), and therefore higher ξ disks which become binaries should have smaller scaleheights to begin with, we observe a transition in scaleheight when a disk fragments and becomes a binary. Large plumes seen in single disks, like those shown in Figure 5.11 contain relatively low density, high angular momentum material being flung off of the disk. The relatively sharp

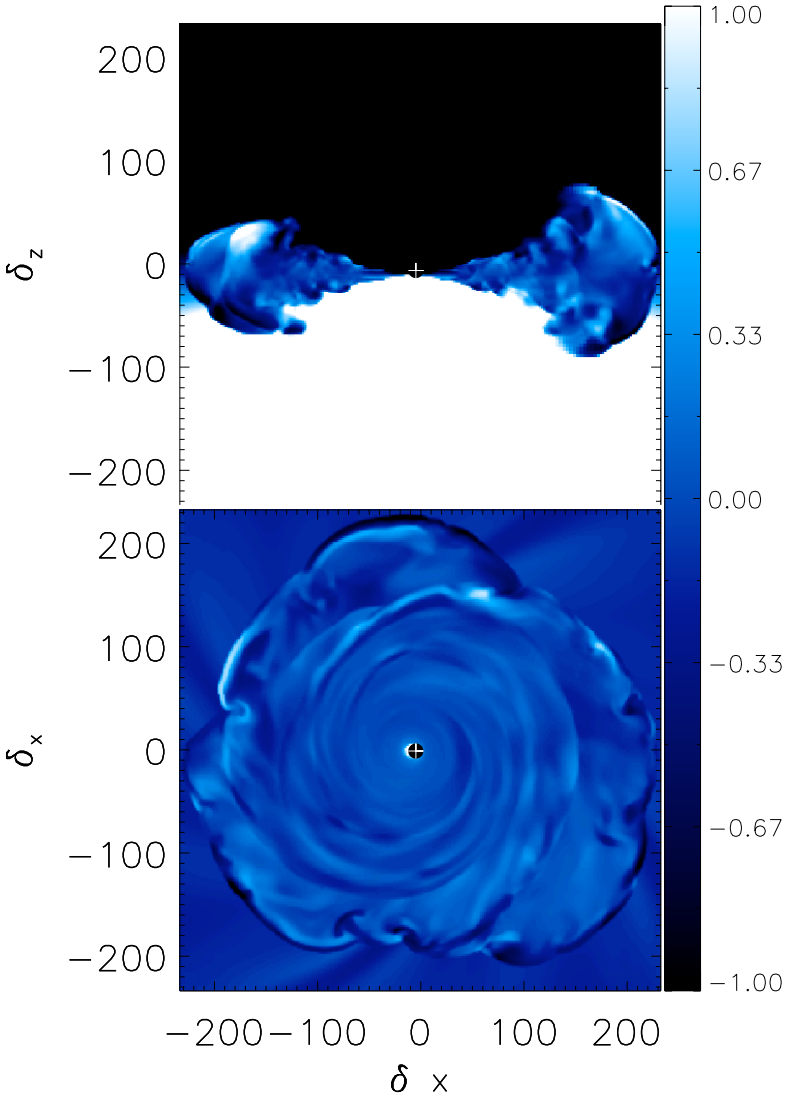

Figure 5.8: Cuts along the vertical axis and disk midplane of the vertical velocity, normalized to the disk sound speed. Clearly most of the vertical motions in the disk are transonic, although at the edges of the disk the velocities exceed $\mathcal{M} \sim 1$.

outer edges are created by the accretion shock of infalling material onto these plumes. We observe small scale circulation patterns which support these long lived structures. Disks surrounding binaries, by comparison remain relatively thin; in particular while the circumprimary disks are slightly puffier than expected from pure thermal support, the circumbinary disk (when present) is sufficiently thin that we do not consider it well resolved. This implies that the effective Γ values that binary disks see declines more than ξ according to equation (5.18). This is consistent with the statement that some of the infalling angular momentum is transferred into the orbit instead of on to the disks themselves.

5.5.6 Fourier Component Analysis

In order to characterize the accretion mechanism we compute the relative radially integrated amplitudes of the low order azimuthal modes, or C_m. We map the disk column density onto a polar grid and compute the amplitude in each fourier mode as:

$$C_m = \frac{\left| \int_0^{2\pi} \int_{r_{in}}^{r_d} \Sigma(r,\phi) r e^{-im\phi} dr d\phi \right|}{\left| \int_0^{2\pi} \int_{r_{in}}^{r_d} \Sigma(r,\phi) r dr d\phi \right|}, \tag{5.35}$$

or the absolute value of the strength in the mode normalized to the $m = 0$ mode. We find that while the relative amplitudes change in time for a given run, and vary from one run to another, the $m = 1$ and $m = 2$ modes are dominant. The power typically decreases towards higher modes, though there is some variation. The presence of strong odd-m modes is also apparent from the wobble of the central star. Binary formation due to the saturation of an $m = 1$ mode was predicted by Adams et al. (1989) and Shu et al. (1990). The SLING mechanism relies on forcing of $m = 1$ modes by the indirect potential of the moving central mass. Waves are launched at the outer Lindblad resonance, get refracted at the Q barrier surrounding corotation, propagate back out to the outer Lindblad resonance, refract again at the Q barrier, propagate out towards the disk edge, and get reflected back in (see figure 1 of Shu et al. 1990). While we see evidence for this in some disks, we are unable to confirm that this is the dominant mechanism for fragmentation in all of our disks.

To assess the effectiveness of the SLING mechanism we measured the orbital velocity of the central star about the center of mass, prior to fragmentation. As seen in Fig. 5.9, in run #14, we see clear growth of the orbital velocity (normalized to the sound speed) up until fragmentation. This same pattern is not seen in all other fragmenting runs.

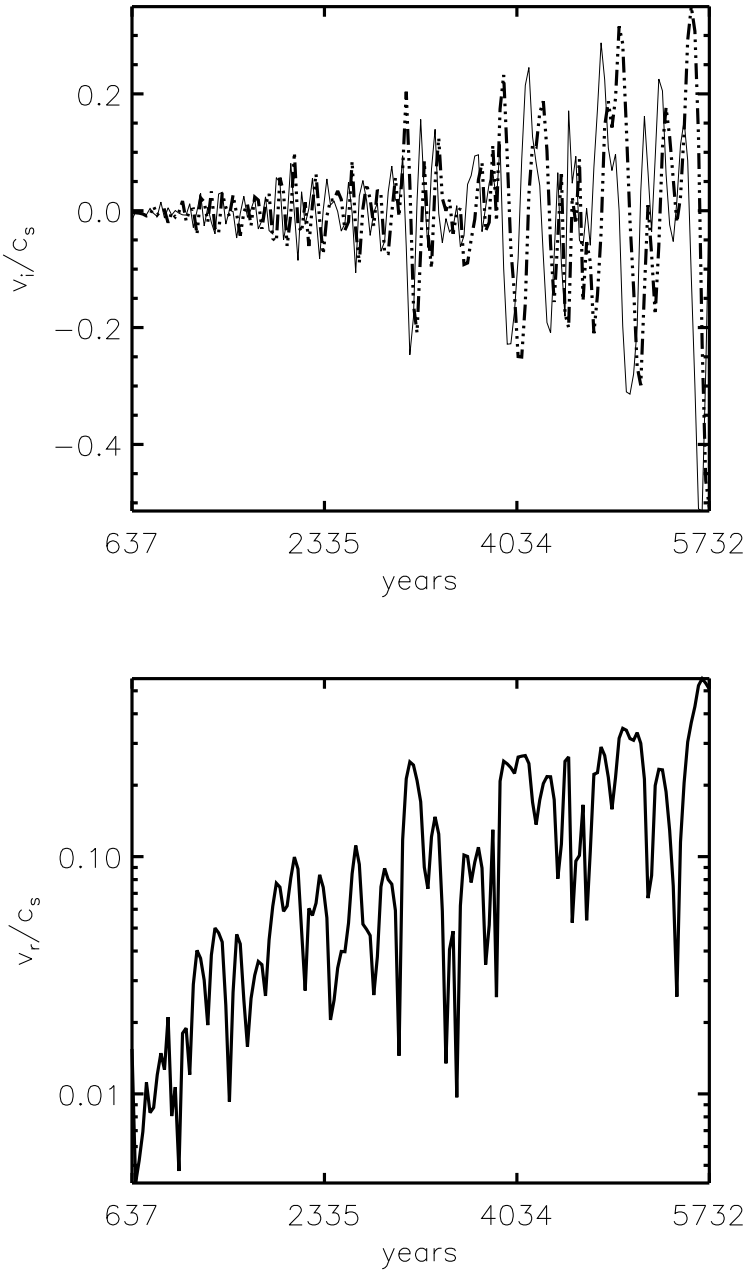

Figure 5.9: Top: the x and y components of the velocity of the central star normalized by the disk sound speed for run #14. Bottom: the combined orbital velocity of the star normalized to the sound speed. The velocity offset grows until the disk fragments.

In addition, while Adams et al. (1989) predict an upper mass limit to disks due to the SLING mechanism (of about 1/3 the central object mass) we find disk masses can grow comparable to the central star. We expect that this difference in the mass at saturation may be due to leakage of waves at the outer edge of the disks, as the SLING mechanism relies on sharp disk outer boundaries to reflect the waves.

We find that prior to binary formation, the $m = 1$ mode often grows and becomes dominant over $m = 2$, yet single star disks exist with more power in $m = 1$ than $m = 2$, and disks fragment when the $m = 2$ is dominant. In some runs there are velocity offset spikes prior to fragmentation, but most exhibit the gradual growth seen in Fig. 5.9, though the progression is less smooth.

We interpret this to be evidence that multiple modes may coexist and contribute to fragmentation, as discussed by Laughlin & Korchagin (1996b). While we do not observe the precise mode coupling that these authors describe, there appear to be some correlations between the $m = 1 - 3$ modes.

Figure 5.10 shows the mode power spectrum juxtaposed with the column density just before binary formation for runs #13 and # 8, demonstrating the appearance of disks with different dominant fourier modes.

There has been much discussion in the literature on the relative strength of global versus local modes dominating the accretion flow. Typically the assumption has been that low order modes signify globally-dominated accretion, and high order modes locally-dominated accretion (Balbus & Papaloizou, 1999; Laughlin et al., 1997b; Gammie, 2001; Adams et al., 1989; Lodato & Rice, 2005; Kratter et al., 2008). This of course depends on how tightly wound the spirals are. We can clearly observe that the structures in the disk are "global" in that they extend over more than a scale height in radius. However, because the modes do not appear to be long-lived, it is difficult to measure their wavenumbers, or the pitch angle of the spirals.

5.6 The formation of binaries and multiples

As shown by Figure 5.2, a large swath of our parameter space is characterized by binary and multiple formation. We find that the division between fragmenting and non-fragmenting disks can be characterized by a minimum value of Γ at which disks of a given ξ are stable. In Figure 5.2 we have plotted this boundary as $\Gamma = \xi^{2.5}/850$.

While we do not claim that our numerical experiments are a true representation of the

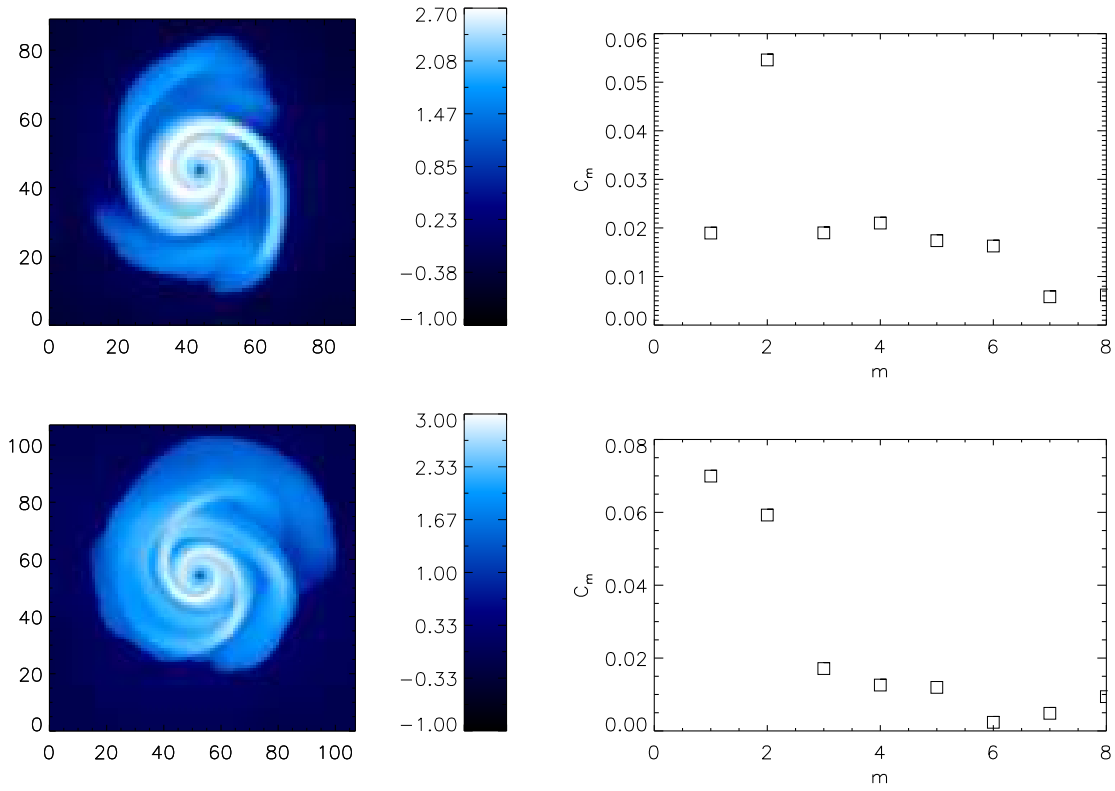

Figure 5.10: Examples of the log of the disk surface density and corresponding fourier mode strengths when an $m = 2$ mode dominates (top, run #13) and when an $m = 1$ mode dominates bottom (run #8), both within about one disk orbit of fragmentation. At bottom one can clearly see both the overall asymmetry and the pronounced $m = 2$ spiral. Note that run #8 shows a similar growth pattern to Fig. 5.9, while the top image, run #13 does not.

binary formation process, we do expect to find binaries in much of the parameter space characteristic of star formation, as nearly half of all stars are in binaries (Duquennoy & Mayor, 1991; Duchêne et al., 2007). Moreover, as the binary forming parameters are typical of higher mass star formation, where binaries and multiples are expected to comprise perhaps 75% of systems, these findings are encouraging (Mason et al., 1998, 2009). We discuss several general trends here.

Are these equal mass binaries? Low mass stellar companions? Or maybe even massive planets? In a self-similar picture it is difficult to tell. In an actively accreting multiple system, as long as the mass reservoir has angular momentum such that the circularization radius of the infalling material is comparable to the separation between objects, the smaller object, which is further from the center of mass, will accrete due to the torque imbalance (Bate & Bonnell, 1997; Bonnell & Bate, 1994b). Similarly, in thick, gravitationally unstable disks, the isolation mass approaches the stellar mass:

$$M_{\rm iso} = 4\pi f_H r_H r_d \Sigma \approx 30 \frac{f_H}{3.5} \left(\frac{H}{R}\right)^{3/2} Q^{-3/2} M_*. \tag{5.36}$$

Here, $r_H = (M_s/3M_*)^{1/3}$ is the Hill radius, M_s, and M_* are the masses of the secondary and primary, and the numerical factor f_H, represents how many Hill radii an object can feed from in the disk – numerical simulations suggest $f_H \sim 3.5$ (Lissauer, 1987; Rafikov, 2002). Therefore the evolution of these objects in our models is clear: they tend to equalize in mass. The binary separation will also grow if any of the infalling angular momentum is transferred to the orbits as opposed to the circumstellar disks. These trends are borne out in our experiments: binary mass ratios asymptote to values of $0.8 - 0.9$ and separations to $\sim 60\%$ of $R_{\rm k,in}$.

In a realistic model for star formation, the parameters that characterize a single run in this chapter will represent only one phase in the life of a newborn system. The trajectory through $\xi - \Gamma$ space which the systems take following binary formation will strongly influence the outcome in terms of separation and mass ratio. For example, should the disk stabilize and accretion trail off quickly following binary formation, it is quite likely that a large mass ratio would persist as the disk drains preferentially onto the primary object once the secondary reaches its isolation mass. By contrast, in systems which fragment before most of the final system mass has accreted, we expect more equal mass ratios.

5.6.1 Hierarchical multiples and resolution dependence

Disks which are at the low ξ end of the binary forming regime tend to form binaries at later times, and therefore at higher disk resolution. One consequence of this is the formation of hierarchical multiples. When disks become violently unstable, they fragment into multiple objects. Because of the numerical algorithm which forces sink particles within a gravitational softening length of each other to merge, at lower resolution many of these particles merge, leaving only two distinct objects behind. At higher resolution, while some of the particles ultimately merge, we find that three or four objects typically survive this process. We cannot distinguish between merging and the formation of very tight binaries. In addition to merging, small mass fragments are occasionally ejected from the system entirely. This appears be a stochastic process, though we have not done sufficient runs to confirm this conclusion.

Disks which form binaries at early times and develop two distinct disks can also evolve into multiples when each disk becomes large enough and sufficiently unstable to fragmentation. In general, once a binary forms, the system becomes characterized by new values of ξ and Γ which are less than those in the original disk. As the distribution of mass and angular momentum evolves in the new system, the relative values of ξ and Γ evolve as well. However, once the mass ratios have reached equilibrium as is the case for run #16 shown in the bottom center of Figure 5.1, each disk sees ξ of roughly half the original value, which for an initial $\xi \sim 24$ is still well into the fragmenting regime. As a result, the fact that the two disks ultimately fragment is expected. On the contrary, for the lowest ξ binary runs, once one fragmentation event occurs, the new ξ may be sufficiently low to suppress further fragmentation. The evolution of Γ in the newly formed disks is more complicated, depending on how much angular momentum is absorbed into the orbit as compared to the circumstellar disks.

It is clear that there is a numerical dependence to this phenomenon which we discuss in §5.7.3, but there is a correspondence with the physical behavior of disks as well. The radius and mass of a fragmenting disk are likely to influence the multiplicity outcome of a real system. Cores with high values of ξ that form binaries early in our numerical experiments correspond to cores whose disks fragment into binaries at small physical size scales, where the disk may only be a few fragment Hill radii wide, and contain a relatively small number of Jeans masses. It is possible that at these size scales, numerous bound clumps in a disk might well merge leaving behind a lower multiplicity system.

5.7 Caveats and Numerical Effects

5.7.1 Isothermal equation of state

Many simulations have shown the dramatic effects that thermodynamics have on disk behavior (Boss et al., 2000; Gammie, 2001; Rice et al., 2005; Lodato & Rice, 2005; Boley et al., 2006; Krumholz et al., 2007b; Offner et al., 2009a). Since we are concerned with fragmentation, we must be aware of the potential dependencies of the fragmentation boundary on cooling physics. Starting with Gammie (2001), there has been much discussion of the "cooling time constraint" that states that a disk with $Q \sim 1$ will only fragment if the cooling time is short. While this is a valuable analysis tool for predicting the evolution of a system from a snapshot and for quantifying the feedback from gravitoturbulence, for most of the protostellar disks that we are modeling, the cooling time at the location of fragmentation is short because irradiation is the dominant source of heating (D'Alessio et al., 1997; Matzner & Levin, 2005; Krumholz et al., 2007b; Kratter et al., 2008).

Passively heated disks behave more like isothermal disks than barotropic disks, because the energy generation due to viscous dissipation is small compared to the energy density due to radiation. Consequently, feedback from accretion in the midplane does not alter the disk temperature significantly. Numerical simulations such as Krumholz et al. (2007b) find that strongly irradiated disks appear locally isothermal. In fact, the morphological outcome is similar to those of Krumholz et al. (2007b) with comparable values of ξ.

Another possible concern is the lack of a radial temperature gradient, independent of the equation of state. Both passively and actively (through viscous dissipation) heated disks will be warmer at small radii. In these experiments, we find spiral arms persist in regions where the average value of Q is well above that at which instability is presumed to set in, with local values exceeding this by an order of magnitude. It seem plausible that due to the global nature of the low-m spiral modes, angular momentum transport may still occur in regions one would assume stable against GI. As discussed by Adams et al. (1989), $m = 1$ modes can have appreciable growth rates for $Q > 1$ even when the evanescent region covers as much as 70% of the disk radius. At small radii where the disk becomes stable, another mechanism for transport must take over. Alternatively, material from the outer, unstable portion of the disk will likely accumulate until the

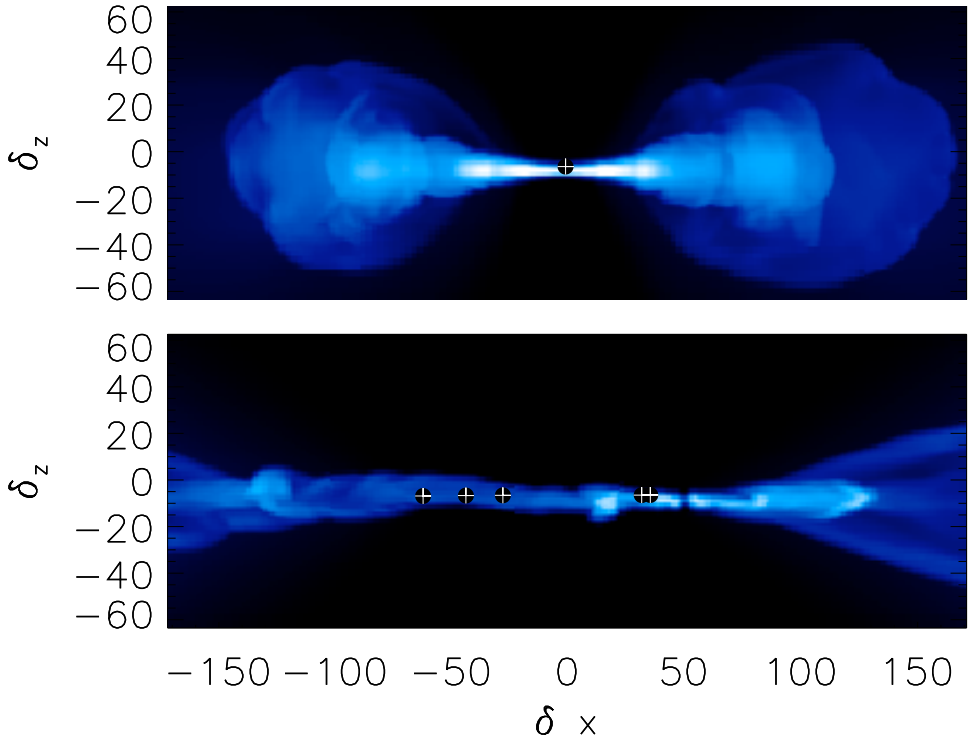

Figure 5.11: Density slices showing vertical structure in a single and binary disk. The top plot is a single star with $\xi = 1.6, \Gamma = 0.09$, while the bottom is a fragmenting binary system with $\xi = 24.3, \Gamma = 0.008$. The extended material in the binary system is generated by a combination of large scale circumbinary torques and the infalling material. Colorscale is logarithmic. The box sizes are scaled to $1.5R_{\rm k,in}$ in the plane of the disk.

critical surface density for GI is reached.

In order to test the effects of the gas stiffening we introduced to avoid unphysical merging of our sink particles (see §5.3.1), we have conducted several purely isothermal experiments in which it is turned off. The removal of the barotropic switch artificially enhances accretion at early times due to sink particles formed via numerical fragmentation merging with the central star. Removing the barotropic switch is equivalent to increasing the resolution of the fragmentation process, but decreasing the resolution of the scale of fragmentation relative to λ, the disk resolution. Using a barotropic switch allows the disk to reach a higher λ before fragmentation sets in for a given set of parameters.

5.7.2 Insensitivity of disk dynamics to core temperature

Our parameterization of disk dynamics is based on the idea that thermodynamics can be accounted for by one parameter, ξ, which compares the accretion rate to the disk sound speed $c_{s,d}$. A basic corollary of this notion is that the core temperature $c_{s,\mathrm{core}}$ has no effect on disk dynamics, except insofar as it affects the accretion rate. We have defined ξ with respect to the disk sound speed, but since our disks and cores are the same temperature, we could equally well have used the core sound speed. Therefore the question arises whether ξ should be computed by normalizing the accretion rate to the disk sound speed, $c_{s,d}$, or the core sound speed, $c_{s,c}$. To test this, we ran simulations in which $c_{s,d}$ and $c_{s,\mathrm{core}}$ differed: we imposed a change in temperature over a range of radii in which infall is highly supersonic.

To demonstrate that ξ defined with respect to the disk sound speed is indeed a better predictor of the morphological and physical behavior of the disk, we compare λ at the time of fragmentation, λ_f to both ξ and the equivalent parameter defined in terms of the core sound speed, $\xi_{\mathrm{core}} = G\dot{M}/c^3_{s,\mathrm{core}}$ for runs with similar values of Γ. We observe a correlation between resolution at the time of fragmentation and ξ at fixed Γ, and so if core temperature is irrelevant, these runs should follow the same trend.

Figure 5.12, shows that λ_f correlates extremely well with ξ at similar values of Γ, but poorly with ξ_{core} for the heated runs. The scaling of λ_f with ξ is also related to the existence of an upper limit on μ as a function of Γ: disks with higher ξ approach this critical value of μ faster, and thus at lower λ.

5.7.3 Resolution

We have shown in §5.5.4 that the observed accretion is consistent with the combined gravitational torques and Reynold stresses, and that these are dominant over that expected purely from numerical diffusion. Because of the self-similar infall, convergence to a steady state within a given run is a good indicator that numerics are not determining our result; in effect, every run is a resolution study. That we observe a range of behavior at the same resolution but different input parameters also implies that numerical effects are sub-dominant. We consider our disks to begin to be resolved when they reach radii such that $R_{\mathrm{k,in}}/\Delta x \geq 30$. The effective numerical diffusivity, which we plot in Figure 5.7,

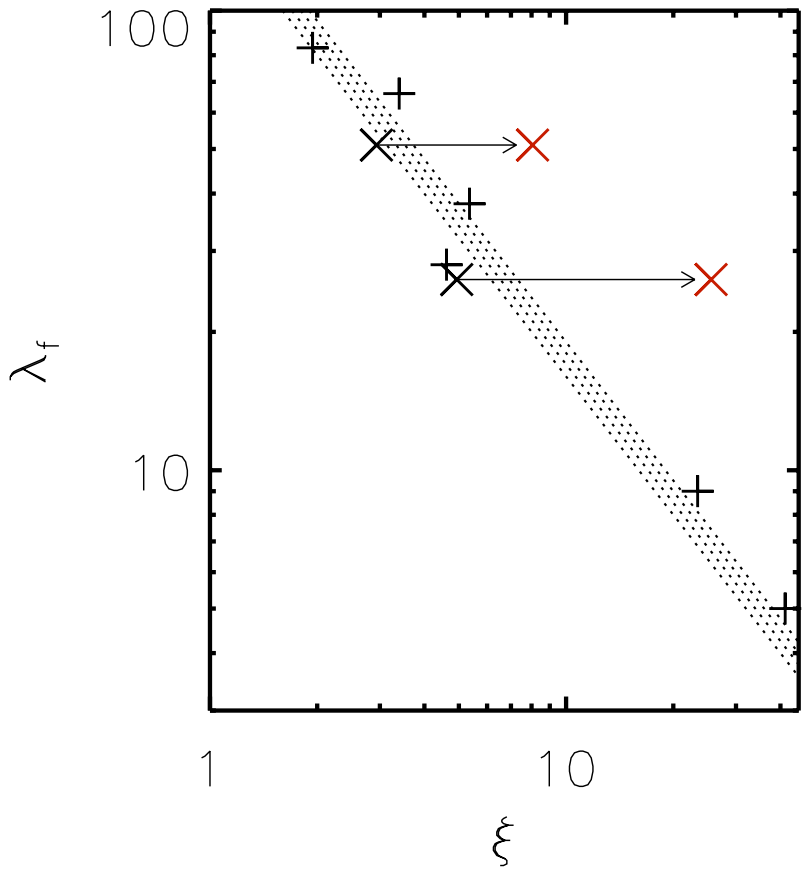

Figure 5.12: Correlation between λ_f and the infalling accretion rate for heated and non heated runs with comparable Γ. Plus symbols indicate non-heated runs, and the crosses are heated runs. The arrows and red crosses indicate the position of the runs evaluated with respect to $\xi_{\rm core}$. Runs shown have Γ values ranging from 0.006 to 0.009. The shaded region illustrates the scaling $\lambda_f \propto \xi^{-1}$. This scaling is related not only to the existence of a critical value of μ, but also tied to the effect of resolution on fragmentation.

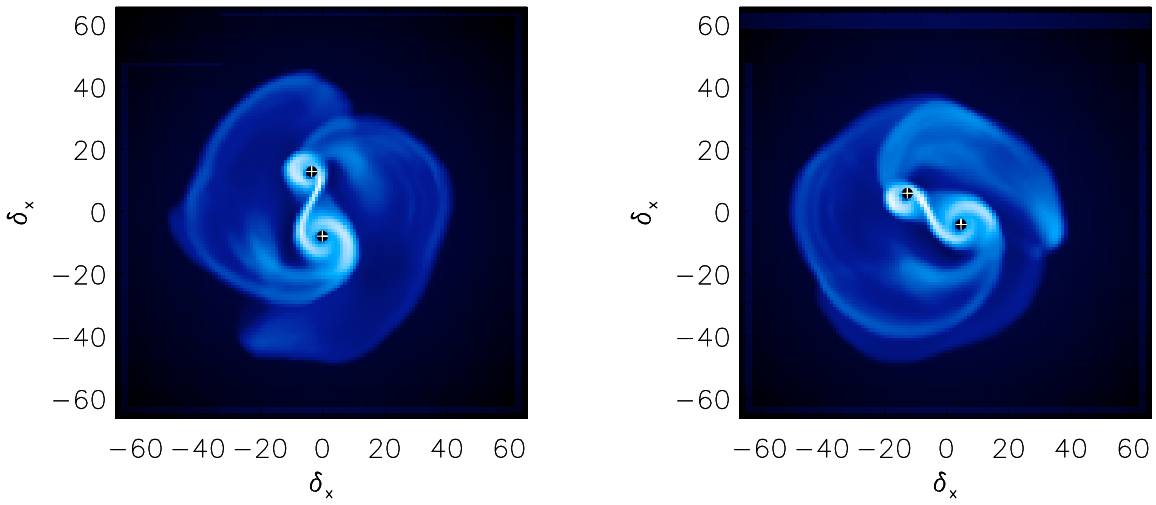

Figure 5.13: At left: a snapshot of the standard resolution of run #16 shortly after binary formation. At right, the same run at double the resolution. Because of the self-similar infall prescription, we show the runs at the same numerical resolution, as time and resolution are interchangeable. In this case the high-resolution run has taken twice the elapsed "time" to reach this state. The two runs are morphologically similar and share expected disk properties.

has been estimated by Krumholz et al. (2004) for ORION. Specifically they find that:

$$\alpha_{\rm num} \approx 78 \frac{r_B}{\Delta x} \left(\frac{r}{\Delta x} \right)^{-3.85}. \tag{5.37}$$

where

$$r_B = \frac{GM_*}{c_s^2} \tag{5.38}$$

is the standard Bondi radius.

For our typical star and disk parameters, this implies numerical α's of order $0.1 - 0.3$ at the minimum radius at which we are resolved. This implies that for our "low" accretion rate cases, at most 1/3 of our effective alpha could be attributed to numerical effects at low resolution. See discussions by Offner et al. (2008); Krumholz et al. (2007b, 2004) for a detailed analysis of disk resolution requirements. At a resolution of 50-100 radial cells across the disk, the dominant effect of numerical diffusion is likely a suppression of fragmentation (Shetty & Ostriker, 2006; Nelson, 2006). Because the isothermal spiral arms can become very narrow prior to fragmentation, numerical diffusion across an arm may smear out some overdensities faster than they collapse. Therefore the conclusions regarding the fragmentation boundary are likely conservative.

We demonstrate morphology convergence in one of our binary runs. We rerun run #16 (as labelled in table 5.1) at double the resolution (128^3 with 10 levels of refinement as opposed to 9). Increasing the physical resolution also decreases the code time step proportionally so that the ratio of the timestep to orbital period as a function of λ should be preserved. In fact, there is little that can be different between the runs at two resolutions at the same effective λ.

The two runs have the same morphology, and characteristic disk properties as a function of λ, as expected. We show in Figure 5.13 snaphots of the standard and high resolution runs. The standard resolution run (left) is at twice the elapsed "time" of the high resolution one (right), and so the same numerical resolution, λ. We confirm that the mass accretion rate is consistent between the two runs: at the snapshots shown the mass ratio of the lower resolution run is 0.46, while the higher resolution run is 0.48.

To the extent that numerical artifacts are seeding instabilities, we expect some stochasticity in the details of the fragmentation between any two runs. Although the effect is small, it is also possible that since the physical size of the disk (and the radius from which material is currently accreting) relative to the box size is larger at the same value of λ for the low resolution run, the large scale quadrupole potential from the image masses is stronger in the low resolution case.

We also compare a multiple run at a lower resolution by a factor of two. Again we find the same morphological outcome. We find that the disks behave equivalently at the same radial resolution although the elapsed time, and dimensional masses are different.

The scaling of λ_f with ξ in Figure 5.12 also demonstrates that resolution plays a role in determining when disks fragment. Although the infall is self-similar, the disks approach a steady state as parameters like Q and μ evolve toward constant values. This evolution, and sometimes fragmentation, is influenced by the interplay between decaying numerical viscosity and increasing gravitational instability in the disk as a function of λ.

5.7.4 Sink Particles

The accretion algorithm for sink particles is well calibrated for accretion in laminar and turbulent flows, however, There are two possible concerns with this specific algorithm in it's application to fragments in accretion disks both related to the method for checking that gas is bound to the particles. Gas within a few cells of the sink is discretized into 8^3 particles per grid cell. Ballistic trajectories for each particle are then calculated, and only material that will actually collide with the particle (which has a physical size less than a grid cell) is accreted. The first concern is that gas accreting onto a fragment in an accretion disk does not act as a pressureless fluid, even though circular velocities may well be supersonic. Secondly, fragments that form do not cool instantly, and therefore may have physical sizes larger than the grid scale. Including pressure would likely decrease the accretion rate onto the particles, while giving them a larger cross section would enhance the accretion rate. Whether these two effects balance out remains to be tested.

5.8 Comparison to Previous Studies

The literature is replete with useful simulations of protostellar and protoplanetary disks at various stages of evolution, however most involve isolated disks, without infall at large radii (Laughlin & Bodenheimer, 1994; Laughlin & Rozyczka, 1996; Rice et al., 2005; Lodato & Rice, 2005; Fromang & Nelson, 2006; Shetty & Ostriker, 2006; Boley et al., 2006; Lodato et al., 2007; Cai et al., 2008). These simulations include a wide range of physics, from magnetic fields to radiative transfer, but due to the lack of infalling matter, they neither develop disk profiles (surface density, temperature) self-consistenly, nor do they enter the regime of interest in this work: rapid accretion in the embedded phase.

For a review of many of the issues addressed by current GI disk simulations, see Durisen et al. (2007).

There are a few simulations of self-consistent growth and evolution (Vorobyov & Basu, 2007, 2008). These are ideal for following the long term evolution of more quiescient lower mass disks. However, because they are two dimensional, and lack a moving central potential, they cannot follow the evolution of non-axisymmetric modes which are driven by the displacement of the central star from the center of mass, nor can they accurately simulate the formation of multiple systems. Other authors have investigated the initial stage of core collapse onto disks (Banerjee & Pudritz, 2007; Tsuribe & Inutsuka, 1999a), however these authors focus on the effects of magnetic fields and fragmentation of the core prior to disk formation respectively. Tsuribe & Inutsuka (1999b) and Matsumoto & Hanawa (2003) have also investigated the collapse of cores into disks and binaries, though they do not investigate many disk properties (see §5.8.1 for detailed comparisons). Krumholz et al. (2007b) and Krumholz et al. (2009) have conducted three dimensional radiative transfer calculations, but due to computational cost can only investigate a small number of initial conditions.

In addition to numerical work, there are a range of semi-analytic models which follow the time evolution of accreting disks (Hueso & Guillot, 2005, KMK08). KMK08 examined the evolution of embedded, massive disks in order to predict regimes in which gravitational instability, fragmentation of the disk, and binary formation were likely. They concluded that disks around stars greater than $1 - 2M_{\odot}$ were likely subject to strong gravitational instability, and that a large fraction of O and B stars might be in disk-born binary systems. Hueso & Guillot (2005) have also made detailed models of disk evolution, though they examine less massive disks, and do not include explicitly gravitational instability, and disk irradiation.

In KMK08 we hypothesized that the disk fragmentation boundary could be drawn in Q- μ parameter space, where small scale fragmentation was characterized by low values of Q and binary formation by high values of μ. Due to the self-similar nature of these simulations, the distinction between these two types of fragmentation is difficult, as the continued accretion of high angular momentum material causes the newly formed fragment to preferentially accrete material and grow in mass (Bonnell & Bate, 1994a). Moreover, because the disks are massive and thick, the isolation mass of fragments is comparable to the disk mass, and so there is little to limit the continued growth of fragments.

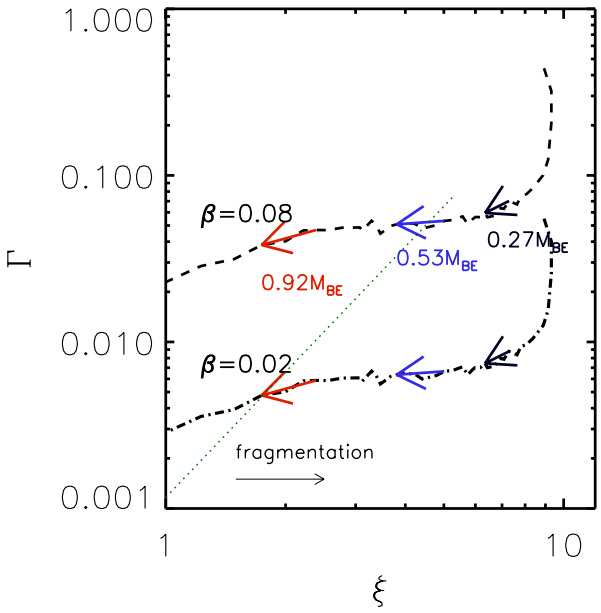

Figure 5.14: Trajectory of a Bonnor-Ebert sphere through $\xi - \Gamma$ space. The two lines show values of $\beta = 0.02, 0.08$ as defined in Matsumoto & Hanawa (2003). Arrows indicate the direction of time evolution from $t/t_{\rm ff,0} = 0 - 5$. $t_{\rm ff,0}$ is evaluated with respect to the central density, and arrows are labelled with the fraction of the total Bonnor-Ebert mass which has collapsed up to this point. The dotted line shows the fragmentation boundary from Figure 5.2.

5.8.1 The evolution of the accretion parameters in the isothermal collapse of a Bonnor-Ebert Sphere

While self-similar scenarios are useful for numerical experiments, they do not accurately capture the complexities of star formation. In particular, in realistic cores, ξ and Γ evolve in time. Therefore it is interesting to chart the evolution of a more realistic (though still idealized) core through our parameter space. We consider the isothermal collapse of a Bonnor-Ebert sphere initially in solid-body rotation (Bonnor, 1956). Such analysis allows us to compare our results with other numerical simulations that have considered global collapse and binary formation such as Matsumoto & Hanawa (2003) via the parameters laid out in Tsuribe & Inutsuka (1999a).

We use the collapse calculation of a 10% overdense, non-rotating Bonnor -Ebert sphere from Foster & Chevalier (1993), and impose angular momentum on each shell to emulate

solid body rotation. Figure 5.14 shows the trajectory of a rotating Bonnor-Ebert sphere through $\xi - \Gamma$ parameter space as a function of the freefall time $t/t_{\rm ff,0}$, for two different rotation rates corresponding to $\beta = E_{\rm rot}/E_{\rm grav} = 0.02, 0.08$. The free fall time is evaluated with respect to central density.

The early spike in ξ is due to the collapse of the inner flattened core at early times. Similarly, the corresponding decline in Γ is a result of the mass enclosed increasing more rapidly than the infalling angular momentum. The long period of decreasing ξ and constant Γ arises from the balance between larger radii collapsing to contribute more angular momentum, and the slow decline of the accretion rate. This trajectory may explain several features of the fragmentation seen in Matsumoto & Hanawa (2003). Although not accounted for in Figure 5.14, cores with high values of β have accretion rates supressed at early times due to the excess rotational support, while those with low β collapse at the full rate seen in Foster & Chevalier (1993). In cores with small β, the high value of ξ may drive fragmentation while the disk is young. Alternatively, for modest values of β, Γ may be sufficiently low while ξ is declining that the disk mass surpasses the critical fragmentation threshold, and fragments via the so-called satellite formation mechanism. For very large values of β, a core which is only moderately unstable will oscillate and not collapse as seen in Matsumoto & Hanawa (2003) for $\beta > 0.3$.

5.9 Discussion

We have examined the behavior of gravitationally unstable accretion disks using three-dimensional, AMR numerical experiments with the code ORION. We characterize each experiment as a function of two dimensionless parameters, ξ and Γ, which are dimensionless accretion rates comparing the infall rate to the disk sound speed and orbital period respectively. We find that these two global variables can be used to predict disk behavior, morphological outcomes, and disk-to-star accretion rates and mass ratios. In this chapter, we discuss the main effects of varying these parameters. Our main conclusions are:

- Disks can process material falling in at up to $\xi \sim 2 - 3$ without fragmenting. Although increasing Γ stabilizes disks at fixed values of ξ those fed at $\xi > 3$ for many orbits tend to fragment into a multiple or binary system.

- Disks can reach a statistical steady state where mass is processed through the disk at a fixed fraction of the accretion rate onto the disk. The discrepancy between these two rates, μ, scales with Γ; disks with larger values of Γ can sustain larger maximum disk masses before becoming unstable. The highest disk mass reached in a non-fragmenting system is $\mu \approx 0.55$ or $M_* \sim M_d$.

- Gravitational torques can easily produce effective accretion rates consistent with a time averaged $\alpha \approx 1$.

- The minimum value of Q at which disks begin to fragment is roughly inversely proportional to the disk scale height. It is therefore important to consider not only Q but another dynamical parameter when predicting fragmentation, at least in disks which are not thin and dominated by axisymmetric modes.

- The general disk morphology and multiplicity is consistent between isothermal runs and irradiated disks with similar effective values of ξ.

These conclusions are subject to the qualification that fragmentation occurs for lower values of ξ as the disk resolution increases, and so it is possible that the location of the fragmentation boundary will shift with increasing resolution. However we expect that our results are representative of real disks and other numerical simulations in so far as they have comparable dynamic range of the parameters relevant to fragmentation such as λ_J/λ.

Chapter 6

Gravitational Instability and Wide Orbit Planets

A version of this chapter has been published in The Astrophysical Journal as "The Runts of the Litter: Why Planets Formed Through Gravitational Instability Can Only Be Failed Binary Stars", Kratter, K. M., Murray-Clay, R. A., Youdin, A. N., vol. 710, pp1375-1386, 2010. Reproduced by permission of the AAS.

6.1 Introduction

In the previous chapters we have mainly consider the role of gravitational instability in driving accretion and binary formation. Motivated by the recent discovery of massive planets on wide orbits, we now explore the requirements for making gas giants at large separations from their host star via gravitational instability, hereafter, GI. In particular, we consider the formation mechanism for the system HR 8799 which contains three $\sim 10 M_{\rm Jup}$ objects orbiting at distances between $\sim$ 30 and 70 AU (Marois et al., 2008). The standard core accretion model for planet formation, already strained in the outer solar system, has difficulty explaining the presence of these objects. While GI is an unlikely formation mechanism for close in planets (Rafikov, 2005), for more widely separated planets, or sub-stellar companions, the viability of GI-driven fragmentation deserves further investigation.

In the inner regions of a protoplanetary disk, gas cannot cool quickly enough to allow a gravitationally unstable disk to fragment into planets (Rafikov, 2005; Matzner & Levin, 2005). For this reason, core accretion—in which solid planetesimals collide

and grow into a massive core which then accretes a gaseous envelope—has emerged as the preferred mechanism for forming planets at stellar separations $\lesssim 10$ AU. Planets at wider separations have only recently been discovered by direct imaging around the A-stars HR 8799 (Marois et al., 2008), Fomalhaut (Kalas et al., 2008), and possibly Beta Pic (Lagrange et al., 2009). Searches at large radii surrounding solar-type stars have yet to turn up similar companions (Nielsen & Close, 2009). Standard core accretion models cannot form these planets, though further investigation is warranted.

In favor of this possibility, all three systems show some evidence of processes related to core accretion: all have infrared excess due to massive debris disks at large radii. This is at least partially a selection effect as these systems were targeted due to the disks' presence. Nevertheless, these debris disks are composed of reprocessed grains from collisions of planetesimals. The disks' long lifetimes prohibit a primordial origin for small grains—they are removed quickly by radiation pressure and Poynting-Roberston drag (Aumann et al., 1984) and so must be regenerated from collisions between larger bodies that formed through the coagulation of solids at early times. Therefore, planetesimal formation, a necessary ingredient in core accretion models, has taken place (e.g., Youdin & Shu, 2002; Chiang & Youdin, 2009).

In addition, other A-stars host planets at 1–2 AU (Johnson et al., 2007) which, although they have a distinct semi-major axis distribution from planets orbiting G and M stars, are likely formed by core accretion. If future surveys demonstrate that this distribution extends smoothly to wide separation planets, then simplicity would argue against a distinct formation mechanism for the wide giants.

Yet the standard core accretion model faces a serious problem at large distances. The observed lifetimes of gas disks are short, at most a few Myr (Hillenbrand et al., 1992; Jayawardhana et al., 2006). In contrast, typical core accretion times increase with radius and exceed 10 Myr beyond 20 AU (e.g. Levison & Stewart, 2001; Goldreich et al., 2004). Whether or not this theoretical difficulty can be overcome will require careful modeling of the interactions between planetesimals and the young gas disk.

Could wide orbit planets have formed at smaller radii, and migrated outwards? Dodson-Robinson et al. (2009), have investigated the possibility of forming the HR 8799 system via scattering in the absence of dynamically important gas, but find that putting three massive planets into such closely spaced yet wide orbits is unlikely. Crida et al. (2009) have suggested that under favorable circumstances outward migration in resonances might be feasible. Alternatively, the core of a giant planet could be scattered

outward by a planet, or migrate outward before accreting its gas envelope, either by interactions with the gas disk (Type III migration; e.g. Masset & Papaloizou 2003) or with planetesimals embedded in the gas (Capobianco, Duncan, & Levison, in prep). Neither mechanism has yet been shown to move a core to such large distances, though this possibility has not been ruled out.

Given these difficulties, it is natural to search for other formation mechanisms, and GI (Boss, 1997) stands out as a promising alternative. If any planets form by GI, the recently discovered directly imaged planets are the most likely candidates (Rafikov, 2009; Boley, 2009; Nero & Bjorkman, 2009). In this chapter, we examine this possibility in more detail, considering the expected mass scale of fragments and the effect of global disk evolution on the formation process.

The inferred masses for the HR 8799 planets are close to the deuterium burning limit of $13 M_{\rm Jup}$ (Chabrier & Baraffe, 2000). For simplicity, we take this as a the dividing line between planets and brown dwarfs and we refer to the HR 8799 objects as planets throughout. However, there is no reason for a given formation mechanism to function only above or below this threshold, and in fact, we will argue that if the HR 8799 planets formed by GI, their histories are more akin to those of higher-mass brown dwarfs than to lower-mass planets.

To constrain GI as a mechanism for wide giant planet formation, we set the stage by describing the HR 8799 system in §6.2. We review the standard requirements for fragmentation in §6.3 and discuss the initial mass scale of fragments in §6.4. In §6.5 we show that under typical disk conditions, fragments will continue to accrete to higher masses. We then discuss important global constraints on planet formation provided by star formation models, disk evolution timescales, and migration mechanisms in §6.6, and §6.7. We compare predictions of our analysis with the known wide substellar companions and exoplanets in §6.8, suggesting that future observations will provide a definitive answer to the formation mechanism for HR 8799. In the appendices we re-examine the heating and cooling properties of disks that are passively and actively heated, with special attention to the implications for irradiated disks, which become increasingly relevant for more massive stars.

6.2 The HR 8799 system

The planets around HR 8799 probe a previously unexplored region of parameter space (Marois et al., 2008; Lafrenière et al., 2009) because they are more distant from their host star. The three companions to HR 8799 are observed at separations from their host star of 24, 38, and 68 AU. Their masses, estimated using the observed luminosities of the planets in conjunction with cooling models, have nominal values of 10, 10, and 7 $M_{\rm Jup}$, respectively. A range in total mass of 19–37 $M_{\rm Jup}$ is derived from uncertainties in the age of the host star (Marois et al., 2008). Interpretation of the cooling models generates substantial additional systematic uncertainty—recent measurements suggest that these models may overpredict the masses of brown dwarfs by ∼25% (Dupuy et al., 2009). Fabrycky & Murray-Clay (2008) have demonstrated that for planetary masses in the stated range, orbital stability over the age of the system requires that the planets occupy at least one mean-motion resonance, and that for doubly-resonant orbital configurations total masses of up to at least $54M_{\rm Jup}$ can be stable.

HR 8799 has been called a "scaled-up solar system" in terms of the stellar flux incident on its giant planets (Marois et al., 2008; Lafrenière et al., 2009). However for understanding the formation of this system it is more useful to consider dynamical times, and disk mass requirements. Because the dynamical time at fixed radius scales only as $M_*^{1/2}$, the dynamical times are larger at the locations of the HR 8799 planets that at the solar system giants. Since the total mass in planets greatly exceeds the $\sim 1.5\ M_{\rm Jup}$ in the solar system, we can infer that (as with some other extrasolar systems) the primordial disk around HR 8799 was more massive than the solar nebula and/or there was greater efficiency of planet formation, especially in the retention of gas. Compared to solar system giants, longer dynamical times make core accretion more difficult and larger disk masses make GI more plausible.

6.3 Ideal Conditions for GI-driven Fragment Formation

We first determine where, and under what local disk conditions, fragmentation by GI is possible. Following Gammie (2001), Matzner & Levin (2005) and Rafikov (2005), we argue that for a disk with surface density Σ and temperature T to fragment, it must

satisfy two criteria. First, it must have enough self-gravity to counteract the stabilizing forces of gas pressure and rotational shear, as quantified by Toomre's Q:

$$Q \equiv \frac{c_s \Omega}{\pi G \Sigma} < Q_o \sim 1 \tag{6.1}$$

(Safronov, 1960; Toomre, 1964), where $c_s = \sqrt{kT/\mu}$ is the isothermal sound speed of the gas with mean particle weight $\mu = 2.3 m_{\rm H}$ appropriate for a molecular gas, G is the gravitational constant, k is the Boltzmann constant, and Ω is the orbital frequency. Equation (6.1) specifies the onset of axisymmetric instabilities in linear theory that can give rise to bound clumps (Goldreich & Lynden-Bell, 1965). In a realistic disk model, clumps likely form within spiral arms formed via non-axisymmetric, non-linear instabilities, although the critical value of Q at which fragmentation occurs should remain similar.

The second criterion that must be satisfied for fragmentation to proceed is the so-called cooling time criterion. The heat generated by the release of gravitational binding energy during the contraction of the fragment must be radiated away on the orbital timescale so that increased gas pressure does not stall further collapse (Gammie, 2001). This implies

$$t_{\rm cool} = \frac{3\gamma \Sigma c_s^2}{32(\gamma - 1)} \frac{f(\tau)}{\sigma T^4} \lesssim \zeta \Omega^{-1}. \tag{6.2}$$

Here ζ is a constant of order unity, γ is the adiabatic index of the gas, and σ is the Stefan-Boltzmann constant. We take $f(\tau) = 1/\tau + \tau$ (Rafikov, 2005) for disk vertical optical depth $\tau = \kappa\Sigma/2$ and gas opacity κ. Numerical models of collapse in barotropic disks measure the critical value ζ through the inclusion of a loss term $u/t_{\rm cool}$ in the equation for the internal energy, u. Estimates of ζ range from $\sim 3 - 12$, depending on γ (Rice et al., 2005), the numerical implementation of cooling (Clarke et al., 2007), and the vertical stratification in the disk. We assume $\gamma = 7/5$, appropriate for molecular hydrogen, and we adopt $\zeta = 3$ here. Although ζ was measured in disks whose temperature is controlled by viscous heating, we show in Appendix 6.10 that the same expression (modulo slightly different coefficients) should apply when irradiation sets the disk temperature, as will be the case in disks prone to fragmentation (see Appendix 6.11).

A disk satisfying Toomre's criterion for instability (equation 6.1) but not the cooling time criterion (equation 6.2) experiences GI-driven angular momentum transport which regulates the surface density of the disk so that $Q \sim Q_o \sim 1$ and Q does not reach substantially smaller values (c.f. Appendix 6.10). We can therefore use Toomre's criterion

to define a relationship between Σ and T at fragmentation, as a function of period:

$$\Sigma = \frac{c_s \Omega}{\pi G Q_o} = f_q \sqrt{T} \Omega \tag{6.3}$$

where for convenience we define $f_q \equiv (k/\mu)^{1/2} (\pi G Q_o)^{-1}$. We shall hereafter set $Q_o = 1$.

Given equation (6.3), we can rewrite equation (6.2) to generate a single criterion for fragmentation which depends on temperature and location:

$$\frac{\Omega t_{\rm cool}}{\zeta} \quad = \quad (f_q f_t) \, \frac{\Omega^2}{T^{5/2}} f(\tau) \leq 1, \tag{6.4}$$

where $f_t \equiv (3/32)\gamma(\gamma - 1)^{-1} k (\mu \sigma \zeta)^{-1}$. Somewhat counterintuitively, the critical cooling constraint requires that a disk be sufficiently hot to fragment. The value of $f(\tau)$ depends on both Ω and T. Evaluating this criterion relies on the disk opacity, which we return to in §6.4.2.

6.4 Minimum fragment masses and separations

6.4.1 Initial masses of GI-born fragments

We take the initial mass of a fragment to be the mass enclosed within the radius of the most unstable wavelength, $\lambda_Q = 2\pi H$ in a $Q = 1$ disk, or:

$$M_{\rm frag} \approx \Sigma (2\pi H)^2 \tag{6.5}$$

(Levin, 2007), where $H = c_s/\Omega$ is the disk scaleheight. Cossins et al. (2009) have shown that even when the GI is non-axisymmetric, the most unstable axisymmetric wavelength λ_Q is one of the dominant growing modes, suggesting that this is a reasonable estimate. While more numerical follow up will be necessary to pin down the true distribution of fragments born through GI, at present simulations show that this estimate may well be a lower limit, but is the correct order of magnitude (Boley, 2009; Stamatellos & Whitworth, 2009).

Using equation (6.3), we rewrite the fragment mass explicitly as a function of temperature and location:

$$M_{\rm frag} \approx 4\pi \left(\frac{H}{r} \right)^3 M_* = f_m \frac{T^{3/2}}{\Omega} \tag{6.6}$$

where $f_m \equiv (2\pi)^2 f_q k/\mu$. Equation (6.6) demonstrates that at a given disk location, fragment masses depend only on temperature, with lower temperatures generating smaller

fragments, subject to the minimum temperature required for fragmentation by equation (6.4).

Rafikov (2005) pointed out that there exists an absolute minimum fragment mass at any disk location, when the disk satisfies the equalities in equation (6.1) and equation (6.2) and has $\tau = 1$. The minimum temperature required for fragmentation scales as $T \propto (\tau + 1/\tau)^{2/5}$ (equation 6.4), so the critical temperature and fragment mass are minimized at $\tau = 1$, the optical depth for which cooling is most efficient. The corresponding minimum mass as a function of location is:

$$M_{\rm f,min} = f_m (f_q f_t)^{3/5} \Omega^{1/5} \tag{6.7}$$

$$= 1.5 M_{\rm Jup} \left(\frac{r}{100 \text{ AU}} \right)^{-3/10} \left(\frac{M_*}{1.5 M_\odot} \right)^{1/10} \tag{6.8}$$

which occurs for disk temperatures:

$$T_{\rm f,min} = 7{\rm K} \left(\frac{\rm r}{100 \text{ AU}} \right)^{-6/5} \left(\frac{\rm M_*}{1.5 M_\odot} \right)^{2/5} \tag{6.9}$$

Equation (6.7) corresponds to $Q = 1$, $\Omega t_{\rm cool} = 3$, and $\tau = 1$. This minimum mass is only achieved for temperatures consistent with $T_{\rm f,min}$. Once an opacity law is specified which relates T and τ, the problem becomes overconstrained— these three criteria can only be satisfied at a single disk location, and equations 6.7-6.9 are valid at only one radius in the disk. We now proceed to evaluate the critical disk temperatures and fragment masses for realistic opacity laws, demonstrating that planetary-mass fragments can only form at large separations from their host star.

6.4.2 Opacity

At low temperatures, when $T \lesssim 155$ K, ice grains are the dominant source of opacity (Pollack et al., 1985). Above ∼155 K, ices begin to sublimate. In the cold regime applicable to the outer regions of protoplanetary disks, we consider two realistic opacity laws, one which is characteristic of grains in the interstellar medium (ISM), and one which is characteristic of grains that have grown to larger sizes due to processes within the disk. We assume a Rosseland mean opacity which scales as

$$\kappa \approx \kappa_\beta T^\beta \tag{6.10}$$

where the both the exponent, β, and the constant κ_β are not well constrained in protoplanetary disks. They depend on the number-size distribution and composition of the

dust grains, and on the dust-to-gas ratio. For ISM like grains, the Rosseland mean opacity may be approximated by an opacity law with $\beta = 2$, or

$$\kappa \approx \kappa_2 T^2 \tag{6.11}$$

(Pollack et al., 1996; Bell & Lin, 1994; Semenov et al., 2003) as long as the ice grains dominating the opacity are smaller than a few tens of microns. This opacity law is observationally confirmed in the ISM (Beckwith et al., 2000, and references therein). For our fiducial model we use $\kappa_2 \approx 5 \times 10^{-4}\mathrm{cm}^2/\mathrm{g}$ for T in Kelvin, a fit to the standard dust model by Semenov et al. (2003). Throughout, we quote κ per gram of gas for a dust-to-gas ratio of 10^{-2}.

As grains grow larger, they eventually exceed the wavelength of the incident radiation, and so the opacity is determined by the geometric optics limit. In this case the Rosseland mean opacity is independent of temperature, so the exponent $\beta = 0$. In this limit:

$$\kappa \approx \kappa_0 \tag{6.12}$$

For a fixed dust mass in grains of size s, $\kappa_0 \propto s^{-1}$. For our fiducial model we choose $\kappa_0 \approx 0.24$ cm^2/g which is valid for $T \gtrsim 20$ K and typical grain sizes of order $300\mu m$ (see Figure 6 of Pollack et al., 1985).

Observations of emission from optically thin protoplanetary disks show evidence of grain growth at millimeter wavelengths. Specifically the measured opacities $\kappa_\nu \propto \nu^\alpha$ with $\alpha \simeq 0.5$—1.5 in the Rayleigh-Jeans tail imply particle growth toward the millimeter wavelengths of the observations (D'Alessio et al., 2001). Although most observed disks have had more time for grain growth to proceed, Class 0 sources also show evidence of grain growth (D'Alessio et al., 2001). Alternatively, these objects could be optically thick at millimeter wavelengths, which would mimic the effects of grain growth.

Using these opacity laws we see that cooling proceeds with a different functional form in the optically thick and optically thin limits. In the optically thick regime, $f(\tau) \approx \tau = (\kappa_\beta T^\beta \Sigma)/2$, which when combined with equation (6.4) indicates that to fragment, the disk must have temperature

$$T > \left(f_t f_q^2/2\right)^{1/(2-\beta)} \left(\Omega^3 \kappa_\beta\right)^{1/(2-\beta)} \tag{6.13}$$

for $\beta \neq 2$. In the special case $\beta = 2$, the fragmentation constraint is temperature-independent, as discussed in §6.4.2.

In the optically thin regime, $f(\tau) = 1/\tau = 2/(\kappa_\beta T^\beta \Sigma)$. The cooling time is independent of Σ, so we can rewrite equation (6.4) as:

$$T > (2f_t)^{1/(3+\beta)} \left(\frac{\Omega}{\kappa_\beta}\right)^{1/(3+\beta)}, \tag{6.14}$$

Fig. 6.1 shows the dependence of the cooling time on disk temperature for each opacity law at two different radii. Since fragmentation can only occur when $\Omega t_{\rm cool} < \zeta$, the minimum temperatures at which fragmentation is allowed are specified by the intersection of the cooling curves with the $\Omega t_{\rm cool}$ boundary.

Small grain opacity law

For an optically thin disk with $\beta = 2$, equation (6.14) implies that in order to fragment, the disk must have temperatures in excess of:

$$\begin{aligned} T \;>\; T_{\rm thin} = 9{\rm K} &\left(\frac{\rm r}{100\ {\rm AU}}\right)^{-3/10} \\ &\left(\frac{\kappa_2}{5\times 10^{-4}{\rm cm^2/g}}\right)^{-1/5} \left(\frac{M_*}{1.5M_\odot}\right)^{1/10} \end{aligned} \tag{6.15}$$

Colder disks, even when optically thin, cannot cool quickly enough to fragment.

For an optically thick disk, $\beta = 2$ turns out to be a special case: the temperature dependence drops out of equation (6.13), giving instead a critical radius beyond which fragmentation can occur, independent of the disk temperature:

$$r \gtrsim 70\ {\rm AU} \left(\frac{M_*}{1.5M_\odot}\right)^{1/3} \left(\frac{\kappa_2}{5\times 10^{-4}{\rm cm^2/g}}\right)^{-2/9}. \tag{6.16}$$

Matzner & Levin (2005) first pointed out the existence of a minimum critical radius for fragmentation. In Fig. 6.2 we illustrate how the two fragmentation criteria create a radius rather than temperature cutoff. At radii larger than the critical radius defined above, any $\Sigma - T$ combination which gives $Q \leq 1$ will fragment (so long as the opacity law remains valid). At smaller radii, no combination of Σ and T which gives $Q \leq 1$ will fragment because the disk cannot simultaneously satisfy the cooling time criterion.

Large grain opacity law

As shown in Fig. 6.1, for the large grain opacity, $\tau > 1$ for all relevant temperatures. In this case equation (6.13) requires:

$$T > 65K \left(\frac{M_*}{1.5M_\odot}\right)^{3/4} \left(\frac{r}{43\ {\rm AU}}\right)^{-9/4} \left(\frac{\kappa_0}{0.24\ {\rm cm^2/g}}\right)^{1/2}. \tag{6.17}$$

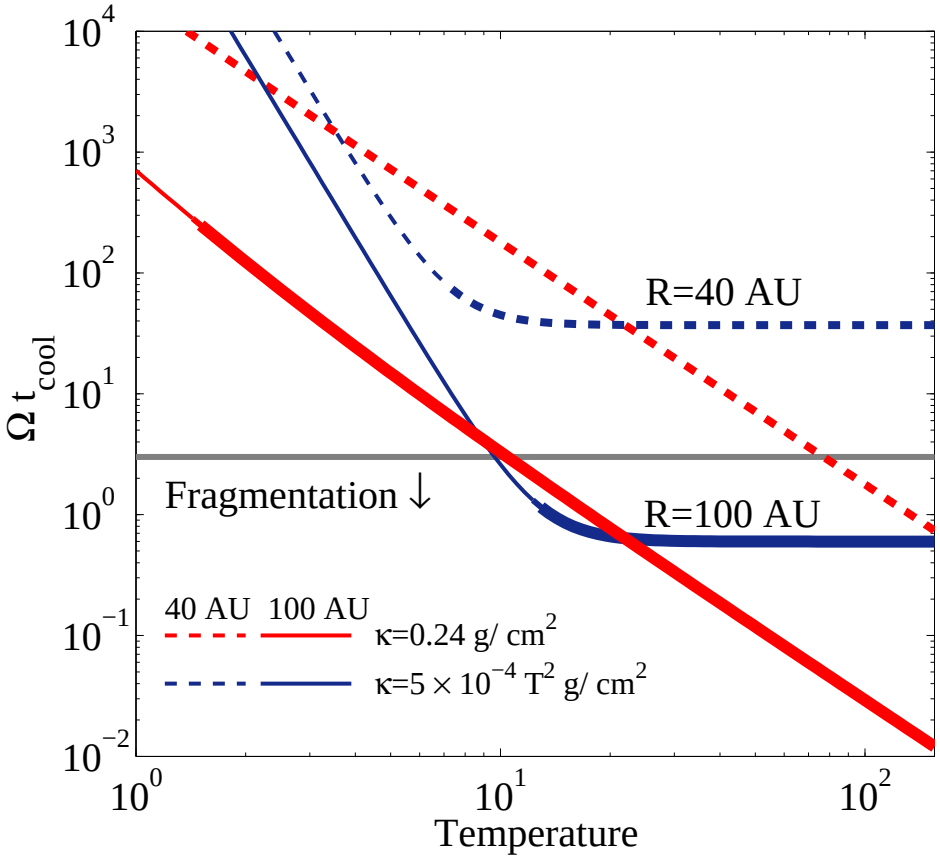

Figure 6.1: The disk cooling time as a function of tempertature for different opacity laws at radii of 40 AU (dashed) and 100 AU (solid). The cooling time is calculated assuming that $Q = 1$. The temperature independent (large grain) opacity law is shown in red, while the ISM opacity law: $\kappa \propto T^2$ is shown in blue. The line thickness indicates the optical depth regime. When lines drop below the critical cooling time (grey), disk fragmentation can occur. The bend in the ISM opacity curve indicates that in the optically thick regime, the cooling time becomes constant as a function of temperature.

The corresponding minimum mass for these temperatures is:

$$M_{\rm min} = 13 M_{\rm Jup} \left(\frac{M_*}{1.5 M_\odot}\right)^{5/8} \left(\frac{r}{43{\rm AU}}\right)^{-15/8} \left(\frac{\kappa_0}{0.24{\rm cm}^2/{\rm g}}\right)^{3/4}. \quad (6.18)$$

We have scaled equations (6.17) and (6.18) to an effective critical radius for this opacity law. Although fragmentation can occur inside 43 AU at sufficiently high temperatures, the fragments exceed $13 M_{\rm Jup}$, making it irrelevant for planet formation. Smaller values of κ_0 move this boundary inward, allowing for fragmentation into lower mass objects at smaller radii, although the scaling with opacity is shallow. Grain growth to larger sizes could plausibly reduce κ_0. If, for example, grains dominating the disk opacity have grown up to 1mm without altering the dust-to-gas ratio, equation (6.12) implies that in the geometric optics limit $\kappa_0 = 0.072{\rm cm}^2/{\rm g}$. In this case, the minimum radius is pushed inward to 26 AU (see also Nero & Bjorkman, 2009).

Thus far we have determined the minimum masses allowed as a function of radius with the temperature as a free parameter. We now calculate actual disk temperatures, which at large radii are typically higher than the minima. In this case we must evaluate fragment masses using equation (6.6).

6.4.3 Initial fragment masses with astrophysical disk temperatures

To consider the case favorable to GI planet formation, we consider the lowest plausible disk temperatures in order to minimize the fragment masses. We estimate the disk temperature using the passive flared disk models of Chiang & Goldreich (1997). This model likely underestimates the temperatures in actively accreting systems because it ignores significant "backheating" from the infall envelope and surrounding cloud (Chick & Cassen, 1997; Matzner & Levin, 2005). Although viscous heating will also contribute to the temperature, we ignore its modest contribution to obtain the lowest reasonable temperatures and fragment masses. Disk irradiation dominates over viscous heating in this regime (see Appendix B).

We consider the inner region where the disk is optically thick to blackbody radiation. In this regime, the temperature of a flared disk in radiative and hydrostatic equilibrium

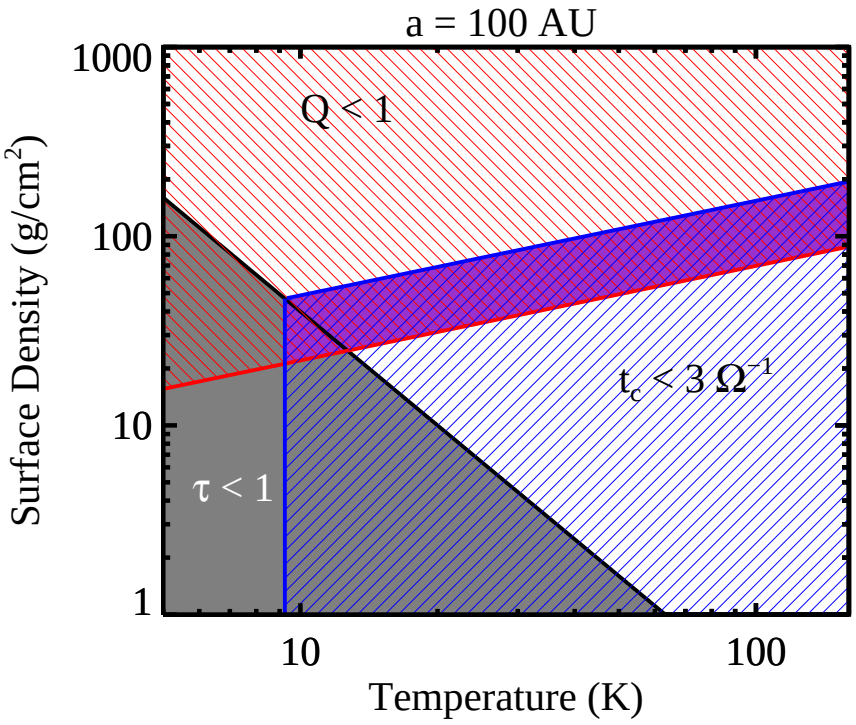

Figure 6.2: Fragmentation can only occur in the region of parameter space indicated by the overlapping hashed regions for ISM opacities at radii of 100 AU. The upper, shaded region (red) shows where Toomre's parameter $Q < 1$. The lower, shaded region (blue) indicates where $t_{\rm cool} \leq 3\Omega^{-1}$. At radii less than 70 AU, fragmentation is prohibited because the two regions no longer overlap. That the boundaries of these regions are parallel lines reflects the $\kappa \propto T^2$ form of the ice-grain-dominated opacity at low temperatures.

is:

$$T_m = \left(\frac{\alpha_F}{4}\right)^{1/4} \left(\frac{R_*}{r}\right)^{1/2} T_* \propto L^{2/7} r^{-3/7} \tag{6.19}$$

where α_F measures the grazing angle at which starlight hits the disk; α_F is dependent on the degree of disk flaring measured at the height of the photosphere (Chiang & Goldreich, 1997). Grain settling may reduce the height of the photosphere (set here to 4 times the scaleheight) and thus α_F. For the standard radiative equilibrium model, the disk flaring scales approximately as $H/r \propto r^{2/7}$. We shall find when we calculate the disk temperature that a gravitationally unstable disk remains optically thick, justifying the use of this formula.

To estimate the the stellar luminosity we use the stellar evolution models of Krumholz & Thompson (2007), which include both nuclear burning and accretion energy. The accretion luminosity depends on both the current accretion rate and the accretion history (in so far as it effects the stellar radius), so we obtain the lowest luminosity estimates by allowing the star to accrete at a constant, low accretion rate. We use the stellar luminosity after accreting to 90% of its current mass (or $1.35 M_\odot$ assuming roughly 10% is still in the disk). We choose an accretion rate of $10^{-7} M_\odot$/yr as a lower bound because a star accreting at a lower accretion rate throughout its history has a formation timescale that is too long. Accretion rates an order of magnitude larger give comparable luminosity (when the star has only reached $1.35 M_\odot$) to the present day luminosity of $5 L_\odot$ (Marois et al., 2008). Lowering the accretion rate below this value does not significantly lower the stellar luminosity because the accretion energy contribution is small.

The luminosity calculated for an accretion rate of $10^{-7} M_\odot$/yr translates to temperatures of:

$$T \approx 40 \text{ K } \left(\frac{r}{70 \text{ AU}}\right)^{-3/7}, \tag{6.20}$$

which we shall use as our fiducial temperature profile. In the outer regions of the disk where fragmentation is allowed, the disk temperatures are of order $30 - 50$K. These temperatures exceed the minimum threshold for fragmentation, and so the mass of fragments will be set by equation (6.6).

Other analytic and numerical models of stellar irradiation predict temperatures in agreement with or higher than our estimate. (Rafikov & De Colle, 2006; Offner et al., 2009b). Similarly, models of disks in Ophiuchus have similar temperatures for 1 Myr old stars of lower mass (and thus luminosity), implying that our model temperatures are low, though not unrealistic (Andrews et al., 2009).

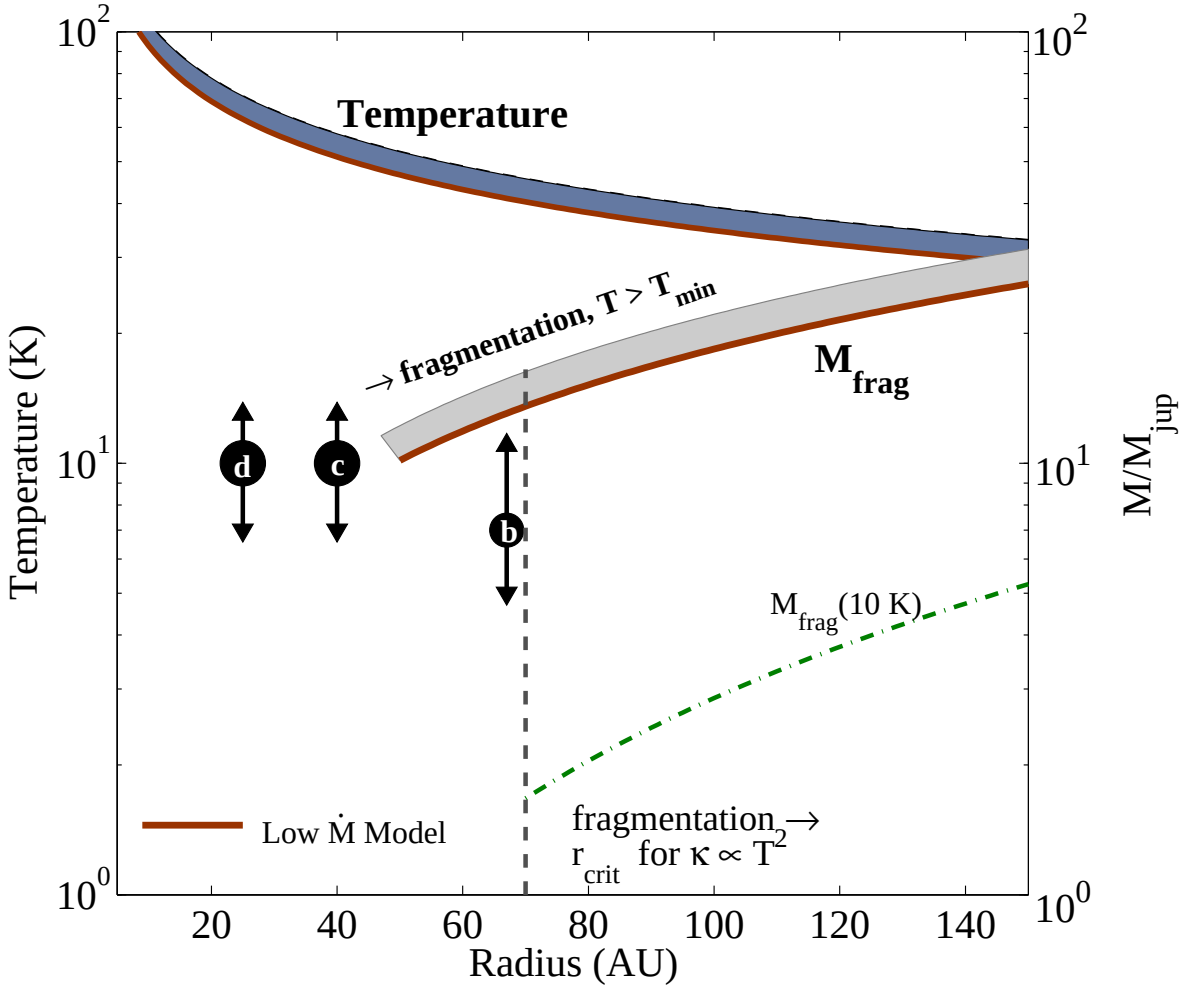

Figure 6.3: Depiction of the current configuration of HR 8799 and formation constraints for realistic disk temperatures. We show the lowest expected irradiated disk temperatures (blue) and corresponding fragment masses (grey), as a function of radius. The lower bound on both regimes (burgundy) is set by the irradiation model described in §6.4.3, with $\dot{M} = 10^{-7} M_{\odot}$/yr. The upper boundary is set by the current luminosity of HR 8799, $\sim 5 L_{\odot}$. The green dashed-dotted line shows the mass with disk temperatures of 10 K, a lower limit provided by the cloud temperature. The vertical line shows the critical fragmentation radius for the ISM opacity law; fragmentation at smaller radii requires grain growth. Fragment masses are shown for radii at which the irradiation temperatures are high enough to satisfy the cooling time constraint of equation (6.17). At smaller radii, fragmentation is possible at higher disk temperatures, but the resulting fragments have correspondingly higher masses, and planet formation is not possible.

In Fig. 6.3 we illustrate the constraints on fragment masses from this irradiation model, calculated using equation (6.6). We show the fiducial disk temperatures of equation (6.20), along with temperatures consistent with luminosities up to the present-day luminosity. For our fiducial opacity laws, the expected fragment masses are only marginally consistent with GI planet formation— fragments form near the upper mass limit of $13 M_{\rm Jup}$. Lower opacities produced by grain growth might allow fragmentation into smaller objects at closer radii. Whether grain-growth has proceeded to this extent in such young disks is unclear.

6.5 Growth of fragments after formation

For realistic disk temperatures, it is conceivable that fragments may be born at several $M_{\rm Jup}$. We now consider their subsequent growth, which may increase their expected mass by an order of magnitude or more.

The final mass of a planet depends sensitively on numerous disk properties (effective viscosity, column density, scaleheight) and the mass of the embedded object. In order to constrain the mass to which a fragment will grow, we can compare it to two relevant mass scales: the disk isolation mass and the gap opening mass.

Halting the growth of planetary mass objects is a relevant problem independent of the formation mechanism. However the GI hypothesis requires that the disk is (or was recently) sufficiently massive to have $Q \sim 1$, implying that the disk is actively accreting. The core accretion scenario does not face this restriction.

6.5.1 Isolation Mass

We estimate an upper mass limit for fragments by assuming that they accrete all of the matter within several Hill radii:

$$M_{\rm iso} \approx 4\pi f_H \Sigma R_H r. \tag{6.21}$$

Here $f_H \sim 3.5$ is a numerical constant representing from how many Hill radii, $R_H = r(M_{\rm iso}/3M_*)^{1/3}$, the planet can accrete (Lissauer, 1987).

It is instructive to compare the ratio of the isolation mass to the stellar mass:

$$\frac{M_{\rm iso}}{M_*} = 4.6 f_H^{3/2} Q^{-3/2} \left(\frac{H}{r}\right)^{3/2}. \tag{6.22}$$

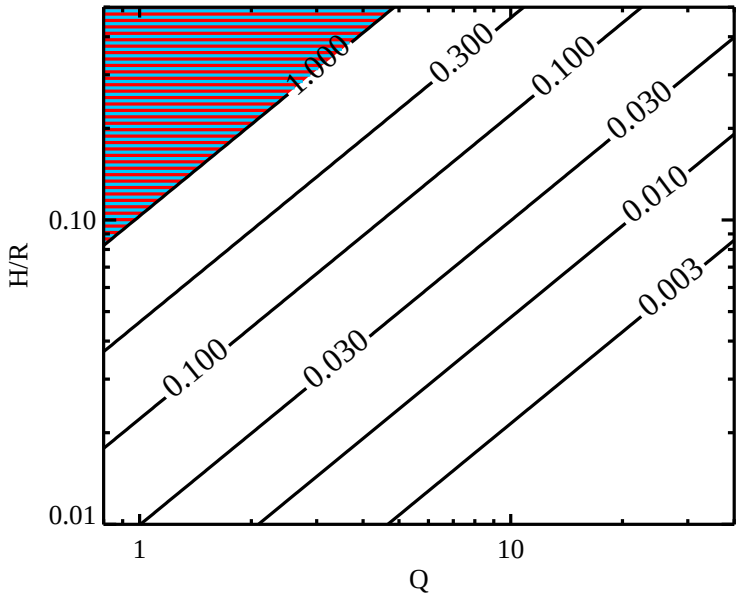

Figure 6.4: Contours of the ratio of planetary isolation mass to stellar mass as a function of Toomre's Q and the disk aspect ratio H/r, illustrating that the isolation mass is always large in unstable disks. For disks with higher Q's consistent with core accretion models, the isolation mass remains small. The shaded region indicates where the isolation mass exceeds the stellar mass.

We find that large isolation masses are always expected in gravitationally unstable disks. Fig. 6.4 illustrates the scaling of equation (6.22) with Q and the disk aspect ratio, H/r. For our fiducial temperature profile, $H/r \approx 0.09$ at 70 AU. For low values of Q and comparable H/r, the isolation mass exceeds 10% of the stellar mass. For the ideal disk values cited above (equation 6.16), the isolation mass is:

$$M_{\rm iso} \approx 400 M_{\rm Jup} \left(\frac{r}{70 \text{ AU}} \right)^{6/5} \left(\frac{M_*}{1.5 M_\odot} \right)^{1/10} . \tag{6.23}$$

This mass is nearly two orders of magnitude larger than the minimum mass. Growth beyond the isolation mass is possible either through mergers or introduction of fresh material to accrete by planet migration or disk spreading.

Objects which grow to isolation mass cannot be planets, and so we turn to mechanisms that truncate fragment growth below the isolation mass.

6.5.2 Gap opening mass

Massive objects open gaps in their disks when gravitational torques are sufficiently strong to clear out nearby gas before viscous torques can replenish the region with new material. (Lin & Papaloizou, 1986; Bryden et al., 1999). The gap width is set by the balance between the two torques:

$$\frac{\Delta}{r} = \left(\frac{f_g q^2}{3\pi\alpha} \frac{r^2}{H^2} \right)^{1/3}, \tag{6.24}$$

where Δ is the gap width, $f_g \approx 0.23$ is a geometric factor derived in Lin & Papaloizou (1993), q is the planet to star mass ratio, and α is the Shakura & Sunyaev (1973) effective viscosity. This can be used to derive the standard minimum gap opening mass by requiring that $\Delta > H$:

$$\begin{aligned} q &> \left(\frac{H}{r}\right)^{5/2} \sqrt{\frac{3\pi\alpha}{f_g}} \\ &\approx 4 \times 10^{-3} \left(\frac{\alpha}{0.1}\right)^{1/2} \left(\frac{T}{40\ \mathrm{K}}\right)^{5/4} \left(\frac{r}{70\ \mathrm{AU}}\right)^{5/4} \\ &\quad \left(\frac{M_*}{1.5\ M_\odot}\right)^{-5/4}. \end{aligned} \tag{6.25}$$

Gap opening requires $\Delta > R_\mathrm{H}$ and $R_\mathrm{H} > H$. The latter requirement is automatically satisfied for fragments formed by GI.

While the effects of GI are often parameterized through an α viscosity, Balbus & Papaloizou (1999) have pointed out that α, a purely local quantity, may not adequately describe GI driven transport, which is inherently non-local. Lodato & Rice (2005) have shown that for sufficiently thin disks, the approximation is reasonable: in order to form objects of planetary mass, the disk must be relatively thin and at least marginally within this limit. However, even in this thin-disk limit, it is not clear that GI driven torques will exactly mimic viscous ones at gap-opening scales.

Equation (6.25) implies that the gap opening mass is less than or equal to the fragment mass for effective viscosities consistent with GI. We use $\alpha \approx 0.1$, as this is consistent with active GI (Gammie, 2001; Lodato & Rice, 2005; Krumholz et al., 2007b). If the local disk viscosity is lower, fragments will always form above the gap-opening mass.

Gap-opening starvation mass

Gap-opening slows accretion onto the planet, but does not starve it of material completely. Accretion rates through gaps remain uncertain for standard core accretion models, and numerical models are not available for accretion onto the distended objects formed through GI fragmentation. Nevertheless simulations of accretion through gaps in low viscosity disks (Lubow et al., 1999) demonstrate that accretion is slower through larger gaps, and this qualitative conclusion likely remains valid as long as gaps form.

Analogous to the isolation mass, we consider a "gap starvation mass" that is related to the ratio of the gap width to planet Hill radius. Rewriting equation (6.24) we find the ratio of gap width to Hill radius is:

$$\frac{\Delta}{R_H} = \left(\frac{f_g q}{\pi \alpha} \frac{r^2}{H^2} \right)^{1/3} \tag{6.26}$$

Note that $\Delta > R_H$ recovers the canonical gap opening estimate appropriate for Jupiter: $q > 40\nu/(r^2\Omega)$, modulo order unity coefficients (cf. Crida et al., 2006).

If we make the simplifying assumption that gap accretion terminates when the gap width reaches a fixed number of Hill radii, f_S, we can calculate a gap starvation mass. We expect that for a gap to truncate accretion, $f_S \gtrsim f_H = 3.5$, the width in Hill radii used to calculate the isolation mass (§6.5.1). Terminating accretion is an unsolved problem for Jupiter in our own solar system, and so to provide a further constraint on f_S, we refer to the numerical simulations of Lissauer et al. (2009) (See also D'Angelo et al. (2003) for a detailed explanation of the numerical work). Their runs 2l and 2lJ exhibit asymptotic mass growth after ∼2.5 Myr for a constant-mass, low viscosity ($\alpha = 4 \times 10^{-4}$) disk under conditions appropriate to the formation of Jupiter. Using equation (6.26), we solve for the width of the gap generating this fall-off in accretion rate and find $f_S = \Delta/R_H \sim 5$. The need for an extremely large and well-cleared gap reflects the integrated effects of low-level accretion through the gap and onto the planet over the disk lifetime of a few Myr. Even a slow trickle of material onto the planet can contribute to significant growth.

Using $f_S = 5$, the gap-opening starvation mass for HR 8799 scaled to both the simulated solar-system viscosity and to the expected GI viscosity is:

$$M_{\rm starve} \approx 8 M_{\rm Jup} \left(\frac{\alpha}{4 \times 10^{-4}} \right) \left(\frac{\Delta}{5 R_H} \right)^3 \left(\frac{T}{40 \text{ K}} \right) \left(\frac{r}{70 \text{ AU}} \right) \tag{6.27}$$

$$\approx 2000 M_{\rm Jup} \left(\frac{\alpha}{0.1}\right) \left(\frac{\Delta}{5 R_H}\right)^3 \left(\frac{T}{40\ {\rm K}}\right) \left(\frac{r}{70\ {\rm AU}}\right).$$

In order to limit growth to planetary masses, the effective viscosity must be two orders of magnitude below that expected in GI unstable disks, roughly $\alpha \sim 10^{-3}$. More restrictively this requires that other local transport mechanisms such as the MRI be weaker than currently predicted by simulations—they produce $\alpha \sim 10^{-2}$ at least in disks with a net magnetic flux (Fleming et al., 2000; Fromang et al., 2007; Johansen et al., 2009). Fig. 6.5 illustrates the scaling of gap starvation mass with radius for several values of α. It appears that active disks face severe obstacles in producing planetary mass objects unless the disk disappears promptly after their formation. Although we expect fragmentation to make the disk more stable by lowering the local column density, there is little reason to expect a recently massive disk to be so quiescent.

Planet starvation through gap overlap

Although it is unlikely that the disk will fragment into a sufficiently large number of planetary mass objects to completely deplete the disk of mass (Stamatellos & Whitworth, 2009), the formation of multiple fragments simultaneously may limit accretion through competition for disk material by opening overlapping gaps. The current separation between the planets is such that gaps larger than roughly three Hill radii overlap, so depending on their migration history, this could limit growth (see also §6.7). From equation (6.27) we see that if gaps are forced to be smaller by a factor of two due to competition with another planet, the expected masses are decreased by a factor of 8. This effect would imply that fragments in multiple systems should be lower in mass. Note that when simulated disks fragment into multiple objects simultaneously, they generally have orbital configurations like hierarchical multiples rather than planetary systems (Stamatellos & Whitworth, 2009; Kratter et al., 2010). Whether the same conditions required to limit fragment growth—reduced disk mass and/or viscosity after fragmentation—can allow the retention of a planetary system of fragments remains to be simulated.

6.5.3 Disk dispersal as a means to limit fragment growth

Mechanisms for gas dispersal such as photoevaporation may be necessary to stunt planetary growth, even for models of Jupiter in our own solar system (Lissauer et al., 2009).

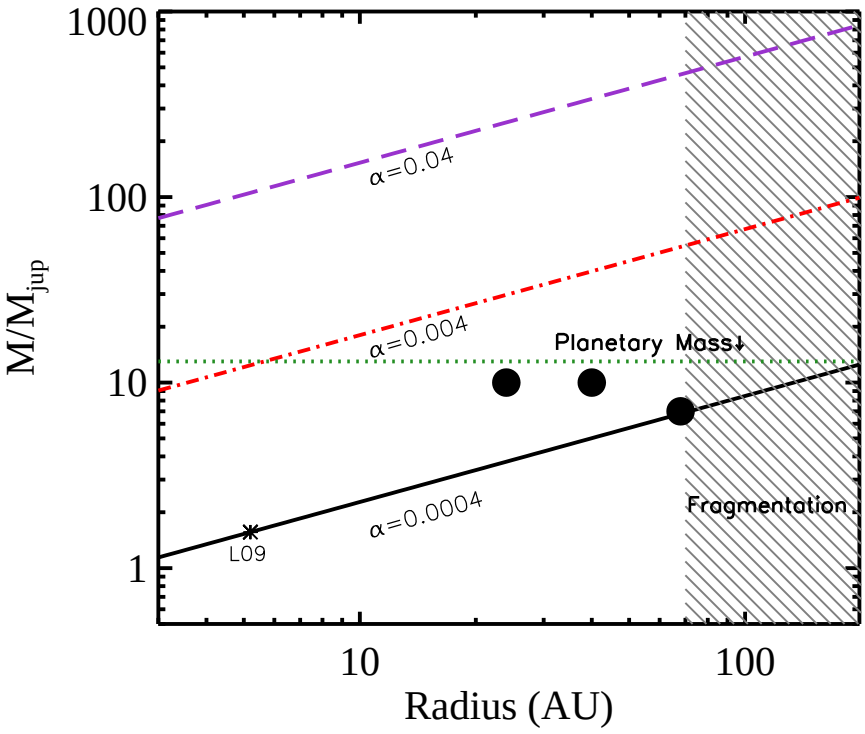

Figure 6.5: The gap starvation mass as a function of disk radius. We show curves for several values for α, and indicate the planetary mass regime, and the region in which disk fragmentation is likely. We use $f_S = 5$, scaled to simulation 2lJ of Jupiter formation in Lissauer et al. (2009) (labeled L09 in the figure). The radial scaling is derived assuming $H/r \propto r^{2/7}$. For the low viscosity case, we normalize the scale height to Jupiter at 5.2 AU in a 115 K disk for comparison with L09. For the higher viscosities, we normalize the disk scale height to the lowest expected temperatures (equation 6.20). For comparison we show the HR 8799 planets as black circles.

Dissipation timescales for A-star gas disks are thought to be short, less than 2-3 Myr (Carpenter et al., 2006), which could halt growth before the gap-opening starvation mass is achieved. Radiative transfer models such as Gorti & Hollenbach (2009) have calculated that photoevaporation by the central star will become important at radii of $\sim$ 100 AU around one Myr for an A star (see also Ercolano et al., 2009). This timescale coincides with the expected fragmentation epoch, and may aid in shutting off accretion both onto the disk, and onto the planets.

6.6 GI planet formation in the context of star formation

We now consider how the disk can reach the fragmentation conditions described in §6.3 in the context of a model for star formation. Due to the effects of infall onto the disk, we find that planet formation via GI can only occur when the fragmentation epoch is concurrent with the end of the main accretion phase, as the protostar transitions from a Class I to a Class II object (Andre & Montmerle, 1994). Fragmentation at earlier times leads to the formation of more massive companions, while fragmentation at later times is unlikely because disks are too low in mass (Andrews et al., 2009).

6.6.1 Ongoing accretion and the formation of binaries and multiples

Because the cooling time constraint is easily satisfied for expected disk temperatures, disks are likely driven to fragmentation by lowering Q. Even when Q is above the threshold for fragmentation, torques generated by self-gravity (e.g. spiral arms) can drive accretion. When the infall rate onto the disk is low, a self-gravitating disk regulates its surface density and hence Q so that the torques are just large enough to transport the supplied mass down to the star, thereby avoiding fragmentation. However, GI cannot process matter arbitrarily quickly because the torques saturate. Thus the disk will be driven toward fragmentation if the infall rate becomes too high. This critical accretion rate is a function of disk temperature:

$$\dot{M}_{\rm crit} \approx \frac{3c_s^3\alpha_{\rm sat}}{GQ} \tag{6.28}$$

(Gammie, 2001; Matzner & Levin, 2005). Numerical simulations show that GI saturates at $\alpha_{\rm sat} \sim 0.3 - 1$ (Gammie, 2001; Krumholz et al., 2007b; Lodato & Rice, 2005; Kratter et al., 2010). If the infall rate onto the disk exceeds $\dot{M}_{\rm crit}$ the disk can no longer regulate the surface density to keep Q just above unity, and fragmentation will occur. Because the conversion of accretion energy to thermal energy at large radii is inefficient, disks cannot restabilize through heating to arbitrarily high accretion rates (Kratter & Matzner, 2006).

If fragmentation occurs due to rapid accretion, as described above, it is difficult to limit subsequent fragment growth. As demonstrated in §6.5.2, gap opening does not limit accretion efficiently when the effective viscosity, in this case, $\alpha_{\rm sat}$, is high.

A more general barrier to making small fragments during rapid infall is the large reservoir of material passing by the fragment as star formation proceeds (Bonnell & Bate, 1994a). The specific angular momentum, j, of accreting disk material typically increases with time (modulo small random fluctuations in a turbulent core), landing at a circularization radius, $r_{\rm circ} = j^2/GM_*$, which is larger than the fragment's orbit. Since the fragment's Hill radius is roughly 10% of the disk radius, newly accreted material undergoes many orbits in the fragment's sphere of influence as it tries to accrete onto the central star, and some fraction will accrete onto the fragment itself. This process is less efficient if global GI modes drive fragments to smaller radii, because their Hill radii shrink. However, growth to stellar (or sub-stellar) masses may still occur as long as migration timescales are not faster than accretion timescales. The latter scenario implies that the disk cannot fragment at early times and still reproduce a single-star system like HR 8799.

The trend toward continued growth and even mass equalization following disk fragmentation is observed in numerous simulations with ongoing accretion (Bonnell & Bate, 1994a; Bate, 2000; Matsumoto & Hanawa, 2003; Walch et al., 2009b; Kratter et al., 2010; Krumholz et al., 2009). Simulations of planet formation by GI with ongoing accretion also illustrate this behavior (Boley, 2009).

Consequently, if the HR 8799 planets formed by GI, they must have fragmented at the tail end of accretion from the protostellar core onto the disk. Most likely, this requires that the protostellar core have properties such that its infall rate reaches the critical value in equation (6.28) just as the core is drained of material. If this coincidence in timing does not occur, fragmentation produces a substellar, rather than a planetary, companion. Whether fragmentation at this epoch can produce non-heirarchical orbits like HR 8799 remains to be explored.

6.6.2 Reaching Instability in the absence of infall: FU Orionis outbursts

Driving the disk unstable with external accretion corresponds to excessive growth of fragments. It is therefore tempting to consider mechanisms to lower Q through disk cooling, while holding the column density fixed. Because the disks are dominated by irradiation, changes in the viscous dissipation due to accretion are unlikely to affect a significant temperature change, and so lowering Q requires order of magnitude changes in the stellar luminosity due to the weak scaling of $T \propto L^{2/7}$. FU Orionis type outbursts (Hartmann & Kenyon, 1996) can cause rapid changes in luminosity. To result in planetary mass fragments, the luminosity drop following an FU Ori outburst would need to reach at least the minimum luminosity used in equation (6.20) on timescales shorter than an outer disk dynamical time.

The accretion of GI formed embryos onto the protostar is a proposed source of the outbursts (Vorobyov & Basu, 2006). If this occurs, perhaps a final generation of gravitational fragments, the so-called "last of the Mohicans" (Gonzalez, 1997), would remain as detectable companions. Although the lack of infall in this scenario might ease the gap opening constraints, fragments face all of the other difficulties discussed above in remaining low in mass.

6.7 Migration in a multi-planet system

A final consideration for making wide orbit planets through GI is their subsequent migration history. If formed via GI, the HR 8799 planets had to migrate inward to their current locations. There is an independent reason to believe that migration did in fact take place in this system. As discussed by Fabrycky & Murray-Clay (2008), the long term stability of HR 8799 requires a resonant orbital configuration, most plausibly a 4:2:1 mean motion resonance, which likely resulted from convergent migration in the protoplanetary gas disk. We demonstrate below that while this history is plausible, it requires special disk conditions.

Inward Type II migration (appropriate for gap opening planets) is expected at formation, because the fragmenting region is within the part of the disk accreting onto the

star. Type II migration of a single planet occurs on the disk viscous timescale:

$$\tau_\nu \approx \frac{r^2}{\nu} = \frac{r^2\Omega}{\alpha c_s^2} \tag{6.29}$$

$$\approx 0.4\,\mathrm{Myr}\left(\frac{\mathrm{r}}{70\ \mathrm{AU}}\right)^{13/14}\left(\frac{\mathrm{M}_*}{1.5\mathrm{M}_\odot}\right)^{1/2}\left(\frac{\alpha}{0.1}\right)^{-1} \tag{6.30}$$

where we have used $\nu = \alpha c_s^2/\Omega$. This timescale is short enough to allow substantial migration during the lifetime of the gas disk.

If fragments migrated inward independently, they could never become captured in resonance, as the innermost planet would migrate farther and farther from its neighbor. However, as shown in §6.5, planetary gaps may overlap if they are within several Hill radii of each other, comparable to the current separations between the HR 8799 planets. This overlap alters the torques felt by, and thus the migration of, the planets. As shown by Kley (2000), if multiple planetary gaps interact, convergent migration is possible. Gap interaction allows an outer planet to shield an inner planet from the material, and thus torques, of the outer disk, slowing or halting its inward migration and allowing the outer planet to catch up. This mechanism is invoked by Lee & Peale (2002) to generate convergent migration and resonance capture in the planets orbiting GJ 876.

Under the assumption that gap overlap allows convergent migration and resonance capture, we now ask: What is the overall direction of the subsequent migration? We note that if the planets migrated a substantial distance after resonance capture, eccentricity damping by the gas disk was likely necessary (c.f., Lee & Peale, 2002). We do not consider eccentricity damping further here. Once two planets are caught in mean-motion resonance, the torque on an individual planet from the gas disk can cause both planets to migrate, with angular momentum transfer mediated by the resonance. Masset & Snellgrove (2001) (see also Crida et al., 2009) have argued that the torque imbalance on a pair of gap-opening resonant planets can even reverse the direction of migration, although this relies on a significant difference between planet masses.

Nevertheless, understanding the planets' overall migration requires understanding how overlapping gaps alter the torque balance on the group of planets. Guided by our interest in clean gaps that limit the growth of planets (§6.5–6.6), we consider the following simplified problem.

We imagine that the three planets have cleared, and are embedded in, a single large gap which is sufficiently clean that any disk gas passing through is dynamically unimportant. Because the system is locked in a double mean-motion resonance, we assume

that an imbalance in the torques acting on the two edges of the gap can cause all three planets to migrate. We can then ask: is there a sufficient flux of angular momentum from the outer disk to cause the planets to migrate inward with the viscous accretion of the disk?

When in the 4:2:1 resonance, the total angular momentum of the planets is roughly $2.4 M_p \Omega_p r_p^2$, where we have assumed that the planets are roughly equal in mass, M_p, while r_p and Ω_p are the separation and Keplerian angular velocity of the outermost planet. The angular momentum flux from the outer disk is large enough to move the planets on a viscous time r_p^2/ν when:

$$\dot{M} \Omega_p r_p^2 \gtrsim 2.4 M_p \Omega_p r_p^2 (\nu / r_p^2) \ , \tag{6.31}$$

where $\dot{M} = 3\pi\Sigma\nu$ is the mass flux through radius r_p.

Using the above inequality, we can calculate a critical disk surface density at the current location of the outer planet such that the disk can push the planets inward:

$$\Sigma \gtrsim \frac{M_p}{4 r_p^2}. \tag{6.32}$$

For $M_p = 10 M_{\rm Jup}$ and our fiducial disk temperatures (equation 6.20), this constraint is always satisfied when $Q = 1$. The disk is unable to cause inward migration when $\Sigma \lesssim 4 {\rm g/cm^2}$ at 70 AU, which is equivalent to $Q \sim 20$.

If the planets do share a clean common gap, a large fraction of the disk would be effectively cleared of gas while a massive outer disk is still present. A similar mechanism has been invoked to explain transitional disks, which contain holes at radii of a few tens of AU and smaller (Calvet et al., 2002). Transport of disk gas through a less well-cleared gap could substantially alter this picture.

In summary, it is possible to envision a scenario in which the HR 8799 planets migrate inward to their current locations in such a way that their orbits converge, allowing resonance capture. This scenario is consistent with other constraints on GI planet formation: shortly after formation, the disk must have low accretion rates and decline in mass in order to (a) limit the growth of fragments, (b) allow for large, overlapping gaps.

More stringent constraints will require future work on migration in gravitationally unstable disks, particularly in the presence of multiple planets massive enough to clear large, overlapping gaps.

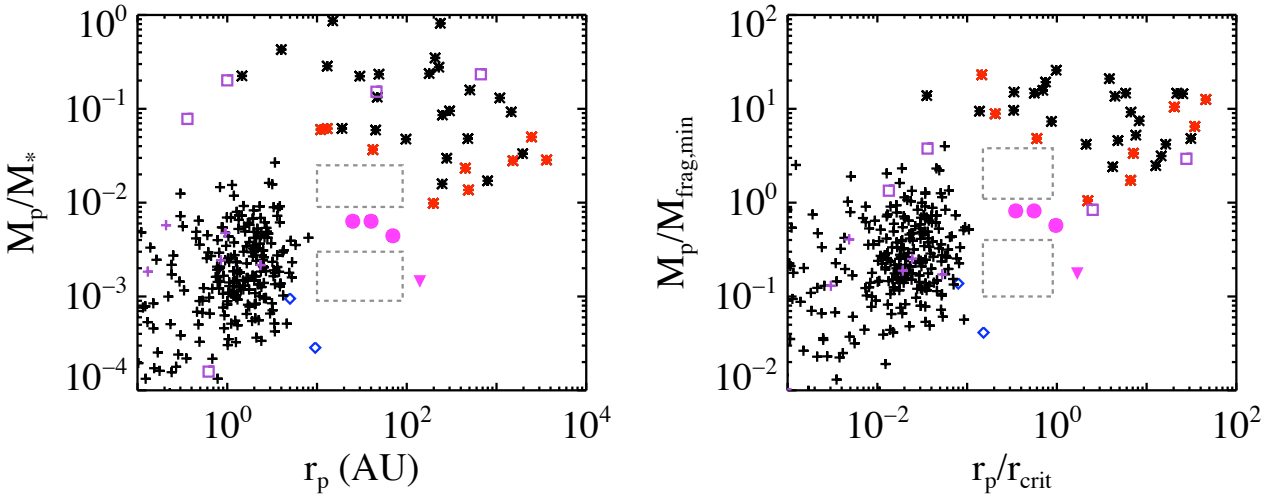

Figure 6.6: (Left) Known substellar companions (stars) and planets (plusses) as a function of mass ratio and projected separation. The three objects in the HR 8799 system are shown by pink circles, and a pink triangle denotes the upper-limit mass ratio for Fomalhaut b based on the dynamical mass estimate of Chiang et al. (2009). Grey squares indicate the gap regions. Ongoing surveys are necessary to determine whether there is a continuous distribution between Jupiter/Saturn (blue diamonds) and HR 8799, or HR 8799 and brown dwarf companions. Planets around very low mass primaries with $M_* = 0.02$–$0.1 M_\odot$ are marked by purple squares. These systems have mass ratios more akin to the substellar companions than to the remainder of the population of planets. Primary masses range from $M_* = 0.02 M_\odot$–$1 M_\odot$ (black) and $M_* = 1 M_\odot$–$2.9 M_\odot$ (red) for substellar companions and from $M_* = 0.1$–$0.4 M_\odot$ (purple) and $M_* = 0.4$–$4.5 M_\odot$ (black) for planets. (Right) The same objects plotted as function of the minimum fragment mass, $M_{\rm frag,min}$ and critical radius, $r_{\rm crit}$. We use equation (6.16) to calculate $r_{\rm crit}$. For $M_{\rm frag,min}$, we apply equation (6.6) at radius $r_{\rm crit}$ under the simplified assumption that the disk temperature is set by the stellar luminosity: $L/L_\odot = (M_*/M_\odot)^{3.5}$ for $M_* > 0.43 M_\odot$ and $L \propto M_*^{2.3}$ for lower-mass stars. The temperatures used to calculate fragment masses are not allowed to dip below 20K. Masses below $M_{\rm frag,min}$ are unlikely to result from GI.

6.8 Current Observational Constraints

While there is a regime of parameter space in which planet formation is possible, typical conditions produce more massive ($> 13 M_{\rm Jup}$) companions. If GI fragmentation ever forms planets, then fragmentation should typically form more massive objects. Consequently, these planets would constitute the low mass tail of a distribution of disk-born companions. If the mass distribution is continuous there should be more sub-stellar companions than planets at comparable distances of 50-150 AU. Observing this population is a strong constraint on the formation mechanism, but current data are insufficient to draw conclusions.

Zuckerman & Song (2009) have compiled the known sub-stellar companions in this range of radii to date. This range of separations falls beyond the well-established inner brown dwarf "desert" (McCarthy & Zuckerman, 2004), and has not been well probed due to observational difficulties at these low mass ratios. Note that the overall dearth of brown dwarf companions to solar mass stars is not a selection effect (Metchev & Hillenbrand, 2009; Zuckerman & Song, 2009).

We illustrate the observational constraints by plotting the companions from Zuckerman & Song (2009) along with the known exoplanets compiled by the Exoplanet Encyclopedia[1] as a function of mass ratio and projected separation in Fig. 6.6a, and as a function of minimum fragment masses and fragmentation radii in Fig. 6.6b. We compare these with the HR 8799 planets, Fomalhaut b, and the solar system giants. We distinguish between stars of different masses because disk fragmentation becomes more likely for higher mass stars (Kratter et al., 2008).

At present, neither the population of substellar companions nor the population of exoplanets is continuous out to HR 8799. Many selection biases are reflected in Fig. 6.6, and these gaps in particular may be due to selection effects; resolution and sensitivity make it difficult to detect both wide orbit planets, and close-in low mass brown dwarfs. We note that while there are actually fewer planets at distances less than 1 AU, the cutoff above 5 AU is unphysical. There is not yet any indication of an outer cut off radius in the exoplanets: if they continued out to larger separation, the distribution would easily encompass the HR 8799 and Fomalhaut systems.

Data from ongoing surveys like that which found HR 8799 are necessary to verify the true companion distribution as a function of mass and radius. If these planets are

[1]October 2009, http://exoplanet.eu, compiled by Jean Schneider

formed through GI, we would expect observations to fill in the gap between HR 8799 and higher mass ratio objects to show a continuous distribution. If these planets are formed via core accretion, than observations may fill in the plot on the opposite side of HR 8799, occupying a region of parameter space for which neither core accretion nor GI is currently a successful formation mechanism.

6.9 Summary

We have demonstrated that while GI-driven fragmentation is possible at wide distances from A stars, fragment masses typically exceed the deuterium burning "planet" limit. In contrast, the formation of sub-stellar and stellar companions is more likely because moderate disk temperatures and active accretion onto and through the disk drive disk-born objects to higher masses.

If the HR 8799 planets did form by GI, the following criteria had to be met:

1. Fragments should form beyond $40 - 70$ AU: inside of this location the disk will not fragment into planetary mass objects even if $Q \lesssim 1$. Grain growth is required for fragmentation at the lower end of this range.

2. Temperatures must be colder than those of typical disks to limit the initial fragment masses.

3. The disk must be driven unstable at a special time: infall onto the disk must be low, but the disk must remain massive (e.g. the end of the Class I phase). The disk must only become unstable to fragmentation at this point because earlier episodes of instability should lead to sub-stellar or stellar companion formation.

4. The subsequent growth of fragments must be limited through efficient gap clearing necessitating low disk viscosity or early gap overlap. Disk dispersal via photoevaporation may also be necessary.

5. The three fragments must form at the same epoch separated by several Hill radii, implying that the entire outer disk becomes unstable simultaneously.

6. Migration must be convergent. This likely requires the gaps of the planets to overlap so as to starve the inner most planet of disk material, thereby preventing runaway inward migration.

If these conditions are met, then the planets in HR 8799 could comprise the low-mass tail of the disk-born binary distribution, the runts of the litter. In this case one would expect to find a larger number of brown dwarfs or even M stars in the same regime of parameter space – surrounding A-stars at distances of $50 - 150$ AU.

Ongoing direct imaging surveys of A and F stars will provide a strong constraint on the formation mechanism for this system: if HR 8799 is the most massive of a new distribution of widely separated planets, our analysis suggests that formation by GI is unlikely. On the contrary, the discovery of a population of brown dwarf and M-star companions to A-stars would corroborate formation via disk fragmentation.

6.10 Appendix A. Cooling and Fragmentation in Irradiated disks

Rafikov (2009) has suggested that the cooling time might be altered in an irradiated disk. Here we consider the cooling time for thermal perturbations to a disk, and show that a simple formula [equation (6.39)] gives the cooling time for arbitrary levels of irradiation, at least in radiative optically thick disks.

Consider ambient radiation striking an optically thick disk with a normal flux $F_o = \sigma T_o^4 \equiv (3/8) F_{\rm irr}$ (where the numerical factor in the last definition is purely for later convenience). Note that T_o depends both on the irradiation field (from the host star and/or light emitted and reflected from a surrounding envelope) and also on the disk's surface geometry, e.g. flaring angle. By incorporating these variables into T_o we attempt a general calculation. At the photosphere, where the optical depth to the disk's self-emission $\tau = \tau_{\rm phot} \approx 1$, energy balance gives:

$$\sigma T_{\rm eff}^4 \simeq \sigma T_o^4 + F/2 \,. \tag{6.33}$$

Here, F is the luminous flux from any internal sources of energy dissipation, e.g. viscous accretion, shocks, or the gravitational binding energy released by a collapsing fragment. The factor of two reflects that half of the radiation is emitted from each surface of the disk. Since optical light is absorbed above the IR photosphere, about half the irradiation free streams out before it heats the disk (Chiang & Goldreich, 1997). We can absorb this reduction into the definition of T_o.

We assume heat is transferred by radiative diffusion as:

$$\frac{4}{3}\sigma\frac{dT^4}{d\tau} = \frac{F}{2}. \tag{6.34}$$

since convection is suppressed by irradiation and may be a negligible correction in any event (Rafikov, 2007). Integration from the midplane at $\tau = \tau_{\rm tot}$ and $T = T_{\rm m}$ to the photosphere gives:

$$(4/3)\sigma(T_{\rm m}^4 - T_{\rm eff}^4) = (F/2)(\tau_{\rm tot} - \tau_{\rm phot})\,. \tag{6.35}$$

We now drop the subscripts from $\tau_{\rm tot}$ and the midplane $T_{\rm m}$, which we will soon take as the characteristic temperature (ignoring order unity corrections from height averaging). Furthermore we apply equation (6.33) and take the $\tau_{\rm phot} \ll \tau_{\rm tot} \to \tau$ limit (meaning that we don't need to know the precise location of the photosphere) to express

$$F \simeq \frac{8\sigma}{3\tau}(T^4 - T_o^4) = \frac{1}{\tau}\left(\frac{8\sigma T^4}{3} - F_{\rm irr}\right)\,, \tag{6.36}$$

which shows that the midplane temperature is controlled by the larger of $F\tau$ and $F_{\rm irr}$.

The cooling timescale to radiate away thermal fluctuations (generated e.g. by GI) is

$$t_{\rm cool} = \frac{\Sigma\delta U}{\delta F} \tag{6.37}$$

where a temperature perturbation δT has an excess heat $\delta U \approx c_P\delta T$, and $c_P = (k/\mu)\gamma/(\gamma - 1)$ is the specific heat for a mean molecular weight μ and adiabatic index γ. Strongly compressive motions, which are not at constant pressure, will introduce order unity corrections that we ignore.

The excess luminous flux, using equation (6.36), is

$$\begin{aligned}\delta F &= \frac{8\sigma}{3\tau}\frac{\delta T}{T}\left[(4-\beta)T^4 + \beta T_o^4\right] \\ &= \frac{32\sigma T^3\delta T}{3\tau}\times\left\{\begin{array}{cc}(1-\beta/4) & \text{if } T \gg T_o, \beta \neq 4 \\ 1 & \text{if } T \simeq T_o\end{array}\right.\,,\end{aligned} \tag{6.38}$$

where $\tau = \kappa\Sigma/2 \propto T^\beta$. The point is that the escaping flux varies by only an order unity factor between the strongly ($T \simeq T_o$) and weakly ($T \gg T_o$) irradiated regimes. Typical grain opacities, $0 < \beta < 2$, ensure the correction is order unity (and also ensure that we can ignore the catastrophic heating that would occur if $\beta > 4$).

Combining equations (6.37) and (6.38) with the definition of heat capacity we find that the cooling time is simply

$$t_{\rm cool} \approx \frac{3\gamma\Sigma c_s^2\tau}{32(\gamma-1)\sigma T^4}\times\left\{\begin{array}{cc}(1-\beta/4)^{-1} & \text{if } T \gg T_o, \beta \neq 4 \\ 1 & \text{if } T \simeq T_o\end{array}\right.\,, \tag{6.39}$$

where the isothermal sound speed $c_s = \sqrt{kT/\mu}$.

From this derivation, we see that the cooling time obeys the simple form of equation (6.39) for all levels of irradiation — which only introduces an order unity β correction. The cooling time depends on β for weakly irradiated disks because changes to the opacity alter the amount of flux that escapes from the midplane. In highly irradiated disks, opacity changes have little effect because the small difference between the midplane and surface temperatures drives a weak flux.

While increasing the irradiative flux incident on a disk decreases the cooling time by raising T, it will not trigger fragmentation in a $Q \sim 1$ disk, since it increases Q. We will not explore optically thin or convective disks at this time.

We assume that $\Omega t_{\rm cool} < \zeta \sim 3$ is the fragmentation criterion independent of irradiation. When the cooling time is longer, the disk is presumed to enter a state of gravito-turbulence (Gammie, 2001). We take this term to mean a quasi-steady state of gravitationally driven turbulence, on scales $\lesssim H$ wherein viscous dissipation of GI turbulence regulates $Q \sim 1$. Thus the cooling time can be translated to a the critical value of α at which gravito-turbulent accretion disks will fragment. While Rice et al. (2005) find that an α-threshold is more robust than one for $t_{\rm cool}$ when the adiabatic index varies, they did not include irradiation, which we contend would reveal that cooling is ultimately the more physical criterion, but the issue is best settled by simulation. The emitted flux with an α-viscosity and $Q \sim 1$ gives

$$F \approx (9/4)\nu\Sigma\Omega^2 \approx 9/(4\pi)\alpha c_s^3 \Omega^2/G \tag{6.40}$$

which combined with equation (6.36) and equation (6.39) without the β correction gives

$$\Omega t_{\rm cool} \approx \left(\frac{\gamma}{\gamma-1}\right)\frac{\Omega\Sigma c_s^2}{4\left(F + F_{\rm irr}/\tau\right)} \approx \left(\frac{\gamma}{\gamma-1}\right)\frac{1}{9\alpha}\left(1+\frac{F_{\rm irr}}{F\tau}\right)^{-1} \tag{6.41}$$

When irradiation is weak enough that $F_{\rm irr} \lesssim F\tau$, we recover the standard $\alpha \gtrsim 1$ criterion for fragmentation (ignoring the accumulated order unity coefficients). However for stronger irradiation with $F_{\rm irr} \gtrsim F\tau$, fragmentation occurs for $\alpha \gtrsim F\tau/F_{\rm irr}$, a lower threshold.

Gravito-turbulent models require modification when $F_{\rm irr} \gtrsim F$, i.e. an even lower level of irradiation than needed to affect the α fragmentation threshold. In this case the disk shows some similarities to isothermal disks, and should have lower amplitude density perturbations, because there is insufficient viscous dissipation to support order unity thermal

perturbations (see the related discussion in Rafikov, 2009). We note that simulations of isothermal disks do develop GI, exhibit GI-driven transport and fragment (Krumholz et al., 2007b; Kratter et al., 2010), but they do not appear particularly turbulent.

6.11 Appendix B. Temperature due to Viscous Heating

We now show that viscous heating is relatively unimportant in the outer reaches of irradiated A-star disks (see also section 3 of Rafikov 2009). For an optically thick disk with an ISM opacity law, balancing viscous heating and emitted radiation gives

$$\frac{8}{3\tau}\sigma T^4 \approx \frac{3}{8\pi}\dot{M}\Omega^2 \tag{6.42}$$

The solution for the midplane temperature is

$$T \approx \left(\frac{9}{128\pi^2}\frac{\dot{M}\kappa_o\sqrt{k/\mu}}{\sigma G Q_o}\right)^{2/3}\Omega^2 \approx 9\text{ K}\left(\frac{\dot{M}}{10^{-6}M_\odot/\text{yr}}\right)^{2/3}Q_o^{-2/3}\left(\frac{r}{70\text{ AU}}\right)^{-3}, \tag{6.43}$$

lower than the irradiation temperatures shown in Fig. 6.3 by more than a factor of four. Note that the surface density falloff

$$\Sigma = \frac{c_s\Omega}{\pi G Q_o} \approx 35\text{ g/cm}^2\left(\frac{r}{70\text{ AU}}\right)^{-3}\left(\frac{\dot{M}}{10^{-6}M_\odot/\text{yr}}\right)^{1/3} \tag{6.44}$$

is also quite steep for a constant $Q_0 = 1$, viscous disk with the ISM opacity law.

If the disk is optically thin, then the balance between heating and cooling gives:

$$4\tau\sigma T^4 \approx \frac{3}{8\pi}\dot{M}\Omega^2 \tag{6.45}$$

$$T \approx \left(\frac{3G\dot{M}Q_o\Omega}{16\sigma\kappa_o\sqrt{k/\mu}}\right)^{2/13} \tag{6.46}$$

$$\approx 9\text{ K}\left(\frac{\dot{M}}{10^{-6}M_\odot/\text{yr}}\right)^{2/13}\left(\frac{M_*}{1.5M_\odot}\right)^{1/13}Q_o^{2/13}\left(\frac{r}{70\text{ AU}}\right)^{-3/13} \tag{6.47}$$

This temperature profile is shallow, but still colder than the irradiation temperature at large radii where the disk becomes optically thin.

Bibliography

Adams, F. C., Lada, C. J., & Shu, F. H. 1987, ApJ, 312, 788

Adams, F. C., Proszkow, E. M., Fatuzzo, M., & Myers, P. C. 2006, ApJ, 641, 504

Adams, F. C., Ruden, S. P., & Shu, F. H. 1989, ApJ, 347, 959

Andre, P., & Montmerle, T. 1994, ApJ, 420, 837

Andre, P., Ward-Thompson, D., & Barsony, M. 1993, ApJ, 406, 122

Andrews, S. M., & Williams, J. P. 2007, ApJ, 659, 705

Andrews, S. M., Wilner, D. J., Hughes, A. M., Qi, C., & Dullemond, C. P. 2009, ApJ, 700, 1502

Anglada, G., Rodríguez, L. F., Osorio, M., Torrelles, J. M., Estalella, R., Beltrán, M. T., & Ho, P. T. P. 2004, ApJ, 605, L137

Artymowicz, P., & Lubow, S. H. 1996, ApJ, 467, L77+

Aumann, H. H., Beichman, C. A., Gillett, F. C., de Jong, T., Houck, J. R., Low, F. J., Neugebauer, G., Walker, R. G., & Wesselius, P. R. 1984, ApJ, 278, L23

Balbus, S. A., & Hawley, J. F. 1994, MNRAS, 266, 769

—. 2006, ApJ, 652, 1020

Balbus, S. A., & Papaloizou, J. C. B. 1999, ApJ, 521, 650

Ballesteros-Paredes, J., Klessen, R. S., Mac Low, M.-M., & Vazquez-Semadeni, E. 2007, in Protostars and Planets V, ed. B. Reipurth, D. Jewitt, & K. Keil, 63–80

Bally, J., Cunningham, N., Moeckel, N., & Smith, N. 2005, in IAU Symposium, ed. R. Cesaroni, M. Felli, E. Churchwell, & M. Walmsley, 12–22

Banerjee, R., & Pudritz, R. E. 2007, ApJ, 660, 479

Barnes, P. J., Yonekura, Y., Ryder, S. D., Hopkins, A. M., Miyamoto, Y., Furukawa, N., & Fukui, Y. 2008, ArXiv e-prints

Bate, M. R. 2000, MNRAS, 314, 33

Bate, M. R., & Bonnell, I. A. 1997, MNRAS, 285, 33

Bate, M. R., Bonnell, I. A., & Bromm, V. 2003, MNRAS, 339, 577

Beckwith, S. V. W., Henning, T., & Nakagawa, Y. 2000, Protostars and Planets IV, 533

Beckwith, S. V. W., Sargent, A. I., Chini, R. S., & Guesten, R. 1990, AJ, 99, 924

Bell, K. R., & Lin, D. N. C. 1994, ApJ, 427, 987

Beltrán, M. T., Cesaroni, R., Codella, C., Testi, L., Furuya, R. S., & Olmi, L. 2006, *Nature*, 443, 427

Bernard, J. P., Dobashi, K., & Momose, M. 1999, A&A, 350, 197

Bertin, G. 1983, A&A, 127, 145

Bertin, G., & Lodato, G. 1999, A&A, 350, 694

Beuther, H. 2006, in IAU Symposium 237: Triggered Star Formation in a Turbulent ISM, ed. B. G. Elmegreen & J. Palous, in press, astro-ph/0610411

Beuther, H., Churchwell, E. B., McKee, C. F., & Tan, J. C. 2006, ArXiv Astrophysics e-prints

Beuther, H., Churchwell, E. B., McKee, C. F., & Tan, J. C. 2007, in Protostars and Planets V, B. Reipurth, D. Jewitt, and K. Keil (eds.), University of Arizona Press, Tucson, 951 pp., 2007., p.165-180, ed. B. Reipurth, D. Jewitt, & K. Keil, 165–180

Bodenheimer, P. 1995, ARA&A, 33, 199

Bodenheimer, P., Tohline, J. E., & Black, D. C. 1980, ApJ, 242, 209

Boley, A. C. 2009, ApJ, 695, L53

Boley, A. C., Mejía, A. C., Durisen, R. H., Cai, K., Pickett, M. K., & D'Alessio, P. 2006, ApJ, 651, 517

Bonnell, I. A., & Bate, M. R. 1994a, MNRAS, 269, L45

—. 1994b, MNRAS, 271, 999

Bonnell, I. A., Vine, S. G., & Bate, M. R. 2004, MNRAS, 349, 735

Bonnor, W. B. 1956, MNRAS, 116, 351

Boss, A. P. 1997, Science, 276, 1836

Boss, A. P., Fisher, R. T., Klein, R. I., & McKee, C. F. 2000, ApJ, 528, 325

Bower, G. C., Plambeck, R. L., Bolatto, A., McCrady, N., Graham, J. R., de Pater, I., Liu, M. C., & Baganoff, F. K. 2003, ApJ, 598, 1140

Bryden, G., Chen, X., Lin, D. N. C., Nelson, R. P., & Papaloizou, J. C. B. 1999, ApJ, 514, 344

Burgasser, A. J., Dhital, S., & West, A. A. 2009, AJ, 138, 1563

Burkert, A., & Bodenheimer, P. 2000, ApJ, 543, 822

Cai, K., Durisen, R. H., Boley, A. C., Pickett, M. K., & Mejía, A. C. 2008, ApJ, 673, 1138

Calvet, N., D'Alessio, P., Hartmann, L., Wilner, D., Walsh, A., & Sitko, M. 2002, ApJ, 568, 1008

Calvet, N., D'Alessio, P., Watson, D. M., Franco-Hernández, R., Furlan, E., Green, J., Sutter, P. M., Forrest, W. J., Hartmann, L., Uchida, K. I., Keller, L. D., Sargent, B., Najita, J., Herter, T. L., Barry, D. J., & Hall, P. 2005, ApJ, 630, L185

Carpenter, J. M., Mamajek, E. E., Hillenbrand, L. A., & Meyer, M. R. 2006, ApJ, 651, L49

Caselli, P., & Myers, P. C. 1995, ApJ, 446, 665

Cesaroni, R. 2005, Ap&SS, 295, 5

Cesaroni, R., Galli, D., Lodato, G., Walmsley, C. M., & Zhang, Q. 2007, in Protostars and Planets V, B. Reipurth, D. Jewitt, and K. Keil (eds.), University of Arizona Press, Tucson, 951 pp., 2007., p.197-212, ed. B. Reipurth, D. Jewitt, & K. Keil, 197–212

Cesaroni, R., Galli, D., Lodato, G., Walmsley, M., & Zhang, Q. 2006, *Nature*, 444, 703

Cesaroni, R., Neri, R., Olmi, L., Testi, L., Walmsley, C. M., & Hofner, P. 2005, A&A, 434, 1039

Chabrier, G., & Baraffe, I. 2000, ARA&A, 38, 337

Chandrasekhar, S. 1961, Hydrodynamic and hydromagnetic stability (International Series of Monographs on Physics, Oxford: Clarendon, 1961)

Chang, P., Strubbe, L. E., Menou, K., & Quataert, E. 2009, ArXiv e-prints

Chiang, E., Kite, E., Kalas, P., Graham, J. R., & Clampin, M. 2009, ApJ, 693, 734

Chiang, E., & Youdin, A. 2009, ArXiv e-prints

Chiang, E. I., & Goldreich, P. 1997, ApJ, 490, 368

Chick, K. M., & Cassen, P. 1997, ApJ, 477, 398

Chini, R., Hoffmeister, V., Kimeswenger, S., Nielbock, M., Nürnberger, D., Schmidtobreick, L., & Sterzik, M. 2004, *Nature*, 429, 155

Clarke, C. J., Harper-Clark, E., & Lodato, G. 2007, MNRAS, 381, 1543

Clarke, C. J., & Pringle, J. E. 1991, MNRAS, 249, 584

Cossins, P., Lodato, G., & Clarke, C. J. 2009, MNRAS, 393, 1157

Crida, A., Masset, F., & Morbidelli, A. 2009, ApJ, 705, L148

Crida, A., Morbidelli, A., & Masset, F. 2006, Icarus, 181, 587

D'Alessio, P., Calvet, N., & Hartmann, L. 1997, ApJ, 474, 397

—. 2001, ApJ, 553, 321

D'Angelo, G., Kley, W., & Henning, T. 2003, ApJ, 586, 540

Davis, S. W., Stone, J. M., & Pessah, M. E. 2010, ApJ, 713, 52

De Buizer, J. M. 2006, ApJ, 642, L57

De Buizer, J. M., & Minier, V. 2005, ApJ, 628, L151

de Marchi, G., Clampin, M., Greggio, L., Leitherer, C., Nota, A., & Tosi, M. 1997, ApJ, 479, L27+

Dodson-Robinson, S. E., Veras, D., Ford, E. B., & Beichman, C. A. 2009, ApJ, 707, 79

Dubinski, J., & Chakrabarty, D. 2009, ApJ, 703, 2068

Dubinski, J., Narayan, R., & Phillips, T. G. 1995, ApJ, 448, 226

Duchêne, G., Delgado-Donate, E., Haisch, Jr., K. E., Loinard, L., & Rodríguez, L. F. 2007, in Protostars and Planets V, ed. B. Reipurth, D. Jewitt, & K. Keil, 379–394

Dupuy, T. J., Liu, M. C., & Ireland, M. J. 2009, ApJ, 692, 729

Duquennoy, A., & Mayor, M. 1991, A&A, 248, 485

Durisen, R. H., Boss, A. P., Mayer, L., Nelson, A. F., Quinn, T., & Rice, W. K. M. 2007, in Protostars and Planets V, ed. B. Reipurth, D. Jewitt, & K. Keil, 607–622

Eisner, J. A., Plambeck, R. L., Carpenter, J. M., Corder, S. A., Qi, C., & Wilner, D. 2008, ApJ, 683, 304

Enoch, M. L., Evans, N. J., Sargent, A. I., & Glenn, J. 2009, ApJ, 692, 973

Ercolano, B., Clarke, C. J., & Drake, J. J. 2009, ApJ, 699, 1639

Evans, N. J., Dunham, M. M., Jørgensen, J. K., Enoch, M. L., Merín, B., van Dishoeck, E. F., Alcalá, J. M., Myers, P. C., Stapelfeldt, K. R., Huard, T. L., Allen, L. E., Harvey, P. M., van Kempen, T., Blake, G. A., Koerner, D. W., Mundy, L. G., Padgett, D. L., & Sargent, A. I. 2009, ApJS, 181, 321

Fabrycky, D. C., & Murray-Clay, R. A. 2008, ArXiv e-prints

Faúndez, S., Bronfman, L., Garay, G., Chini, R., Nyman, L., & May, J. 2004, A&A, 426, 97

Figer, D. F., Kim, S. S., Morris, M., Serabyn, E., Rich, R. M., & McLean, I. S. 1999, ApJ, 525, 750

Fisher, R. T. 2002, PhD thesis, AA(UNIVERSITY OF CALIFORNIA, BERKELEY)

—. 2004, ApJ, 600, 769

Fleck, Jr., R. C. 1987, ApJ, 315, 259

Fleming, T. P., Stone, J. M., & Hawley, J. F. 2000, ApJ, 530, 464

Forgan, D., & Rice, K. 2010, MNRAS, 402, 1349

Foster, P. N., & Chevalier, R. A. 1993, ApJ, 416, 303

Frank, J., King, A., & Raine, D. J. 2002, Accretion Power in Astrophysics: Third Edition (Accretion Power in Astrophysics, by Juhan Frank and Andrew King and Derek Raine, pp. 398. ISBN 0521620538. Cambridge, UK: Cambridge University Press, February 2002.)

Fromang, S., & Nelson, R. P. 2006, A&A, 457, 343

Fromang, S., Papaloizou, J., Lesur, G., & Heinemann, T. 2007, A&A, 476, 1123

Gammie, C. F. 1996, ApJ, 457, 355

—. 2001, ApJ, 553, 174

Gilbert, A. M., & Graham, J. R. 2001, Bulletin of the American Astronomical Society, 33, 1330

Goldreich, P., Lithwick, Y., & Sari, R. 2004, ARA&A, 42, 549

Goldreich, P., & Lynden-Bell, D. 1965, MNRAS, 130, 125

Goldreich, P., & Tremaine, S. 1979, ApJ, 233, 857

Gonzalez, G. 1997, MNRAS, 285, 403

Goodman, A. A., Benson, P. J., Fuller, G. A., & Myers, P. C. 1993, ApJ, 406, 528

Goodman, J., & Tan, J. C. 2004, ApJ, 608, 108

Goodwin, S. P., & Kroupa, P. 2005, A&A, 439, 565

Goodwin, S. P., Whitworth, A. P., & Ward-Thompson, D. 2004, A&A, 414, 633

Gorti, U., & Hollenbach, D. 2009, ApJ, 690, 1539

Greenberg, R. 1988, Icarus, 75, 527

Griv, E. 2006, MNRAS, 365, 1007

Hale, A. 1994, AJ, 107, 306

Hartmann, L., & Kenyon, S. J. 1996, ARA&A, 34, 207

Hernández, J., Calvet, N., Hartmann, L., Briceño, C., Sicilia-Aguilar, A., & Berlind, P. 2005, AJ, 129, 856

Hernández, J., Hartmann, L., Megeath, T., Gutermuth, R., Muzerolle, J., Calvet, N., Vivas, A. K., Briceño, C., Allen, L., Stauffer, J., Young, E., & Fazio, G. 2007, ApJ, 662, 1067

Hillenbrand, L. A., & Hartmann, L. W. 1998, ApJ, 492, 540

Hillenbrand, L. A., Strom, S. E., Vrba, F. J., & Keene, J. 1992, ApJ, 397, 613

Hinkley, S., Oppenheimer, B. R., Soummer, R., Sivaramakrishnan, A., Roberts, Jr., L. C., Kuhn, J., Makidon, R. B., Perrin, M. D., Lloyd, J. P., Kratter, K., & Brenner, D. 2007, ApJ, 654, 633

Hirose, S., Krolik, J. H., & Blaes, O. 2009, ApJ, 691, 16

Hoyle, F. 1953, ApJ, 118, 513

Hueso, R., & Guillot, T. 2005, A&A, 442, 703

Inutsuka, S.-I., & Miyama, S. M. 1992, ApJ, 388, 392

Jappsen, A.-K., & Klessen, R. S. 2004, A&A, 423, 1

Jayawardhana, R., Coffey, J., Scholz, A., Brandeker, A., & van Kerkwijk, M. H. 2006, ApJ, 648, 1206

Jiménez-Serra, I., Martín-Pintado, J., Rodríguez-Franco, A., Chandler, C., Comito, C., & Schilke, P. 2007, ApJ, 661, L187

Johansen, A., Youdin, A., & Klahr, H. 2009, ApJ, 697, 1269

Johnson, J. A., Fischer, D. A., Marcy, G. W., Wright, J. T., Driscoll, P., Butler, R. P., Hekker, S., Reffert, S., & Vogt, S. S. 2007, ApJ, 665, 785

Johnstone, D., Fich, M., Mitchell, G. F., & Moriarty-Schieven, G. 2001, ApJ, 559, 307

Kalas, P., Graham, J. R., Chiang, E., Fitzgerald, M. P., Clampin, M., Kite, E. S., Stapelfeldt, K., Marois, C., & Krist, J. 2008, Science, 322, 1345

Kenyon, S. J., Hartmann, L. W., Strom, K. M., & Strom, S. E. 1990, AJ, 99, 869

Kenyon, S. J., Whitney, B. A., Gomez, M., & Hartmann, L. 1993, ApJ, 414, 773

Keto, E. 2007, ApJ, 666, 976

Kim, S. S., Figer, D. F., Lee, H. M., & Morris, M. 2000, ApJ, 545, 301

Kirk, H., Johnstone, D., & Basu, S. 2009, ApJ, 699, 1433

Klein, R. I. 1999, Journal of Computational and Applied Mathematics, 109, 123

Kley, W. 2000, MNRAS, 313, L47

Kouwenhoven, M. B. N., Goodwin, S. P., Parker, R. J., Davies, M. B., Malmberg, D., & Kroupa, P. 2010, MNRAS, 361

Kratter, K. M., & Matzner, C. D. 2006, MNRAS, 373, 1563

Kratter, K. M., Matzner, C. D., & Krumholz, M. R. 2008, ApJ, 681, 375

Kratter, K. M., Matzner, C. D., Krumholz, M. R., & Klein, R. I. 2010, ApJ, 708, 1585

Krumholz, M. R. 2006, ApJ, 641, L45

Krumholz, M. R., Klein, R. I., & McKee, C. F. 2007a, ApJ, 665, 478

—. 2007b, ApJ, 656, 959

Krumholz, M. R., Klein, R. I., McKee, C. F., Offner, S. S. R., & Cunningham, A. J. 2009, Science, 323, 754

Krumholz, M. R., McKee, C. F., & Klein, R. I. 2004, ApJ, 611, 399

—. 2005, ApJ, 618, L33

—. 2006, ApJ, 638, 369

Krumholz, M. R., & Thompson, T. A. 2007, ApJ, 661, 1034

Lada, C. J. 2006, ApJ, 640, L63

Lafrenière, D., Marois, C., Doyon, R., & Barman, T. 2009, ApJ, 694, L148

Lagrange, A.-M., Gratadour, D., Chauvin, G., Fusco, T., Ehrenreich, D., Mouillet, D., Rousset, G., Rouan, D., Allard, F., Gendron, É., Charton, J., Mugnier, L., Rabou, P., Montri, J., & Lacombe, F. 2009, A&A, 493, L21

Larson, R. B. 1972, MNRAS, 156, 437

—. 1984, MNRAS, 206, 197

Laughlin, G., & Bodenheimer, P. 1994, ApJ, 436, 335

Laughlin, G., & Korchagin, V. 1996a, ApJ, 460, 855

—. 1996b, ApJ, 460, 855

Laughlin, G., Korchagin, V., & Adams, F. C. 1997a, ApJ, 477, 410

—. 1997b, ApJ, 477, 410

—. 1998, ApJ, 504, 945

Laughlin, G., & Rozyczka, M. 1996, ApJ, 456, 279

Lee, M. H., & Peale, S. J. 2002, ApJ, 567, 596

Lesur, G., & Ogilvie, G. I. 2010, MNRAS, 404, L64

Lesur, G., & Papaloizou, J. C. B. 2010, A&A, 513, A60+

Levin, Y. 2003, ArXiv Astrophysics e-prints

—. 2007, MNRAS, 374, 515

Levison, H. F., & Stewart, G. R. 2001, Icarus, 153, 224

Li, P. S., Norman, M. L., Mac Low, M.-M., & Heitsch, F. 2004, ApJ, 605, 800

Li, Z.-Y., & Shu, F. H. 1996, ApJ, 472, 211

Lightman, A. P., & Eardley, D. M. 1974, ApJ, 187, L1+

Lin, C. C., & Shu, F. H. 1964, ApJ, 140, 646

Lin, D. N. C., & Papaloizou, J. 1986, ApJ, 309, 846

Lin, D. N. C., & Papaloizou, J. C. B. 1993, in Protostars and Planets III, ed. E. H. Levy & J. I. Lunine, 749–835

Lin, D. N. C., & Pringle, J. E. 1987, MNRAS, 225, 607

—. 1990, ApJ, 358, 515

Lissauer, J. J. 1987, Icarus, 69, 249

Lissauer, J. J., Hubickyj, O., D'Angelo, G., & Bodenheimer, P. 2009, Icarus, 199, 338

Lithwick, Y. 2007, ApJ, 670, 789

Lodato, G., & Bertin, G. 2001, A&A, 375, 455

—. 2003, A&A, 408, 1015

Lodato, G., Meru, F., Clarke, C. J., & Rice, W. K. M. 2007, MNRAS, 374, 590

Lodato, G., & Rice, W. K. M. 2004, MNRAS, 351, 630

—. 2005, MNRAS, 358, 1489

Lubow, S. H., Seibert, M., & Artymowicz, P. 1999, ApJ, 526, 1001

Lynden-Bell, D., & Kalnajs, A. J. 1972, MNRAS, 157, 1

Marois, C., Macintosh, B., Barman, T., Zuckerman, B., Song, I., Patience, J., Lafrenière, D., & Doyon, R. 2008, Science, 322, 1348

Mason, B. D., Gies, D. R., Hartkopf, W. I., Bagnuolo, Jr., W. G., ten Brummelaar, T., & McAlister, H. A. 1998, AJ, 115, 821

Mason, B. D., Hartkopf, W. I., Gies, D. R., Henry, T. J., & Helsel, J. W. 2009, AJ, 137, 3358

Masset, F., & Snellgrove, M. 2001, MNRAS, 320, L55

Masset, F. S., & Papaloizou, J. C. B. 2003, ApJ, 588, 494

Mathieu, R. D. 1994, ARA&A, 32, 465

Matsumoto, T., & Hanawa, T. 2003, ApJ, 595, 913

Matzner, C. D. 2007, ApJ, 659, 1394

Matzner, C. D., & Levin, Y. 2005, ApJ, 628, 817

Matzner, C. D., & McKee, C. F. 2000, ApJ, 545, 364

McCarthy, C., & Zuckerman, B. 2004, AJ, 127, 2871

McKee, C. F., & Ostriker, E. C. 2007, ARA&A, 45, 565

McKee, C. F., & Tan, J. C. 2002, *Nature*, 416, 59

—. 2003, ApJ, 585, 850

McLaughlin, D. E., & Pudritz, R. E. 1997, ApJ, 476, 750

Mellon, R. R., & Li, Z. 2008, ApJ, 681, 1356

Metchev, S. A., & Hillenbrand, L. A. 2009, ApJS, 181, 62

Mitchell, J. 1767, Philos. Trans. R. Soc., 76 , 97

Miyama, S. M., Hayashi, C., & Narita, S. 1984, ApJ, 279, 621

Moeckel, N., & Bally, J. 2007, ApJ, 656, 275

Moeckel, N., & Bate, M. R. 2010, MNRAS, 274

Monnier, J. D., & Millan-Gabet, R. 2002, ApJ, 579, 694

Myers, P. C., & Fuller, G. A. 1992, ApJ, 396, 631

Nakamoto, T., & Nakagawa, Y. 1994, ApJ, 421, 640

—. 1995, ApJ, 445, 330

Nakamura, F., & Li, Z.-Y. 2007, ApJ, 662, 395

Nelson, A. F. 2006, MNRAS, 373, 1039

Nero, D., & Bjorkman, J. E. 2009, ApJ, 702, L163

Nielsen, E. L., & Close, L. M. 2009, ArXiv e-prints

Offner, S. S. R., Klein, R. I., & McKee, C. F. 2008, ApJ, 686, 1174

Offner, S. S. R., Klein, R. I., McKee, C. F., & Krumholz, M. R. 2009a, ArXiv e-prints

—. 2009b, ApJ, 703, 131

Olmi, L., Cesaroni, R., Hofner, P., Kurtz, S., Churchwell, E., & Walmsley, C. M. 2003, A&A, 407, 225

Osorio, M., D'Alessio, P., Muzerolle, J., Calvet, N., & Hartmann, L. 2003, ApJ, 586, 1148

Padgett, D. L., Brandner, W., Stapelfeldt, K. R., Strom, S. E., Terebey, S., & Koerner, D. 1999, AJ, 117, 1490

Padoan, P., & Nordlund, Å. 2002, ApJ, 576, 870

Palla, F., & Stahler, S. W. 1992, ApJ, 392, 667

Papaloizou, J. C. B., & Lin, D. N. C. 1995, ARA&A, 33, 505

Patel, N. A., Curiel, S., Sridharan, T. K., Zhang, Q., Hunter, T. R., Ho, P. T. P., Torrelles, J. M., Moran, J. M., Gómez, J. F., & Anglada, G. 2005, *Nature*, 437, 109

Pelletier, G., & Pudritz, R. E. 1992, ApJ, 394, 117

Pessah, M. E., Chan, C.-k., & Psaltis, D. 2007, ArXiv e-prints, 705

Pinsonneault, M. H., & Stanek, K. Z. 2006, ApJ, 639, L67

Plume, R., Jaffe, D. T., Evans, N. J., I., Martin-Pintado, J., & Gomez-Gonzalez, J. 1997, ApJ, 476, 730

Pollack, J. B., Hubickyj, O., Bodenheimer, P., Lissauer, J. J., Podolak, M., & Greenzweig, Y. 1996, Icarus, 124, 62

Pollack, J. B., McKay, C. P., & Christofferson, B. M. 1985, Icarus, 64, 471

Porter, D. H., Pouquet, A., & Woodward, P. R. 1992, Physical Review Letters, 68, 3156

Price, D. J., & Bate, M. R. 2009, MNRAS, 398, 33

Rafikov, R. R. 2001, MNRAS, 323, 445

—. 2002, ApJ, 572, 566

—. 2005, ApJ, 621, L69

—. 2007, ApJ, 662, 642

—. 2009, ApJ, 704, 281

Rafikov, R. R., & De Colle, F. 2006, ApJ, 646, 275

Rees, M. J. 1976, MNRAS, 176, 483

Rice, W. K. M., Armitage, P. J., Bate, M. R., & Bonnell, I. A. 2003, MNRAS, 339, 1025

Rice, W. K. M., Lodato, G., & Armitage, P. J. 2005, MNRAS, 364, L56

Robitaille, T. P., Whitney, B. A., Indebetouw, R., & Wood, K. 2007, ApJS, 169, 328

Rodríguez, L. F., Garay, G., Brooks, K. J., & Mardones, D. 2005, ApJ, 626, 953

Ryu, D., & Goodman, J. 1992, ApJ, 388, 438

Safronov, V. S. 1960, Annales d'Astrophysique, 23, 979

Savonije, G. J., Papaloizou, J. C. B., & Lin, D. N. C. 1994, in NATO ASIC Proc. 417: Theory of Accretion Disks - 2, ed. W. J. Duschl, J. Frank, F. Meyer, E. Meyer-Hofmeister, & W. M. Tscharnuter, 363–+

Sellwood, J. A. 2010, ArXiv e-prints

Sellwood, J. A., & Carlberg, R. G. 1984, ApJ, 282, 61

Semenov, D., Henning, T., Helling, C., Ilgner, M., & Sedlmayr, E. 2003, A&A, 410, 611

Shakura, N. I., & Sunyaev, R. A. 1973, A&A, 24, 337

Shepherd, D. S., Claussen, M. J., & Kurtz, S. E. 2001, Science, 292, 1513

Shetty, R., & Ostriker, E. C. 2006, ApJ, 647, 997

Shlosman, I., & Begelman, M. C. 1987, *Nature*, 329, 810

Shu, F., Najita, J., Ostriker, E., Wilkin, F., Ruden, S., & Lizano, S. 1994, ApJ, 429, 781

Shu, F. H. 1977a, ApJ, 214, 488

—. 1977b, ApJ, 214, 488

Shu, F. H., Galli, D., Lizano, S., Glassgold, A. E., & Diamond, P. H. 2007a, ApJ, 665, 535

—. 2007b, ArXiv e-prints

Shu, F. H., Tremaine, S., Adams, F. C., & Ruden, S. P. 1990, ApJ, 358, 495

Stamatellos, D., & Whitworth, A. P. 2009, MNRAS, 392, 413

Tan, J. C., & Blackman, E. G. 2005, MNRAS, 362, 983

Tan, J. C., Krumholz, M. R., & McKee, C. F. 2006, ApJ, 641, L121

Tan, J. C., & McKee, C. F. 2004, ApJ, 603, 383

Terebey, S., Shu, F. H., & Cassen, P. 1984, ApJ, 286, 529

Tobin, J. J., Hartmann, L., Looney, L. W., & Chiang, H. 2010, ApJ, 712, 1010

Tohline, J. E. 1981, ApJ, 248, 717

Toomre, A. 1964, ApJ, 139, 1217

—. 1977, ARA&A, 15, 437

Toomre, A. 1981, in Structure and Evolution of Normal Galaxies, ed. S. M. Fall & D. Lynden-Bell, 111–136

Toro, E. F. 1997, Riemann Solver and Numerical Methods for Fluid Dynamics (Springer-Verlag Telos)

Torrelles, J. M., Patel, N. A., Curiel, S., Ho, P. T. P., Garay, G., & Rodríguez, L. F. 2007, ApJ, 666, L37

Tout, C. A., Pols, O. R., Eggleton, P. P., & Han, Z. 1996, MNRAS, 281, 257

Truelove, J. K., Klein, R. I., McKee, C. F., Holliman, II, J. H., Howell, L. H., & Greenough, J. A. 1997, ApJ, 489, L179+

Truelove, J. K., Klein, R. I., McKee, C. F., Holliman, II, J. H., Howell, L. H., Greenough, J. A., & Woods, D. T. 1998, ApJ, 495, 821

Tsuribe, T., & Inutsuka, S.-I. 1999a, ApJ, 526, 307

—. 1999b, ApJ, 523, L155

Turner, J. L., Beck, S. C., & Ho, P. T. P. 2000, ApJ, 532, L109

van den Bergh, S., Morbey, C., & Pazder, J. 1991, ApJ, 375, 594

Vorobyov, E. I., & Basu, S. 2005, ApJ, 633, L137

—. 2006, ApJ, 650, 956

—. 2007, MNRAS, 381, 1009

—. 2008, ApJ, 676, L139

Walch, S., Burkert, A., Naab, T., & Gritschneder, M. 2009a, ArXiv e-prints

Walch, S., Burkert, A., Whitworth, A., Naab, T., & Gritschneder, M. 2009b, MNRAS, 400, 13

Webbink, R. F. 1985, Stellar evolution and binaries, ed. Pringle, J. E. & Wade, R. A., 39–+

Whitney, B. A., & Hartmann, L. 1993, ApJ, 402, 605

Williams, J. P., & Myers, P. C. 1999, ApJ, 511, 208

Wolfire, M. G., & Cassinelli, J. P. 1987, ApJ, 319, 850

Youdin, A. N., & Shu, F. H. 2002, ApJ, 580, 494

Zhang, Q., Hunter, T. R., Sridharan, T. K., & Ho, P. T. P. 2002, ApJ, 566, 982

Zhu, Z., Hartmann, L., & Gammie, C. 2008, ArXiv e-prints

Zuckerman, B., & Song, I. 2009, A&A, 493, 1149